NASA

Technical Memorandum **80253**

Atmospheric and Oceanographic Research Review - 1978

Laboratory for Atmospheric Sciences Modeling and Simulation Facility

DECEMBER 1978

National Aeronautics and
Space Administration

Goddard Space Flight Center
Greenbelt, Maryland 20771

TM80253

ATMOSPHERIC AND OCEANOGRAPHIC RESEARCH REVIEW

- 1978 -

LABORATORY FOR ATMOSPHERIC SCIENCES
MODELING AND SIMULATION FACILITY

DECEMBER 1978

GODDARD SPACE FLIGHT CENTER
GREENBELT, MARYLAND

TABLE OF CONTENTS

TABLE OF CONTENTS (Continued)

TABLE OF CONTENTS (Continued)

I. INTRODUCTION

I. INTRODUCTION

The global atmospheric and oceanographic research activities of the Goddard Institute for Space Studies were transferred to the Modeling and Simulation Facility of the new Goddard Laboratory for Atmospheric Sciences (GLAS) in 1977.

This Research Review presents a synopsis of studies conducted at the Facility during the past year. The Review is organized according to three research areas: global weather, ocean/air interactions, and climate. A list of recent publications by the staff scientists and visiting scientists is presented at the end of the Review.

II. GLOBAL WEATHER

MODEL-DEPENDENCE STUDIES OF THE EFFECTS OF SOUNDING TEMPERATURE ASSIMILATION ON WEATHER FORECASTING

(M. Ghil, M. Halem, and R. Atlas)

In comparing various methods for the assimilation of remote sounding information into numerical weather prediction models, the problem of model dependence for the different results obtained is clearly important. Most assimilation experiments have not addressed this problem directly, every research and development group working essentially with one numerical model.

GLAS has started to investigate two aspects of the model dependence question: (1) the effect of increasing horizontal resolution within a given model on the assimilation of sounding data, and (2) the effect of using two entirely different models with the same assimilation method and sounding data. In order to study the first aspect, GLAS has applied its four-dimensional (4-D) time-continuous statistical assimilation method (SAM, Ghil et al., 1979) to the assimilation of sounding data from the Data Systems Tests (DST) period DST-6 (February 1976) into the GLAS general circulation model with a coarse resolution (4°lat.x5°long.) and with a fine resolution (2.5°lat.x3°long.). To study the second aspect of model dependence, an asynoptic, time-continuous successive correction method (SCM, Ghil et al., 1979) was applied to the global, ninelevel, primitive-equation model of the U. S. National Meteorological Center (NMC, Stackpole, 1976). Results of SCM assimilations with the latter model are compared with those of previous SCM experiments with DST-6 data using the GLAS coarse-mesh model.

Preliminary results of comparisons between SAM assimilations with the coarse-mesh and the fine-mesh GLAS model show that increased model resolution does not affect the impact of satellite data on weather forecasts in any negative way; the effects of increased resolution and of satellite data assimilation are cumulative: they both tend to improve forecasting accuracy by a similar fractional amount. This fact is reflected in the usual numerical measures of forecast accuracy, viz., RMS errors and S1 skill scores. It is also reflected in synoptic-case studies of the large-scale forecast fields.

Assimilation cycles were run using data from January 29 until February 21, 1976, with both the coarse and the fine GLAS models. For each model resolution, one cycle was run including all data from the NOAA-4 and Nimbus-6 satellites, and another one was run with the same data, but excluding the temperature sounding information: they are referred to, respectively, as the 2SAT and NOSAT cycle. For each one of these four experiments, 72-hour forecasts were performed from the analyses produced by the corresponding assimilation cycle at 48-hour intervals, starting on February 1. The forecasts were verified at 48 hours

and at 72 hours against NMC operational analyses. The quantities verified and regions of verification are the same as in Ghil et al. (1979).

The results are summarized in Table 1, according to the methods outlined in Ghil et al. (1979). It is seen that the effect of model improvement, specifically increased resolution on the one hand, and utilization of satellite data on the other, act both in the direction of improving the forecast accuracy. In fact, the two effects appear to be nearly additive, as indicated by a comparison of the results in the last three rows of the table. Note also that the 2SAT experiment 2F, with the fine model, consistently gave impacts that are significantly higher than those of the corresponding experiment with the coarse model 2C, when measured against the common standard of the coarse NOSAT experiment 0C (viz. the second and the last row of the table).

Table 1. Summary of Results for Model-Dependence Experiments.

Experiment No.	Comparison Code	Impact (%)		Statistical Signif. (average/standard error)	
		S_1	RMS	S_1	RMS
0C	0C	0	0	-	-
2C	2CC	4.46	12.41	1.85	2.59
0F	0F	0	0	-	-
	0FC	5.86	7.30	1.62	1.35
2F	2FF	4.49	7.98	1.40	1.71
	2FC	10.01	14.47	2.67	2.47

The symbol 0 stands for a NOSAT experiment, 2 stands for a 2SAT experiment; the symbol C stands for an experiment with the coarse model, F for one with the fine model. The results of the 2SAT experiment with the fine model 2F were compared with those of the coarse NOSAT experiment 0C and with those of the fine NOSAT experiment 0F; these comparisons are denoted by 2FC and by 2FF, respectively. The NOSAT experiment 0F appears both as a control for 2F, viz., as 0F, and in a comparison versus the coarse NOSAT 0C, viz., as 0FC.

Previous results with the GLAS coarse-mesh model (Ghil et al., 1979) indicated that by using a time-continuous 4-D method with statistical features (SAM or SCM) the assimilation of remote sounding temperature data can lead to numerical forecasts that show a modest, but statistically significant, improvement over forecasts started from analyzed fields not containing the remote sounding information. To determine whether the translation of GLAS methods into operational practice is feasible, it was decided to apply them to the model used by NMC to produce their operational analyses (Stackpole, 1976), which shall be called in the sequel the 9LG (nine-level global) model.

As a first step, SCM was adapted to and reprogrammed for the 9LG model. Numerous problems arose in the adaptation, due to differences between the models, and some of these problems await better solutions than the ones given to them at the present. NOSAT and 2SAT assimilation cycles were started and carried out from February 1 until February 7, 1976, using the same data sets as for the corresponding GLAS model cycles. Forecasts were carried out from the analyzed fields generated on February 3, 5, and 7. These experiments are being continued and will be discussed more completely in a future publication.

At this point, a comparison of results with those of SCM experiments performed on the GLAS model (Ghil et al., 1979) shows that the differences between analyzed fields from the NOSAT and 2SAT cycles do not seem to depend on the model: the differences produced by the utilization method of satellite data are of similar magnitude for the 9LG model as they were for the GLAS 4°x5° model. These differences range up to 100 m in the 500 mb geopotential height field, especially over the North Pacific, where conventional data coverage is relatively poor. These initial state differences lead also to correspondingly large differences in 48-hour and 72-hour forecasts. GLAS intends to examine further the question of whether or not these differences are due solely to the assimilation of satellite data.

The GLAS experiments on model dependence of sounding temperature assimilation suggest the following tentative conclusions:

1. That model improvement, as exemplified by increased resolution, can act in the same direction as judicious 4-D assimilation of remote sounding information to improve 2-3 day numerical weather forecasts. The effect of model improvements and the effect of an observational data base augmented by the proper inclusion of sounding temperatures, when combined, can lead to numerical prognoses which achieve improvements of meteorological significance more easily than either effect separately.

2. That the time-continuous 4-D methods developed at GLAS have similar beneficial effects when used in the assimilation of remote sounding information into NWP models with very different

numerical and physical characteristics. This suggests the possibility of the eventual implementation of these time-continuous methods in an operational environment, in which they might contribute to noticeable improvement in routine weather forecasting.

References

Ghil, M., R. Dilling, and H. Carus, 1977: Proc. 5th Conf. Probability Stat. Atmos. Sci., Amer. Meteor. Soc., Boston, MA, pp. 320-324.

_____, M. Halem, and R. Atlas, 1979: Time-continuous assimilation of remote-sounding data and its effect on weather forecasting. Mon. Wea. Rev., in press.

Halem, M., M. Ghil, R. Atlas, J. Susskind, and W. J. Quirk, 1978: The GISS Sounding Temperature Impact Test. NASA Tech. Memo. 78063, 421 + viii pp.

_____, M. Ghil, and R. Atlas, 1978: Some experiments on the effect of remote sounding data upon weather forecasting. Remote Sensing of the Atmosphere: Inversion Methods and Applications, A. L. Fymat and V. E. Zuev., eds., Elsevier, Amsterdam.

Stackpole, J. D., 1976: Proc. 6th Conf. Weather Forecasting Analysis, Amer. Meteor. Soc., Boston, MA, pp. 112-116.

SYNOPTIC EVALUATION OF THE IMPACT OF SOUNDING DATA INSERTIONS AND INCREASED HORIZONTAL RESOLUTION ON GLAS MODEL FORECASTS

(R. Atlas, R. Rosenberg, and M. Eaton)

The impact of satellite-derived temperature soundings on short-term (0-72 hour) weather forecasting has been expressed in terms of statistical measures of forecast accuracy, regional differences in prognostic flow patterns, and automated local forecasts of precipitation occurrence (Halem, et al., 1978). As an additional measure of the impact on forecast utility, a synoptic evaluation was performed by directly comparing the prognostic charts generated from 2SAT and NOSAT initial conditions (with and without satellite data insertions respectively) with each other and with the corresponding NMC analyses for verification. Comparisons were made every 12 hours for a variety of prognostic fields for eleven different forecasts from February 1976. The results of our comparisons for the sea-level pressure and 500 mb height fields generated from the GLAS 4° latitude by 5° longitude model and verified over North America are presented in Table 1.

This table gives the consensus of experienced forecasters in their subjective assessment of the prognostic charts. During this phase of the evaluation, the forecasters had no knowledge of which prognostic charts were based on 2SAT initial conditions. Following Atkins and Jones (1975), each forecast has been classified according to the following scale:

A - 2SAT significantly better than NOSAT,
B - 2SAT better than NOSAT,
C - 2SAT and NOSAT of equal quality,
D - 2SAT worse than NOSAT,
E - 2SAT much worse than NOSAT.

This classification system is designed to represent the relative utility of the prognostic charts generated from 2SAT and NOSAT initial conditions. The term significant in categories A and E implies that major prognostic differences have occurred. Categories B and D imply that there has been only a minor alteration of the prognostic pattern or that the net impact for the entire forecast region is small.

From the table it can be seen that at sea level, none of the prognostic charts have been classified as A or E and that an almost equal number of B and D marks have been assigned. Although no significant impact has occurred at this atmospheric level, a tendency for more beneficial impacts at 48, 60, and 72 hours is evident.

At 500 mb, two 72-hour prognostic charts have been classified as A and there were no E marks. In addition more than three times as many B than D marks have been assigned. Impacts at this level are most consistently beneficial at 60 and 72 hours.

Table 1. Results of a subjective assessment of 2SAT and NOSAT forecasts using the GLAS 4°x5° model.

1a. Sea Level Pressure

CATEGORY	12h	24h	36h	48h	60h	72h	TOTAL*
A	0	0	0	0	0	0	0
B	0	1	1	4	3	4	13
C	8	8	7	5	6	5	39
D	3	2	3	2	2	2	14
E	0	0	0	0	0	0	0

1b. 500 mb Geopotential Height

CATEGORY	12h	24h	36h	48h	60h	72h	TOTAL*
A	0	0	0	0	0	2	2
B	2	2	2	3	4	4	17
C	8	9	9	5	7	4	42
D	1	0	0	3	0	1	5
E	0	0	0	0	0	0	0

* Total number of prognostic charts in each category.

A synoptic evaluation in the same manner as that described above has also been conducted in order to evaluate the effect of increasing the horizontal resolution of the GLAS model and to assess the impact of sounding data with this higher resolution model. Table 2 presents the results of changing from a 4°x5° to a 2 1/2°x3° horizontal grid. It is clear from the table that the overall effect of increasing the horizontal resolution is to improve the quality of both sea-level and 500 mb prognoses.

Table 3 presents the impact of satellite sounding data insertions on synoptic forecasts with the 2 1/2°x3° model. Comparison of this table with Table 1 reveals that a more substantial beneficial impact from satellite data has resulted with the use of the higher resolution model. No major changes for the worse have resulted from the inclusion of satellite data while five sea-level and four 500 mb prognostic charts have been significantly improved. Once again the effect of satellite data is largest during the latter half of the forecast period.

As an illustration of the impact of satellite-derived temperature soundings on prognostic flow patterns, the 72-hour forecast from February 19, 00Z is included in this paper. This was a case in which large beneficial impact was also evident in the statistical scores. At the initial time of the forecast, the analysis showed a moderately intense low-pressure system located off the northwest coast of the United States. As this system moved inland, a new low developed along an already existing stationary front and became the dominant feature. During the first 48 hours of the model forecast, only slight differences existed between the 2SAT and NOSAT sea-level prognoses as both correctly predicted the intensification and southeastward displacement of this low. After 48 hours, however, a radically different pattern emerged: the 2SAT forecast predicted the low to recurve and accelerate to the northeast, while the NOSAT forecast failed to move the low center. The NMC operational PE hemispheric forecast model also failed to move the low northeastward. This low was associated with both heavy snow and severe local storms during its displacement, and significantly different local weather forecasts of those major events would have resulted from the different prognoses.

Figures 1a and 1b depict the 72-hour sea-level pressure prognoses from February 19 for the 2SAT and NOSAT cases, respectively, while the corresponding analysis is depicted in Figure 1c. Figure 1d shows the NMC operational 72-hour forecast. A comparison of these charts reveals the very significant improvement in the displacement of the low-pressure system that resulted from the inclusion of satellite data. Substantial improvements in the displacement of the associated upper-level trough and vorticity maximum (charts not shown) were also observed.

Table 2. Results of a subjective assessment of NOSAT forecasts from the GLAS 2½°x3° and 4°x5° models.

2a. Sea Level Pressure

CATEGORY	12h	24h	36h	48h	60h	72h	TOTAL*
A	0	0	1	1	0	0	2
B	2	6	3	2	3	4	20
C	6	3	5	6	7	3	30
D	2	1	1	1	0	1	6
E	0	0	0	0	0	0	0

2b. 500 mb Geopotential Height

CATEGORY	12h	24h	36h	48h	60h	72h	TOTAL*
A	0	0	0	1	0	1	2
B	0	2	4	4	6	1	17
C	10	7	5	5	4	5	36
D	0	1	1	0	0	1	3
E	0	0	0	0	0	0	0

* Total number of prognostic charts in each category.

Table 3. Results of a subjective assessment of 2SAT and NOSAT forecasts using the GLAS 2½°x3° model.

3a. Sea Level Pressure

CATEGORY	12h	24h	36h	48h	60h	72h**	TOTAL*
A	0	0	0	1	2	1	5
B	0	2	2	2	1	3	10
C	11	8	7	7	5	5	43
D	0	1	2	1	3	1	8
E	0	0	0	0	0	0	0

3b. 500 mb Geopotential Height

CATEGORY	12h	24h	36h	48h	60h	72h**	TOTAL*
A	0	0	0	1	1	2	4
B	0	1	3	2	3	1	10
C	11	9	7	7	6	5	45
D	0	1	1	1	1	0	4
E	0	0	0	0	0	0	0

* Total number of prognostic charts in each category.
**3 forecasts missing.

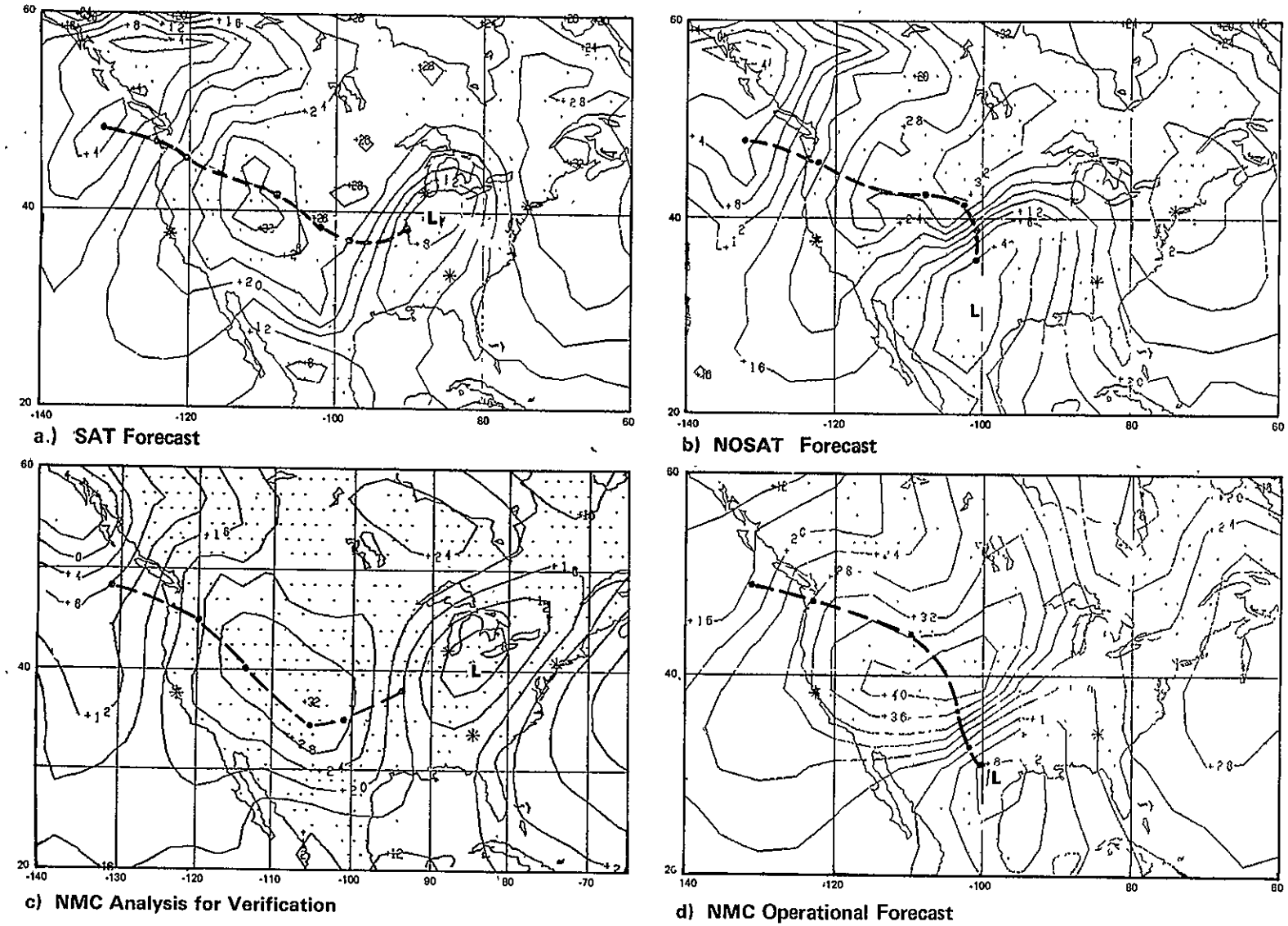

Figure 1. Sea level pressure plots for 0000GMT 22 February 1976. Figure 1a shows the 72h forecast from SAT initial data at 0000GMT 19 February 1976; Figure 1b shows the corresponding NOSAT forecast; Figure 1c shows the verification analysis (operational NMC analysis); Figure 1d shows the NMC operational 72h forecast. Dots represent past positions of low at 12h intervals.

References

Atkins, M. J., and M. V. Jones, 1975: An experiment to determine the value of satellite infrared spectrometer (SIRS) data in numerical forecasting. Meteor. Mag., 104, pp. 125-142.

Halem, M., M. Ghil, R. Atlas, J. Susskind, and W. J. Quirk, 1978: The GISS Sounding Temperature Impact Test. NASA Tech. Memo. 78063, 421 + xiii pp.

QUANTITATIVE PRECIPITATION FORECASTS FROM THE GLAS MODEL

(R. Atlas)

The skill of the GLAS 4° latitude by 5° longitude general circulation model (GCM) model in predicting precipitation amount at U. S. gridpoints has been evaluated for 10 of the forecasts that were generated during the February 1976 DST period. Observed accumulations of precipitation at each of the 57 gridpoints located within the continental U. S. were obtained by first subjectively drawing isohyets on facsimile charts of observed 24-hour accumulation at first-order U. S. stations, and then interpolating these observations to the model gridpoints. Since these observations cover the 24-hour period beginning at 1200 GMT while all of the forecasts in the GLAS sample were generated from 0000 GMT, only the 12-36 hour and 36-60 hour forecasts of precipitation amount were verified.

Figures 1 through 4 present the model's skill in forecasting measurable precipitation >.01 in., and precipitation amounts of >.1 in. for each of the 24-hour periods. The three curves in the lower portion of each figure are:

- FC - the number of gridpoints at which precipitation in a given category was forecast correctly,
- PF - the total number of gridpoints at which precipitation in a given category was forecast,
- PO - the total number of gridpoints at which precipitation in a given category was observed.

The ratio PF/PO is the bias and represents the degree to which the model overforecasts or underforecasts the extent of precipitation. This is indicated by the distance between the PF and PO curves on the graph. FC/PO is called the prefigurence and measures the areal extent of precipitation that is correctly forecast in each category; FC/PF is the post agreement and measures the percentage of precipitation forecasts which verify. These latter measures are represented by the distance between the FC and PO curves and FC and PF curves, respectively.

The bias, prefigurence, and post agreement can be combined into a single ratio, known as the threat score (Th), and this latter quantity is plotted as the upper curve in Figures 1 through 4. The threat score is defined as follows:

$$Th = FC/(PF + PO - FC)$$

A threat score of zero represents no skill, while higher values denote increasing skill.

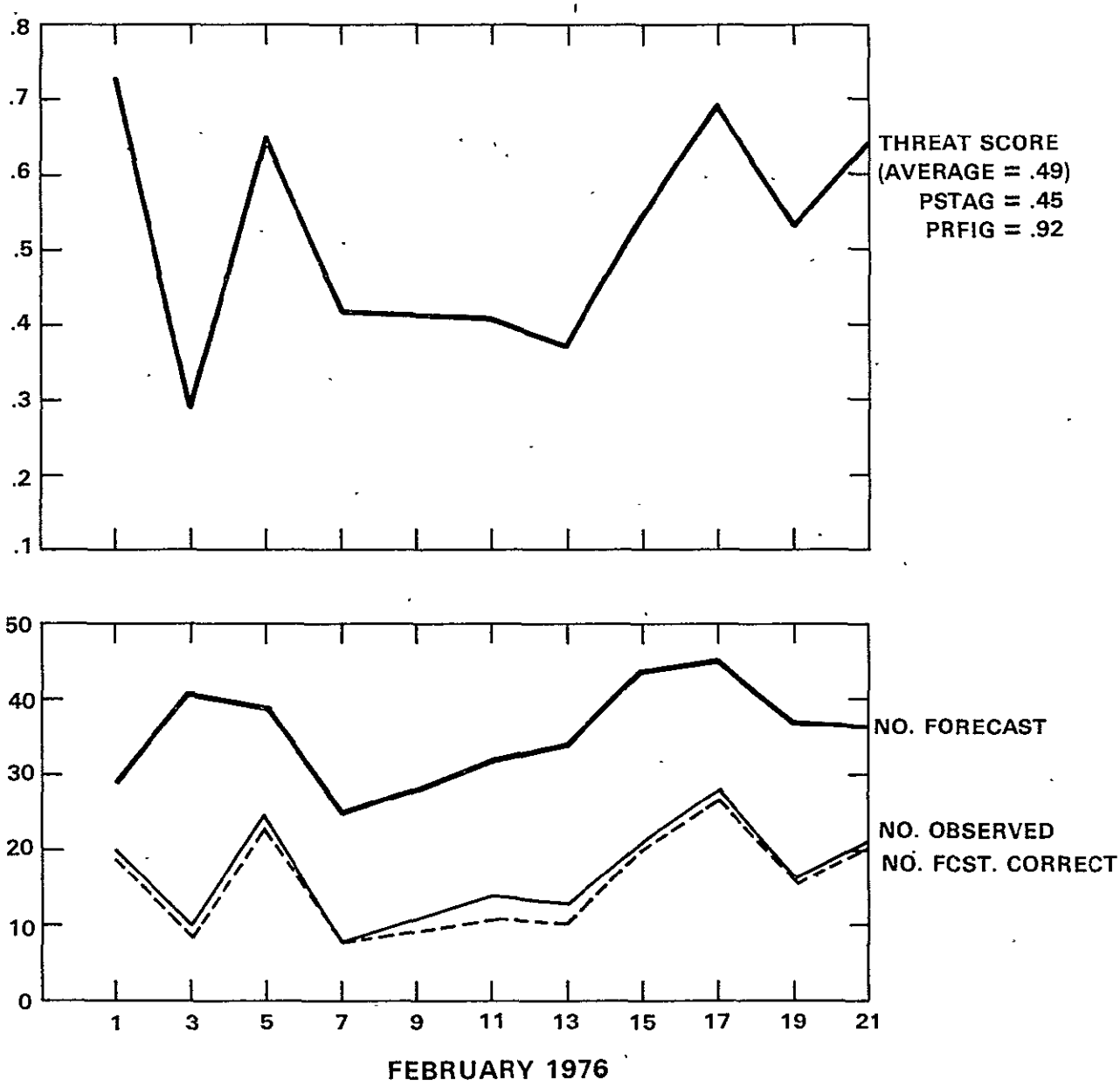

Figure 1. Verification of 12-36 hour QPF for $\geq$ .01".

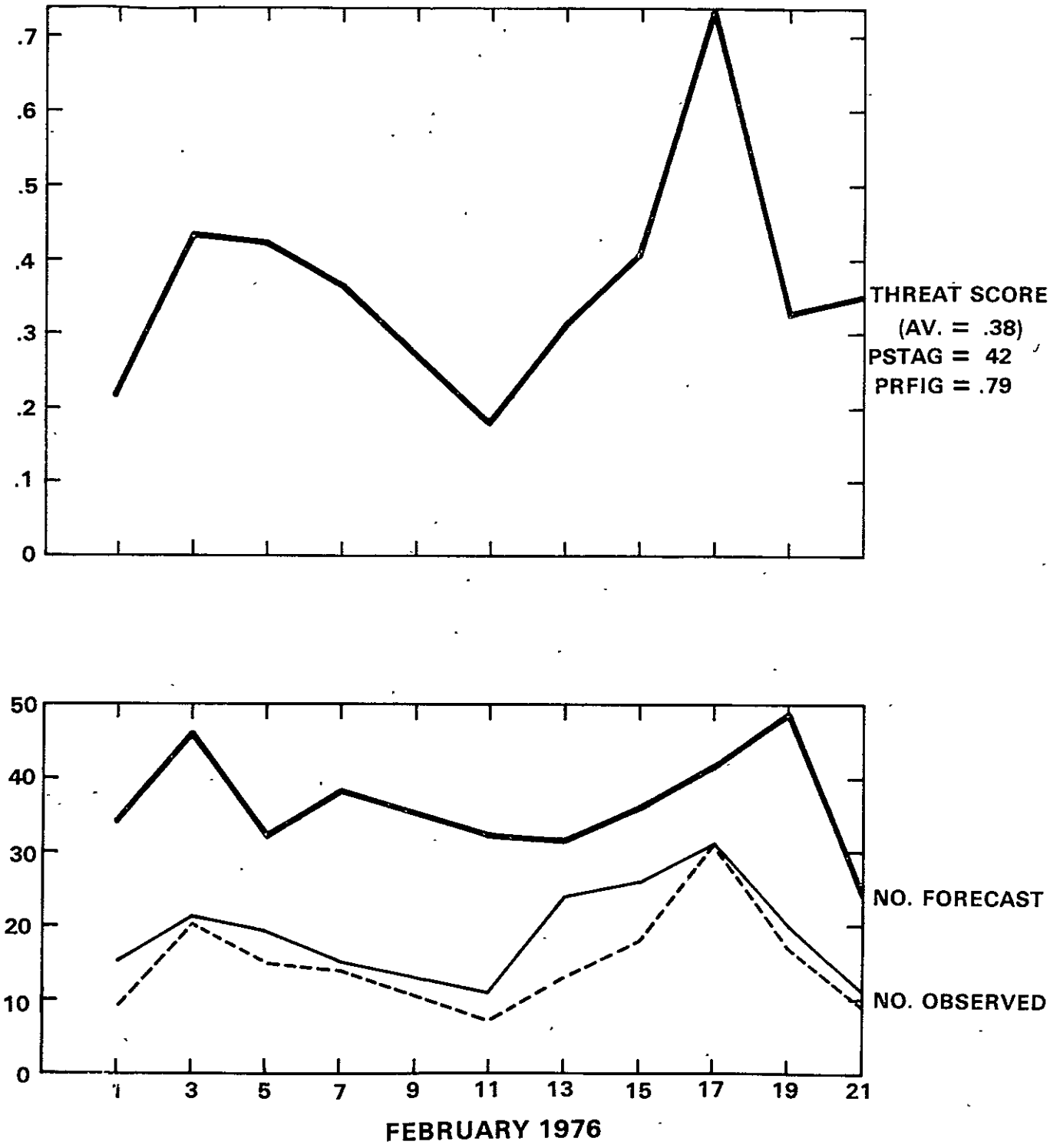

Figure 2. Verification of 36-60 hour QPF for $\geq$ .01".

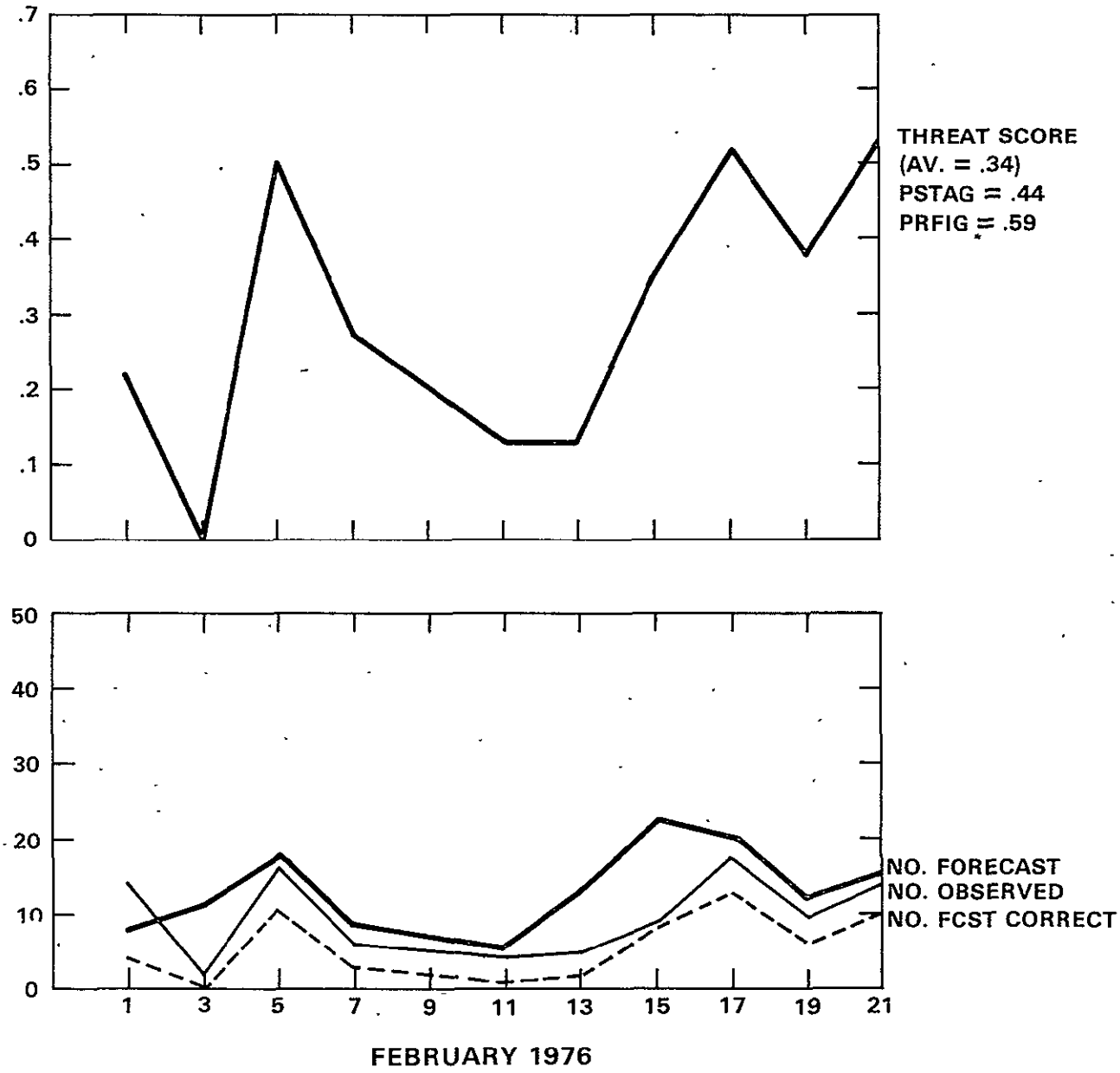

Figure 3. Verification of 12-36 hour QPF for ≥ .1".

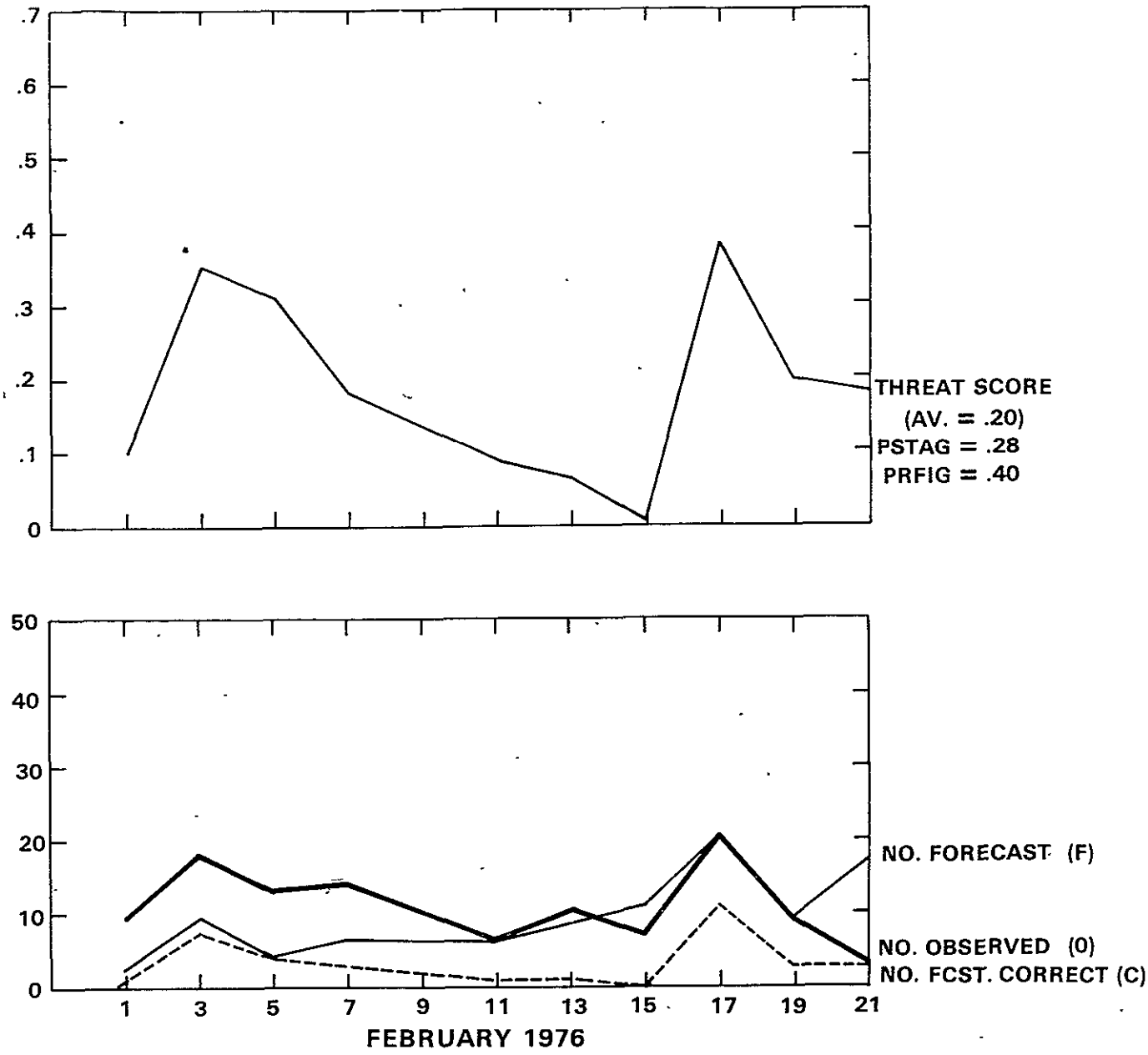

Figure 4. Verification of 36-60 hour QPF for ≥ .1".

From Figures 1 and 2, it can be seen that the GLAS model possesses a high degree of skill in forecasting the areas where measurable precipitation occurs (as measured by the prefigurence), but that a considerable bias toward overforecasting exists. The large degree of day-to-day variability of the threat score is due almost entirely to changes in the amount of bias of the forecasts. The average threat score for the entire sample compares favorably with results previously reported by Druyan, et al. (1975).

Figures 3 and 4 show that the GLAS model possesses considerably less skill in predicting precipitation amounts of >.1 in. even though the bias of the forecasts has been substantially reduced. It is interesting to note that the loss of skill in going to higher precipitation amounts is greater than the loss of skill due to time, as can be seen from a comparison of the threat scores in Figures 2 and 3. This loss of skill and decrease in overforecasting continues as the precipitation amount category increases. The GLAS model failed to predict any of the gridpoints in this sample with precipitation amounts of >1 in. In this category FP, FC, and Th were equal to zero.

All of the forecasts described above were generated from NOSAT initial conditions, in which no satellite-derived temperature soundings were included. When the forecasts were rerun from SAT initial conditions, with satellite soundings inserted, a small improvement in the average threat score of +3 percent occurred for the entire sample. A time stratification of the impact revealed a slight decrease in skill of -2 percent in the 12-36 hour predictions of >.01 in. and >.1 in. combined, and a more significant increase in skill of +6 percent in the 36-60 hour predictions. This agrees with our synoptic evaluations which indicated the maximum impact of sounding data over the U.S. to occur in the latter half of the forecast period.

Reference

Druyan, L. M., R. C. J. Somerville, and W. J. Quirk (1975): Extended range forecasts with the GISS model of the global atmosphere. Mon. Wea. Rev., 103, pp. 779-795.

DEVELOPMENT OF A COMPUTERIZED PROCEDURE FOR THE PREDICTION OF SEVERE LOCAL STORM POTENTIAL

(R. Atlas)

The development of severe thunderstorms and tornadoes occurs on a much smaller scale than is currently resolved by the operational observational network or numerical weather prediction (NWP) models. However, these phenomena are usually imbedded within a larger region of instability and destabilization, and, therefore, the prediction of severe local storm potential depends to a large extent upon the ability to predict the synoptic scale setting favorable for intense convective development.

If it is assumed that equivalent potential temperature (θe) is conservative following the motion and let $\sigma = \partial \theta e / \partial z$, evaluated between the 850 mb and 500 mb levels, represent convective instability (negative if unstable), then the following equation for local destabilization may be readily derived:

$$\frac{\partial \sigma}{\partial t} = -\frac{\partial}{\partial z}(\vec{V} \cdot \nabla \theta e) - \frac{\partial (w\sigma)}{\partial z}$$

(1) (2)

This equation states that the local rate of change of convective instability depends upon the effects of differential equivalent potential temperature advection (term 1) and vertical stability advection (term 2). Accordingly, whenever an initially unstable environment is coupled with increasing upward vertical motion with elevation in the lower atmosphere, then $-\frac{\partial}{\partial z}(\vec{V} \cdot \nabla \theta e)$ must be negative for convective instability to be increased or maintained. This occurs whenever there is a horizontal transport of warm, moist air at low levels of the atmosphere and/or cold, dry air at higher levels.

Previous studies have shown the tendency for severe weather to develop in regions of strong differential advection and have suggested utilizing differential advection as a severe storms predictor. According to Whitney and Miller (1956), differential advection increases the potential for severe convective activity in three ways: (i) it decreases the amount of work required to lift low level air; (ii) it decreases the height through which the air must be lifted before it will rise freely; and (iii) it increases the amount of energy that is available to a convective system. This process is often initiated by the movement of a cold trough toward the central United States (Newton, 1963) but may be present in a variety of synoptic situations.

The purpose of this investigation is to determine the magnitudes of convective instability and differential advection associated with severe storm developments and to develop a computerized procedure for evaluating the potential for severe storms for a particular area. To this end, it is necessary to determine (i) the percentage of severe local storm development in which differential advection plays a significant role, (ii) what parameters must be considered in conjunction with differential advection, (iii) with what resolution differential advection must be resolved, and (iv) how well current NWP models can predict differential advection.

A preliminary version of a computerized severe storm model (CSSM) was developed at the outset of this investigation in order to provide a logical framework for evaluating the relative utility of various large-scale indicators of severe storm potential. The model uses a grid system of 4° lat. by 5° long. to be compatible with the GLAS GCM, and covers the continental U.S. However, in this study only the 22 gridpoints east of 105°W longitude were considered. This area was chosen for its high frequency of severe weather and to mitigate the effects of topography. A second version of the CSSM compatible with the 2 1/2° latitude by 3° longitude version of the GLAS model is also being tested. In this case only the U. S. gridpoints east of 102°W are considered.

Input into the model consists of specific humidity, temperature, and wind velocity from either an objective analysis or numerical forecast tape. From these a storm potential index (SPI), differential advection (DA), convective instability (σ) and twelve other measures of instability or destabilization are derived. The calculation of storm potential for this initial version of CSSM was based to a large extent upon a diagnostic study of 20 different severe storm outbreaks by Goldstein (1976). In this study it was shown that in each of the outbreaks virtually all of the severe weather occurred within much larger regions where differential advection of -.5°C per hour between the 850 mb and 500 mb levels coincided with an initially unstable environment. Accordingly, the CSSM utilizes σ and DA as its primary indicators of storm potential. However, it also attempts to delineate the severe weather areas more precisely by considering conventional indicators as well. It begins by testing the model atmosphere for convective instability and differential advection in combination, and then tests for additional destabilizing effects due to vorticity advection and wind shear. On the basis of how these factors combine, a number of +1 to +12 for initially unstable situations or -1 to -12 for initially stable situations can be assigned to each grid box surrounding a model gridpoint, where ±12 indicates the highest potential in each case.

Two phases of experimentation have been partially completed. The first phase of testing of the CSSM has been to

conduct diagnostic studies to assess the potential usefulness of DA and σ as specified by GLAS model analyses. Since analyses can be considered as "perfect prognostic charts," this study can be used to determine the maximum predictive capability of the CSSM for medium-range forecasts (greater than 12 hours) or the actual predictive capability for short-range forecasts (0-12 hours).

Table 1 presents (in abridged form) some of the preliminary results of this study for the period February 2-29, 1976. During this period 109 severe thunderstorms and tornadoes were reported within the CSSM's region. From the table, it can be seen that negative differential advection occurred in a large percentage of the severe weather reports and that utilizing σ and DA in combination is considerably more useful than convective instability alone in specifying areas of severe weather potential. Modifications to the original SPI calculation are currently being made to reflect these results.

Table 1. Percentage of Storms Occurring 0-12 Hrs. After σ and DA Analysis.

DA	≤ -10	≤ -5	≤ 0	$\leq +5$	$\leq +10$	TOTAL
$\leq -1.$	21.1	0	11.0	13.9	9.1	55.1
$-.5$	0	4.6	0	0	10.1	14.7
0	0	0	1.8	11.0	1.8	14.6
$+.5$	0.9	13.8	0.9	0	0	15.6
TOTAL	22.0	18.4	13.7	24.9	21.0	100

In the second phase of experimentation, the CSSM has been applied to actual forecasts from the GLAS GCM. As an example of the skill of this model in predicting σ, DA, and absolute values of SPI (representing the combination DA with vorticity advection and wind shear), the mean absolute errors from the 72-hour forecast from February 19, 1976, 00Z (using the 2 1/2° x 3° version of the model) are presented in Figures 1 through 3. This period contained the largest of the severe storm outbreaks that occurred during February 1976 and also was a case in which a major improvement to the predicted development and displacement of synoptic scale features resulted from the insertion of satellite-derived temperature soundings in data sparse regions (Atlas, et al, 1978).

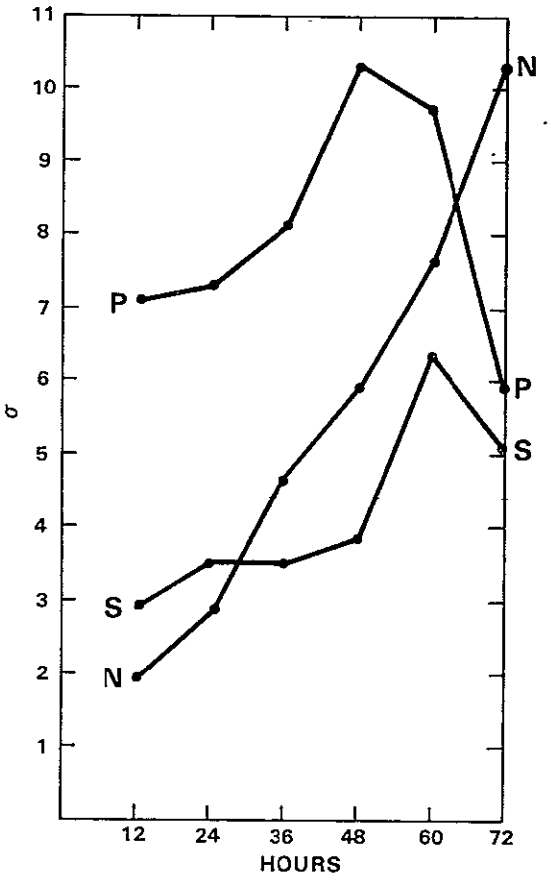

Figure 1. Mean absolute errors in the 72-hour prediction of convective instability (σ) from February 19, 1976 00Z.

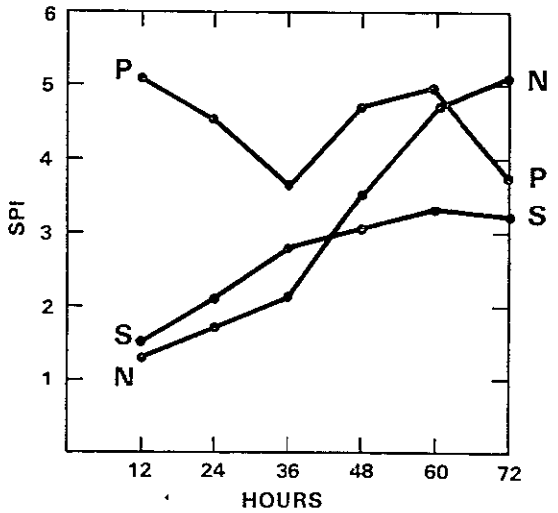

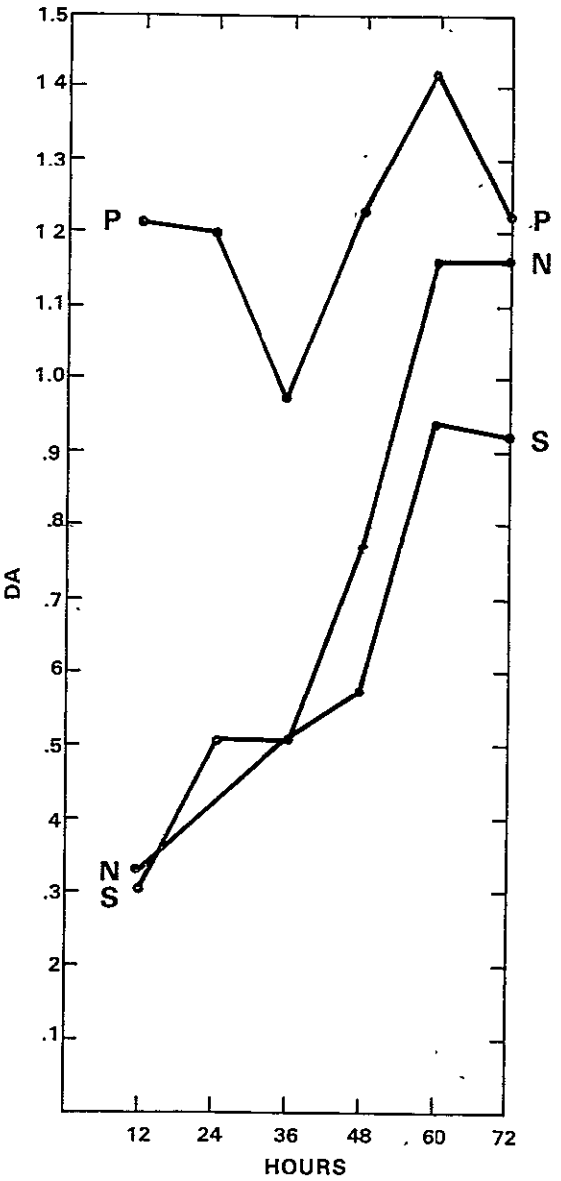

Figure 2. Mean absolute errors in the 72-hour prediction of differential advection (DA) from February 19, 1976 00Z.

Figure 3. Mean absolute errors in the 72-hour prediction of the storm potential index (SPI) from February 19, 1976 00Z.

Curves N and S represent the forecast errors resulting from NOSAT and SAT initial conditions, respectively, while curve P represents a persistence forecast for the same time period. A comparison of these curves in each of the figures reveals that both versions of the GLAS model possess considerable skill over persistence throughout the first 48 hours of the forecast, and that a significant reduction in the magnitude of the errors during the latter half of the forecast has resulted from the insertion of satellite-derived temperature soundings in data sparse regions. In this case the 48-60 hour predicted area of high severe storm potential generated from SAT initial conditions contained more than 70 percent of all reported severe thunderstorms and tornadoes while the corresponding NOSAT prediction accounted for only 40 percent of the severe reports.

References

Atlas, R., R. Rosenberg, and M. Eaton, 1978: Synoptic evaluation of the impact of sounding data insertions and increased horizontal resolution on GLAS Model forecasts. Research Review, GSFC.

Goldstein, M. G., 1976: Severe storm development and the importance of differential advection. Ph.D. Thesis, New York Univ.

Newton, C. W., 1963: Dynamics of severe convective storms. Meteor. Monographs, Vol. 5, No. 77.

Whitney, L. F., and J. E. Miller, 1956: Destabilization by differential advection in the tornado situation of June 8, 1953. Bull. of the Amer. Meteor. Soc., Vol. 37.

TROPICAL DISTURBANCES IN THE GLAS GCM SIMULATIONS

(M. A. Estoque)

An important aspect of general circulation modeling work that has not yet received sufficient attention is the verification of the model simulations of tropical weather disturbances. A 1-month study was conducted to examine the GLAS general circulation model (GCM) simulations of such disturbances. The area of study was limited to the tropical Pacific region, together with the so-called Indonesian Maritime Continent. This area extends from 90°E to 150°W longitude and from 25°S to 25°N latitude. The Indonesian region has been included because it is the strongest source of heat for the global atmosphere during the winter season. This heat source is, therefore, an important component for driving the general circulation of the atmosphere.

Some of the interesting questions that could eventually be answered by a study such as that envisioned above are:

> What types of synoptic scale disturbances are generated by the GLAS GCM? What are their characteristic three-dimensional structures, wavelengths, and speeds of propagation? What physical processes are responsible for their generation, maintenance, and dissipation? What large-scale flow parameters determine their wavelengths and phase speed?

Partial answers to the above questions are available from previous observational as well as theoretical studies. These studies indicate that tropical weather disturbances may be classified primarily into three categories: wavelike disturbances, vortices, and linear disturbances. The waves are characterized, in general, by cold troughs in the lower half of the troposphere; they are most intense near the 700 mb level. The typical wavelength is about 3000 Km and the phase speed is about 7 m sec^{-1} westward. Cloudiness and rainfall occur most often to the east of the surface trough. Vortices may be of two kinds--low-level and high-level cyclones. Low-level cyclones are warm-cored in the entire troposphere and are most intense in the middle and the upper troposphere. The best known example of the low-level cyclone is the hurricane. Upper level cyclones are cold-cored in the troposphere. They are most intense in the middle and the upper troposphere. In the last category, the linear disturbances are those whose cloudiness and rainfall patterns tend to be oriented along a line. A common example of a linear weather disturbance is the intertropical convergence zone (ITCZ). Another example is the shear line, which is simply an extension of a temperate latitude cold front into the tropics.

The specific objective of the initial study was to make a general survey of the types of tropical disturbances that

occur in the GLAS GCM simulations. For this purpose, the results of a numerical integration for a winter season were used. Simulated winds at individual gridpoints were available at 12 hourly intervals for various levels in the atmosphere. Other variables, such as temperature, surface pressure, specific humidity, and vertical velocity, were also available. It was noticed that the gridpoint distributions of these variables were characterized by large-amplitude, spurious waves with wavelengths equal to double the grid length. In order to eliminate these waves, Shuman's 9-point smoother was applied. Various types of analysis (e.g., streamline, time cross-sections) were done on the smoothed and unsmoothed array of gridpoint values. Some of the more interesting results of the analysis are presented below.

The results indicated, in general, that the three categories of tropical disturbances described above occurred in the GLAS GCM simulations. The streamline fields at the 900 mb level often showed vortices and the ITCZ. An example of a 900 mb map is shown in Figure 1. One may see two vortices, a cyclonic vortex (longitude 135°E, latitude 15°S) and an anticyclonic vortex (longitude 150°E, latitude 4°S). It is interesting to note the unusual wind convergence towards the center of the anticyclonic vortex. In the same figure, one may see the ITCZ along an east-west direction just south of the equator over the western and eastern sections of the region. The orientation and the location of the ITCZ is rather realistic. Wave-type disturbances may be seen in Figure 2; this map represents conditions near the 700 mb level. The axis of the troughs are indicated by dashed lines.

Although the results of the analysis presented above are very encouraging, there appear to be many unrealistic features of the simulations. One such feature is the abrupt changes in the wind with height. This is illustrated strikingly in Figure 3, which shows a vertical time cross-section over a gridpoint near the equator. In this diagram, the horizontal wind vector is drawn in the conventional meteorological sense, i.e., arrow pointing upward on the page means northward flow; downward means southward flow. Note especially the winds on the right half of the diagram. One can see changes from one direction to the opposite direction, going from Level 8 to Level 7. The same abrupt changes occur from Level 4 to Level 3. These anomalous changes in the wind with height may be due to numerical scheme for integrations.

Another unrealistic feature of the simulations is concerned with the motion of disturbances. It has been noted that the simulated disturbances tend to be stationary or move slowly eastward; whereas, in the real atmosphere, the disturbances almost always move westward in the tropics. This unrealistic characteristic of the simulations is illustrated in Figures 4

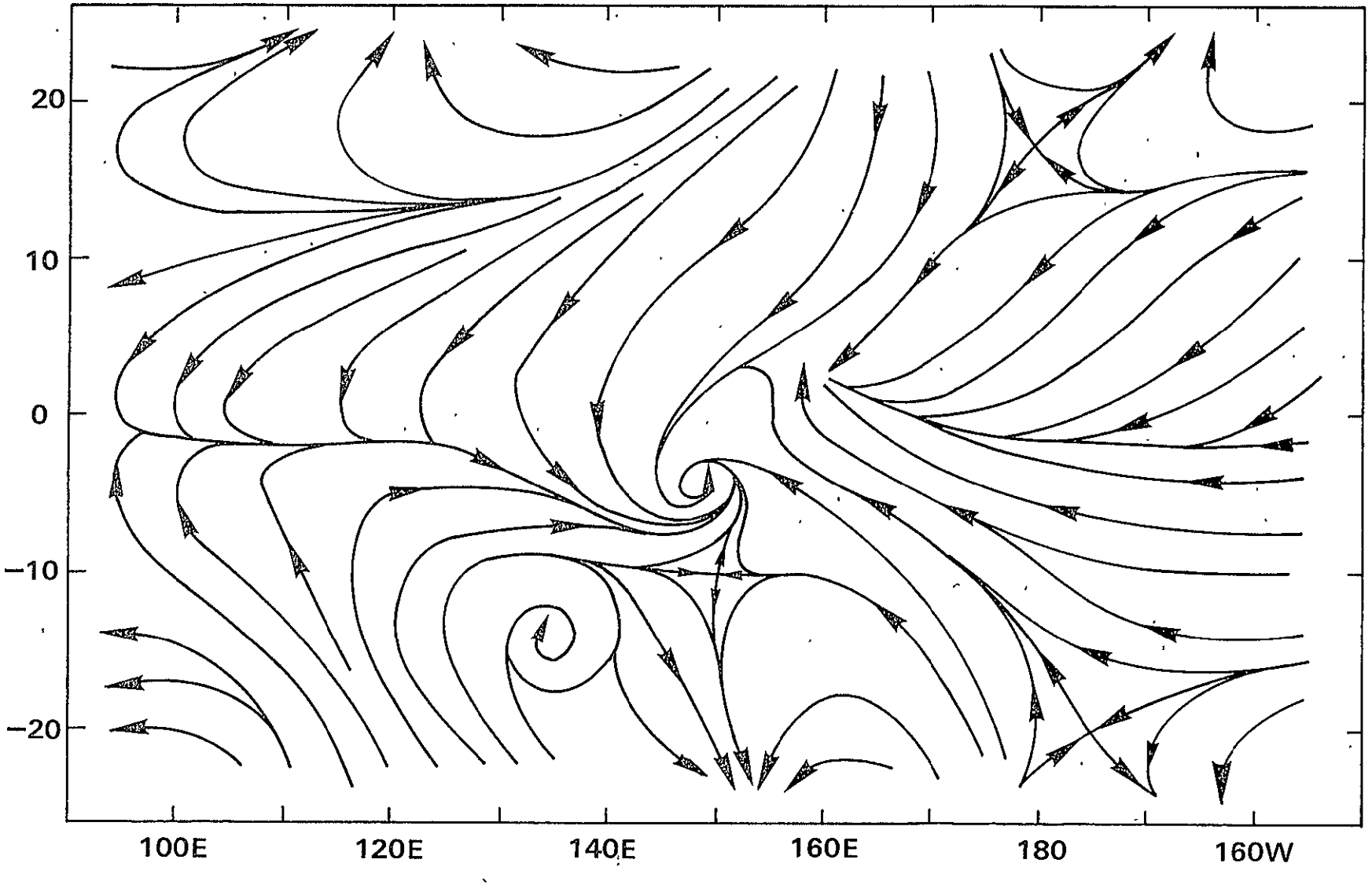

Figure 1. Simulated 900 mb synoptic streamline map for the Pacific Ocean.

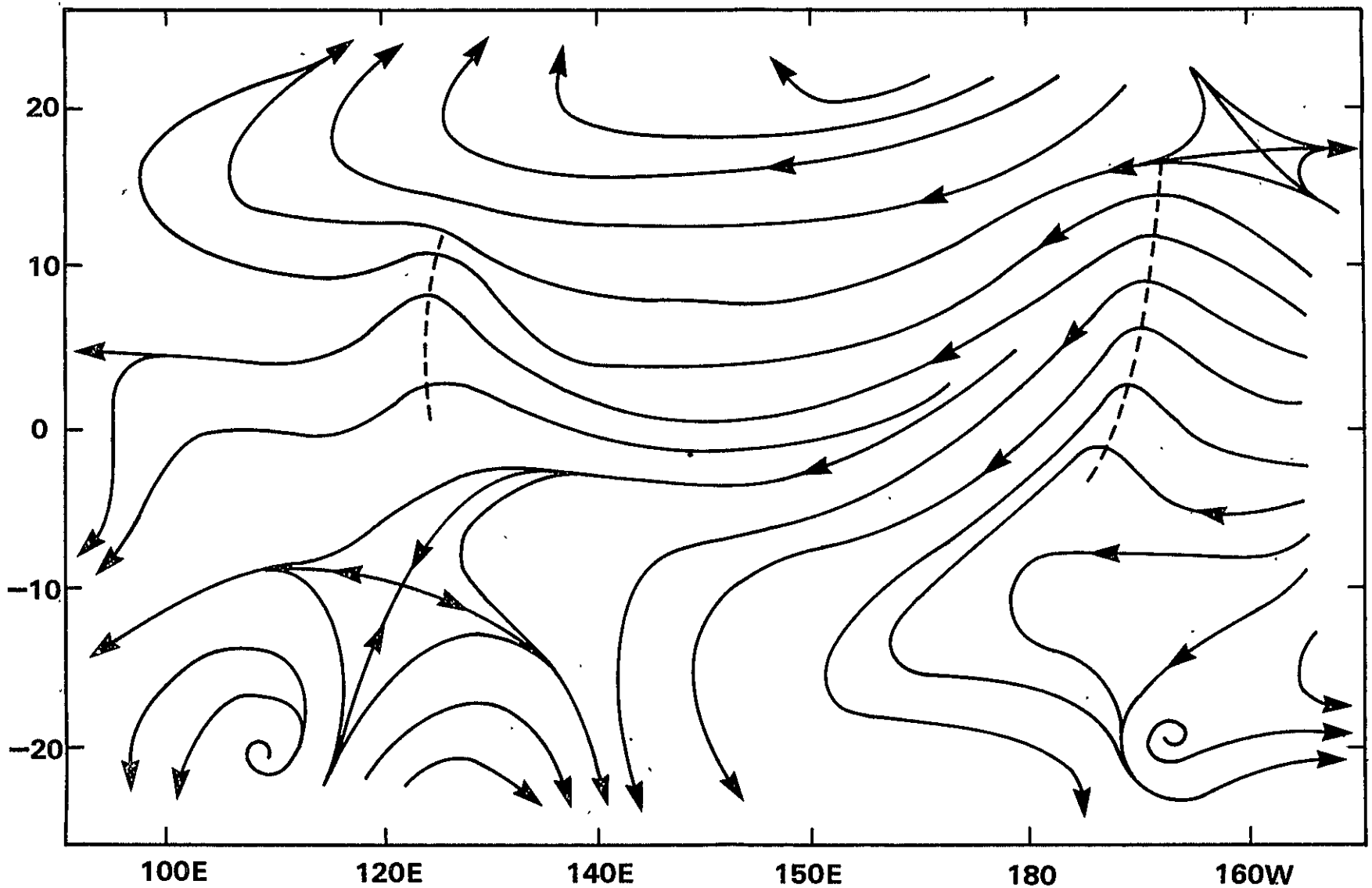

Figure 2. Simulated 700 mb synoptic streamline map for the Pacific Ocean.

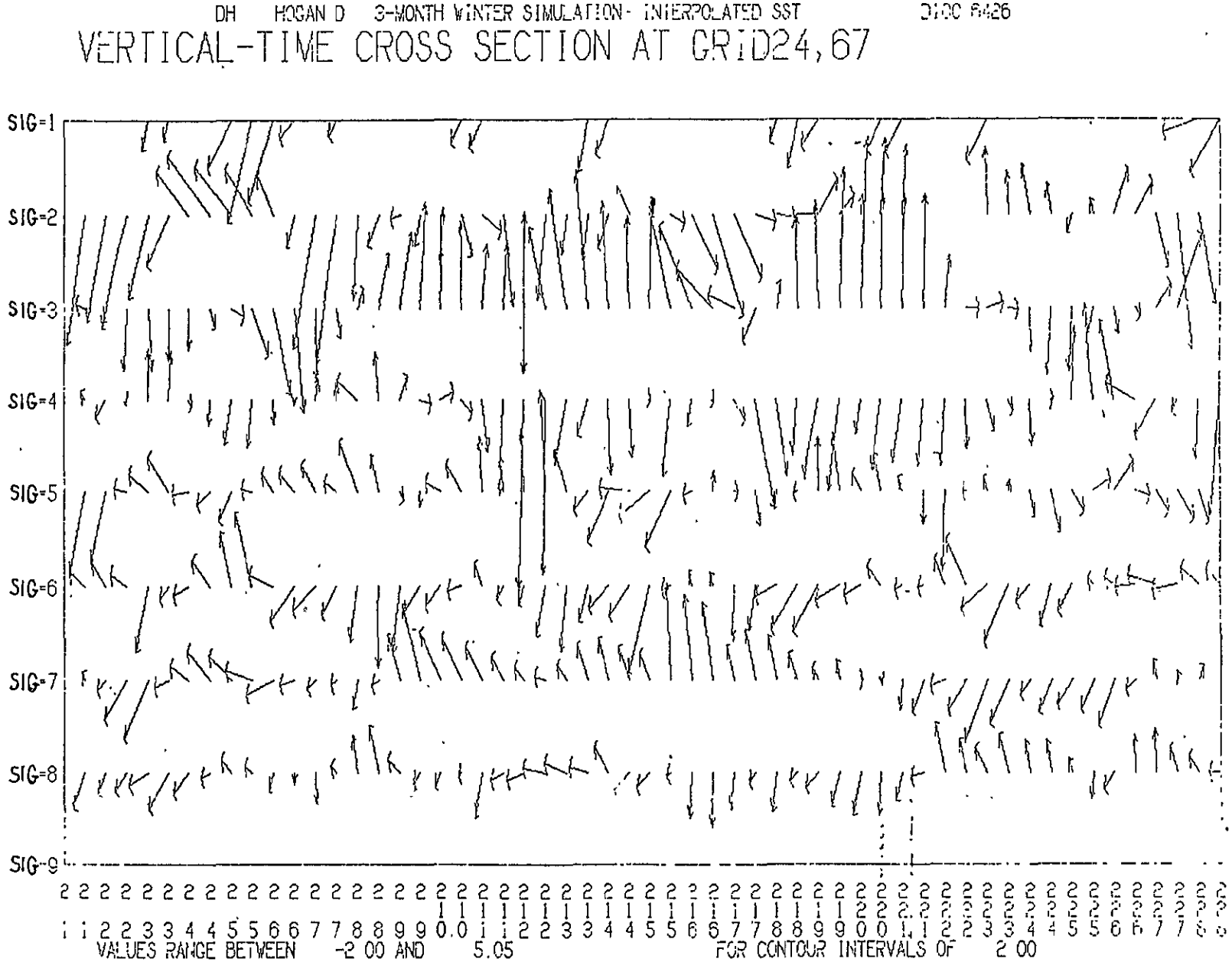

Figure 3. Vertical-time cross-section of the wind.

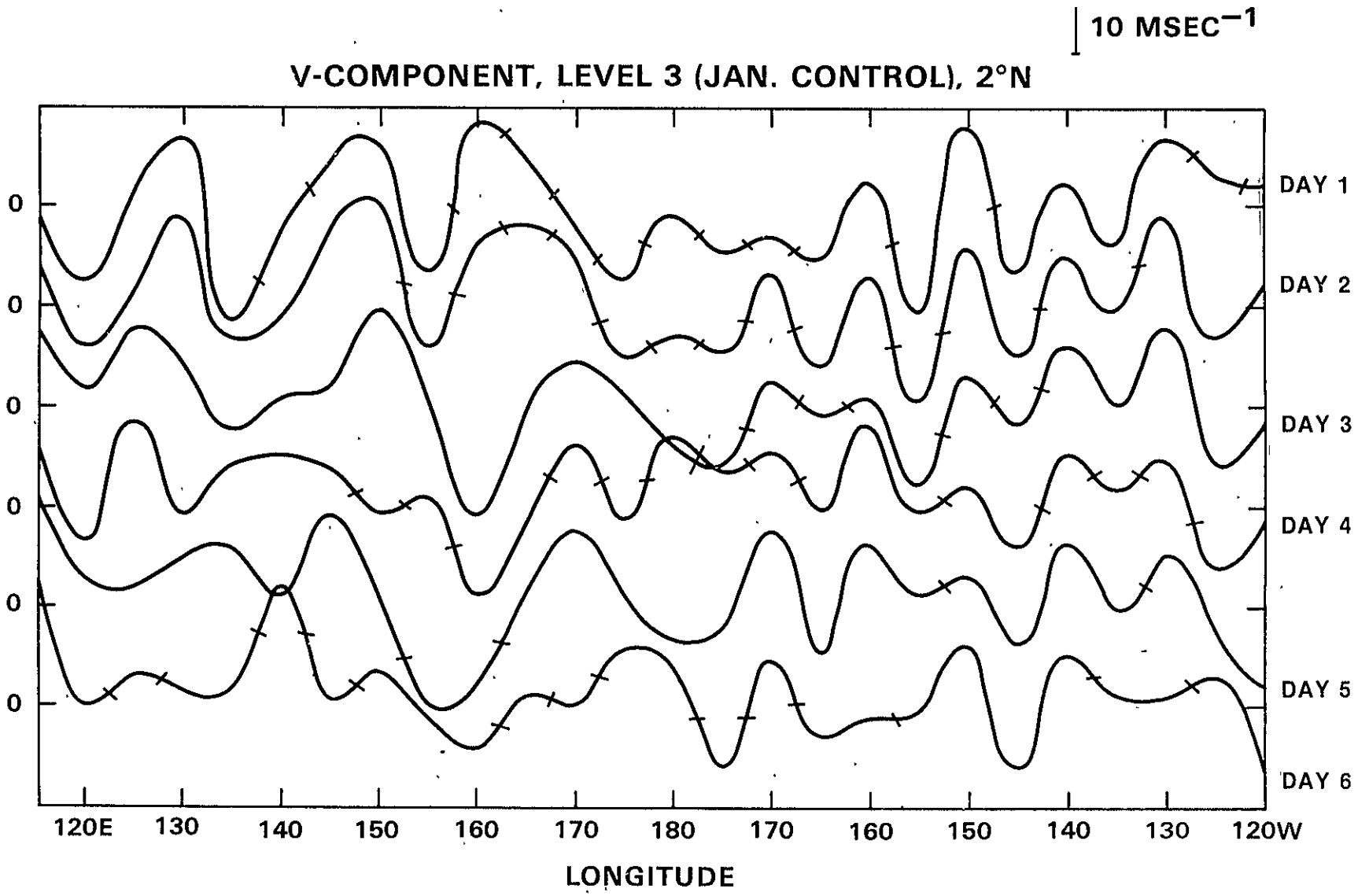

Figure 4. East-West profiles of the northward wind component (unsmoothed).

and 5. In these diagrams, the horizontal profiles (along 2°N latitude at the 300 mb level) of the northward wind component are plotted for successive days. Figure 4 represents unsmoothed profiles; Figure 5 shows the corresponding smoothed profiles. Note the overall lack of appreciable displacement of the wave forms along the east-west direction. There are other shortcomings of the simulations which cannot be described in detail in this brief report. One of the more glaring ones is the large variations (horizontal and time) in the surface pressure and the temperature. Another is the general lack of time and space continuity in the intensity and the motion of the simulated disturbances.

In summary, the goal of the study was to make an initial determination of the realism of the GLAS GCM simulations of tropical disturbances. This was done by performing a synoptic analysis of the gridpoint values of various meteorological variables from a winter simulation. The analysis indicated that the GLAS GCM was able to generate various types of tropical disturbances--waves, vortices, and linear disturbances--which exhibited many realistic features. On the other hand, the analysis also revealed various shortcomings in the simulations. It is desirable that this initial study be continued to make a thorough validation of the structure, phase speeds, and other characteristics of the simulated synoptic disturbances. The results of such a validation would be valuable in further improvement of the present GLAS general circulation model.

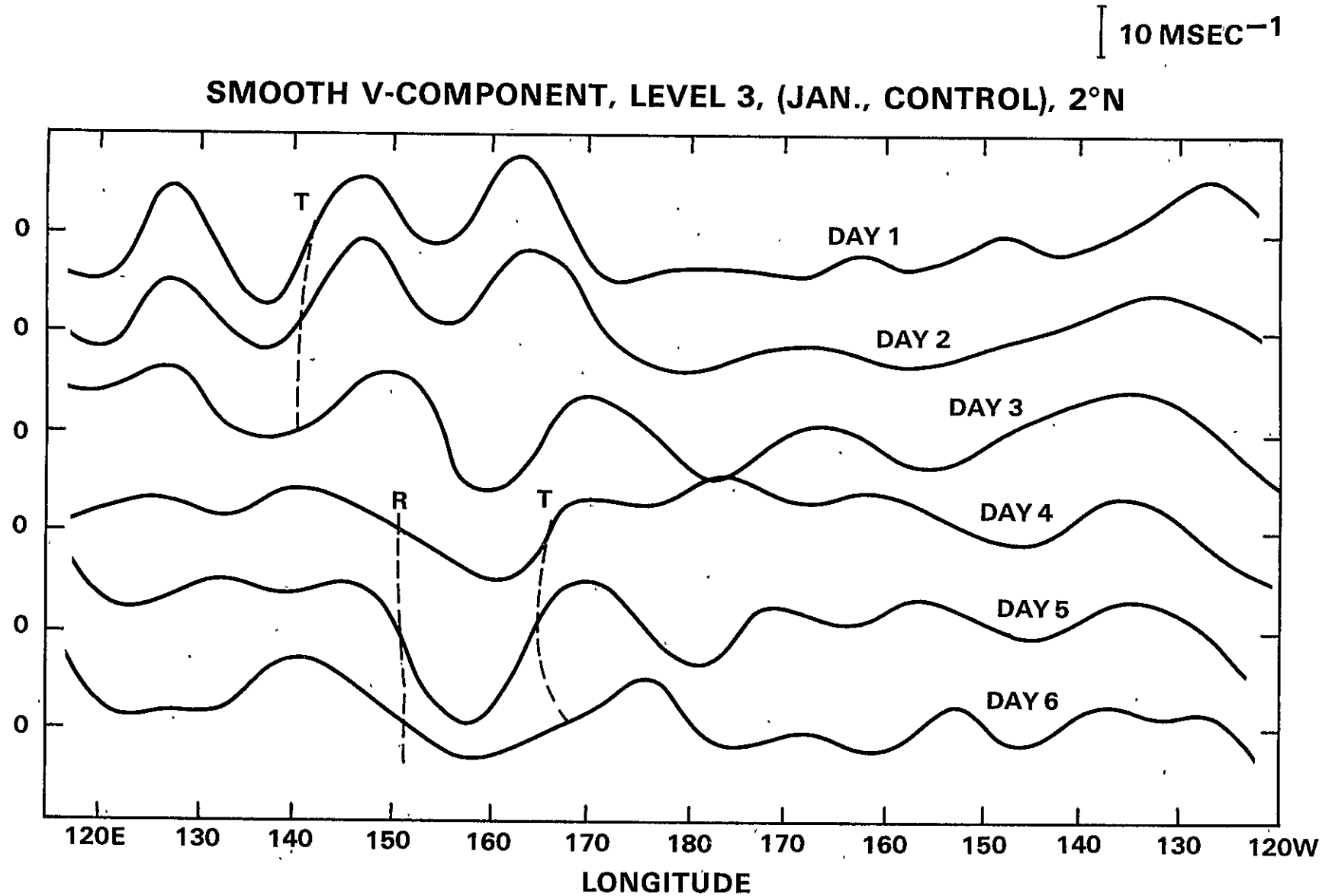

Figure 5. East-West profiles of the northward wind component (smoothed).

TIME-CONTINUOUS ASSIMILATION OF REMOTE-SOUNDING DATA AND ITS EFFECT ON WEATHER FORECASTING

(M. Ghil, M. Halem, and R. Atlas)

Time-continuous methods for the four-dimensional assimilation of remote-sounding temperatures are presented in this paper to include time-continuous versions of direct insertion, successive correction, and statistical linear regression. They are applied to temperature sounding data obtained from radiance measurements performed by instruments aboard the polar-orbiting satellites NOAA-4 and Nimbus-6. The data were collected during the U. S. Data System Test in January-March 1976.

A comprehensive series of experiments was performed to study the effects of using various amounts of satellite data and differing methods of assimilation. The experiments included the assimilation of data from the NOAA-4 satellite only, from Nimbus-6 only, and combined data from both satellites. Other experiments involved variations in the application of the GLAS time-continuous statistical assimilation methods and of asynoptic successive correction methods. Intermittent assimilation was also experimented with, and its results compared with those of time-continuous assimilation.

Atmospheric states determined in the assimilation experiments were then used as initial states for a number of 3-day forecasts corresponding to each experiment. The effect of the satellite data was studied using the following criteria: (1) differences between the initial states produced with and without utilization of satellite data, (2) differences between numerical predictions made from these initial states, and (3) differences in local weather forecasts resulting from the large-scale numerical predictions.

Initial state differences were evaluated in terms of magnitude and location of large-scale differences between meteorological fields. Numerical prediction differences were evaluated in terms of S_1 skill scores and RMS errors, as well as by synoptic case studies. An automated forecasting model (AFM) based on quasi-geostrophic theory and on subjective forecasting principles was developed to facilitate the objective evaluation of differences produced in local weather forecasts, especially precipitation forecasts.

Conclusions from these studies are that: (1) satellite-derived temperature data can have a modest, but statistically significant positive impact on numerical weather prediction in the 2- to 3-day range; (2) this impact is highly sensitive to the quantity of data available and increases with data quantity; and (3) the assimilation method plays a major role in the magnitude of the impact obtained for the same data.

RECURSIVE ESTIMATION FOR NUMERICAL WEATHER PREDICTION

(M. Ghil and J. Tavantzis)

The initialization problem of numerical weather prediction (NWP) consists in providing the initial data necessary for solving the prognostic systems used in NWP. These data are not provided with the required completeness or with sufficient accuracy by existing observing systems. Hence, the need to compute the data at initial time, $t = 0$, from incomplete and error-contaminated observations at preceding times $-T < t < 0$. Such observations are provided by a variety of unconventional, asynoptic observing systems, in particular by polar-orbiting and by geostationary satellites; these observations add information to that obtained by the conventional, ground-based synoptic meteorological network. Given both asynoptic and synoptic data, GLAS proposes to obtain optimal estimates of initial states for numerical forecasts using a systematic approach to four-dimensional (4-D) data assimilation. The approach is based on the control-theoretical methods of filtering and of optimal estimation. These methods, commonly associated with the work of Kalman, Bucy and many others, have proven remarkably successful in a number of engineering problems. Attempts have also been made to apply them to problems in dynamic meteorology by Miyakoda and Talagrand (1971), Petersen (1968, 1970), Phillips (1971), and Talagrand and Miyakoda (1971).

The application of recursive estimation methods to a simple model exhibiting important features of large-scale atmospheric flow will be studied, namely to a shallow-fluid model. In a rotating Cartesian x,y-coordinate system, the equations governing the model are

$$\begin{aligned} u_t + uu_x + vu_y + \phi_x - fv &= 0, \\ v_t + uv_x + vv_y + \phi_y + fu &= 0, \\ \phi_t + u\phi_x + v\phi_y + \phi(u_x+v_y) &= 0; \end{aligned} \qquad (1)$$

here u and v are the velocities in the x and y directions, respectively, and ϕ is the geopotential (Ghil et al., 1977). The domain of definition is a rectangle in the x,y-plane with u, v, ϕ periodic in x, so that the domain represents in fact a zonal channel.

For system (1) the estimation problem can be formulated as follows: the state of the system $\underset{\sim}{w} = (\phi,u,v)$ is approximated at $t = -T$ and the statistical structure of the error in this approximation is assumed to be known. Then some of the variables are observed continuously or discretely with a certain error

in the interval $-T < t < 0$. The best estimate $\underset{\sim}{w} = (\hat{\phi},\hat{u},\hat{v})$ of w at $t = 0$ is sought. This estimate will then be used as the initial state for a numerical forecast starting at $t = 0$.

The effect of different observational configurations and of various error structures on the results of the optimal estimation will be studied. The approach will then be compared with previous methods for 4-D data assimilation: updating (Charney et al., 1969), optimal interpolation (Rutherford, 1972; Ghil et al., 1979a) and others.

The first model considered is a linearized β-plane approximation of (1):

$$\begin{aligned} u_t + Uu_x + \phi_x - fv &= 0 \\ v_t + Uv_x + fu &= 0 \\ \phi_t + U\phi_x + \Phi u_x - fUv &= 0 \end{aligned} \qquad (2)$$

Assuming u, v and φ are independent of y, the domain is the line interval which represents the 45°N latitude circle, and requires periodicity at the end points. Therefore $\underset{\sim}{w}=(u,v,\phi)$. For geostrophic initial conditions, i.e.,

$$\underset{\sim}{w}(x,-T) = (0,\phi_x/f,\phi) \quad , \qquad (3)$$

the solution $\underset{\sim}{w}(x,t)$ to (2,3) contains only slow waves. The observed initial condition at $t = -T$ is (3), on which normally distributed noise is superimposed, is assumed. The solution $\underset{\sim}{w}(x,t)$ is further observed during the assimilation period $-T < t < 0$ at discrete values of x and t. These observations are also made in the presence of noise. GLAS is interested in estimating $\underset{\sim}{w}(x,t)$ at $t = 0$, given that new information is made available; in particular, GLAS is interested in estimating the slow waves.

A Richtmeyer two-step scheme is used to solve (2) numerically and express the discretized equations in the form

$$\underset{\sim}{w}_{n+1} = \Psi_n \underset{\sim}{w}_n \quad , \qquad (4)$$

where $\underset{\sim}{w}_n$ is the vector obtained by evaluating $\underset{\sim}{w}(x,t)$ at the grid points $i\Delta x$ at time $-T+n\Delta t$, and Ψ_n is the numerical amplification matrix.

Let $\underset{\sim}{z}_{n+1}$ be the vector of observations at $t = -T+(n+1)\Delta t$. It is expressed as

$$\underset{\sim}{z}_{n+1} = H_{n+1}\,\underset{\sim}{w}_{n+1} + \underset{\sim}{v}_{n+1} \quad , \tag{5}$$

where $\underset{\sim}{v}_{n+1}$ is the observational noise. The observation matrix H_{n+1} reflects the fact that in general it is not the state variables $\underset{\sim}{w}_n$ themselves which are observed, and certainly not all of them; thus the dimension of the vector $\underset{\sim}{z}_n$ is smaller than that of $\underset{\sim}{w}_n$. Let $\hat{\underset{\sim}{w}}_{n+1}$ be the estimate at the $(n+1)^{st}$ step, and P_{n+1} be the covariance error matrix,

$$P_{n+1} = E((\underset{\sim}{w}_{n+1} - \hat{\underset{\sim}{w}}_{n+1})(\underset{\sim}{w}_{n+1} - \hat{\underset{\sim}{w}}_{n+1})^T), \tag{6}$$

with E the expectation operator and $(\quad)^T$ the matrix transpose operator.

The problem is now to estimate $\hat{\underset{\sim}{w}}_{n+1}$ so as to minimize the trace of P_{n+1}, i.e., to minimize the expected least-square error in the estimate. The solution to this problem is given by the Kalman filter.

After an observation at time $n\Delta t$, the updated estimate $\hat{\underset{\sim}{w}}_n(+)$ of the solution is given by a certain linear combination of the preliminary estimate $\hat{\underset{\sim}{w}}_n(-)$ and of the observation $\underset{\sim}{z}_n$. This combination is chosen so that the estimation is (a) unbiased and (b) minimizes the trace of the covariance error matrix (6) (Kalman and Bucy, 1961). These two conditions determine the Kalman Gain Matrix at the n^{-th} step (Gelb, 1974)

$$K_n = P_n(-)H_n^T[H_nP_n(-)H_n^T + R_n]^{-1} \quad ; \tag{7}$$

here P_n is the error covariance matrix, H_n the observation matrix (Eq. (5)) and R_n the covariance noise matrix, $R_n=E(\underset{\sim}{v}_n\,\underset{\sim}{v}_n^T)$.

The error covariance matrix update is given by

$$P_n(+) = (I-K_nH_n)P_n(-) \quad , \tag{8a}$$

The state estimate update now becomes

$$\hat{\underset{\sim}{w}}_n(+) = \hat{\underset{\sim}{w}}_n(-) + K_n\,[\underset{\sim}{z}_n - H_n\hat{\underset{\sim}{w}}_n(-)] \quad . \tag{9a}$$

The error covariance matrix P_n evolves in time according to

$$P_{n+1}\ (-) = \Psi_n\ P_n\ (+)\ \Psi_n^T \quad . \tag{10}$$

In the absence of observations at time $t_m = -T+m\Delta t$, the updates of the state $\underset{\sim}{w}_m$ and of P_m are given by

$$P_m\ (+) = P_m\ (-) \quad , \tag{8b}$$

and

$$\underset{\sim}{w}_m\ (+) = \underset{\sim}{w}_m\ (-) \quad , \tag{9b}$$

with

$$\underset{\sim}{w}_m\ (-) = \Psi_{m-1}\ \underset{\sim}{w}_{m-1}\ (+) \quad . \tag{4'}$$

The Kalman filter technique was applied to the advection equation

$$u_t + u_x = 0 \quad , \quad 0 < x < 10 \quad , \quad 0 < t \quad , \tag{11}$$

with a triangular wave as "correct" initial data

$$u(x,0) \quad f(x) = x \quad , \quad 0 < x < 5 \quad , \tag{12a}$$

$$= 10 - x \quad , \quad 5 < x < 10 \quad , \tag{12b}$$

and periodic boundary conditions

$$u(0,t) = u(10,t), \quad 0 < t \quad . \tag{13}$$

The initial data were given with a uniformly distributed random error of amplitude $0.1\ u_{max}$. Later observations were made with a random noise of $0.01\ u_{max}$.

One numerical computation in which the filter was applied to this situation is illustrated in Figures 1 and 2. The interval $0 < x < 10$ has been partitioned into 10 subintervals

$x_i = i\Delta x$, $\Delta x = 1$; the time step is $\Delta t = 1$. The numerical scheme was upwind differencing (first order). The three arrows in Figure 1 indicate the location of observation points, $\underset{\sim}{x}^\circ = (2,5,8)$; in this example, observations were made at every time step. The situation thus corresponds to synoptic observations being provided to a quasigeostrophic model with large time steps by a sparse conventional network $\underset{\sim}{x}^\circ$.

The initial error is given by curve ①. The abscissa in Figure 1 is x and the ordinate represents the error $u - \hat{u}$ between the true value u of the solution to (11-13) and its estimated value $\hat{u}$. One can easily see that, after three time steps, the error becomes negligible. It is clear that the error $u - \hat{u}$ is reduced as the triangular wave f(x-t) travels through the "observational network" $\underset{\sim}{x}^\circ$.

Figure 2 depicts the behavior of the relative L_2-error (RMS), $||u-\hat{u}||_2/||u||_2$, and of the weighted L_2-error given by the trace of the error covariance matrix, tr P. Both error measures decrease rapidly and reach a quasi-steady value after three time steps. The technique worked well in this simple case, yielding estimates of the solution u with errors not exceeding those in the observations.

The Kalman filter has been programmed for the system (2,3). The program is structured as a package to allow the investigation of Kalman filtering for different observation patterns. One test has been carried out in which the computational network included 16 equidistant points. The observational network was $\underset{\sim}{x}^\circ=(x_1,x_2,x_3,x_4,x_9,x_{10},x_{11},x_{12})$, and $\underset{\sim}{w}=(\phi,u,v)$ was observed at each x_i belonging to $\underset{\sim}{x}^\circ$ every third time step $t_n^\circ=3n\Delta t$. This situation is similar to the one reported on for the advection equation (11-13). In this case rapid error decrease occurred also, so that after two observations, or $6n\Delta t$, the error fell from its initial high value of about 10 percent to the low value of observational error of about 1 percent.

Preliminary results indicate that recursive estimation using the Kalman filter is very effective in 4-D data assimilation for the linearized shallow-fluid equations. GLAS intends to study observation patterns that simulate closely both the synoptic and the asynoptic observational network in the mid-latitudes of the Northern Hemisphere (Phillips, 1976). The present technique will then be compared to a number of previously implemented assimilation methods.

It will be especially interesting to compare recursive estimation to the linear regression methods which, under the name of "optimal interpolation," have recently attracted considerable interest in the meteorological community (Bengtsson, 1975; Rutherford, 1972). The latter methods are purely statistical in nature, ignoring the dynamics of the atmosphere, as expressed in the equations of motion used in NWP. A step in the direction of combining dynamics with statistics appears

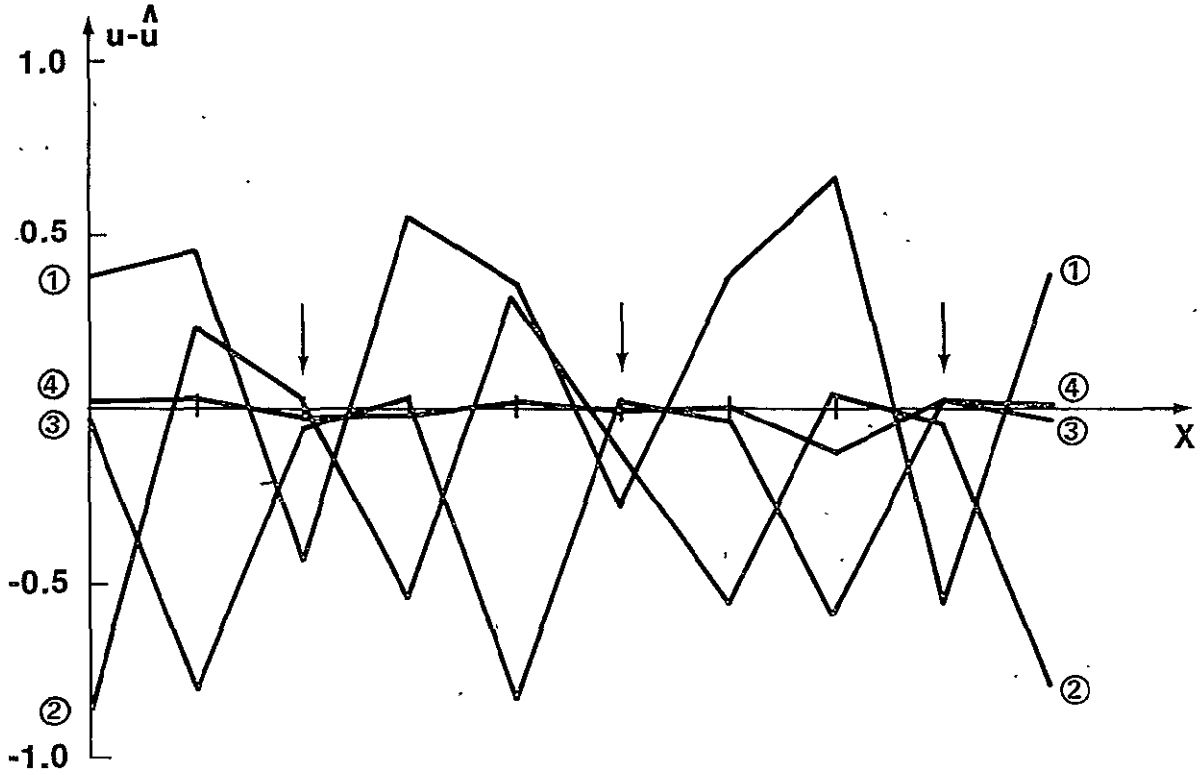

Figure 1. Evolution of pointwise estimation error $u-\hat{u}$. Arrows indicate observation points, x=2,5,8. The curve (n) indicates $u-\hat{u}$ after the n^{-th} observation, $u(i\Delta x, n\Delta t) - \hat{u}(i\Delta x, n\Delta t)$.

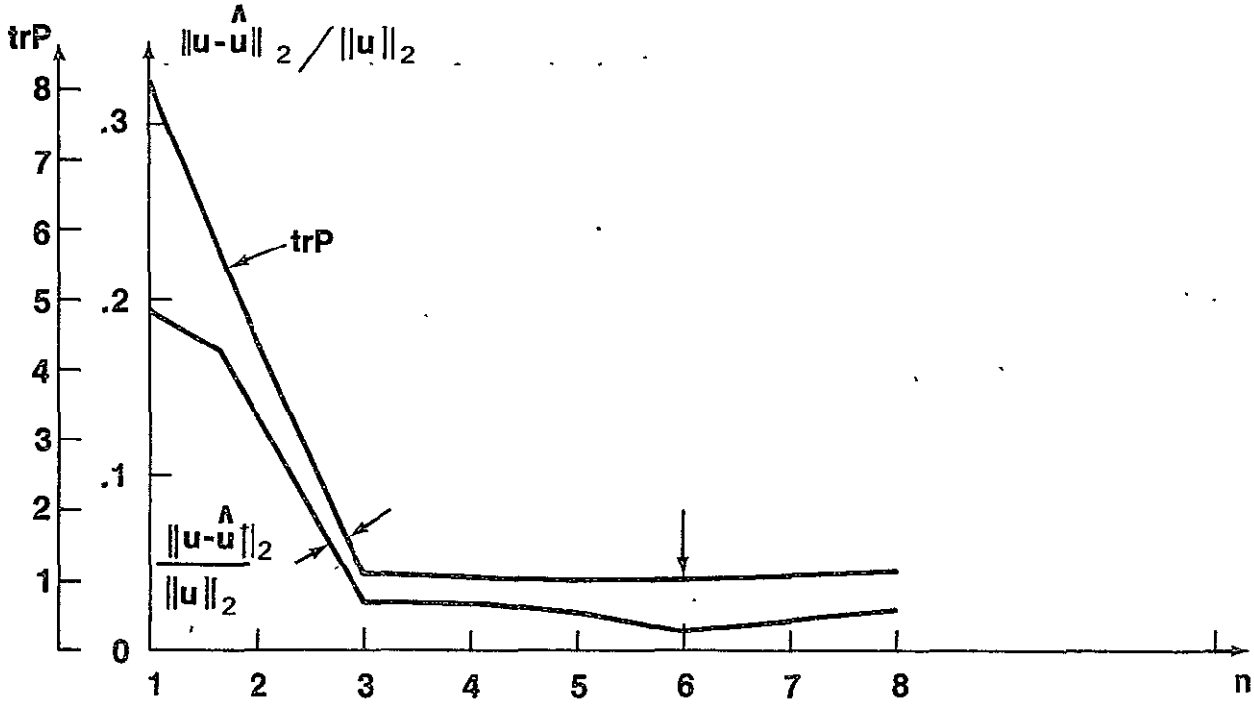

Figure 2. Evolution of two measures of estimation error: the relative L_2-error $||u-\hat{u}||_2 / ||u||_2$ and the weighted L_2-error, $trP = \Sigma_i E(u_i-\hat{u}_i)^2$.

in the time-continuous statistical assimilation method (SAM) of Ghil et al. (1979a,b).

GLAS shall attempt to devise improvements in practical assimilation methods by an increased understanding of recursive estimation for simple prognostic systems. As a first step towards that goal, GLAS plans to extend the results to the non-linear system (1) by applying a generalized Kalman filter (Seinfeld et al., 1970).

Control theory should provide also a unified framework for both data assimilation and initialization methods. Filtering of high-frequency inertia-gravity noise can be performed within the same procedure, which assimilates asynoptic and synoptic observations (Ghil, 1979). This could eliminate the current practice of following an assimilation cycle by a computationally costly initialization calculation.

References

Bengtsson, L., 1975: 4-Dimensional Assimilation of Meteorological Observations. GARP Publications Series, No. 15, WMO-ICSU, Geneva, 76 pp.

Charney, J., M. Halem, and R. Jastrow, 1969: Use of incomplete historical data to infer the present state of the atmosphere. J. Atmos. Sci., 26, pp. 1160-1163.

Gelb, A., 1974: Applied Optimal Estimation. MIT Press, Cambridge, Mass.

Ghil, M., 1979: The compatible balancing approach to initialization and four-dimensional data assimilation. In preparation.

_____, B. Shkoller, and V. Yangarber, 1977: A balanced diagnostic system compatible with a barotropic prognostic model. Mon. Wea. Rev., 105, pp. 1223-1238.

_____, M. Halem, and R. Atlas, 1979a: Time-continuous assimilation of remote-sounding data and its effect on weather forecasting. Mon. Wea. Rev., in press.

_____, 1979b: Effects of sounding temperature assimilation on weather forecasting: model dependence studies. Remote Sounding of the Atmosphere from Space, H.-J. Bolle (ed.), Pergamon Press, in press.

Kalman, R. E., and R. S. Bucy, 1961: New results in linear filtering and prediction theory. J. Basic Eng., Trans. ASME, Ser. D, 83, pp. 95-108.

Miyakoda, K., and O. Talagrand, 1971: The assimilation of past data in dynamical analysis, I. Tellus, 23, pp. 310-317.

References (Continued)

Petersen, D. P., 1968: On the concept and implementation of sequential analysis for linear random fields. Tellus, 20, pp. 673-686.

_____, 1970: Algorithms for sequential and random observations. Meteor. Monogr., 11, No. 33, pp. 100-109.

Phillips, N., 1971: Ability of the Tadjbakhsh method to assimilate temperature data in a meteorological system. J. Atmos. Sci., 28, pp. 1325-1328.

_____, 1976: The impact of synoptic observing and analysis systems on flow pattern forecast. Bull. Amer. Meteor. Soc., 57, pp. 1225-1240.

Rutherford, I. D., 1972: Data assimilation by statistical interpolation of forecast error fields. J. Atmos. Sci., 29, pp. 809-815.

Seinfeld, J. H., G. R. Gavalas, and M. Hwang, 1970: Nonlinear filtering in distributed parameter systems. Joint Automatic Control Conf., Georgia Institute of Tech., Atlanta.

Talagrand, O., and K. Miyakoda, 1971: The assimilation of past data in dynamical analysis, II. Tellus, 23, pp. 318-327.

PARAMETERIZATION OF THE FRICTIONAL TURNING ANGLE FOR THE HOFFERT-SUD PLANETARY BOUNDARY LAYER MODEL

(M. Helfand)

The Hoffert-Sud Planetary Boundary Layer Model (J. Atmos. Sci., 1976) is a similarity model in which the vertical coordinate is normalized by the boundary layer depth, h. The structures predicted by the model can be parameterized in terms of the non-dimensional variables, $Ri_b = h/L$, h/z_o, and h_c/h, where L is the Monin-Obukhov length, z_o the surface roughness length, and $h_c=.35\ u/f$ is the Ekman depth. The model predicts a drag coefficient, C_D, a heat transfer coefficient, C_H, and a frictional turning angle, Ψ_F, as a function of these three similarity parameters. In the past, only C_D and C_H have been used in the parameterization implemented in the GLAS GCM. However, it is necessary to compute the turning angle in order for the GLAS GCM to assimilate sea surface wind observations, such as those soon to be available from the Seasat-A scatterometer.

In order to influence the GCM forecast, the level 9 wind field must be altered to reflect the surface wind information. This requires that the turning of the wind between the surface and 950 mb be accounted for.

Figure 1 shows Ψ_F as a function of Ri_b for four values of Z_o/h and two values of h_c/h as determined by numerous integrations of the Hoffert-Sud model. An analytic approximation to this function has been constructed: Ψ_F is taken as the log linear function of Ri_b for $Ri_b \leq -3$ and as an exponential function of Ri_b for $-3 < Ri_b < 0$. For the stable case ($Ri_b > 0$) the Richardson number is set equal to zero. Unfortunately, integrations of the Hoffert-Sud model imply that Ψ_F increases for decreasing h_c/h for the neutral case, behavior that is not physically reasonable. The reason for this anomalous behavior at neutral stability is currently under investigation.

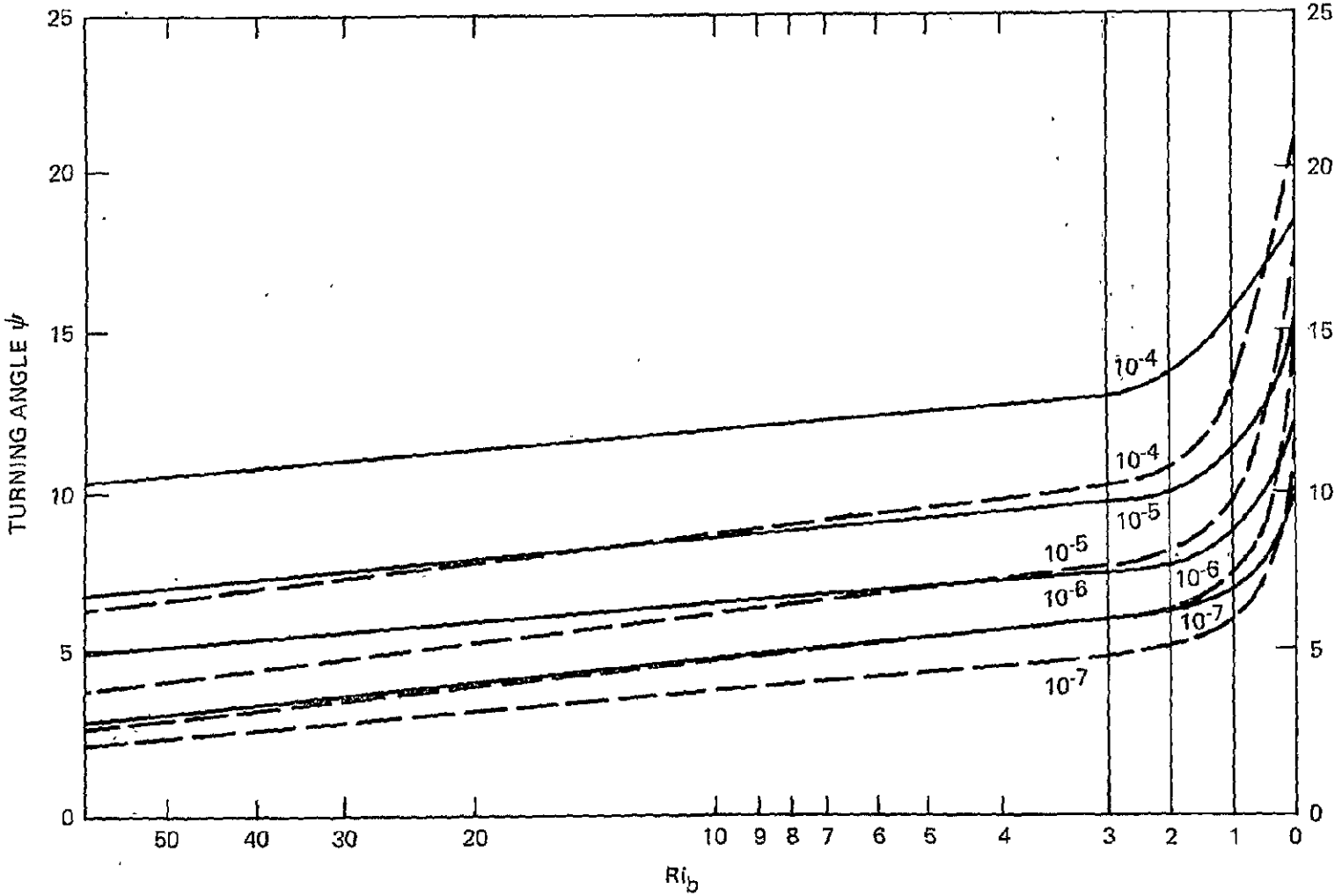

Figure 1. The frictional turning angle χ_F as a function of bulk Richardson number Ri_b for several values of h_c/h and z_o/h. The solid lines represent curves for $h_c/h = 1$, while the dashed lines represent curves for $h_c/h = 2$. The value of z_o/h is presented next to

FURTHER DEVELOPMENTS OF A PLANETARY BOUNDARY LAYER PARAMETERIZATION

(D. Randall)

A realistic parameterization of the planetary boundary layer (PBL) must have the following features:

A. An accurate method for determining the time evolution of the PBL depth during periods of both deepening and shallowing;

B. A method of calculating the turbulent fluxes throughout the depth of the PBL, under all conditions of stability, cloudiness, etc.;

C. A comprehensive parameterization of the interaction of the PBL with clouds;

D. A simple and complete method of incorporating the parameterized PBL into the framework of a numerical prediction model.

Each of these major points was addressed by Randall (1976) in a parameterization for the six- and twelve-level UCLA general circulation models. Development of the parameterization is continuing, however, and all of these features of the parameterization have been or are being significantly revised. The purpose of this report is to summarize the current status of the parameterization.

The Entrainment Parameterization

Because the PBL is defined as the layer within which the turbulence is a dominant process, it is natural to discuss the deepening and shallowing of the PBL in terms of the conservation of turbulence kinetic energy (TKE). In vertically-integrated form, this conservation law is approximately given by

$$Ee_M = B + S - D_M \delta p_M / g, \qquad (1)$$

where E is the entrainment mass flux; e_M is the vertically-averaged TKE density; B and S are the rates of buoyant and mechanical production of TKE, respectively; D_M is the vertically-averaged dissipation rate; δp_M is the PBL depth in terms of pressure; and g is gravity. The gravity wave radiation and cumulus production of TKE are neglected; and it is assumed that the time rate of change of the TKE content, $e_M \delta p_M$, is dominated by the time rate of change

of δp_M. For convenience, a turbulence velocity scale σ is defined by

$$\delta M \sigma^3 \quad D_M \delta p_M / g, \tag{2}$$

where ρ_M is the vertically-averaged density.

It is assumed that

$$e_M = a_1 \sigma^2, \tag{3}$$

and that

$$\rho M \sigma^3 = a_2 P, \tag{4}$$

where P is the gross rate of TKE production, i.e., the integral of the production rate over those levels where it is positive. The constants a_1 and a_2 are the only empirical parameters of the theory. The values $a_1^2 = 0.75$ and $a_2 = 0.84$ are tentatively assigned.

The simple theory sketched above takes into account the production of TKE at all levels within the PBL, including possible cloud layers. It also allows shallowing of the PBL, by permitting negative entrainment whenever the dissipation rate exceeds the net production rate.

The entrainment theory has been tested using a simple mixed layer model. The results (Figure 1) show a realistic diurnal variation of the PBL depth over land.

Revision of the Turbulent Flux Parameterization

Randall (1976) did not propose a new parameterization of the turbulent fluxes, but simply adapted the method of Deardorff (1972). Yamada (1976), Arya (1977), and others have proposed somewhat more sophisticated theories, which are nevertheless generally similar to Deardorff's. But none of these theories takes into account the effects of stratocumulus or cumulus clouds, which may drastically enhance the turbulent fluxes by dominating the production of TKE. This is a particularly serious problem for stratocumulus convection, because it often occurs over cool oceans where conventional theories incorrectly predict very weak turbulent transfer. The existing theories also behave badly in certain special but important limiting cases, such as free convection or equatorial flow. Also, although these theories predict the existence of characteristic interior structures for the PBL in various parameter ranges, and so imply the existence of corresponding characteristic interior flux profiles, the nature of these profiles has not yet been adequately documented. Finally, all of these theories are for the equilibrium structure of the PBL, and the important problem of how near-equilibrium is maintained against the inevitable disturbing influences has not been solved.

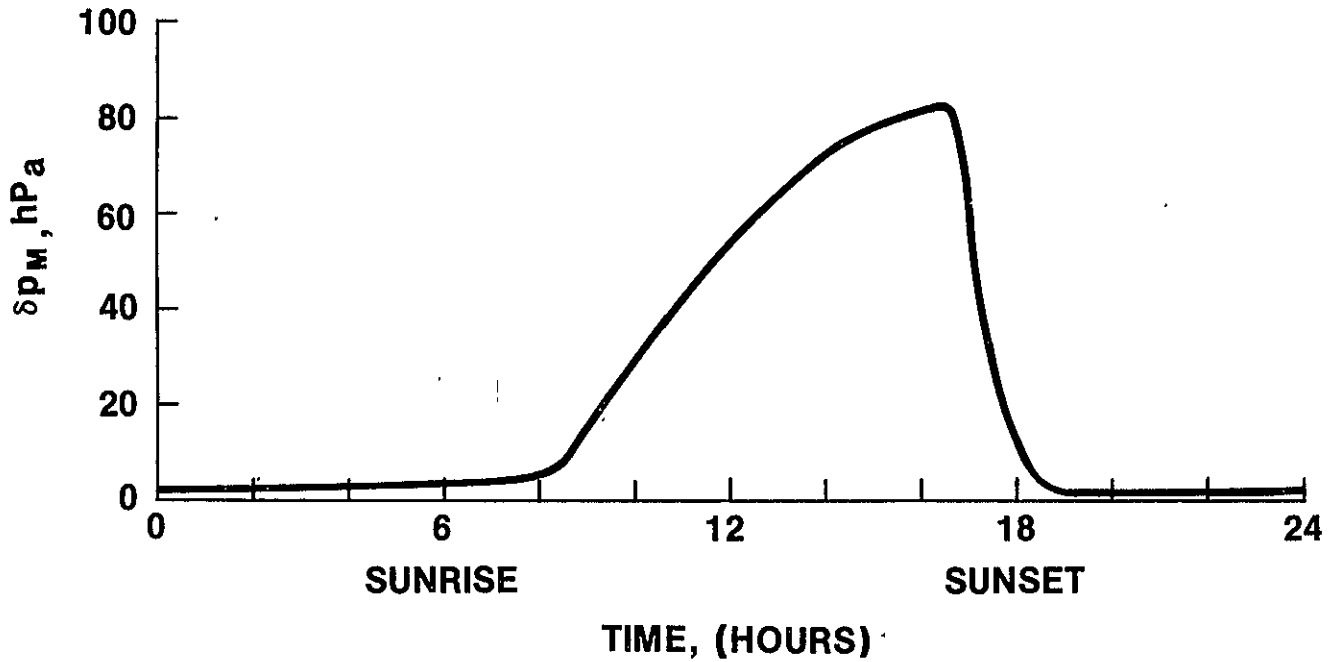

Figure 1. Realistic diurnal variation of PBL depth over land.

A new theory which overcomes these difficulties is currently being tested. For the purpose of determining the similarity functions whose existence is predicted by the theory, a "higher-order closure" model has been developed and thoroughly tested by Joseph Scire, a graduate student at MIT. After the similarity functions have been determined, the next step is to test the theory off-line. Only then will it be incorporated into a GCM.

A Parameterization of the Layer Cloud Instability

As discussed by Randall (1976), under some circumstances a stratocumulus cloud deck is susceptible to penetration by convective downdrafts whose negative buoyancy is maintained by the evaporation of cloud liquid water. Recently, it was discovered that the effects of this instability on the cloud layer can be parameterized on the basis of the assumption that the downdrafts reduce the fractional cloudiness in such a way that the remaining partly cloudy layer is neutrally stable with respect to the downdrafts. The theory not only yields the turbulent flux profiles in the unstable cloud layer, but also, as a bonus, provides a measure of the fractional cloudiness. The latter is predicted to decrease in a natural way as the degree of instability increases. This simple parameterization has already been tested off-line and programmed into the UCLA GCM.

Testing of a Potential Enstrophy Conserving Scheme for Use With the the Parameterization

In order to incorporate the PBL parameterization into a GCM, a generalized σ-coordinate system (Figure 2) was adopted in which both the earth's surface and the PBL top are coordinate surfaces. The PBL then consists of one or more model layers. Although the height and pressure of the PBL top vary in space and time according to a prognostic equation, the value of σ at the PBL top is always the same.

The quasigeostrophic dynamics of large-scale atmospheric flows are governed by the conservation of potential vorticity. For the PBL, the potential vorticity is inversely proportional to the PBL pressure depth, which can change very rapidly from one gridpoint to the next. Therefore, special care is needed to avoid large truncation errors in the advection of PBL potential vorticity if the quasigeostrophic dynamics are to be correctly simulated for the lowest model layers.

Fortunately, a suitable scheme has recently been developed by Arakawa and Lamb. Tests of the scheme, together with the PBL parameterization, are currently in progress at UCLA. But it is desirable to have a "clean" test of the scheme as well, i.e., a test in which the new scheme is the only new feature in the model. With the assistance of Dr. Kingtse Mo, the GLAS GCM has been modified to provide such a clean test, and debugging is now underway. First results should be available in the near future.

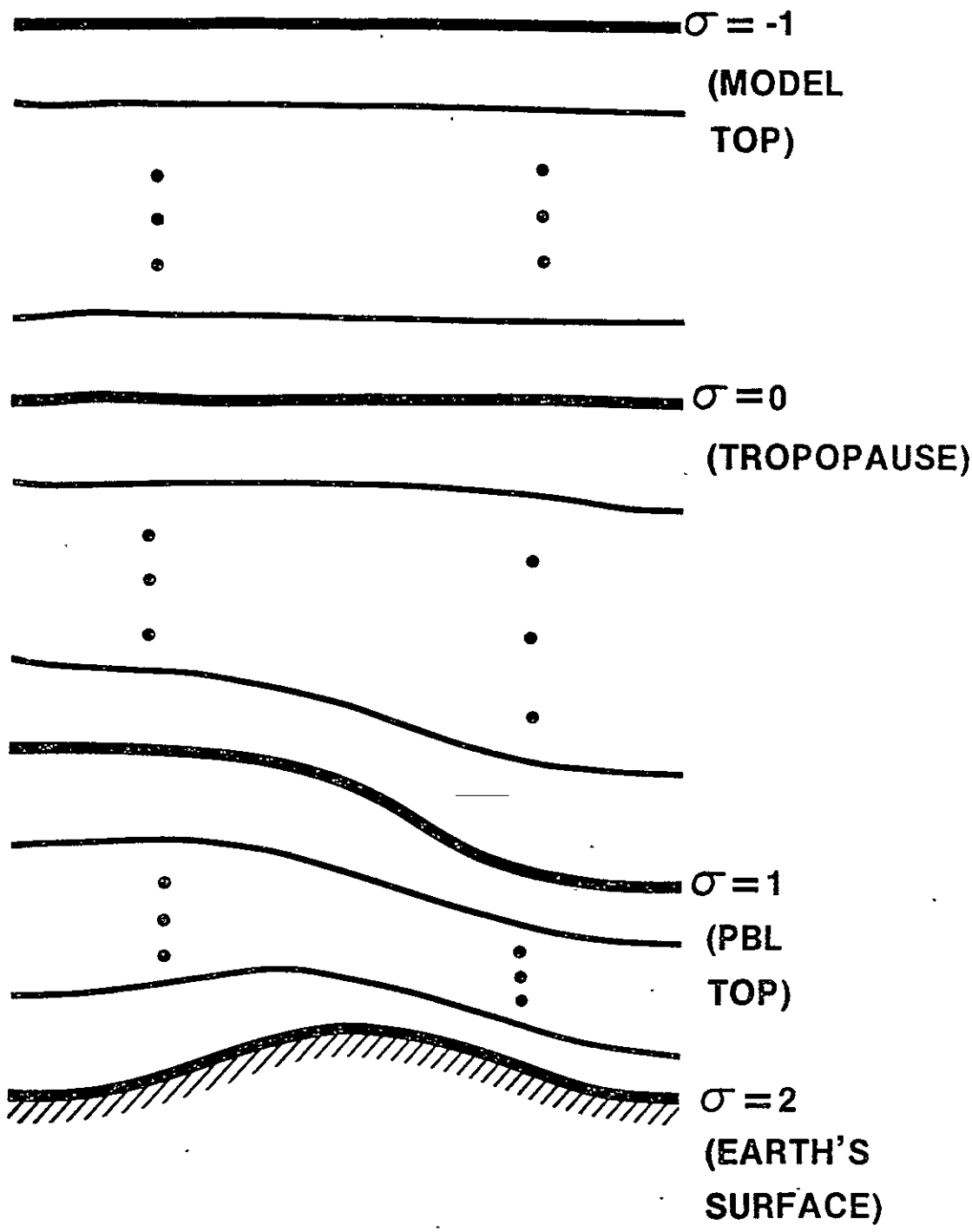

Figure 2. The generalized σ-coordinate.

The GLAS goal is to incorporate the features outlined above into a comprehensive PBL parameterization for GCMs. GLAS is working toward this goal by systematically testing each feature separately. The individual features will be incorporated into the GLAS GCM as each becomes ready.

References

Arya, S. P. S., 1977: Suggested revisions to certain boundary layer parameterization schemes used in atmospheric circulation models. Mon. Wea. Rev., 105, pp. 215-227.

Deardorff, J. W., 1972: Parameterization of the planetary boundary layer for use in general circulation models. Mon. Wea. Rev., 100, pp. 93-106.

Lilly, D. K., 1968: Models of cloud-topped mixed layers under a strong inversion. Quart. J. Roy. Meteor. Soc., 94, pp. 292-309.

Randall, D. A., 1976: The interaction of the planetary boundary layer with large-scale circulations. Ph.D. Thesis, The University of California, Los Angeles, 247 pp.

Yamada, T., 1976: On the similarity functions A, B, and C of the planetary boundary layer. J. Atmos. Sci., 33, pp. 781-793.

A FOURTH-ORDER FORECASTING MODEL

(E. Kalnay-Rivas, D. Hoitsma, and P. Anolick)

The GISS fourth-order model (Kalnay-Rivas, et al., 1977), which is a fourth-order, energy-conserving GCM on an unstaggered grid, had shown promising capabilities. It produced forecasts that showed an improvement over the second-order GISS forecasts with the same fine grid (4° x 5°) resolution, but that were somewhat inferior to the "ultrafine" forecasts. However, the first version of the model required excessive amounts of computer memory and time for execution.

The model has been reprogrammed into the "fourth-order band model." The new program solves the primitive equations one latitude band at a time. The arrays are stored in an interlaced way, with all arrays being updated at the same latitude stored contiguously, and similarly for all arrays used in the computation of the time derivatives. This design of the program makes effective use of the virtual memory capability of the Modeling and Simulation Facility's IBM 370/165 or Amdahl computers. The virtual memory facility permits the execution of programs whose core size is larger than the one available, by placing the excess on disk and reading in those pages of information needed in the current calculations. The band fourth-order data structure and computations were constructed to optimize this virtual I/O process; a possible improvement may be to interlace also the arrays being updated with those used to compute the time derivatives. The use of the virtual memory facility avoids the explicit I/O used in the current Kern model, and yields a simpler program. (The band structure was suggested by G. Russell.)

The band fourth-order model computations have been optimized so that each time step is computed in the Amdahl in half the time required by the old model. The array structure has also been designed to reduce the amount of overall storage and high-speed memory by a factor of two (see Table 1).

Table 1. Comparison of Fourth-Order Model Computing Requirements.

	Original 4th-Order Model	Band 4th-Order Model
Core (bytes)	3500K	1500K
CPU time per step (COMP1, COMP2)	34 sec	17 sec

The model has been programmed so that it can use both the Matsuno and the leapfrog time schemes, the latter with the Robert time smoother. If Q^n and $D(Q^n)$ denote the fields at time $n\Delta t$ and the corresponding time derivative computed from the space differences, the smoothed leapfrog scheme is

$$Q^{n+1} = \overline{Q}^{n-1} + 2\Delta t\, D(Q^n)$$

$$\overline{Q}^n = Q^n + .5\nu(Q^{n-1} + Q^{n+1} - 2Q^n)$$

with $\overline{Q}^0 = Q^0$. The use of a smoothing coefficient requires a slightly smaller time step. For example, with $\nu = .1$, the model is marginally stable with $\Delta t = 288$ sec., compared to $\Delta t = 300$ sec. for the Matsuno and leapfrog schemes.

The smoothed leapfrog scheme is further modified to include the subgrid "physics" terms, and scaling and spatial smoothing procedures. Since the "physics" is called every few time steps, unless the leapfrog scheme is restarted after every call to the "physics," only one of the two consecutive fields will be affected. The restarting procedure is time-consuming, so it has been replaced by the following algorithm

$$Q^{n-1} = Q^{n-1} - Q^n$$

$$\tilde{Q}^n = Q^n + S^n$$

$$Q^{n-1} = Q^{n-1} + \tilde{Q}^n$$

where S^n corresponds to the "physics" terms. This procedure, which ensures that the physics is applied to two consecutive time steps, has been tested with good results.

Preliminary Results. The first numerical integrations performed with the new band fourth-order model show dramatic improvements over forecasts made with the GLAS model with the same resolution ("fine grid" or 4° latitude by 5° longitude). The quality of the forecasts is now comparable with those produced with the "ultrafine" (2.5° latitude by 3° longitude) version of the model. Results from a 3-day numerical integration are presented in Figure 1. During an extended 8-day integration of the new fourth-order model, the atmospheric systems remained remarkably smooth, exhibiting a realistic behavior both with respect to position and intensities.

References

Kalnay-Rivas, E., A. Bayliss, and J. Storch, 1977: The fourth-order GISS model of the global atmosphere. Contributions to Atmos. Phys., 20, pp. 299-311.

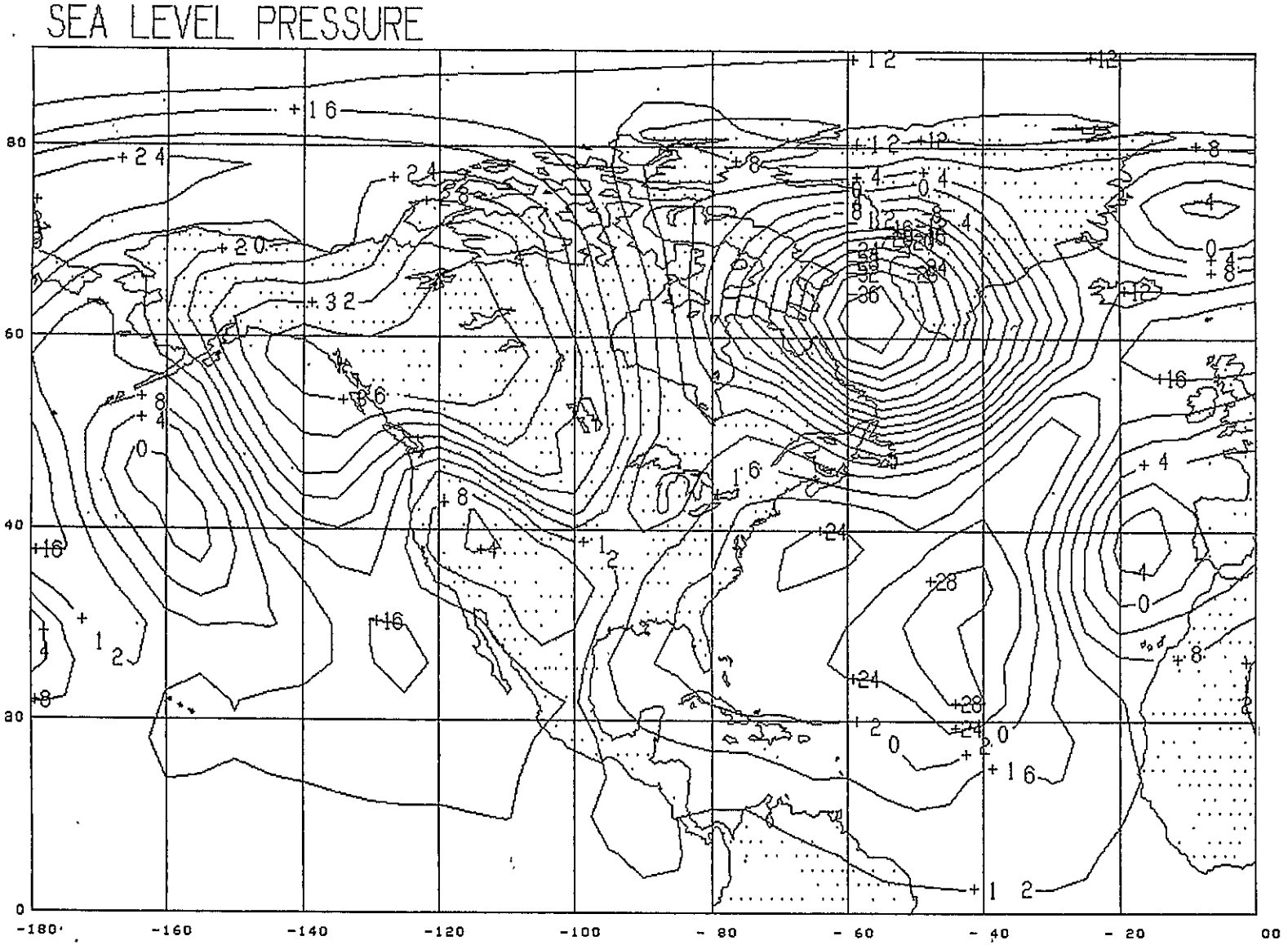

Figure 1a. Observed sea level pressure (February 22, 1976 - 0Z).

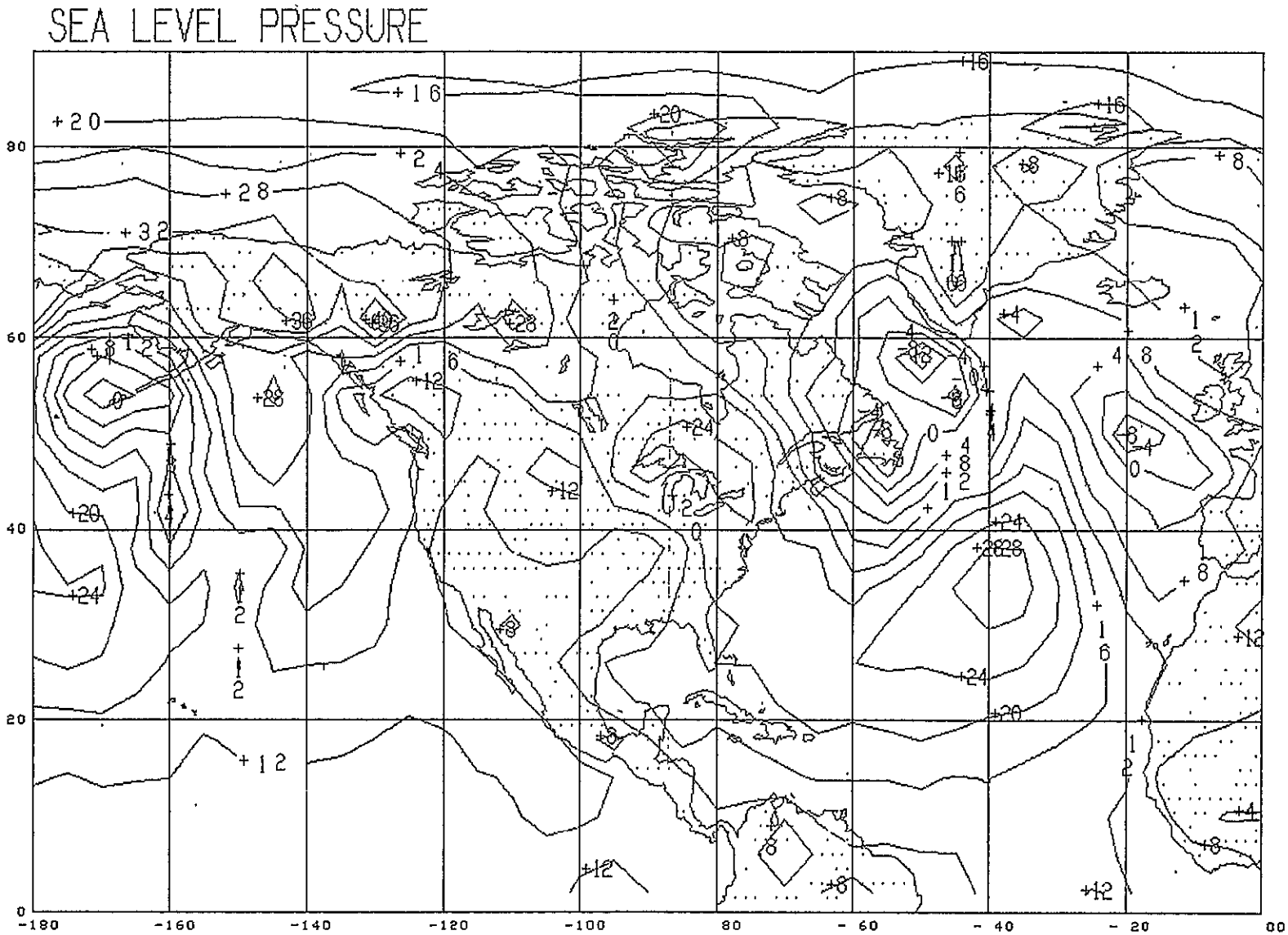

Figure 1b. 72-hour forecast - second-order GLAS model.

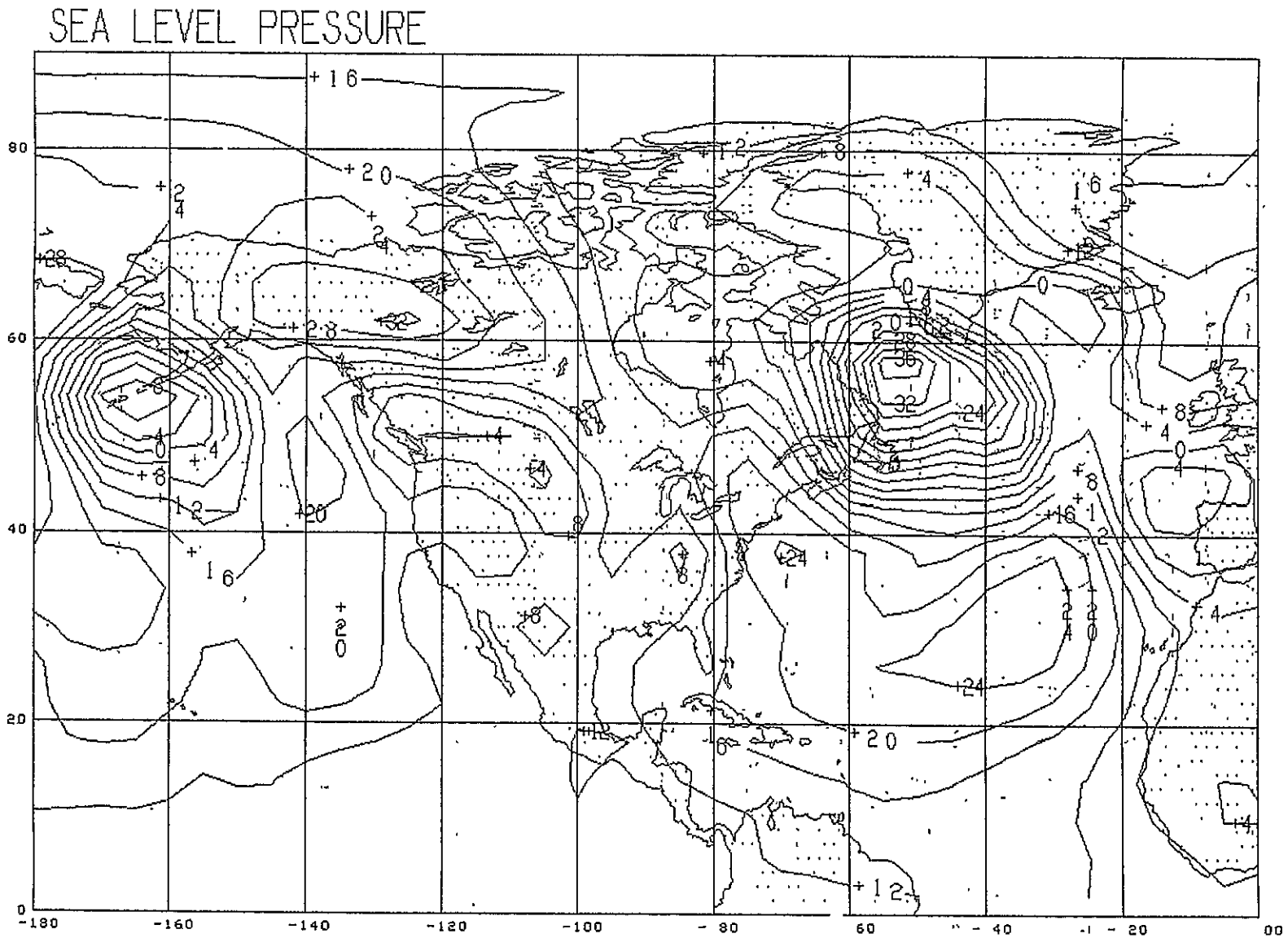

Figure 1c. 72-hour forecast - fourth-order GLAS model.

THE EFFECT OF TIME SCHEMES ON MODEL SIMULATIONS

(E. Kalnay-Rivas)

Numerical experiments with simplified models indicate that the choice of a time scheme can have an important effect on the model limit of predictability. For example, 20-day integrations with a quasigeostrophic model with parameterized radiation, friction and orography were carried out using the Matsuno and Lorenz four-cycle schemes, both with time steps of 1 hour and 1.5 hours. Numerical integrations starting from the same initial conditions and using different time schemes showed significant differences after 2 to 4 days. After 20 days the only similarity between the two forecasts was in the long stationary wave forced by orography. There were significant differences even in the "climate" obtained through a 20-day average. It was found that the differences between forecasts run with the same scheme and different time steps were much less significant than those between different time schemes.

In order to study the properties of efficient time schemes a series of experiments was performed with a simple shallow water equations (SWE) model. The Matsuno (M) scheme, which is currently used in the GLAS model, was modified by using updated pressures in the pressure gradient term of the momentum equations. This was done either in the corrector step (modified Matsuno I or MI), in the predictor step (MII) and in both steps (MIII). The properties of modified leap frog schemes were studied, in which the pressure term ϕ^n computed at time $n\Delta t$, is replaced by (i) $(\phi^{n+1} + \phi^{n-1})/2$ (modified leapfrog I or LFI); (ii) ϕ^{n+1} (LFII); and (iii) $(\phi^{n-1} + 2\phi^n + \phi^{n+1})/4$ (LFIII). This last version was proposed by Shuman. Linear analysis indicates that if the time step is chosen for maximum stability, as is the case in practice, then MI and MII can use a time step $\sqrt{2}$ larger than the regular Matsuno scheme, and they have better stability properties at high frequencies. MIII has worse stability properties than MI or MII. Linear analysis also indicates that the TASU scheme (time alternating, space uncentered), formerly used in combination with the Matsuno scheme in the GLAS model (Arakawa, 1972) is not spacially symmetric and introduces numerical horizontal diffusion with a coefficient $\mu \sim \frac{c^2 \Delta t}{2}$, half as much as the Lax-Wendroff scheme.

Some of the results of the SWE model are the following: (i) MI and MII can be used with a time step about 50 percent larger than the regular Matsuno scheme; (ii) of the modified leapfrog schemes, the only stable one is LFIII (proposed by Shuman), which ran with Δt about 50 percent larger than the regular leapfrog. It can be combined with time smoothing (Robert filter) only for very small smoothing coefficients. The combination of LFIII with a small amount of time smoothing and the periodic application of a Shapiro filter produced

excellent results at a rate three times faster than the regular Matsuno scheme; (iii) Lorenz's N-cycle scheme, which has very attractive properties, and is most stable with N = 4, is not much more efficient than the Matsuno scheme because it requires smaller time steps for stability. In agreement with linear analysis, the size of the maximum time step is very sensitive to diffusion terms.

The modified Matsuno I (MI) scheme has been introduced into the GLAS model, where it has allowed an increase in the time step from 10 min. to 14 min. A 3-day forecast with the new scheme and Δt = 14 min. was virtually identical to the one obtained with the regular Matsuno scheme and Δt = 10 min.

Semi-implicit schemes for the shallow water equations can be easily designed and solved (Kwizak and Robert, 1971). For the baroclinic primitive equations, since there are as many inertia-gravity wave modes as vertical levels, semi-implicit schemes become rather complex and require considerable extra storage, which may offset the advantages of a larger time step. A semi-implicit scheme was designed in which only the external mode is written implicitly to take advantage of the fact that the phase speed of the Lamb wave, or external inertia-gravity wave mode, is $c=\pm\sqrt{\gamma RT}$ ~300 m sec^{-1}, and about 100 m sec^{-1} or less for internal modes. In σ-coordinates this becomes a simple scheme for the following reason: the effect of the external mode enters the momentum equations mainly through the $\sigma\alpha\nabla\pi$ pressure term, where π is the surface minus the top pressure. Linear analysis indicates that this term alone accounts for $c_\pi = \pm\sqrt{RT}$, or 85 percent of the total speed of the external mode. Therefore, a simplified semi-implicit scheme can be defined in which only the $\nabla\pi$ term in the momentum equations, and the $\int_0^1 \nabla\cdot(\pi\mathbf{v})d\sigma$ term in the continuity equation are written implicitly. This scheme is essentially as simple as the corresponding one for the shallow water equations: it requires only the solution of a two-dimensional Helmholtz equation, and is uncoupled from the temperature equation. Simplified semi-implicit schemes were designed for Arakawa's schemes B and C equations and for the fourth-order GISS model on an unstaggered grid (Kalnay-Rivas, et al., 1977).

In preparation for the use of the simplified semi-implicit schemes in GCMs, several experiments were performed with the shallow water equations model. The semi-implicit scheme was combined with the splitting method used by Sundstrom (1974), which allows the reduction of the Helmholtz equation to a set of one-dimensional equations while still retaining formally second-order time truncation errors.

The experiments indicate that whereas the regular leapfrog scheme was marginally stable with a time step of 15 min.,

and the LFIII was stable with a 20-minute time step, the semi-implicit schemes could use much larger steps, up to 50 minutes. However, the results using the split semi-implicit scheme showed serious distortions after a few days, even with time steps as short as 20 minutes. When successive overrelaxation was used, the results showed no distortions until after about 8 days, even with large time steps. An iterative scheme developed by P. Frederickson, in which the norm of the error is reduced after each iteration by a factor that is independent of the number of gridpoints or their closeness, is being tested for the solution of the Helmholtz equation. It should be noted that no checkerboarding pattern was observed, even though four sets of Helmholtz equations were solved each time step, probably because the momentum equations in flux form were used, thus providing a weak coupling between adjacent points.

References

Arakawa, A., 1972: The design of the UCLA general circulation model. Tech. Rep. No. 7, Dept. of Meteorology, UCLA, Calif.

Kalnay-Rivas, E., A. Bayliss, and J. Storch, 1977: The fourth-order GISS model of the global atmosphere. Contributions to Atmos. Phys., 20, pp. 299-311.

Kwizak, M., and A. J. Robert, 1971: A semi-implicit scheme for grid point atmospheric models of the primitive equations. Mon. Wea. Rev., 99, p. 32.

MODEL-SIMULATED TRANSIENT EDDIES IN THE NORTHERN HEMISPHERE

(S. Srivatsangam)

An extensive study of non-stationary eddies in the GLAS model output is being conducted by the GLAS Modeling and Simulation Facility. This study is parallel to Blackmon (1976) and Blackmon, et al., (1977), which shall hereafter be cited as B1 and B2, respectively. B1 and B2 are based on a 10-winter set of meteorological observations.

In B1 and B2 the time series for such variables as sea level pressure and 500 mb geopotential height are first converted to time series of transient eddies of these variables by removing the time averages. Then the seasonal cycle is removed from the transient-eddy data by subtracting either the first four harmonics of the annual cycle or the parabolic fit of each winter's data. Finally, the eddies are separated into three types, which are: (i) low-pass filtered or slow-transient eddies of periods from 10 to 90 days; (ii) band-pass filtered or fast transient eddies of periods from 2.5 to 6 days; and (iii) high-pass filtered fluctuations with periods of less than 2 days.

In this study the filter coefficients reported in B1 were used. The first four harmonics of the annual cycle were considered to be the seasonal cycle. The reader may note that the data are for single seasons only, while the analyses in B1 and B2 are for 10 seasons.

The model integrations studied are called D091 and D100, both being for winter. D091 is characterized by a jump in sea surface temperature from month to month, whereas D100 has a linearly interpolated sea surface temperature from day to day. D100 integration was also performed using a filter for the two-grid wavelength (or $2\Delta x$) eddies in the zonal direction, effective from approximately 60°S to 60°N. In other respects, dynamically, D091 and D100 are similar to earlier GLAS model integrations.

The results of model integrations are available at the σ levels of the model. These are converted to pressure-level values and a time series data set for further computations.

The results are in two parts. The first part contains the statistics for the 500 mb geopotential height, which can be compared with B1, and the second part is for the winds at 500 mb, which are compared with B2.

Figure 1 contains the temporal root mean square (RMS) values of the unfiltered 500 mb geopotential height eddies, both for model simulation D091 (January and February) and for atmospheric observations (B1). The features in mid-latitudes are well defined in the model, and the maxima over the oceans are comparable in magnitude to atmospheric observations. Only the maximum over the U.S.S.R. is of considerably smaller value than in the observations.

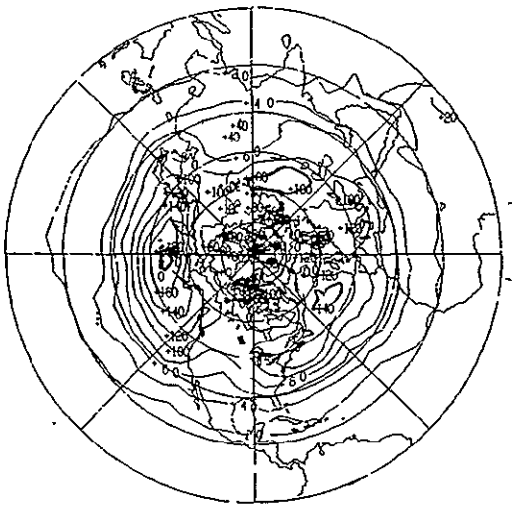

(1a)

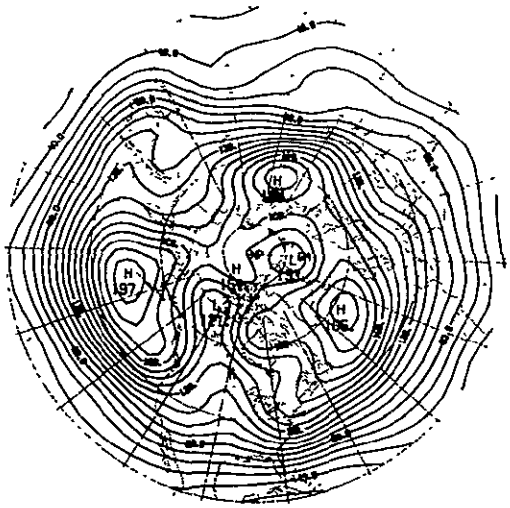

(1b)

Figure 1. Temporal RMS values of 500 mb geopotential height eddies for GLAS model integration D019 (1a) and from Blackmon (1b) (1976). Units: geopotential meters.

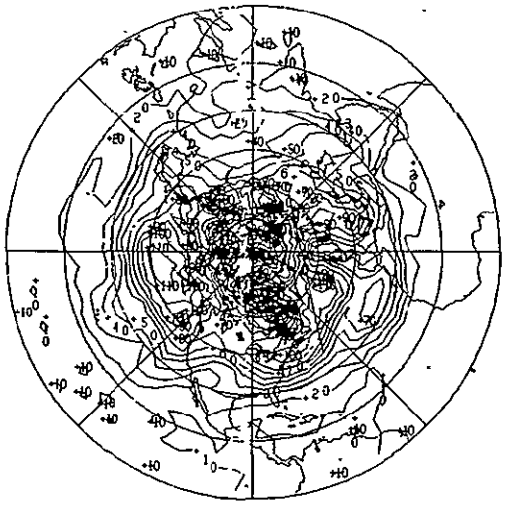

(2a)

(2b)

Figure 2. Temporal RMS values of 500 mb geopotential height eddies -- low-pass filtered component -- for GLAS model integration D091 (2a) and from Blackmon (2b) (1976). Units: geopotential meters.

Figure 2 has the RMS values of the low-pass filtered 500 mb geopotential height eddies. Here the maxima in the model are of smaller value in relation to the observations. The maximum over the U.S.S.R., as shown in the observations, appears only as an increase in value in the model.

Unlike the RMS low-pass filtered values, the band-pass RMS values, given in Figure 3, are over the Pacific and are larger in the model than in the observations. The maximum over the Atlantic is comparable to the observed. The orientation of contours is also in consonance with atmospheric observation.

The rest of the study's results deal with the statistics for the wind at 500 mb, as obtained in the integration D100 for January and February.

The seasonal mean zonal wind is represented in Figure 4. The jet stream maxima straddling the east coasts of North America and Asia and the maximum over the Sahara and Arabia are almost identical to observations. In the polar latitudes a wavenumber 3 pattern prevails, as in B2.

One of the striking results of B2 is the location of the band-pass RMS maxima downstream and poleward of the Asian and North American jet streams. Figure 5 shows the band-pass RMS values of the meridional wind at 500 mb. The maxima in Figures 4 and 5 show clearly that this is also observed in the GLAS model.

References

Blackmon, M. L., 1976: A climatological spectral study of the 500 mb geopotential height of the northern hemisphere. J. Atmos. Sci., 33, pp. 1607-1623.

Blackmon, M. L., J. M. Wallace, N. C. Lau, and S. L. Mullen, 1977: An observational study of the northern hemisphere wintertime circulation. J. Atmos. Sci., 34, pp. 1040-1053.

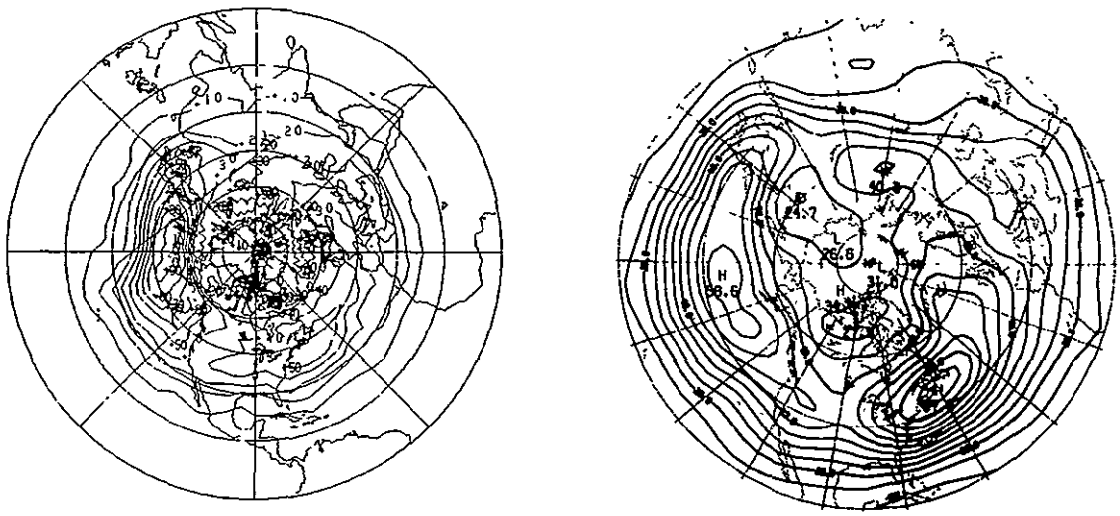

(3a) (3b)

Figure 3. Temporal RMS values of 500 mb geopotential height eddies -- band-pass filtered component -- for GLAS model integration D091 (3a) and from Blackmon (1976) (3b).

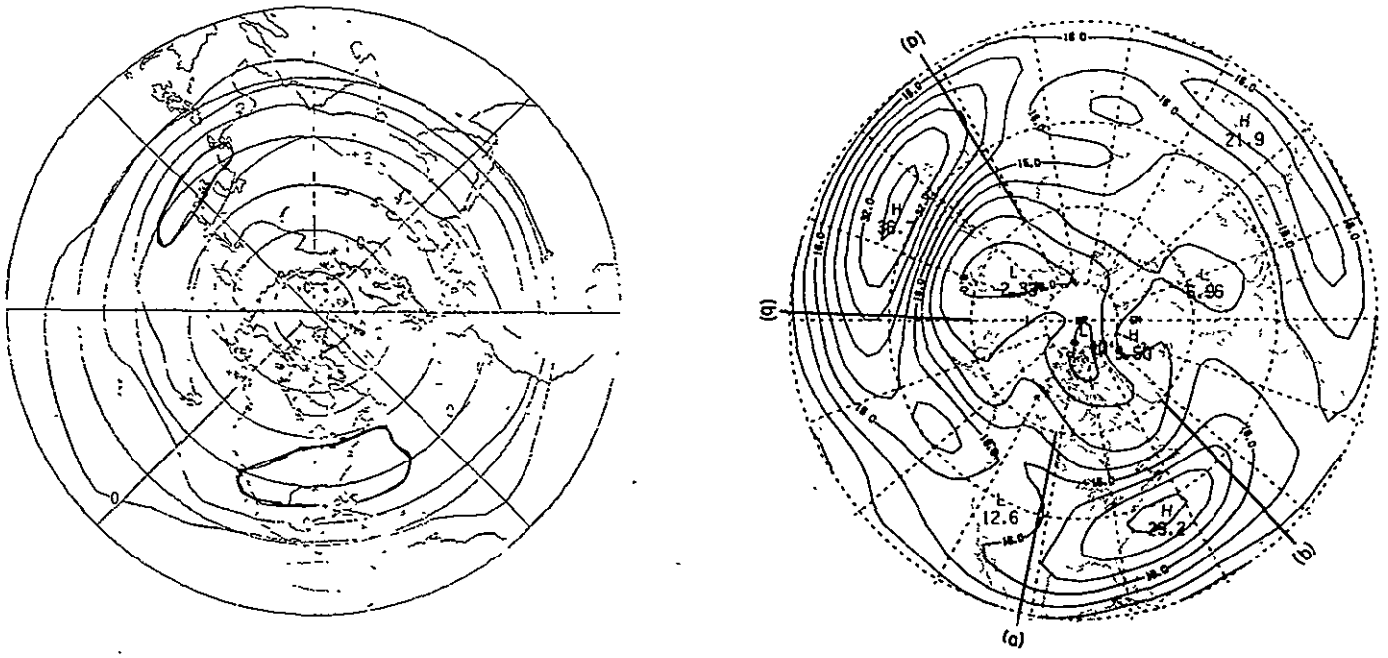

(4a) (4b)

Figure 4. Seasonal mean zonal wind in meters/sec. at 500 mb for GLAS model integration D100 (4a) and from Blackmon, et al. (4b).

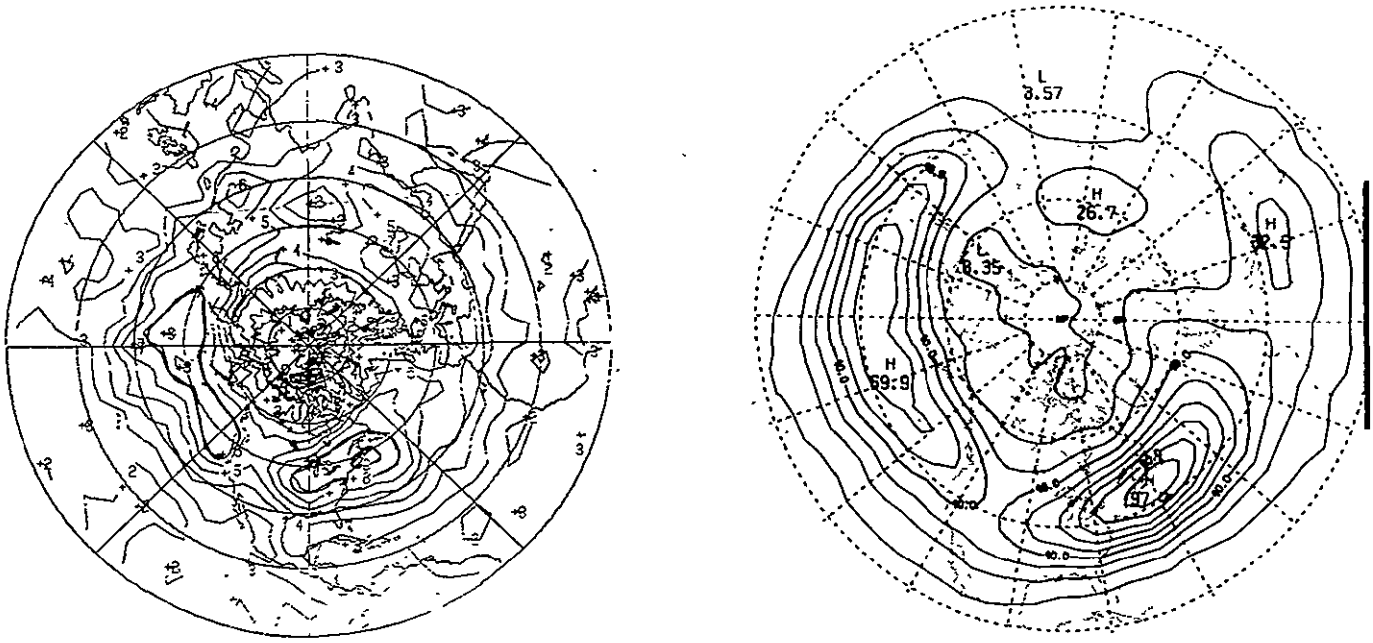

(5a) (5b)

Figure 5. Temporal RMS values of band-pass filtered 500 mb meridional wind for GLAS model integration D100 (5a) and from Blackmon et al. (1977) (5b). Units: ms^{-1}.

ATMOSPHERIC ABSORPTION SPECTRA NEAR 2200 CM^{-1} and 2400 CM^{-1}

(T. Mo and J. Susskind)

The spectral regions near 2200 cm^{-1} and 2400 cm^{-1}, on either side of the 4.3μm CO_2 band, are well suited for temperature sounding of the lower troposphere. Quantitative interpretation of radiometric measurements for temperature profiling requires the ability to accurately calculate the average transmittance across the sounding channel. Therefore, an accurate calculation of atmospheric absorption due to broad banded or continuum absorption features is as significant as one of the features due to individual lines. The important broad banded features affecting atmospheric absorption in the 4.3μm region are due to the pressure induced N_2 fundamental (called the N_2 continuum) and to wings of relatively nearby very saturated CO_2 lines.

An approximate analytical form for the transmittance through an atmospheric path, at zenith angle θ from pressure P to P' (in atmospheres), due to the N_2 continuum is given by (Susskind and Searl, 1977)

$$\tau_{\nu,N_2}(P,P',\theta)=\exp\left[-\int_{P'}^{P}.97k_\nu C_\nu H_o \sec\theta \frac{273}{T(P")}P"dP"\right] \qquad (1)$$

where T(P) is the temperature at pressure P, H_o is the atmosphere scale height at 273K=7.99 km, C_ν is the mixing ratio of N_2=.79, and k_ν is the self-induced absorption coefficient of N_2 ($amag^{-2}$ km^{-1}). The values of k_ν used in this work are derived from Figure 3 of Shapiro and Gush (1966). Sample values of k_ν are .028 at 2180 cm^{-1} and .126 at 2420 cm^{-1}.

It is well known that a Lorentz line shape seriously overestimates the absorption of CO_2 lines at frequencies far from the line centers. Winters, Silverman, and Benedict (1964) and Burch (1969) have introduced empirical sub-Lorentz line shapes to provide an adequate fit for laboratory absorption spectra of CO_2 in the region near 2400 cm^{-1}. Both line shapes can be expressed as

$$k(\nu)=k_L(\nu)\chi(|\nu-\nu_o|) \qquad (2)$$

where $k_L(\nu)$ is the Lorentz line shape and $\chi(|\nu-\nu_o|)$ is a multiplicative correction factor depending only on the distance in frequency from the line center.

Burch presented χ in graphical form, shown in Figure 1. Burch does not state the value of $|\nu-\nu_o|$ above which the line shape becomes sub-Lorentz. The calculations in this work using the Burch χ assume χ=1 for $|\nu-\nu_o|\leq 0.5$ cm^{-1}. Winters, et al. used the following analytical form for χ:

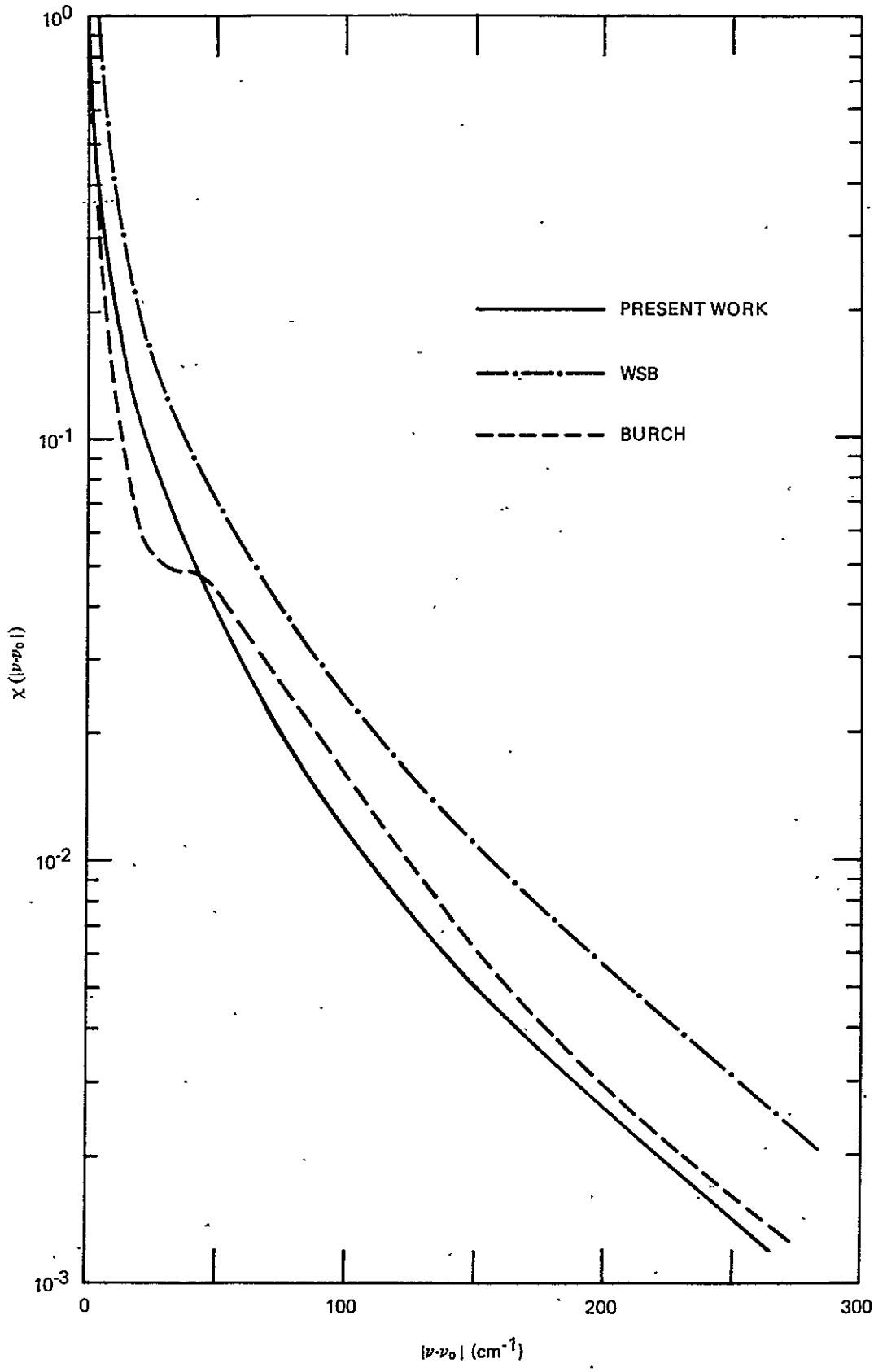

Figure 1. Sub-Lorentz line shape factors derived by Burch et al., Winters, Silverman, and Benedict, and the present work.

$$\chi_{WSB}(|\nu-\nu_o|)=1 \qquad |\nu-\nu_o|\leq 5.0 \text{ cm}^{-1}$$

$$\chi_{WSB}(|\nu-\nu_o|)=\exp[(-.46(|\nu-\nu_o|)-5.)\cdot^{46}] \quad |\nu-\nu_o|>5. \text{ cm}^{-1} \qquad (3)$$

The WSB χ function is always larger than the Burch χ and is also a smooth curve while the Burch χ contains a relatively constant segment between 23 and 50 cm^{-1}. It is shown that the use of a composite χ function

$$\chi_c(|\nu-\nu_o|)=1 \qquad |\nu-\nu_o|\leq .5 \text{ cm}^{-1}$$

$$\chi_c(|\nu-\nu_o|)=\exp[-.601(|\nu-\nu_o|-.5)\cdot^{434}] \quad |\nu-\nu_o|>.5 \text{ cm}^{-1} \qquad (4)$$

having the analytical form of χ_{WSB} but agreeing more closely with the values of χ_B, gives substantially better agreement of calculated and observed spectra.

The observed atmospheric absorption spectra shown in Figures 2 and 3 were taken by Beer using an interferometer with 0.059 cm^{-1} spectral resolution. The surface pressure was 793 mb and the solar zenith angle was 59°. More details are given in Susskind and Searl (1977). The theoretical calculations of atmospheric transmittance shown in Figures 2 and 3 were done according to the method of Susskind and Searl (1978). The monochromatic transmittances were convoluted with a 0.059 cm^{-1} triangular response function.

The main atmospheric absorption from 2385-2440 cm^{-1} arises from broad band features due to wings of the strong CO_2 lines in the vicinity 2325-2375 cm^{-1} and to the N_2 continuum. Superimposed on these are a series of weak CO_2 lines comprising the band head of the ν_3 band. Figures 2a and 2b show a comparison of the calculated and observed spectra from 2385-2405 cm^{-1} using the Burch and WSB line shapes. The WSB line shape produces systematically too much absorption over the whole region. The Burch line shape gives much better overall agreement but has too little absorption in the region 2390-2400 cm^{-1}. This behavior is a result of the flat portion on the Burch χ function with too little absorption below 23 cm^{-1} and too much above 50 cm^{-1}. Figure 2c, showing the results using the composite χ function (Equation 3), gives substantially better agreement with experiment, though it produces slightly too much absorption below 2392 cm^{-1}. The spectra give very little indication of the value of $|\nu-\nu_o|$ beyond which the line shape becomes sub-Lorentz. A function similar to χ_c but becoming sub-Lorentz after 5 cm^{-1} produced only slightly worse agreement with experiment.

Atmospheric absorption in the region 2180 cm^{-1}-2240 cm^{-1}, shown in Figure 3, is due almost exclusively to lines of N_2O, CO_2, and H_2O. The background absorption is much less than in the 2400 cm^{-1} region and arises primarily from the N_2 continuum. The use of any of the sub-Lorentz line shapes in Figure 1 predicts negligible CO_2 absorption in this region. Agreement of theory with experiment is seen to be quite good. Use of a Lorentz line

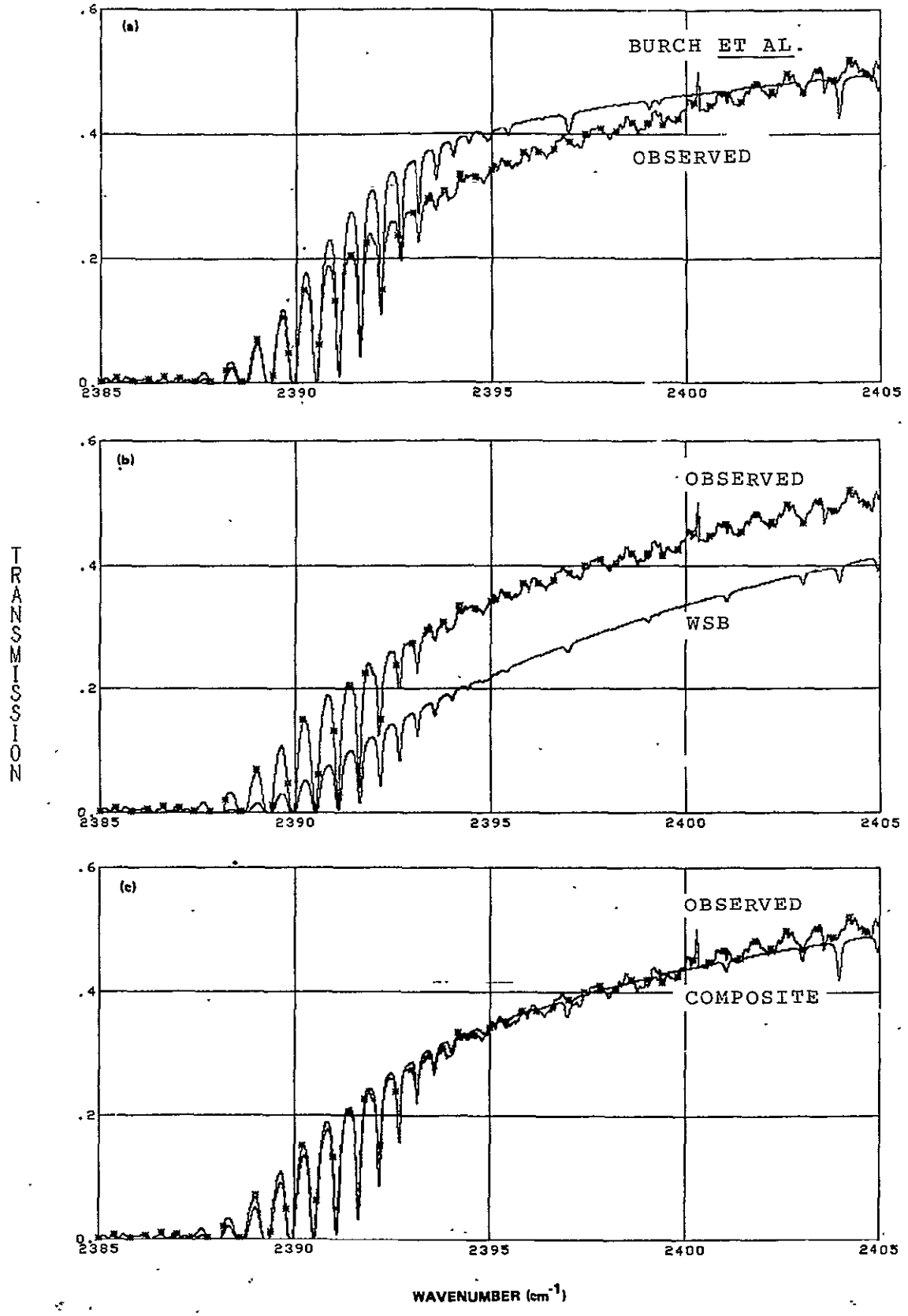

Figure 2. Comparison of observed atmospheric absorption spectra (0.59 cm^{-1} resolution) with calculated spectra using line shapes of Burch et al. , WSB, and that derived in the present work. The surface pressure is 793 mb. The zenith angle is 59°.

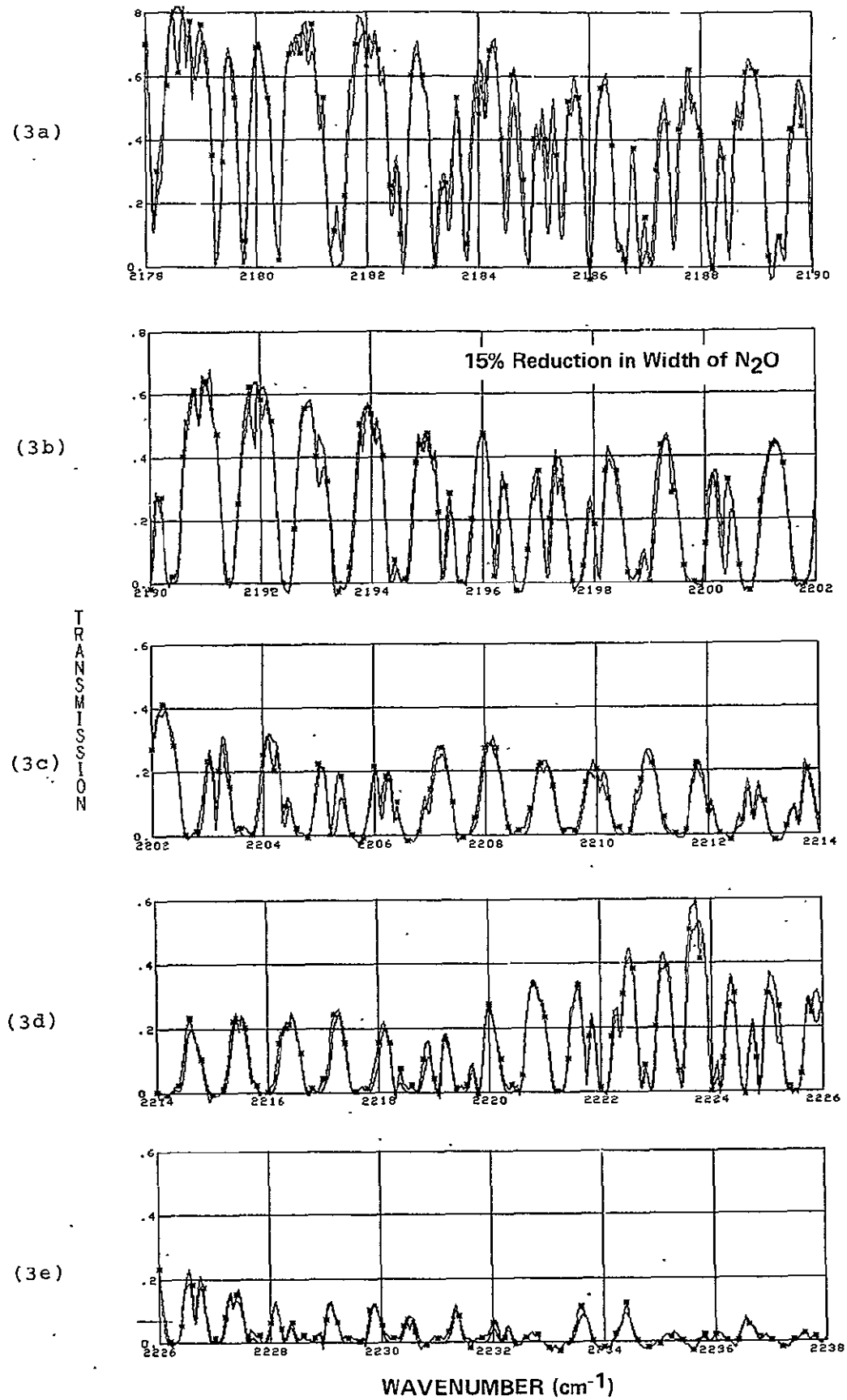

Figure 3. Comparison of observed and calculated atmospheric absorption spectra from 2178-2238 cm^{-1}. Conditions are the same as in Figure 2. Line widths of N_2O were reduced 15 percent from those on the McClatchey tape.

shape for CO_2, however, or neglect of the N_2 continuum, results in significant errors in transmitttance calculations, as shown in Figure 4.

The line parameters taken from the AFCRL compilation appear to be in general quite good. With the exception of the H_2O line at 2184.4 cm^{-1}, the calculated features agree well with observations. Most weak lines in the observed spectra not found in the calculated spectra can be attributed to CO absorption on the sun. The line widths of N_2O may be too large and were reduced by 15 percent to get the agreement shown in Figure 3.

While agreement between observed and calculated spectra is generally satisfactory, more work must be done on obtaining the best CO_2 line shape. For example, while Figures 1 and 2 show a composite χ which gives good agreement with observed spectra from 2390-2400 cm^{-1}, Table 1 shows two other composite line shapes, χ_2 and χ_3, which give essentially equal agreement of theoretical and observed spectra in the same spectral region. These two line shapes are almost identical to χ beyond 20 cm^{-1} from the line center, but are considerably different less than 10 cm^{-1} from the line center. The strong CO_2 lines whose wings give significant contribution to the absorption in the spectral region begin at about 2375 cm^{-1}. Therefore, calculated absorption spectra at about 2395 cm^{-1} using all three line shapes are about the same. Significant differences occur at lower frequencies however which are essentially completely opaque in the observed spectra; hence these spectra cannot be used to select an appropriate line shape. Table 1 gives differences in clear column radiances calculated for a standard atmosphere using χ_1 through χ_4 as compared to the Burch χ. Both the Burch χ and χ_4 (WSB χ) have been shown to be incorrect by Figure 2. Therefore, the relative error of 42 percent in calculated clear column radiance between χ_4 and χ_B only shows the need for care in performing the calculations. More significant however are differences between results using χ_1 through χ_3 which, at this time, are all equally reasonable line shapes. Agreement in calculated clear column radiances is of the order of 1 percent for the channels with centers 2394.5 and 2392.35. Differences become quite significant in the more opaque portions of the band, reaching 9 percent at 2386.10 cm^{-1}, which is well above the acceptable level of 1 percent. Consequently, experiments are currently underway in analysis of high resolution balloon-borne atmospheric absorption measurements which will enable us to examine spectra in the region 2380-2390 cm^{-1} for a more precise determination of an accurate χ function.

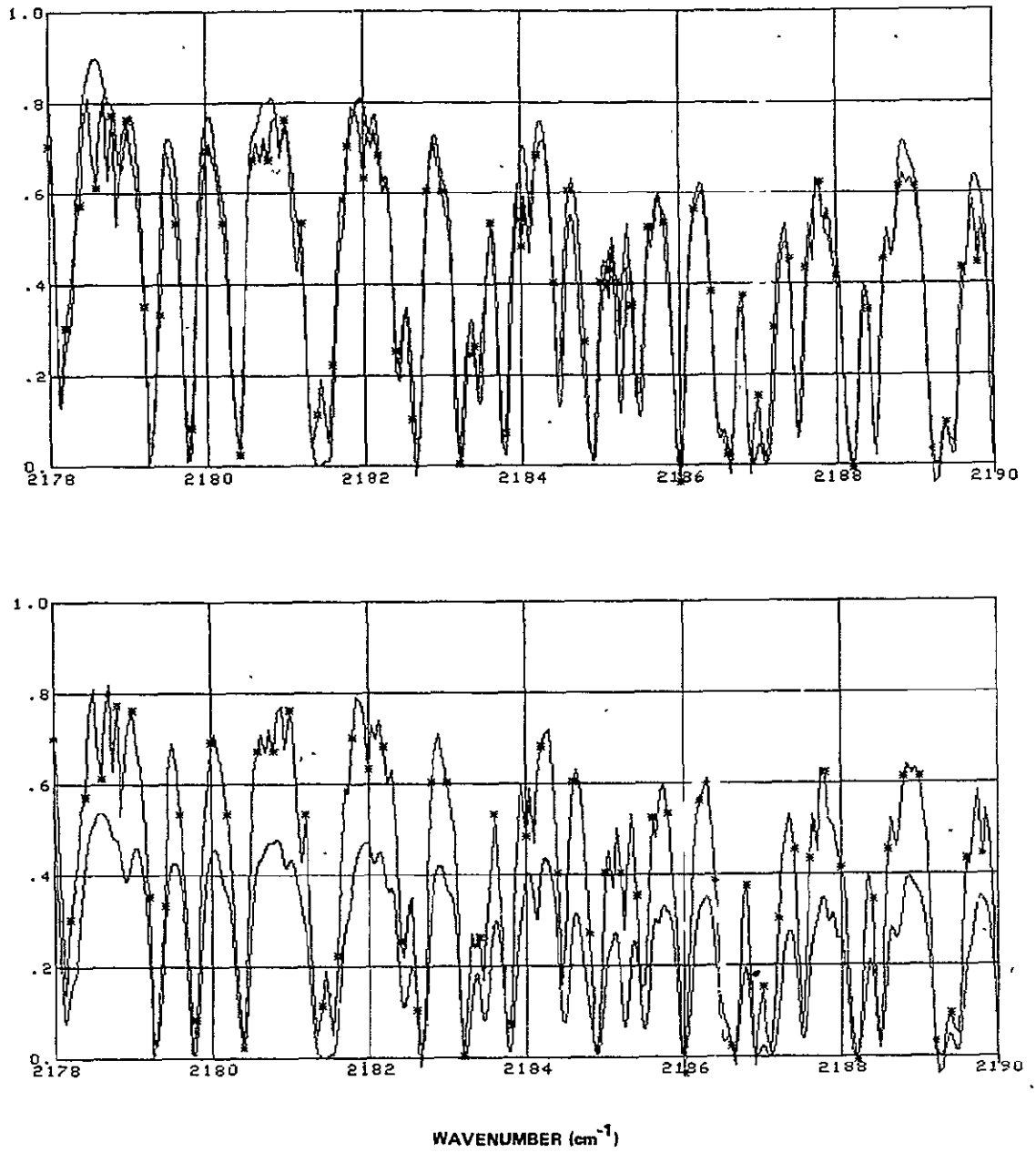

Figure 4. Same as for Figure 3a except that Figure 4a does not include the N_2 continuum in the calculation and Figure 4b uses a Lorentz line shape from CO_2 in the calculation.

Table 1. U. S. Standard Atmosphere Percent Difference in Calculated Radiance Relative to Burch χ.

$\nu(cm^{-1})$	$d\tau/d\ln P$ MAX(mb)	χ_1	χ_2	χ_3	χ_4
2383.75	270	- .75	- 3.85	- 7.33	-13.04
2386.10	390	- 4.15	- 8.13	-13.40	-29.50
2388.20	550	- 8.30	-11.19	-15.85	-40.89
2390.20	700	-10.16	-11.58	-14.36	-42.48
2392.35	975	- 9.50	- 9.91	-10.89	-36.27
2394.50	SURFACE	- 7.77	- 7.85	- 7.97	-28.49

$\chi_1(X)=e^{-.601(X-.5)^{.434}}$

$\chi_2(X)=e^{-.647(X-2)^{.419}}$

$\chi_3(X)=e^{-.749(X-5)^{.390}}$

$\chi_4(X)=e^{-460(X-5)^{.460}}$ (WSB)

References

Burch, D. E., D. A. Gryvnak, R. R. Patty, and C. E. Bartky, 1969: Absorption of infrared radiant energy by CO_2 and H_2O, IV. J. Opt. Soc. Am., 59, pp. 267-280.

Shapiro, M. M., and H. P. Gush, 1966: The collision-induced fundamental and first overtone bands of oxygen and nitrogen. Canada J. Phys., 44, pp. 949-963.

Susskind, J., and J. E. Searl, 1977: Atmospheric absorption near 2400^{-1}. J. Quantitative Spectroscopy Rad. Transfer, 18, p. 581.

Susskind, J., and J. E. Searl, 1978: Synthetic atmospheric transmittance spectra near 15 and 14.3 mm. J. Quantitative Spectroscopy Rad. Transfer, 19, p. 195.

Winters, B. H. S. Silverman, and W. S. Benedict, 1964: Line shape in the wing beyond the band head of the 4.3μm band of CO_2. J. Quantitative Spectroscopy Rad. Transfer, 4, pp. 527-537.

SIMULATION STUDIES OF THE ADVANCED METEOROLOGICAL TEMPERATURE SOUNDER (AMTS)

(A. Rosenberg and J. Susskind)

The AMTS is a new generation, high-resolution passive temperature sounder designed jointly by GSFC and JPL. The objectives of this study are to develop techniques for the analysis of AMTS data and investigate its performance characteristics relative to HIRS.

The theoretical considerations and the full details of the AMTS are given in Kaplan, et al. (1977). It contains twelve temperature sounding channels in the 4.3μm and 15μm regions, capable of sounding temperatures in the stratosphere and in the troposphere. The spectral resolution and the weighting functions are shown in Figure 1a. It contains also three lower tropospheric sounding channels in the 15μm region for cloud filtering, as well as water vapor sounding channels and three 4.0μm window channels for determining surface temperature, surface emissivity, and reflected solar radiation (not shown in Figure 1). For comparison, the weighting functions for the HIRS channels are shown in Figure 1b. The AMTS represents an improvement over previous sounders such as the HIRS because of its narrow weighting functions, obtained by utilizing small spectral band passes in the wings of CO_2 lines, with high transmittance dependence on temperature and pressure. Consequently, it is possible to increase the number of sounding channels, in particular in the stratosphere, and obtain a higher vertical resolution. This property can be best demonstrated by simulated observations and retrievals based on reported significant level radiosonde data containing the full fine structure of the temperature profile.

The general retrieval procedure used is based on the relaxation method outlined by Chahine (1970). In the presence of a cloud field, it is necessary to have observed radiances in two fields of view, $R_{1,i}$ and $R_{2,i}$ for all the channels i. These "observations" are simulated by calculating the radiances $R_{1,i}$ and $R_{2,i}$ for all the channels i using radiosonde temperature profiles $\{T_{ra}\}$, and single layer clouds with latitude dependent cloud top heights and a random distribution of fractional cloud covers, N_1 and N_2, in the two fields of view. A Gaussian distribution of random noise, representative of the performance of the HIRS and AMTS instruments, is added to the calculated radiances of the respective channels.

From the observed radiances in the two fields of view, clear column radiance R_i can be reconstructed from the relation

$$R_i = R_{1,i} + \eta(R_{1,i} - R_{2,i}) \qquad (1)$$

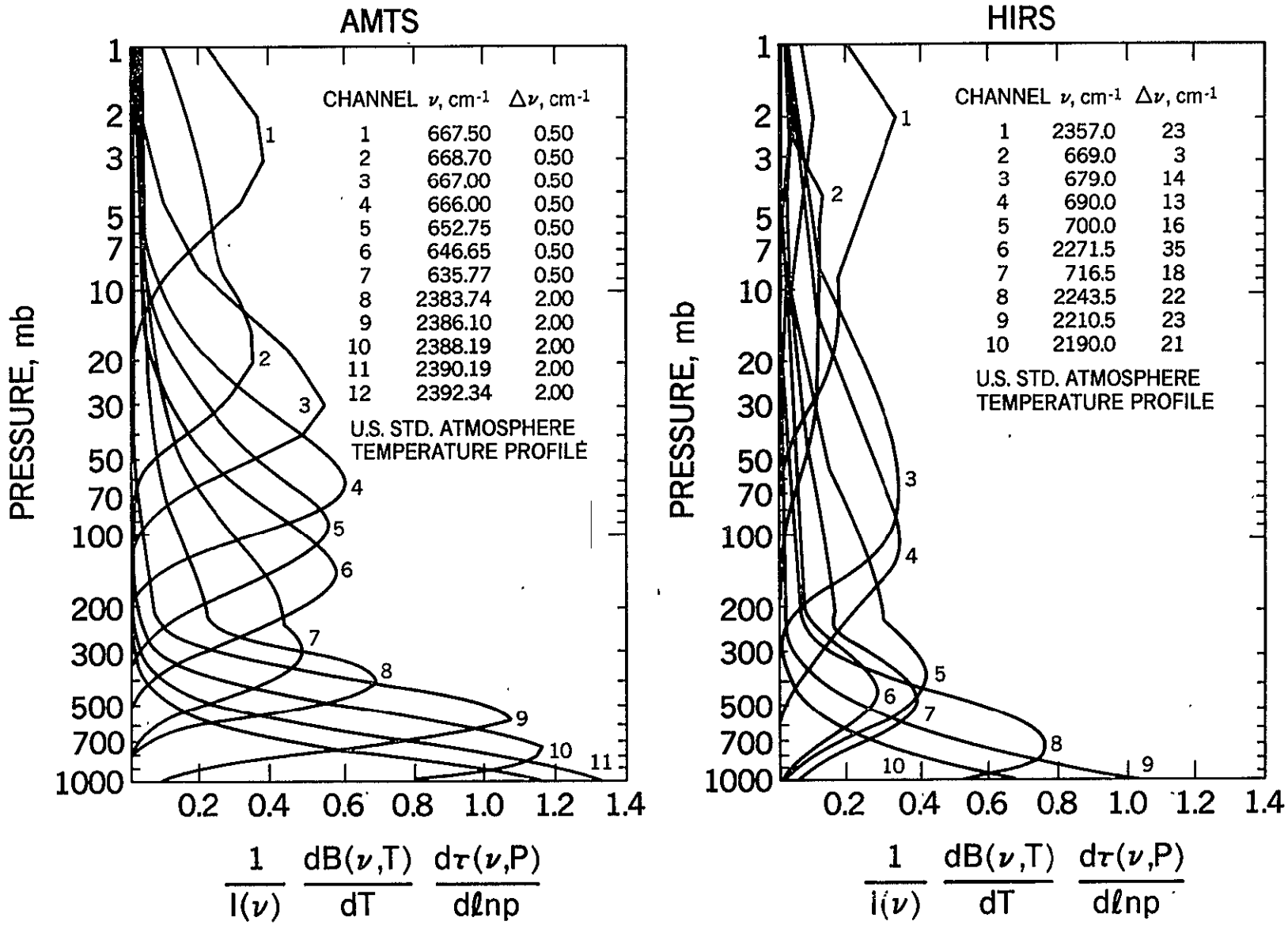

Figure 1. Normalized temperature weighting functions for HIRS and AMTS for nadir viewing.

where η is independent of the channels i, but depends only on N_1 and N_2. Conversely, if $r_i^{(n)}$, an n^{th} estimate of R_i is given, $\eta^{(n)}$ can be determined from:

$$\eta^{(n)} = (r_i^{(n)} - R_{1,i})/(R_{1,i} - R_{2,i}) \qquad (2)$$

The problem of temperature retrievals in cloudy atmospheres involves the simultaneous determination of η from Equation (2) and a temperature profile, $\{T_R\}$, such that Equation (1) will prevail within noise levels for the same value of η for all the channels. $\{T_R\}$ and η are obtained by using the following iterative method. For the n^{th} iteration, the clear column radiances, $r_i^{(n)}$, are calculated from the n^{th} temperature profile $\{T_n\}$ for the temperature sounding channels (t) and for the cloud filtering channels (c). $\eta^{(n)}$ is then determined from the cloud filtering channels by using $r_c^{(n)}$ in Equation (2). Using Equation (1) and $\eta^{(n)}$ again, $R_t^{(n)}$, the reconstructed clear column radiance is determined for each temperature sounding channel. These values are then compared with the clear column radiances computed from the n^{th} temperature profile. If

$$\varepsilon \equiv \left| \frac{R_t^{(n)} - r_t^{(n)}}{r_t^{(n)}} \right| < .001 \ ,$$

the n^{th} temperature profile is taken as the retrieved temperature profile $\{T_R\} = \{T_n\}$. If $\varepsilon > .001$ the iteration is continued by constructing a new temperature profile, $\{T_{n+1}\}$, from $\{T_n\}$ in the following manner. The temperatures $T(P_t)$ corresponding to the pressures, P_t of the peak of the weighting functions for channel t are corrected according to the equation:

$$\frac{B_t[T_{n+1}(P_t)]}{B_t[T_n(P_t)]} = \frac{R_t^{(n)}}{r_t^{(n)}} \qquad (3)$$

The full 66-level temperature profile used to calculate $r_t^{(n+1)}$, $\{T_{n+1}\}$, is obtained by interpolating between the points $T(P_t)$ linear in the logarithm of the pressure, while preserving the shape of the first guess temperature profile (see next section). If $\varepsilon > .001$ after ten iterations, the 10th temperature profile is taken as the retrieved profile $\{T_R\} = \{T_{10}\}$.

The iteration process must start with a first guess temperature profile (FGTP) $\{T_o\}$. Since the shape of $\{T_o\}$ is preserved during the iteration procedure, it is important that the shape of $\{T_o\}$ will be as close as possible to that of the true profile $\{T_{ra}\}$ for a good solution to be obtained. This requirement is particularly important in the tropopause region which is characterized by a sharp discontinuity in the lapse rate $-(\partial T/\partial Z)$.

For HIRS, a zonally-averaged climatology profile was used as an FGTP. The deficiency of this FGTP is that it does not reflect the shape of the individual radiosonde temperature profiles. For the AMTS, an innovative method was developed, making use of the sharpness of the weighting functions to construct an initial FGTP that does not require any prior knowledge of the state of the atmosphere.

The key to the method is the assignment of a characteristic pressure, $P_t^{(c)}$, to each channel, representative of a pressure whose temperature has been shown to be close to the observed brightness temperature by examination of results from a variety of profiles. These characteristic pressures, $P_t^{(c)}$, do not coincide with P_t, the pressures at the peak of the weighting functions. The first guess is constructed by assigning the observed brightness temperatures, T_t, to the corresponding characteristic pressures $P_t^{(c)}$. The full 66-level temperature profile is then obtained by a linear interpolation in the logarithm of the pressure.

This temperature profile is further refined to reflect the shape of the true profile in the tropopause region. Starting from the surface, the lapse rate is calculated for each segment, $P_t^{(c)}$ to $P_{t+1}^{(c)}$, until a segment L is reached in which the lapse rate is less than 2°K/km. The temperature profile in this segment is modified by replacing it with two linear segments, which are extrapolations of the two adjacent segment L-1 and L+1 (see Figure 2). The values of the temperature and the pressure at the intersection of the segments (L-1) and (L+1) are in general fairly close to the corresponding values of the true tropopause.

The FGTP obtained in this manner for the AMTS channels together with the triangulation is greatly superior to the latitude-dependent climatology profile.

This method of constructing an FGTP and obtaining approximately the height of the tropopause by triangulation was not applied to the HIRS because of the broadness of the weighting functions of its stratospheric sounding channels. Therefore, a climatology temperature profile was used as an FGTP. However, studies are underway to modify this method to test whether it is applicable to the HIRS as well.

With the exception of the choice for the FGTP, the retrieval procedure for the two sounders was identical. After a retrieved temperature profile $\{T_R\}$ was obtained, the RMS errors relative to the profile $\{T_{RA}\}$ were calculated for the 12 mandatory levels. The overall and the mandatory levels of RMS errors obtained from 286 global radiosonde stations are given for the AMTS and for the HIRS in Figure 3. The overall RMS errors for AMTS and HIRS are 1.72°K and 2.27°K, respectively. The AMTS is superior to the HIRS particularly in the stratosphere. A typical retrieved temperature profile for the AMTS and the HIRS together with the radiosonde profile used to

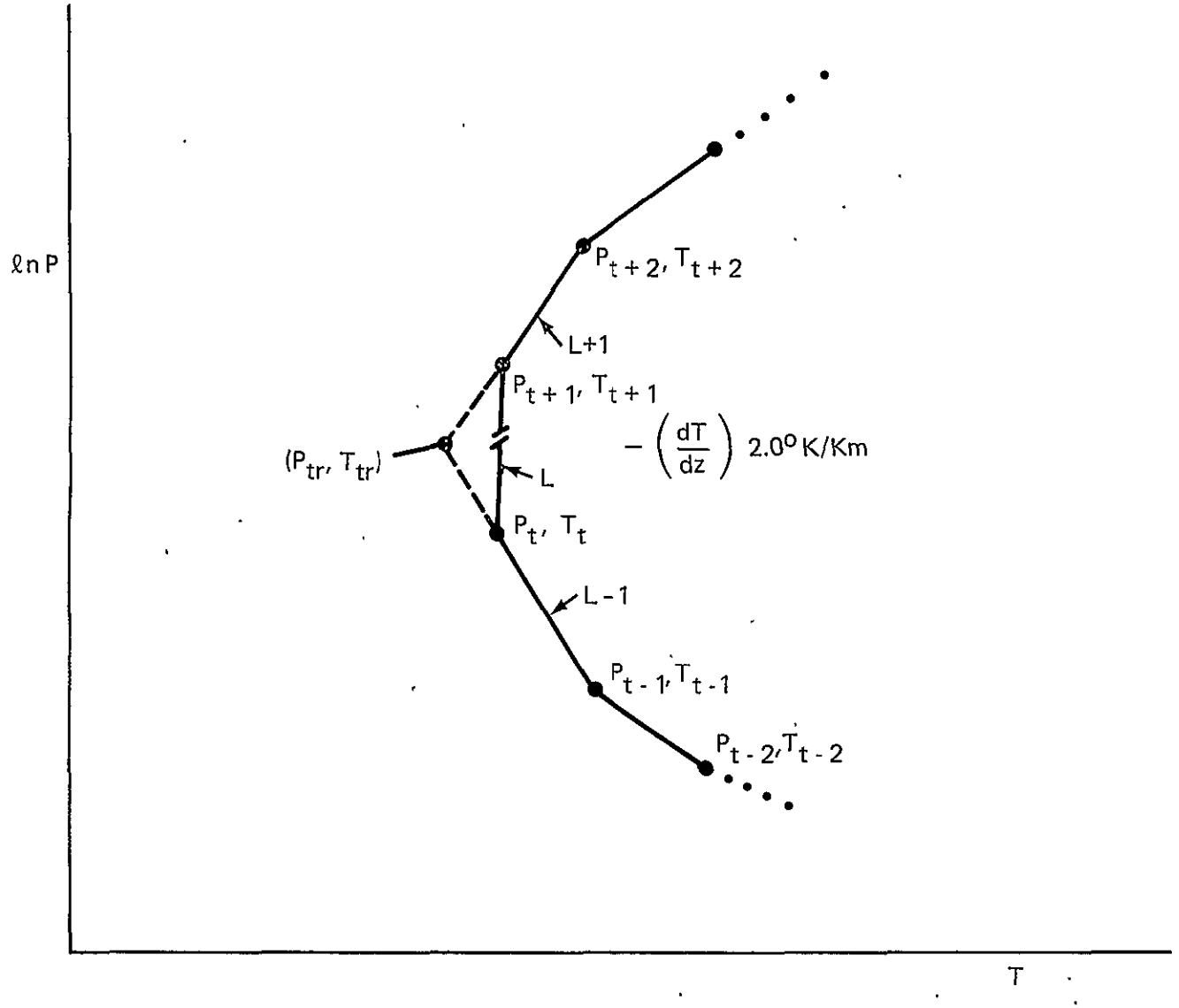

Figure 2. Construction of the first guess temperature profile using characteristic pressures, observed brightness temperatures, linear interpolation of temperature in ℓnP and triangulation in the region of a break in the apparent lapse rate. The first guess temperature pressure is shown as P_{tr}.

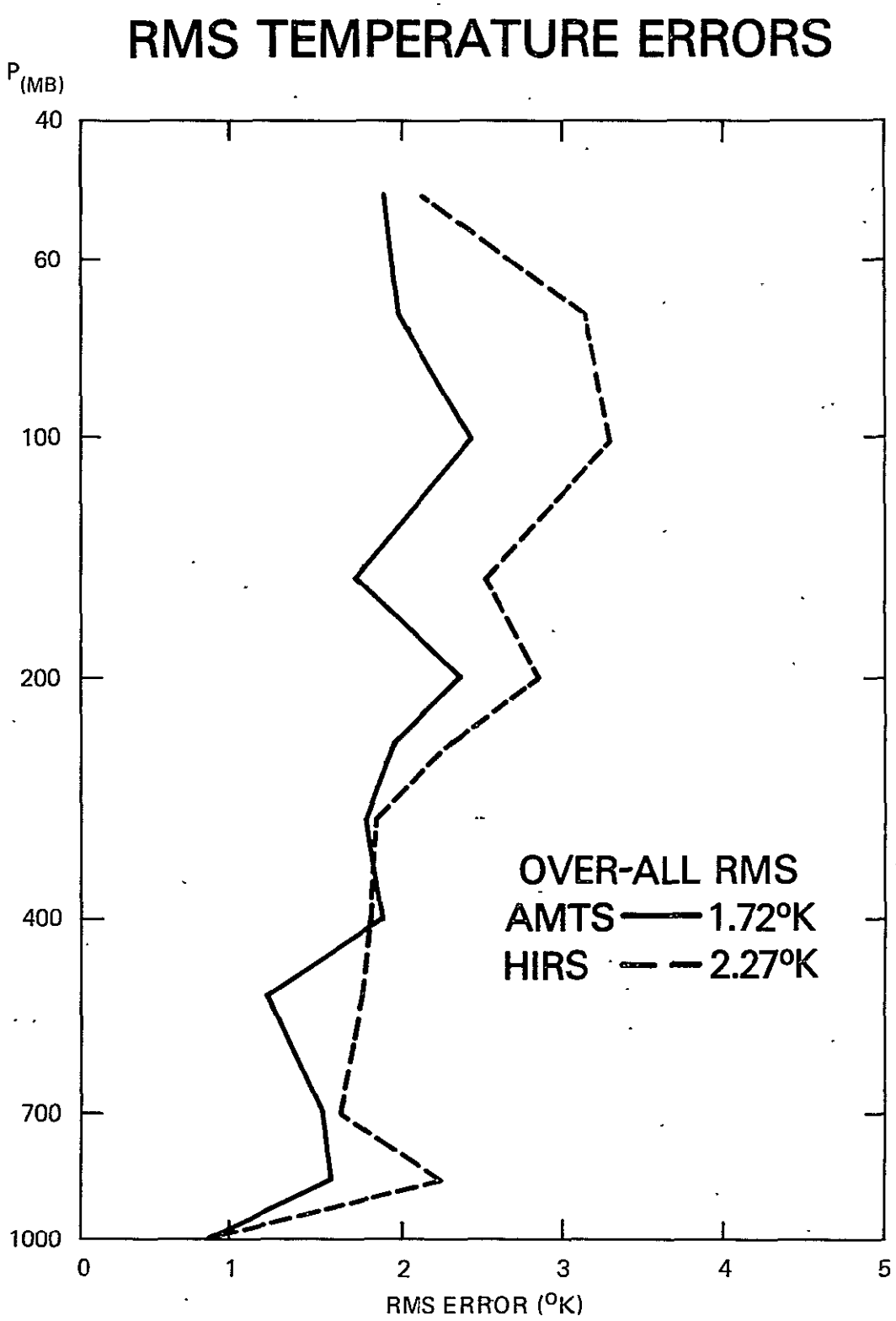

Figure 3. RMS errors versus height of simulated AMTS and HIRS retrievals as compared to radiosonde.

simulate the observations are given in Figures 4a and 4b, respectively. For the AMTS the true and the retrieved tropopause are also given. That portion of the AMTS profile in which triangulation was used to determine the tropopause is shown by dots. As is expected, it can be seen that the AMTS more accurately reproduces the structure of the radiosonde profile, particularly in the tropopause region and the lower troposphere, due to the sharpness of its sounding channels.

The RMS error for the retrieved tropopause heights was calculated for the AMTS and was found to be less than 1.0 km. The general accuracy of this determination can be seen in Figures 5a and 5b showing contour maps for the tropopause pressure over the U. S. as determined from radiosonde reports and simulated AMTS retrievals. The general agreement is seen to be very good.

References

Chahine, M. T., 1970: Inverse problems in radiative transfer: determination of atmospheric parameters. J. Atmos. Sci., 27, p. 960.

Kaplan, L. D., M. T. Chahine, J. Susskind, and J. E. Searl, 1977: Spectral band passes for a high precision satellite sounder. Appl. Optics, 16, p. 322.

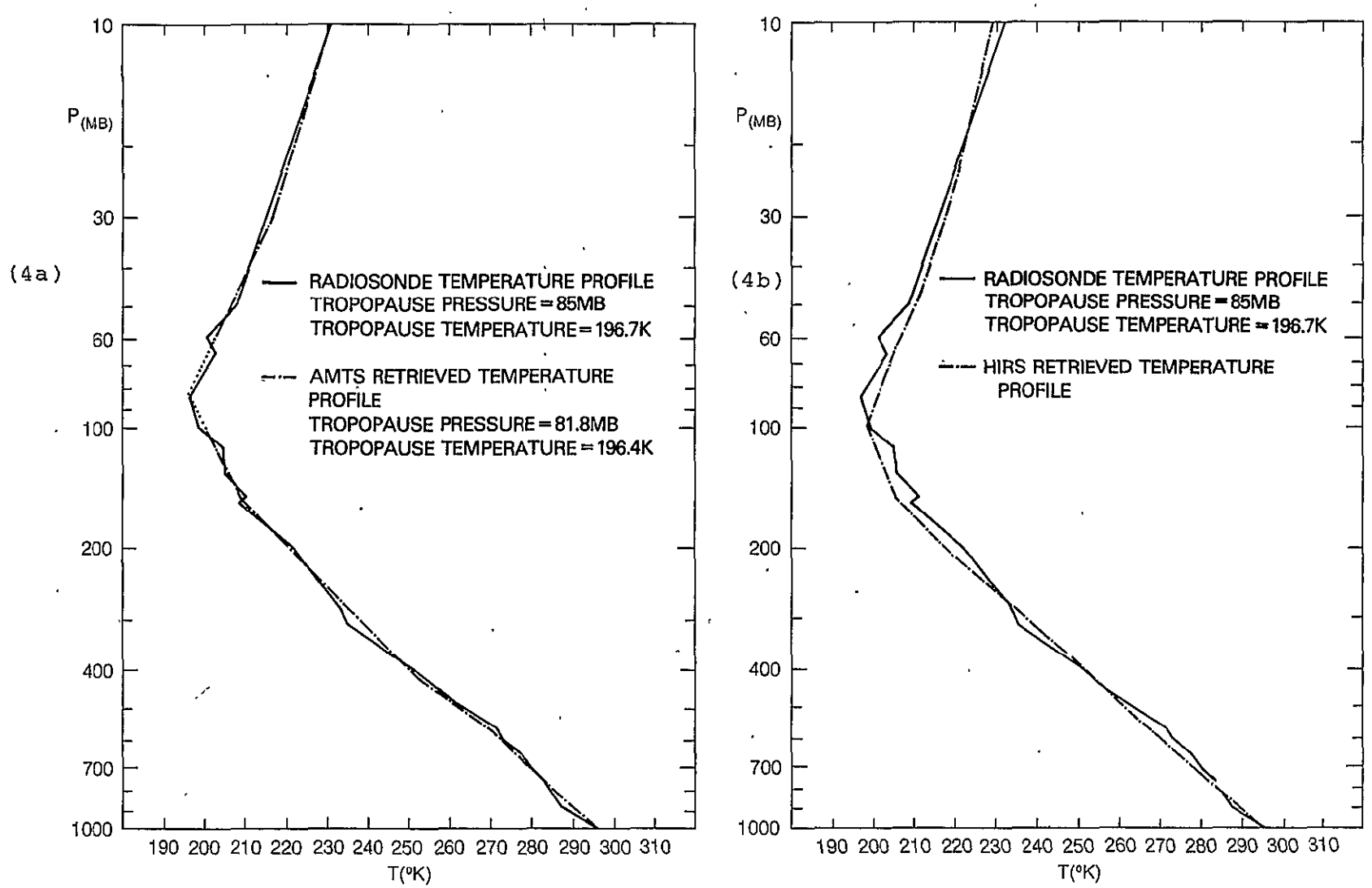

Figure 4. Sample radiosonde profile compared to retrieved AMTS and HIRS profiles. The dotted portion of the retrieved AMTS profile was determined by triangulation.

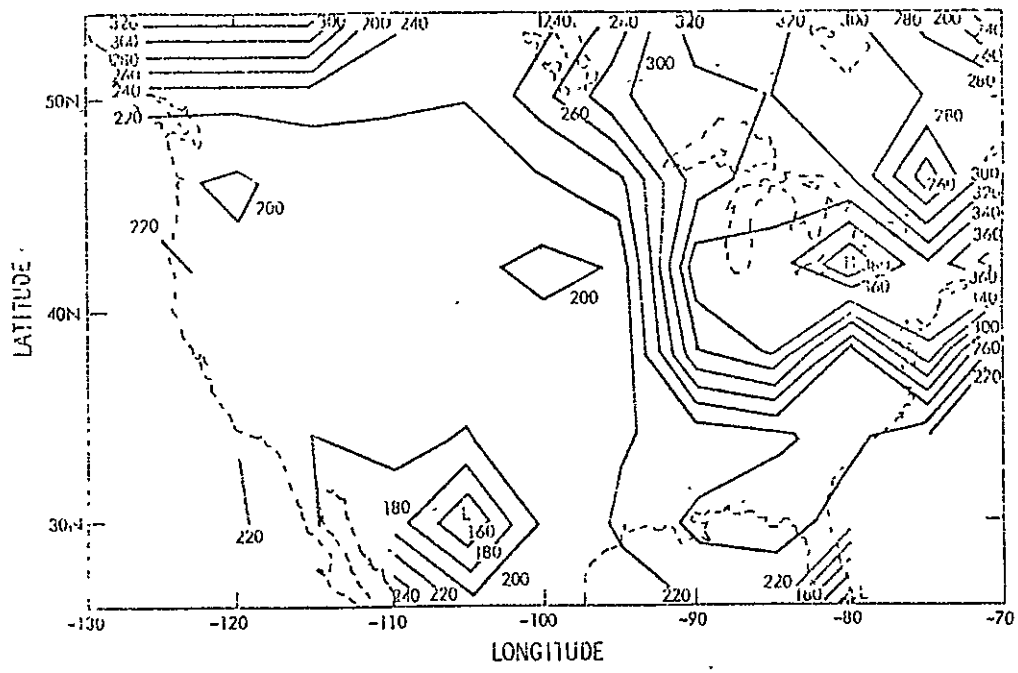

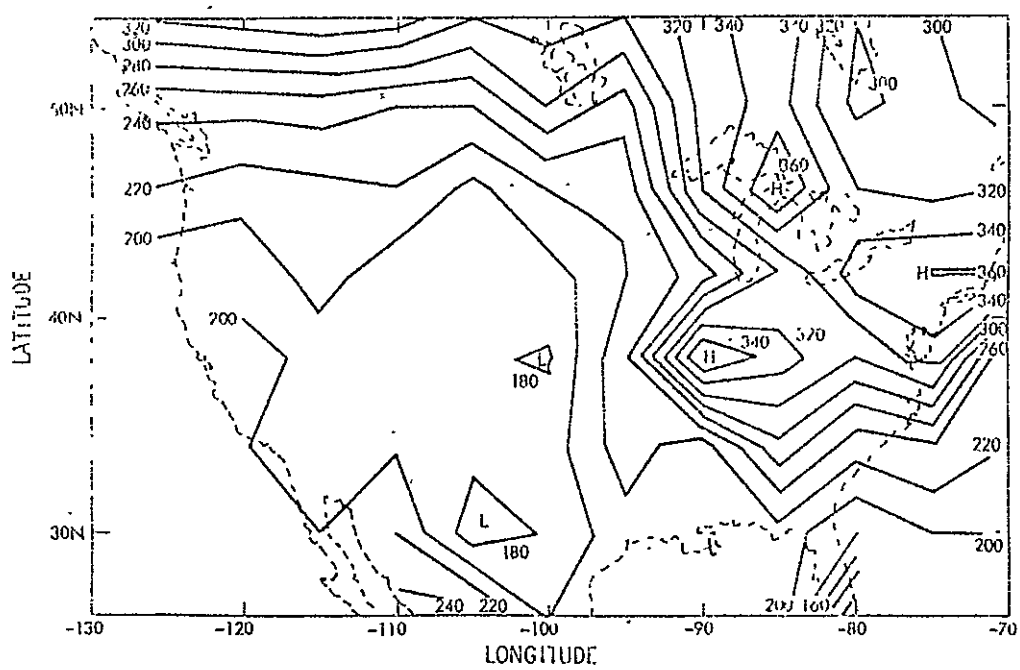

Figure 5. Comparison of tropopause pressure field as obtained from simulated AMTS retrievals with that determined from radiosonde reports.

RAPID ALGORITHM FOR CALCULATION OF TEMPERATURE DEPENDENCE OF HIRS TRANSMITTANCE FUNCTIONS

(T. Mo and J. Susskind)

The purpose of this study is to establish a rapid and accurate algorithm for calculating the temperature and zenith angle dependence of the dry atmospheric transmittance functions for 11 HIRS channels in the Nimbus-6 satellite.

Analytic formulas of atmospheric transmittance functions for 11 HIRS channels are developed and parameterized as functions of atmospheric temperature profiles. Parameters for atmospheric transmittance functions at two solar zenith angles of 0° and 40° are obtained from least-square fit to line-by-line calculated transmittance functions. Based on the two sets of parameters at the angles of 0° and 40°, transmittance at an arbitrary zenith angle θ is obtained by linear interpolation in $\sec\theta$. Atmospheric radiances calculated with the transmittances obtained from the analytic formulas show small errors of the order of 0.5 percent compared to line-by-line calculations. These analytic formulas have been incorporated into the analysis of HIRS observations for determination of atmospheric temperature profiles.

The dry transmittance function $\tau_i(P_n,0,T,\theta)$, from the top of the atmosphere to pressure P_n at zenith angle θ, averaged over channel i, is a function of the entire temperature profile from pressure P_n to the top of the atmosphere. For modeling the temperature dependence of the transmittance function, it is convenient to introduce an effective layer transmittance for a layer between pressure P_n and P_{n-1} defined by,

$$\tau_i(P_n,P_{n-1},T,\theta) \equiv \tau_i(P_n,0,T,\theta)/\tau_i(P_{n-1},0,T,\theta) \qquad (1)$$

For simplicity, this effective layer transmittance is written as $\tau_{i,n}(T,\theta)$.

For monochromatic radiation, the effective atmospheric transmittance for the layer is identical to the atmospheric transmittance through the layer. It therefore depends only on the temperature profile in the layer (taken to be homogeneous for thin layers) and is independent of the temperatures above the layer. While this property is not rigorously true for finite width channels as in the HIRS case, the effective layer transmittance is still dependent primarily only on the temperature of that layer with only a small residual dependence of

the temperature profile above the layer. The procedure used to model the temperature dependence of the HIRS transmittance functions was to calculate transmittance functions for a number of climatological profiles using an accurate line-by-line transmittance program, and model the calculated layer transmittances as a function of layer temperature and another quantity, which may be considered as a mean lapse rate above the layer. A 66-layer pressure mesh was used in all calculations and the effective transmittances were calculated using adjacent layers.

A. Line-by-Line Calculation. The calculations of $\tau_i(P_n,0,T,\theta)$ are done according to the method of Susskind and Searl (1978) using the 1976 version of the AFCRL compilation of atmospheric molecular line parameters. For each channel, the transmittance function was calculated with six climatological temperature profiles corresponding to the U. S. standard atmosphere, January 40°N, 70°N and July 0°N, 40°N, 70°N. Each calculation was done at two zenith angles 0° and 40°N, corresponding to the extreme angles of the HIRS instrument.

A Voigt absorption line shape is assumed for all atmospheric species except CO_2. Following a recent study by Susskind and Mo (1978), an 'empirical' CO_2 line shape is adopted and defined by

$$k(\nu) = k_L(\nu)\, X(\Delta) \tag{2}$$

where $k_L(\nu)$ is the Lorentz line shape and $X(\Delta) \equiv X(|\nu-\nu_o|)$ is an empirical correction factor defined as

$$X(\Delta) = \begin{cases} 1 & \text{for } \Delta \leq 0.5 \text{ cm}^{-1} \\ e^{-\alpha(\Delta-0.5)^{\beta}} & \text{for } \Delta > 0.5 \text{ cm} \end{cases} \tag{3}$$

where $\alpha = 0.601$ and $\beta = 0.434$ are two empirical parameters, determined to give the best fit to an observed atmospheric absorption spectra in the wavenumber region of 2388-2395 cm^{-1} (see Susskind and Mo, 1978). The Voigt function is used for $\Delta \leq .5$ cm^{-1}.

B. Analytic Representation. The analytic formula employed in the present work to represent the line-by-line calculated effective layer transmittance functions, $\tau_{i,n}(T,\theta)$, has the form

$$\tau_{i,n}(T,\theta) = \sigma_{i,n}(\theta) + \omega_{i,n}(\theta)\Delta_n T + \varepsilon_{i,n}(\theta)\Delta_n^2 T \qquad (4)$$

where the three parameters $\sigma_{i,n}(\theta)$, $\omega_{i,n}(\theta)$ and $\varepsilon_{i,n}(\theta)$ are independent of temperature and are obtained by least-square fit to the line-by-line calculated layer transmittance functions for each channel at each of the two angles. The quantities $\Delta_n T$ and

$\Delta_n^2 T$ are defined as

$$\Delta_n T = (T-T_s)_n \qquad (5)$$

and

$$\Delta_n^2 T = \Delta_n T - \Delta_{n-m} T \qquad (6)$$

where T is the temperature at the mid-level of the layer n, and T_s corresponds to the U. S. standard temperature at the layer n. The quantity in Equation (6) is taken to represent the difference in mean lapse rate of the profile at pressure P_n as compared to that of the standard atmosphere. This quantity was difficult to model accurately but the following choice of m values gave reasonable fits for a variety of profiles.

$$m = \begin{cases} 0 & \text{if } n \leq 10, \quad (P \leq 10 \text{ mb}) \\ 5 & \text{if } 10 < n \leq 30, \quad (10 \text{ mb} < P \leq 200 \text{ mb}) \\ n-25 & \text{if } n > 30, \quad (P > 200 \text{ mb}) \end{cases} \qquad (7)$$

The first two terms in the expression on the right hand of Equation (4) are essentially a Taylor series expansion of the layer transmittance at a pressure level P, using the temperature T as variable. Approaches similar to this two-term approximation have been employed by Kondrat'ev and Timofeyev (1969), and by Wang (1978). However, the last term in Equation (4) was found to be important in obtaining substantial improvement in the agreement between the line-by-line calculations and the analytic results.

Physically, the last term in Equation (4) takes into account the temperature 'memory' effect of the upper atmosphere on the transmittances calculated at lower layers. Its importance becomes more pronounced as the pressure increases in the lower atmosphere. Equation (7) shows that this term (with m=0) has no

effect on the transmittances in the upper atmosphere where $P \leq 10$ mb (i.e., the effective lapse rate is always taken as zero in the upper stratosphere). The effective lapse rate correction is taken over a 5-50 mb interval for pressures between 15 mb and 200 mb, and taken over the interval between P and 150 mb for P>200 mb.

Equation (4) was used to fit the line-by-line calculated transmittance at each of the 66 levels (i.e., n=1-66), and a set of best-fit parameters for σ_n, ω_n and ε_n was obtained for each level n, channel i and angle θ. The layered transmittance of an arbitrary angle θ between 0° and 40° is obtained by linear interpolation of the values of ln τ in secθ.

Given the layered transmittance at any angle, the total atmospheric transmittance up to a pressure level P can be obtained from Equation (1),

$$\tau_i(P_n,0,T,\theta) = \tau_{i,n}(T,\theta)\ \tau_i(P_{n-1},0,T,\theta) \qquad (8)$$

The agreements between the results obtained from Equations (4) and (8) using the best-fit parameters, and the line-calculated total transmittance as function of pressure is shown in Figure 1. In this figure, the solid curve represents the total transmittance calculated with the best-fit parameters, and the dots are obtained by line-by-line calculations at $\theta = 20°$. The total errors (including the interpolation in secθ) are of the order of 0.01 percent and are much smaller than the sizes of the dots. The temperature profile used in this calculation is taken from Rodgers and Walshaw (1965) and corresponds to the actual temperature of Nairobi, January 7, 1960.

To demonstrate the accuracy of the fitted results and the usefulness of the analytic formulas developed in this study, the total atmospheric radiances for the 11 HIRS channels were calculated by using the total transmittance from the exact line-by-line calculation and analytic formulas (see Equation 8). The comparison of these calculations is shown in Table 1, which also gives the percentage errors of the calculated radiance resulting from the analytic formula. It can be seen from this table that the magnitude of the errors is less than 1 percent. The last column in Table 1 gives the largest errors, which occur among the 66 total transmittances $\tau_i(P_n,0,T,\theta)$ for each channel i if the analytic formula is employed. In practical application, the

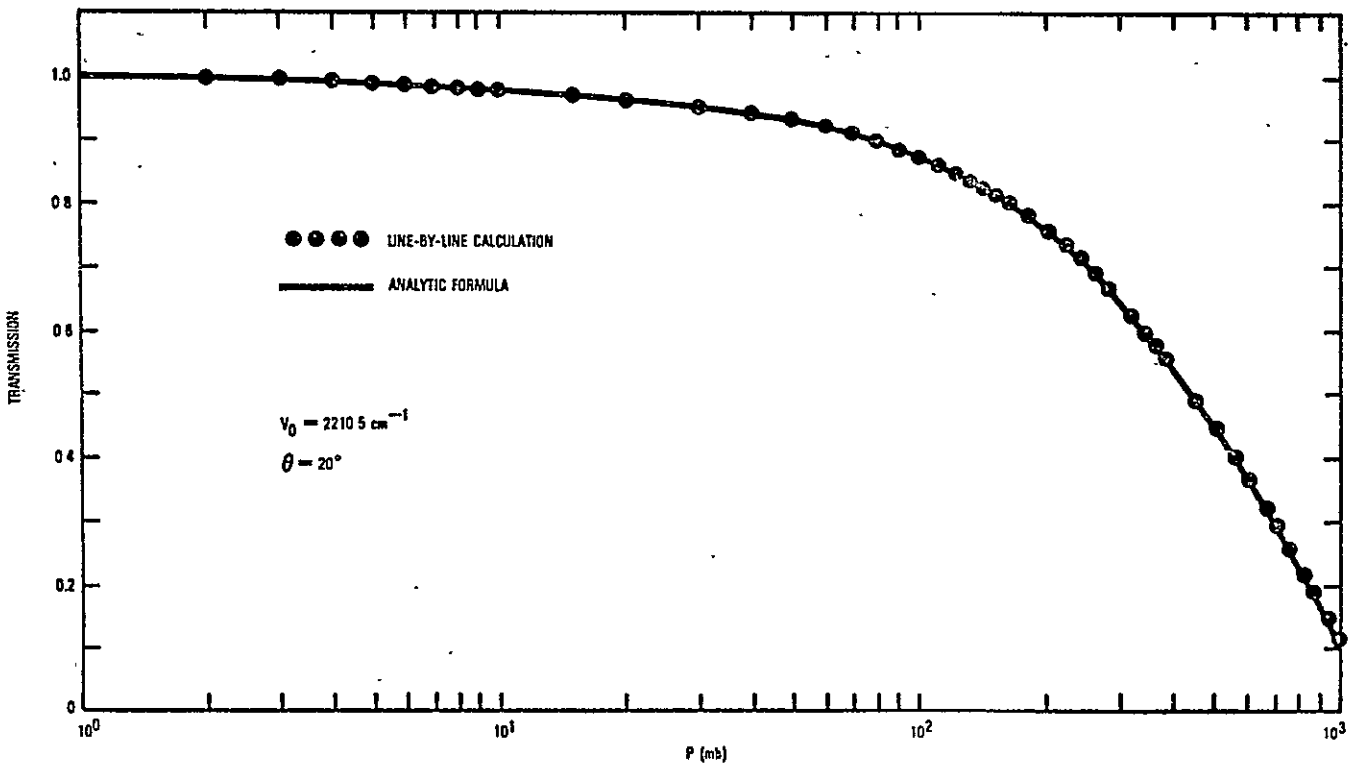

Figure 1. Comparison of the line-by-line calculated transmittance with that obtained from best-fit parameters.

Table 1. Comparison of the total atmospheric radiances obtained from the exact line-by-line calculated transmittance, and from the analytic formulas developed in this study. The temperature profile used in these calculations is taken from the data given by Rodgers and Walshaw (1966), and corresponds to the temperature profile of Nairobi, January 7, 1960. The zenith angle of observation is $\theta = 20°$. The error (in percent) includes that of interpolation in angle for obtaining transmittances at $\theta = 20°$.

ν_o (cm^{-1})	Exact Radiance (erg $sec^{-1}cm^{-2}sr^{-1}$)	Calculated Radiance (erg $sec^{-1}cm^{-2}sr^{-1}$)	Error (%)	Largest Error in τ_i
669.0	58.173	58.153	0.03	-.002
679.0	40.328	40.341	-0.03	-.001
690.0	40.413	40.461	-0.12	-.002
700.0	50.876	51.123	-0.49	-.005
716.5	73.626	74.074	-0.61	-.006
732.0	90.287	90.612	-0.36	-.003
749.5	109.654	110.017	-0.33	-.004
2190.0	2.009	2.014	-0.25	-.002
2210.5	1.138	1.141	-0.22	-.001
2243.5	0.400	0.402	-0.69	-.002
2357.0	0.128	0.128	-0.04	-.001

instrumental measurement of radiance usually has an accuracy of about 1 percent. The analytic formula gives results with an accuracy well within the instrument-error limit, and has been incorporated in the analysis of HIRS data. Use of this new analytical form has produced a significant improvement in the accuracy of retrieved temperature profiles and has removed the need for empirical tuning of transmittance functions.

References

Kondrat'ev, K. Y., and Y. M. Timofeyev, 1969: Numerical modeling of transmission functions for the narrow spectral intervals of the 15μ CO_2 band, Izv. Atmos. Oceanic Phys., 5, pp. 208-213.

Rodgers, C. D., and C. D. Walshaw, 1966: The computation of infra-red cooling rates in planetary atmospheres. Quart. J. Roy. Meteor. Soc., 92, pp. 67-92.

Susskind, J., and T. Mo, 1978: Atmospheric absorption spectra near 2200 cm^{-1} and 2400 cm^{-1}. Third Conf. on Atmos. Rad., Davis, Calif., June 28-30.

Susskind, J., and J. Searl, 1978: Synthetic atmospheric transmittance spectra near 15μm and 4.3μm. J. Quantitative Spectroscopy Rad. Transfer, 19, pp. 195-215.

Wang, J. Y., 1978: Temperature effect on the atmospheric transmission function in the 15μm region. Optics Letters, 2, pp. 169-171.

DETERMINATION OF ATMOSPHERIC WATER CONTENT AND ITS EFFECT ON SCAMS TEMPERATURE RETRIEVALS

(J. Rosenfield and J. Susskind)

The present temperature retrieval methods employed at the Modeling and Simulation Facility make use of the observations from all five microwave channels of the Nimbus-6 SCAMS instrument. Channels 1 and 2, at 22.235 GHz and at 31.4 GHz, are window channels whose observations are primarily determined by the surface temperature, surface emissivity, and atmospheric liquid water and water vapor content. Channels 3, 4, and 5, at 52.85, 53.85, and 55.45 GHz, lie in the wing of the 60 GHz band of oxygen and sound atmospheric emission from roughly 950 mb, 500 mb, and 200 mb, respectively. While brightness temperatures of these channels are primarily a function of the atmospheric temperature profile, the observations in channel 3, and to a lesser extent channel 4, are also affected by surface emissivity and atmospheric water content. In the current operational procedure, these quantities are determined from the brightness temperatures of channels 1 and 2, using an empirical scheme of Waters, et al. (1975). This scheme ignores the effects of atmospheric liquid water content on the observations. This study was undertaken to extend the method of Waters, et al., to include the effects of atmospheric liquid water content on the SCAMS observations. In addition, a technique was developed for the determination of atmospheric liquid water content and water vapor content from these observations.

Theoretical calculations of water vapor transmission in the microwave region were performed for 124 temperature-humidity profiles. The results verify the following empirical relationship of Waters, et al., between the water vapor plus oxygen transmissions in the Nimbus-6 SCAMS microwave channels 1 and 2,

$$\tau_2 (v,O_2) = .32\ \tau_1 (v,O_2) + .666, \qquad (1)$$

to within ±.005 for nadir viewing, with slight degradation at zenith angles up to 50°. The following linear relationship between the water vapor only transmissions in channels 1 and 3 was found to be accurate to .007:

$$\tau_3 (v) = .55\ \tau_1 (v) + .45 \qquad (2)$$

In addition, the channel 1-3 water vapor transmissions were modeled as a function of the water vapor column density, W, as follows:

$$\begin{aligned} &\tau_i(v) = e^{-a_i W}\ ;\ i = 1,2,3 \\ &a_1 = .065 \\ &a_2 = .019 \\ &a_3 = .036 \end{aligned} \qquad (3)$$

where W is in g/cm^2.

In order to evaluate the effect of clouds on the current temperature retrieval scheme, theoretical calculations of brightness temperatures, T_B, for channels 1-3, with and without the inclusion of clouds, were performed. The absorption arising from cloud water droplets was included, but scattering effects, which become significant only in the case of heavy rain, were neglected. A single cloud layer was placed between 1 and 2 km (~850 mb) with water droplet densities, ρ_L, of .1, .2, .3, and .4 g/m^3, corresponding to liquid water contents, L, of 10, 20, 30, and 40 mg/cm^2. Over ocean, brightness temperatures in channel 3 increased by ~2-3°K with clouds corresponding to L up to 40 mg/cm^2. Over land, clouds affect the channel 3 brightness temperature by only .1-.2°K because land emissivities are close to unity.

The extrapolation techniques of the current temperature retrieval program were tested to determine the errors incurred when clouds are not taken into account. Over ocean, when no clouds are present, reconstructed channel 3 brightness temperatures, T_{B3}'s, are ~.1° different from exactly calculated T_{B3}'s. With clouds, errors in T_{B3} are of the order of 1°K for L = 30-40 mg/cm^2. Over land, errors in T_{B3} are ~.1-.2°K, with or without clouds.

In order to modify the current operational temperature retrieval program to take into account the effects of dense clouds on the SCAMS channel 3 brightness temperatures, a procedure has been developed to determine estimates of water vapor and liquid water content from observed brightness temperatures of the SCAMS microwave channels 1 and 2. As a prerequisite to this, it was necessary to model the following three quantities:

1. With a single cloud layer, the effective atmospheric emission temperatures, $T_{AT,1}$ and $T_{AT,2}$, were found to be approximately given by

$$T_{AT,1} = .945\ T_s;\quad T_{AT,2} = .953\ T_s, \tag{4}$$

where T_s is the surface temperature.

2. The following empirical relationship between the liquid water transmissions in channels 1 and 2 was found:

$$\tau_2(\ell) = 1.92\ \tau_1,\ (\ell) - 0.92 \tag{5}$$

3. Liquid water transmissions could be modeled by

$$\exp[-b_i L \exp(2140/T_c)/T_c] \tag{6}$$

where $b_1 = .00012$, $b_2 = .00023$,

T_c = cloud temperature, and L = liquid water content in mg/cm^2.

Given the measurements T_{B1} and T_{B2}, $\tau_1(v,O_2,\ell)$ and $\tau_2(v,O_2,\ell)$ can be reconstructed as follows:

$$\tau_i(\ell,v,O_2) = \frac{(T_s-T_{AT,i})(1-R_i)}{2T_{AT,i}R_i} + \{(T_{AT,i}-T_s)^2(1-R_i)^2 - 4T_{AT,i}R_i(T_{Bi}-T_{AT,i})^{\frac{1}{2}}\}/2T_{AT,i}R_i, \quad (7)$$

where R_i is the reflectivity in channel i which, over ocean, can be modeled accurately given an estimate of the wind speed. Then, knowing that

$$\tau_i(v,O_2,\ell) = \tau_i(v,O_2)\ \tau_i(\ell), \quad (8)$$

and from (1) and (5) one can solve for $\tau_1(v,O_2)$ in terms of the reconstructed $\tau_1(v,O_2,\ell)$ and $\tau_2(v,O_2,\ell)$ as follows:

$$\tau_1(v,O_2) = 1.0435\ \tau_1(v,O_2,\ell) - 1.6984\ \tau_2(v,O_2,\ell) - 1.0406 + 1.6984\ \{[.6144\ \tau_1(v,O_2,\ell) - \tau_2(v,O_2,\ell) - .61272]^2 + 1.50582\ \tau_1(v,O_2,\ell)^{\frac{1}{2}}\} \quad (9)$$

From Equation (8) it follows that

$$\tau_i(\ell) = \tau_i(v,O_2,\ell)/\tau_i(v,O_2). \quad (10)$$

also

$$\tau_i(v) = \tau_i(v,O_2)/\tau_i(O_2),$$

where $\tau_i(O_2)$ has been modeled.

From the quantities $\tau_i(v)$ and $\tau_i(\ell)$ the liquid water content, L, and water vapor content, W, can be reconstructed using Equations (3) and (6).

The agreement of the reconstructed water vapor and liquid water content with the model is very good over ocean. RMS errors in L are 1.61 mg/cm^2, and in W are 0.045 g/cm^2. This agreement is an order of magnitude better than that obtained with schemes (Staelin, et al., 1976; Grody, 1976) using statistical methods. Over land, the error in W is ~1 g/cm^2 and in L is ~12 mg/cm^2. These errors are comparable to those obtained by statistical methods. This is a result of the fact that the effects of liquid water on SCAMS observations over land are small. This being the case, an accurate determination of the liquid water content over land is unnecessary for temperature sounding.

The sensitivity of the reconstructed W and L to errors in the estimated values of the surface temperature, T_s, the cloud temperature, T_c, and the emissivity, ε, were examined. An error in T_s of 3°K leads to ~5 percent errors in W, ~10 percent errors in L; an error in T_c of 5°K leads to ~15 percent errors in L; and an error in ε of .01 leads to ~10 percent errors in W, ~10-30 percent errors in L.

References

Grody, N. C., 1976: Remote sensing of atmospheric water content from satellites using microwave radiometry. IEEE Trans. Antennas and Propog., AP-24, pp. 155-162.

Staelin, D. H., K. F. Kunzi, R. L. Pettyjohn, R. K. L. Poon, R. W. Wilcox, and J. W. Waters, 1976: Remote sensing of atmospheric water vapor and liquid water with the Nimbus 5 microwave spectrometer. J. App. Met., 15, pp. 1204-1214.

Waters, J. W., K. F. Kunzi, R. L. Pettyjohn, R. K. L. Poon, and D. H. Staelin, 1975: Remote sensing of atmospheric temperature profiles with the Nimbus 5 microwave spectrometer. J. Atmos. Sci., 32, pp. 1953-1969.

IMPROVED CALCULATION OF SCAMS BRIGHTNESS TEMPERATURES

(S. Kirschner and J. Susskind)

The SCAMS temperature-humidity sounder on Nimbus-6 is a five-channel passive microwave radiometer. For optimized retrieval of atmospheric temperature profiles from SCAMS measurements, it is necessary to be able to accurately calculate the brightness temperatures for a channel given the temperature profile. The first two channels on SCAMS are atmospheric windows and their radiances are influenced primarily by the surface temperature, surface emissivity, and water vapor and liquid water content of the atmosphere. The remaining three channels are in the O_2 absorption band and sound thermal emission from the earth's atmosphere, being sensitive primarily to temperatures near the peaks of their weighting functions. The channel frequencies are shown in Table 1 together with the peaks of the weighting functions and surface transmittances for nadir viewing.

Channel 3, and to a lesser extent Channel 4, see the surface, and these brightness temperatures are therefore affected by surface emissivity as well as atmospheric temperature profile. In our analysis of SCAMS data, the surface emissivity is estimated from the observations of Channels 1 and 2, and a guess surface temperature, using a procedure developed by Waters, et al. (1975). This technique assuming atmospheric attenuation of radiation in Channels 1 and 2 is due only to water vapor and O_2, and ignores the effects of liquid water clouds. The two observations are used to determine the surface emissivity and atmospheric transmittance in Channel 1, and the corresponding quantities in Channels 2 and 3 are related to those in Channel 1 by theoretical expressions.

In order to obtain accurate temperature profiles from the SCAMS observations, one must be able to calculate brightness temperatures as a function of temperature to an accuracy of about .5°C. This involves a knowledge not only of the surface emissivity but also accurate atmospheric transmission functions for the channels. The attenuation due to O_2 absorption is calculated accurately according to the theory of Rosenkrantz (1975). Additional atmospheric attenuation arises from absorption by liquid water and water vapor. Both effects are small and it was originally thought that the common approximation of neglecting these effects in the calculation of brightness temperatures for the temperature sounding channels was valid, i.e., that the differences in calculated radiances for a given temperature profile, including and excluding the effects of atmospheric water, was less than .5°C for Channels 3-5. In accordance with this, attenuation due to water vapor was ignored in the temperature retrievals done for the DST 5 and 6 periods.

Comparison of retrieved temperatures with colocated radiosondes (mostly over land) produced good results and demonstrated that the approximation was satisfactory. A further study

Table 1. SCAMS Sounding Channels.

Channel	Frequency (GHZ)	Peak of Wt. Function (mb)	Surface Transmittance
1	22.235	window	
2	31.400	window	
3	52.850	950	.33
4	53.850	500	.10
5	55.450	200	.002

C-2

of retrieved surface temperature over the tropical Pacific showed large systematic differences between temperatures retrieved using SCAMS and HIRS (infrared) observations. This led to the examination of the effect of the approximation more closely, and it was found to be extremely bad over tropical oceans but good over land, as shown in the next section.

Sensitivity of Brightness Temperatures to Water Vapor

The brightness temperature observed by a downward looking microwave passive radiometer sounding a frequency ν_i can be written as

$$T_i=\varepsilon_i T_s \tau_i(P_s)+(1-\varepsilon_i)(1-\tau_i(P_s))F_i' T_s \tau_i(P_s)+(1-\tau_i(P_s))F_i T_s \qquad (1)$$

where the first term represents the radiance being emitted by the surface, with emissivity ε_i, temperature T_s, and atmospheric transmittance $\tau_i(P_s)$, the second term represents downward atmospheric flux reflected from the suface, and the last term represents radiation emitted by the atmosphere. The terms $F_i T_s$ and $F_i' T_s$ are the equivalent atmospheric temperatures looking down from the satellite and up from surface, respectively, and represent a weighted mean temperature over the region of atmospheric emission. In the limit of an optically thin atmosphere such as found in Channels 1 and 2, $F_i = F_i'$. Otherwise, F_i' is greater than F_i, that is, the mean emission of radiation in the downward direction takes place lower in the atmosphere than that in the upward direction.

The atmospheric transmittance in Equation (1), $\tau_i(P_s)$, differs from "1" due to attenuation by O_2 and H_2O vapor (liquid H_2O drops are being neglected in this discussion) and can be written as a product

$$\tau_i(P) = [\tau_{i,ox}(P)\ \tau_{i,w}(P)]^{\sec\theta} \qquad (2)$$

where $\tau_{i,ox}(P)$ and $\tau_{i,w}(P)$ represent the nadir transmittances due to oxygen and water vapor, and θ is the zenith angle of observation. $\tau_{i,ox}(P)$ is calculated as a function of temperature profile according to Rosencrantz (1975). Given $\tau_{i,w}(P_s)$, $\tau_{i,w}(P)$ is calculated according to the approximation of a 2.1 km water vapor scale height and temperature independent absorption coefficients, i.e.

$$\tau_{i,w}(P) = \tau_{i,w}(P_s)\ (P/P_s)^{4.8} \qquad (3)$$

It is clear that both addition of water vapor and increase of zenith angle of observation decrease the surface transmittance $\tau_i(P_s)$ and therefore modify the observation as shown in Equation (1). A more subtle effect is the small dependence of F_i and F_i' on water vapor and zenith angle. Increasing θ

will increase the optical path of the atmosphere homogeneously and therefore increase F_i' and decrease F_i. Increasing the water vapor amount also increases the optical path of the atmosphere, but primarily at lower altitudes. Therefore, both F_i and F_i' increase with increasing water vapor.

A change in brightness temperature with τ (addition of water vapor) can be written as

$$\frac{dT_i}{d\tau_i(P_s)} = (G_i - H_i)T_s \tag{4a}$$

where

$$G_i = \varepsilon_i + (1-\varepsilon_i)\left[(1-2\tau_i(P_s)F_i' + \tau_i(P_s)(1-\tau_i(P_s))\frac{dF_i'}{d\tau_i(P_s)}\right] \tag{4b}$$

and

$$H_i = F_i - (1-\tau_i(P_s))\frac{dF_i}{d\tau_i(P_s)} \tag{4c}$$

The two terms in Equation (4a), G_i and H_i represent the increase in radiation coming from the surface and the decrease in radiation coming from the atmosphere, with increasing τ.

Table 2 shows observed and calculated brightness temperatures for a portion of a scan of the SCAMS instrument over the tropical Pacific. The calculations are shown for two models, one neglecting the effect of water vapor on the transmittance and one using water vapor determined from the observations in Channels 1 and 2, by way of Equation (2) and the empirical equation

$$\tau_{3,w}(P_s) = .55\ \tau_{1,w}(P_s) + .45 \tag{5}$$

The emissivity ε_3 was also determined from the observations in Channels 1 and 2. Its zenith angle dependence shows good agreement with theoretical values for sea water with a wind speed of about 12 meters/sec. The temperature profiles used in the calculations were 12-hour forecasts from the GLAS GCM. The forecast surface temperature is included in the table as well as the retrieved surface temperature obtained from inverting the SCAMS observations. Also shown in the table are F, $\frac{dF}{d\tau}$, F', $\frac{dF'}{d\tau}$, G, and H for Channel 3.

It is clear from the table that addition of water vapor over ocean causes a large increase in the brightness temperature of Channel 3, which decreases with increasing zenith angle from 2.6°K at 11 degrees to .9°K at 49 degrees. The effect is due primarily to the low surface emissivity over ocean and the decrease in surface transmittance with increasing zenith angle. The brightness temperatures calculated from the initial guess, including water vapor, are in much better agreement with observations than those calculated ignoring the water vapor absorption. While this

Table 2. Quantities calculated over water for various zenith angles and water vapor models. The temperature retrievals are over the Pacific Ocean for 22Z 21 AUG 75 at -2°(±2°) latitude and 152.5° (±10°) longitude west of Greenwich.

Model	Zenith Angle (deg)	ε_3	τ_3	T_3(K)		T_s(K)		P_s (mb)	F_3	F_3'	$-dF_3/d\tau_3$	$-dF_3'/d\tau_3$	G_3	H_3
				Obs.	Calc.	Fcst.	Ret'd							
(i)	11	.516	.321	262.0	259.0	298.9	304.1	1013	.938	.886	.157	.094	.661	.950
(No	24	.515	.294	262.9	260.2	298.8	302.6	1015	.941	.885	.164	.093	.686	.950
water	36	.518	.253	263.6	261.6	299.5	301.9	1013	.939	.879	.176	.087	.725	.944
vapor)	49	.544	.181	263.2	262.1	298.6	298.2	1016	.946	.873	.209	.083	.805	.941
(ii)	11	.516	.290	262.0	261.5	298.9	298.0	1013	.943	.889	.157	.094	.691	.956
(Water	24	.515	.263	262.9	262.5	298.8	297.7	1015	.946	.888	.164	.093	.716	.956
vapor)	36	.518	.222	263.6	263.5	299.5	297.4	1013	.945	.882	.176	.087	.755	.949
	49	.544	.157	263.2	262.9	298.6	295.3	1016	.951	.875	.209	.083	.828	.945

agreement may be fortuitous depending on the accuracy of the forecast guess, it is significant to note that the differences between observed and calculated brightness temperatures have negligible zenith angle dependence when water is included, but have a large zenith angle dependence when dry transmittances are used.

Table 3 shows the same type of information for a scan over land, which is characterized by a surface emissivity close to 1. In this case the brightness temperature calculated with and without water vapor differ by no more than .2°K. H, the dependence of atmospheric radiation on water vapor, has changed only slightly, but G, the dependence of the surface radiation coming from water vapor, has risen substantially to be slightly larger than H, producing in fact a small drop in brightness temperature with inclusion of water vapor. This drop would have been substantially larger were it not for the term $dF_3'/d\tau_3$, which produces an increase in the effective atmospheric temperature for upwelling radiation with increased atmospheric water vapor.

Incorporation of this algorithm into the HIRS/SCAMS temperature retrieval package led to substantial improvement in the quality of retrieved temperature fields.

References

Rosencrantz, P. W., 1975: Shape of the 5 mm oxygen band in the atmosphere. IEEE Transactions on Antennas and Propagation, 23, pp. 498-506.

Waters, J. W., K. F. Kunzi, R. L. Pettyjohn, R. K. L. Poon, and D. H. Staelin, 1975: Remote sensing of temperature profiles with the Nimbus 5 microwave spectrometer. J. Atmos. Sci., 32, pp. 1953-1969.

Table 3. Quantities calculated over land for various zenith angles and water vapor models. The temperature retrievals are over the United States for 08Z 19 AUG 75 at 50°(±2°) latitude and 112.5° (±10°) longitude west of Greenwich.

Model	Zenith Angle (deg)	ε_3	τ_3	T_3(K)		T_s(K)		P_s (mb)	F_3	F_3'	$-dF_3/d\tau_3$	$-dF_3'/d\tau_3$	G_3	H_3
				Obs.	Calc.	Fcst	Ret'd							
(i)	6	.953	.419	264.4	264.7	282.8	282.8	875	.946	.905	.136	.095	.959	.960
(No	17	.953	.426	264.6	264.2	284.7	285.1	847	.931	.891	.142	.095	.958	.945
water	32	.954	.378	260.6	262.1	284.0	280.2	853	.932	.888	.150	.090	.963	.944
vapor)	45	.956	.277	259.1	260.0	283.1	279.5	898	.947	.892	.170	.084	.973	.953
(ii)	6	.953	.381	264.4	264.7	282.8	282.5	875	.951	.908	.136	.095	.962	.968
(Water	17	.953	.387	264.6	264.1	284.7	285.4	847	.937	.894	.142	.095	.962	.952
vapor)	32	.954	.342	260.6	261.9	284.0	280.2	853	.937	.891	.150	.090	.966	.950
	45	.956	.255	259.1	259.9	283.1	279.6	898	.951	.894	.170	.084	.975	.957

III. OCEAN/AIR INTERACTIONS

REALISTIC SIMULATIONS OF THE GLOBAL OBSERVING SYSTEM AND OF SEASAT-A MARINE WIND DATA

(M. Cane, M. Halem, V. Cardone, I. Halberstam, and J. Ulrich)

A 30-day history run made with the GMSF general circulation model was used to fabricate simulated observations at the times and locations of the conventional surface, radiosonde and ship reports actually received during February 1976. The fabricated observations, suitably degraded for instrument and sampling errors, were then used to create analyzed fields on the GCM grid in an analysis forecast cycle like those in use at major meteorological centers. The control fields so produced are much more representative of actual analyses than those produced by perturbation of initial states with random errors. Significantly, the forecast error growth in five simulated 72-hour forecasts from the control states is similar to that found in operational numerical forecasts.

Further experiments simulated the addition of surface winds derived from Seasat-A to the control run. The Seasat wind data were fabricated directly for the GCM gridpoints intercepted by a Seasat-A scatterometer swath and were assumed to be error-free and representative of the lowest active level of the GCM (level 9). Two different asynoptic assimilation methods were used; direct insertion and successive correction. It was found that assimilation of the wind data by the DIM led to 10-20 percent reduction of error in the specification of the low-level wind field over the ocean relative to the control analysis, and only slight improvement in the simulated 3-day forecasts of sea level pressure in extratropical oceanic regions. Assimilation of wind data by the SCM resulted in a substantial beneficial impact of the satellite data on analyses and forecasts of surface pressure, and low and midtropospheric wind fields in both land and oceanic regions.

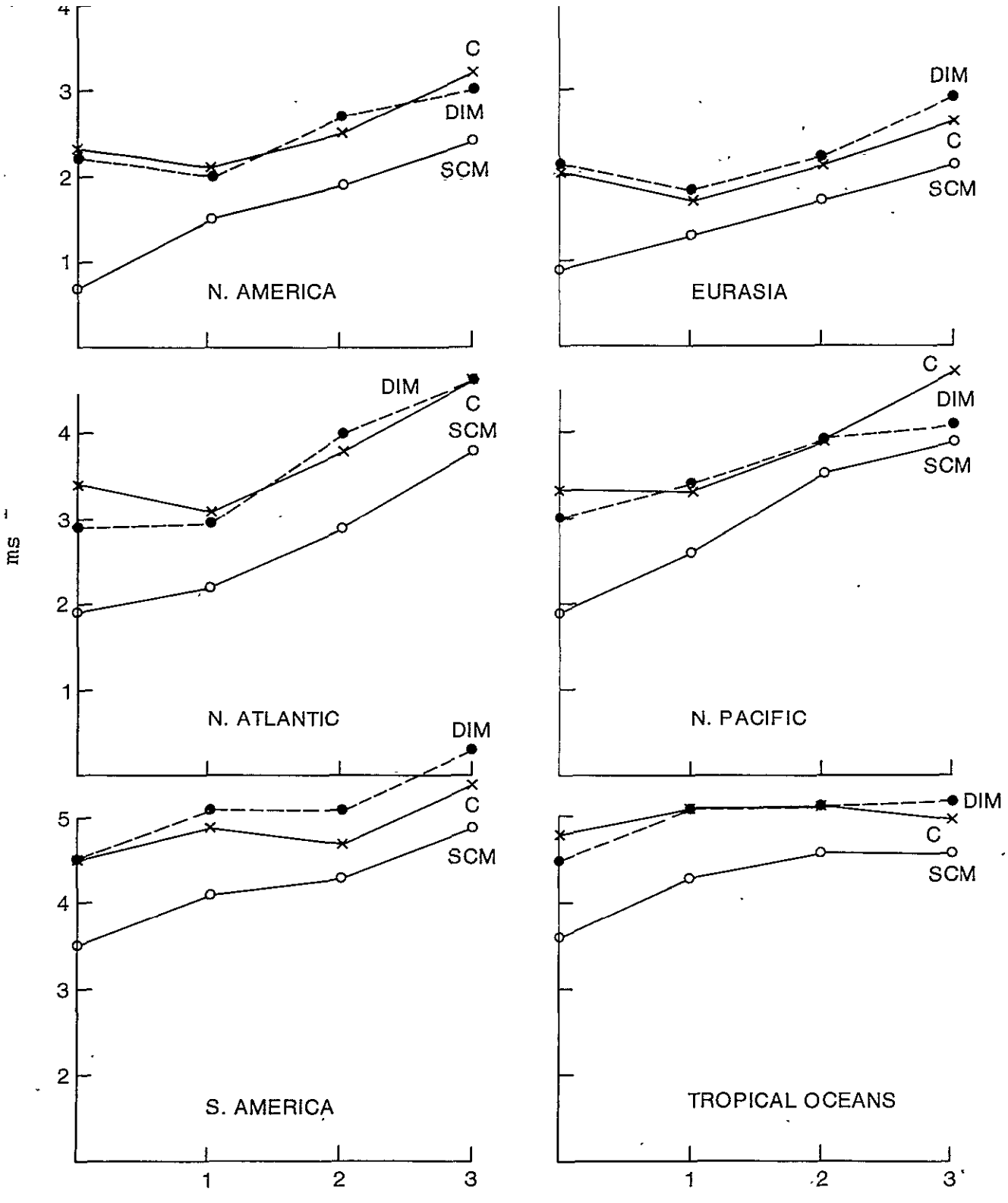

Figure 1. Growth of the level 9 zonal wind errors (RMS) averaged over five simulated forecasts made from Control (C), Seasat direct insertion method (DIM), and Seasat successive correction method (SCM) initial states. The superior analysis (i.e., day 0) in the SCM case results in an improved forecast.

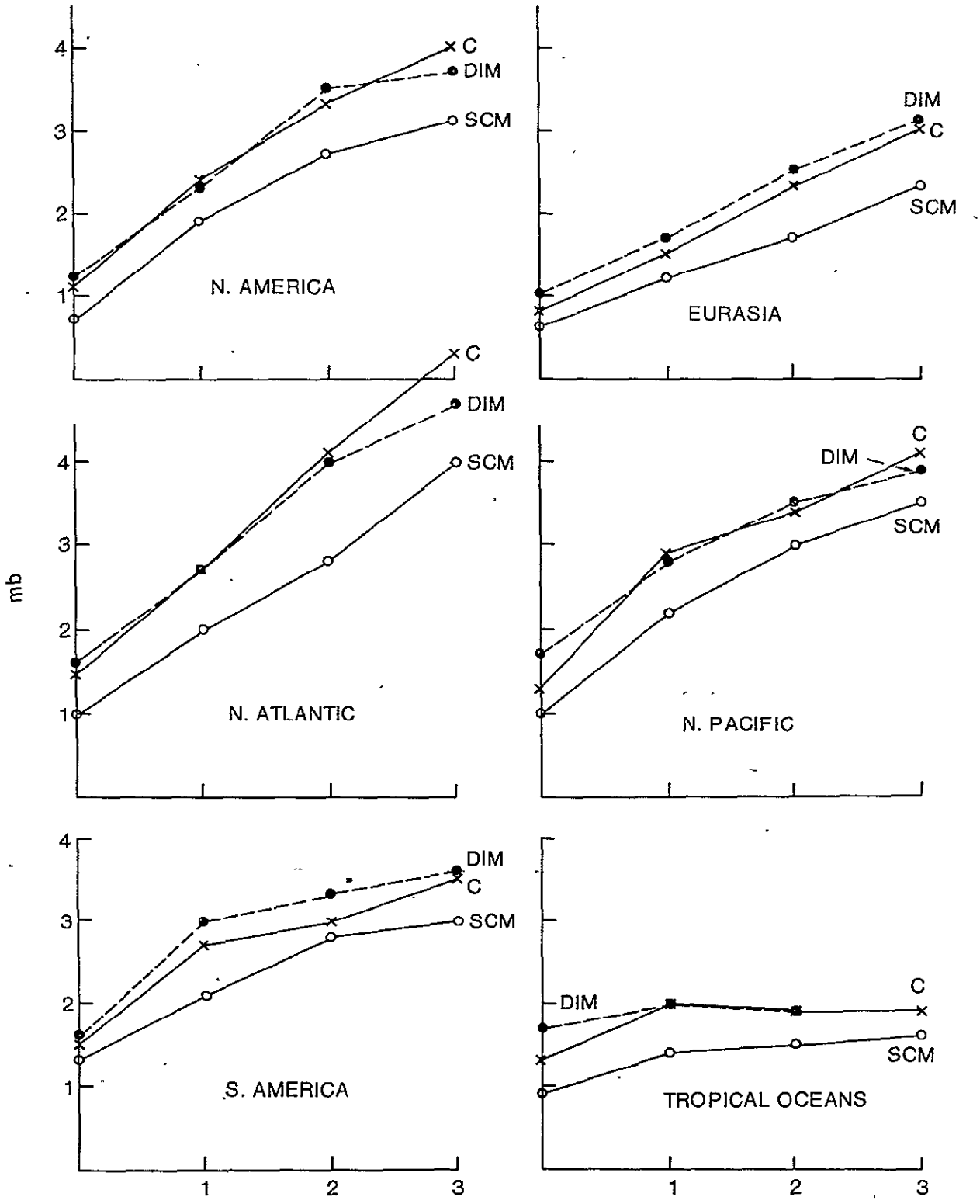

Figure 2. Growth of the sea level pressure errors (RMS) averaged over five simulated forecasts made from Control (C), Seasat DIM, and Seasat SCM initial states. The analysis (i.e., day 0) in the SCM case results in an improved forecast.

ADDITIONAL SEASAT SIMULATION EXPERIMENTS

(M. Cane, V. Cardone, and D. Edelmann)

This brief report updates our detailed account of earlier experiments simulating the global observing system and the Seasat-derived marine winds (Cane, et al., 1978, submitted to Mon. Wea. Rev. and abstracted in this research review). This work is currently being extended in two directions.

The first is to account for the errors in the Seasat-derived surface winds. In a recently completed experiment, random errors of 2 m/s in speed and 20° in direction were added to the inserted level 9 winds. The winds were assimilated by the successive correction method (SCM). Quantitative measures such as RMS sea level pressure errors showed that the resulting forecasts were not significantly different in quality from those made with error-free simulated winds. Table 1 provides measures of 3-day forecast root mean square (RMS) errors from the error-free (SCM) and random error (SCME) initial states.

This lack of difference is attributable to the SCM's ability to smooth random errors. Current work is focused in implementing the actual scatterometer geophysical retrieval algorithms in order to correctly capture the unusual error structure to be expected from this instrument. At the same time the boundary layer parameterization in the GCM is being modified to account for the turning of the wind in the planetary boundary layer. Both types of work serve not only to allow more realistic simulations but also prepare us to handle real Seasat data.

The second extension is a set of experiments designed to determine the optimal assimilation period for Seasat wind data. Current practice is to assimilate data at each model time step--every 10 minutes. Using longer assimilation periods is not only computationally more efficient but may yield better results because it reduces the extent of the boundaries of regions where data are inserted. The model fields necessarily adjust incorrectly at a boundary between forecast and observed values. On the other hand, too long a period clearly degrades the data by increasing the difference between the time the observation was made and the time it is assimilated. Preliminary results thus far suggest that a 3-hour assimilation period yields the same results as a 10-minute one. Table 2 shows errors in forecasts obtained from initial conditions in which the data were assimilated in 1/2-hour, 3-hour, and 6-hour blocks.

Table 1. Comparison of 3-day Forecast Surface Pressure Errors from Control (C), Error Free (SCM) and Random Error (SCME) Initial States (RMS in mb).

REGION	DAY	2/5 C	2/5 SCM	2/5 SCME	2/10 C	2/10 SCM	2/10 SCME	2/15 C	2/15 SCM	2/15 SCME	2/20 C	2/20 SCM	2/25 C	2/25 SCM
Lat 30°- 86°	0	1.08	0.71	0.70	1.11	0.68	0.64	1.14	0.67	0.64	1.18	0.66	1.19	0.76
Lon 0°-165°	1	2.80	2.11	2.29	2.27	2.51	2.28	1.76	1.37	1.30	1.80	1.35	3.49	2.31
LAND	2	5.08	2.85	3.07	2.42	2.95	2.77	2.20	1.89	1.66	2.44	2.07	4.49	3.77
(N. America)	3	6.29	2.90	3.13	3.23	3.14	2.88	3.03	2.51	2.35	3.87	3.15	3.47	4.13
Lat 30°- 86°	0	0.79	0.62	0.63	0.76	0.62	0.62	0.76	0.61	0.61	0.89	0.60	0.92	0.69
Lon 165°-355°	1	1.67	1.21	1.25	1.36	1.09	1.01	1.28	1.07	1.04	1.74	1.07	1.61	1.45
LAND	2	2.22	1.83	1.92	2.16	1.40	1.40	2.02	1.46	1.56	2.30	1.60	2.59	2.28
(Eurasia)	3	2.63	2.52	2.75	3.38	1.90	2.16	2.92	2.29	2.05	3.29	2.14	2.64	2.63
Lat 30°- 86°	0	1.75	1.42	1.47	1.84	1.10	1.14	1.38	0.72	0.66	1.27	0.88	1.42	0.87
Lon 80°-175°	1	3.45	2.49	2.65	3.18	1.68	2.07	2.25	1.79	1.35	2.18	2.02	2.54	1.85
WATER	2	6.20	3.82	3.75	3.62	2.09	2.40	3.33	2.33	2.70	3.54	2.75	3.79	3.21
(N. Atlantic)	3	6.93	5.01	5.18	4.68	2.77	3.16	5.95	3.66	3.82	3.88	3.69	5.12	5.08
Lat 30°- 86°	0	1.45	1.02	1.05	1.25	1.04	1.05	1.19	0.95	1.02	1.47	0.99	1.18	1.02
Lon 275°- 60°	1	4.41	3.45	3.44	2.22	2.06	2.44	2.07	1.72	1.54	3.03	2.03	2.65	1.96
WATER	2	4.62	3.75	3.65	2.72	2.83	3.01	3.20	2.37	2.51	3.08	2.95	3.31	3.14
(N. Pacific)	3	5.08	4.58	4.54	3.20	3.18	3.41	5.23	2.68	3.28	3.78	3.23	3.43	3.70
Lat -26°-+26°	0	1.41	0.96	0.99	1.24	0.95	0.96	1.19	0.78	0.90	1.21	0.88	1.27	0.79
Lon 0°-355°	1	2.55	1.72	1.78	1.94	1.42	1.45	1.90	1.35	1.34	1.97	1.38	1.87	1.25
WATER	2	2.25	1.67	1.63	1.81	1.54	1.44	1.80	1.35	1.41	1.78	1.27	1.87	1.50
(Trop.Ocean)	3	2.26	1.73	1.76	1.87	1.71	1.73	1.74	1.55	1.52	1.73	1.41	1.87	1.49

Table 2. Comparison of 3-day Forecast Surface Pressure Errors from Control (C), 1/2-hour, 3-hour, and 6-hour Periods (RMS Errors in mb).

REGION	DAY	2/5 C	2/5 ½-h	2/5 6-h	2/5 3-h	2/10 C	2/10 ½-h	2/10 6-h	2/10 3-h	2/15 C	2/15 ½-h	2/15 6-h	2/15 3-h
Lat 30°- 86°	0	1.1	0.78	0.71	0.71	1.11	0.60	0.60	0.60	1.14		0.64	
Lon 0°-165°	1	2.8	2.14	2.02	2.19	2.27	2.33	2.22	2.55	1.76		1.29	
LAND	2	5.1	3.06	3.21	3.19	2.32	2.46	2.58	3.02	2.20		1.78	
(N. America)	3	6.3	3.30	3.42	3.38	3.23	3.05	3.10	3.29	3.03		2.31	
Lat 30°- 86°	0	0.8	0.68	0.68	0.68	0.76	0.63	0.62	0.62	0.76		0.57	
Lon 165°-355°	1	1.7	1.33	1.35	1.35	1.36	0.97	0.99	1.03	1.28		1.04	
LAND	2	2.2	2.02	2.06	2.06	2.16	1.55	1.56	1.57	2.02		1.63	
(Eurasia)	3	2.6	3.03	3.02	3.05	3.38	2.13	2.17	2.45	2.92		2.00	
Lat 30°- 86°	0	1.7	1.51	1.54	1.50	1.84	1.03	1.06	1.19	1.38		0.68	
Lon 80°-175°	1	3.4	2.65	2.56	2.59	3.18	1.77	1.55	1.94	2.25		1.52	
WATER	2	6.2	3.69	3.78	3.46	3.62	2.26	2.02	2.53	3.33		2.94	
(N. Atlantic)	3	6.9	5.01	5.08	4.92	4.68	2.91	2.95	3.76	5.95		4.73	
Lat 30°- 86°	0	1.4	1.03	1.07	1.06	1.25	0.97	0.97	1.06	1.19		0.98	
Lon 275°- 60°	1	4.4	2.96	3.01	3.04	2.22	2.25	2.30	2.74	2.07		1.40	
WATER	2	4.6	3.43	3.53	3.50	2.72	2.73	2.70	3.12	3.20		1.99	
(N. Pacific)	3	5.1	4.38	4.49	4.47	3.20	2.73	2.90	2.77	5.23		2.67	
Lat -26°-+26°	0	1.4	0.89	0.89	0.88	1.24	0.89	0.91	0.98	1.19		0.87	
Lon 0°-355°	1	2.5	1.56	1.61	1.57	1.94	1.25	1.39	1.44	1.90		1.27	
WATER	2	2.2	1.59	1.64	1.57	1.81	1.37	1.44	1.52	1.80		1.57	
(Trop.Ocean)	3	2.3	1.78	1.86	1.81	1.87	1.59	1.69	1.69	1.74		1.55	

TROPICAL SEA SURFACE TEMPERATURE: AN INTERACTIVE ONE-DIMENSIONAL ATMOSPHERE-OCEAN MODEL

(E. Sarachik)

Since the atmosphere and ocean are interacting systems, it is inappropriate to specify the sea surface temperature when dealing with the atmosphere or atmospheric anemometer level temperature and moisture when dealing with the ocean. All of these quantities should be determined interactively in terms of the external forcing: the solar constant.

In the tropics, it is shown that the (cumulus) convective processes may be described by a one-dimensional cloud model. The near-surface ocean may similarly be described by a one-dimensional, mixed-layer model. The coupling is achieved through a sea surface flux budget combined with the flux parameterizations implied by the Monin-Obukhov similarity theory.

This coupled one-dimensional atmosphere-ocean model is applied to the equilibrium situation wherein neither the ocean nor the atmosphere is heated or cooled. Since the ocean, lacking an internal heating or cooling mechanism, can only be heated or cooled through sensible heat fluxes through the sea surface, in equilibrium these fluxes must vanish. The atmosphere however maintains a stable lapse rate by balancing cumulonimbus heating against infrared radiative cooling. All water precipitated from cumulonimbus clouds must have evaporated from the sea surface. It is shown that this equilibrium system is closed and determinable solely in terms of the solar constant.

For various values of the solar constant, the sea surface temperature, the flux of latent and sensible heat from the surface, the height of the tropopause, mixed layer, and trade inversion layer, and generally the entire vertical structure of the tropical atmosphere and ocean can be determined. The equilibrium sea surface temperature is shown to be relatively insensitive to changes in the solar constant, additional solar flux being compensated mainly by additional evaporation.

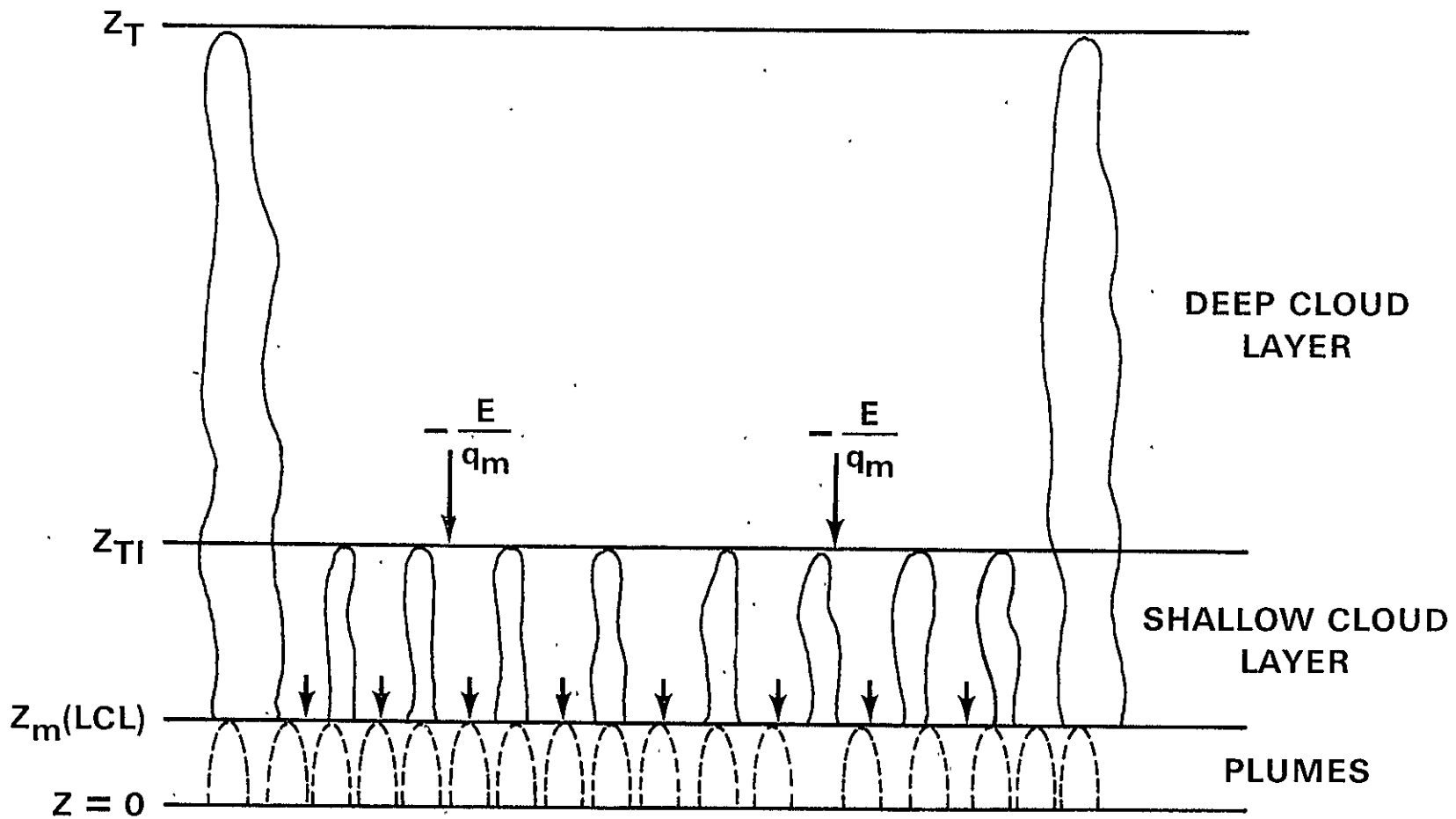

Figure 1. A schematic of the vertical structure of the undisturbed tropical atmosphere (not to scale). Z_m (mixed layer height) ~600 m, Z_{TI} (trade inversion) ~2 km, Z_T (tropopause) ~16.5 km. The subsidence induced by deep cumulus clouds acts to hold down the trade inversion.

A TWO-LAYER DYNAMIC AND THERMODYNAMIC MODEL OF THE UPPER OCEAN

(M. Cane and P. Schopf)

A new model to be used to simulate the thermodynamics and circulation of the upper ocean is currently being coded and tested at GLAS/GMSF. The primary design goal is that the model be capable of state-of-the art simulations of those processes that determine the sea surface temperature. The model has been kept simple so that it is inexpensive to run simulations over several years. A coarse grid version has been structured to be compatible with the GLAS atmospheric GCM. This version is global and is intended to be used in coupled atmosphere-ocean experiments with the GCM. A finer-grid version can be used in a stand-alone mode either as a global model or to do experiments on a regional scale.

The vertical structure of the model is depicted in Figure 1. The upper layer, the mixed layer, is treated as a slab: temperature and current velocities are taken as constant throughout. This is consistent with the bulk mixed-layer models now widespread (see Niiler and Kraus, 1977). The assumption that the layer is indeed well mixed is a good one for temperature (see Figure 2) but less so for currents. The depth of the mixed layer is variable and is determined by the thermodynamics, turbulent mixing, and divergence of fluid due to large-scale motions.

The layer below the mixed layer is taken to extend to the permanent thermocline with the deep ocean approximated as being at rest (cf., e.g., Charney, 1955). In this second active layer, the currents are again assumed to be uniform with depth, but the temperature is now taken to be linear with depth. This is the simplest structure that allows one to model the effects of static stability on mixed-layer entrainment. In both active layers the dynamics are governed by the primitive equations. The mixed-layer depth and temperature are also affected by local mixed-layer processes. These are modeled by a bulk formulation very similar to that of Kraus and Niiler (1977). Thus, in the model, as in nature, the surface temperature is influenced by local surface heating and wind stirring, horizontal advection, and upwelling. (Cooling due to upwelling is simulated by first having surface layer divergence thin the layer, thereby bringing the cold water below nearer to the surface where turbulent mixing processes entrain it into the mixed layer.)

The model will be used to study the relationship between local thermodynamic and large-scale dynamical influences on sea surface temperature.

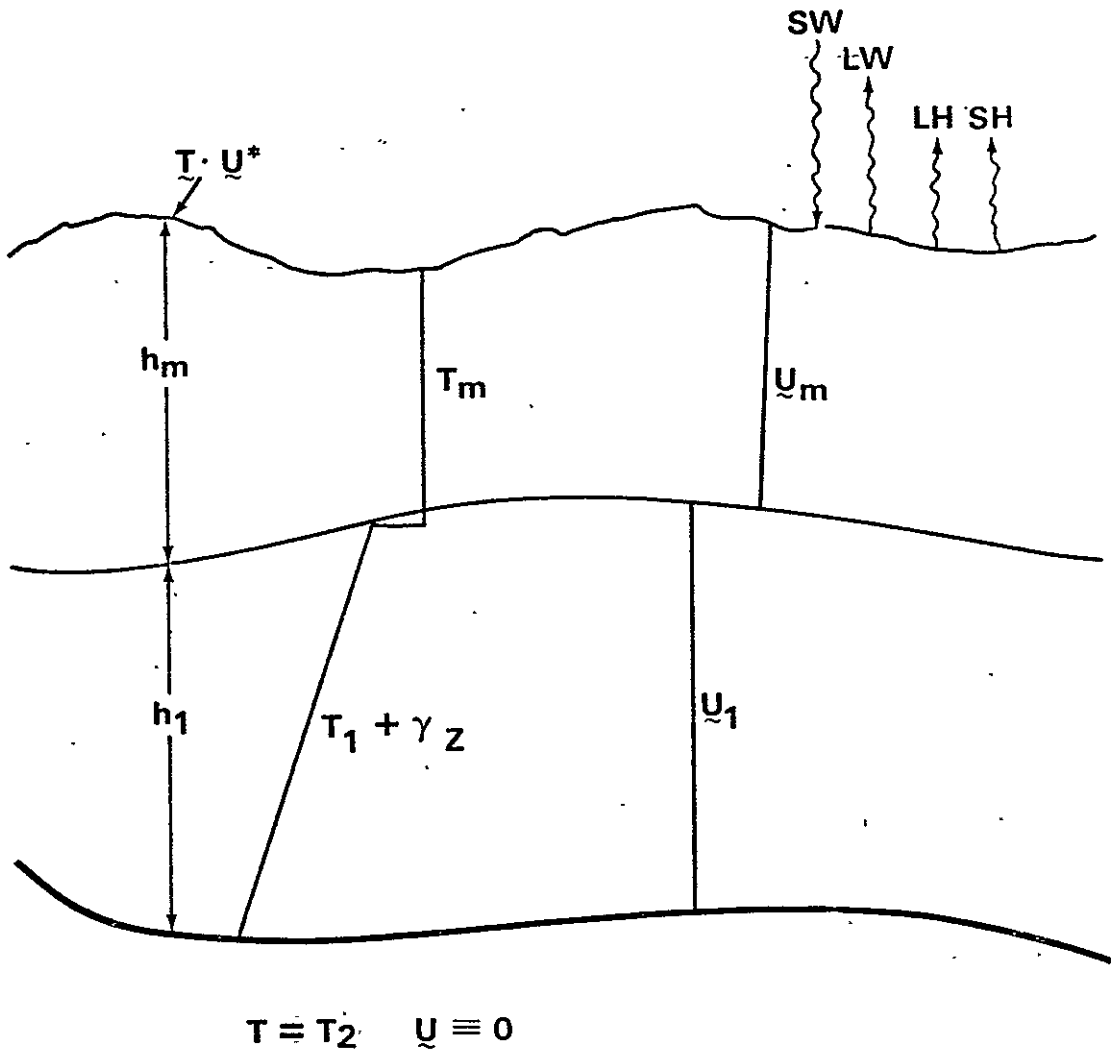

Figure 1. Vertical structure of the model.

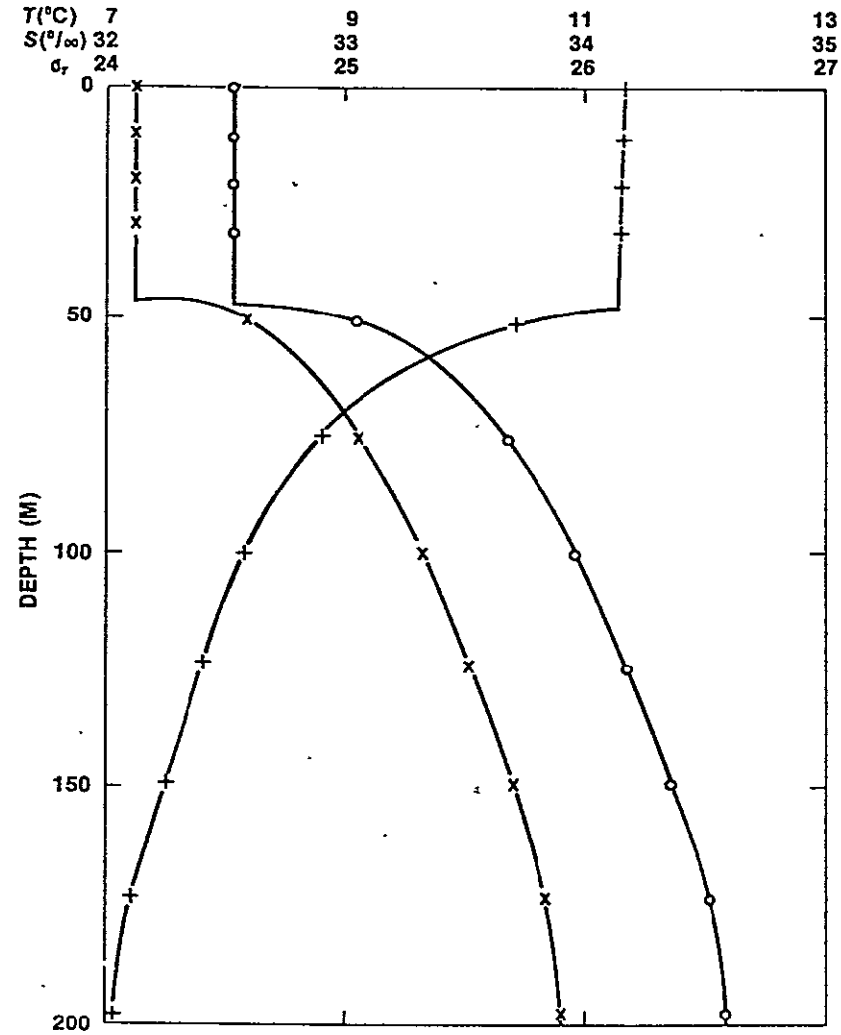

Figure 2. Typical variation of water properties with depth, November 1962. + = temperature, X = salinity, in parts per thousand by weight; O = density anomaly; σ_t = 1000 density-1 where density is in g/cm^3 and is measured at atmospheric pressure. From Grant, H.L., A. Moilliet, and W. M. Vogel, 1968, Some observations of the occurrence of turbulence in and above the thermocline, Journal of Fluid Mechanics, 34, pp 443-448.

References

Charney, J. G., 1955: The generation of ocean currents by wind. J. Mar. Res., 14, pp. 477-498.

Niiler, P. P. and E. B. Kraus, 1977: One-dimensional models of the upper ocean in modeling and prediction of the upper layers of the ocean. E. B. Kraus, ed., Pergamon Press.

A DYNAMIC MODEL FOR THE OCEANIC MIXED LAYER: NON-ADVECTIVE VERSION

(I. Fung and M. Cane)

A necessary prelude to the coupled atmosphere-ocean general circulation model is an ocean model capable of reproducing, at least on the seasonal time scale, the sea surface temperature (SST) patterns given the atmospheric inputs of wind stress and net heat balance at the sea surface. This report outlines the first of a series of global models of the upper ocean currently under development and testing at GLAS/GMSF.

The one-dimensional model of the mixed layer is fashioned after Niiler (1975). It basically consists of a mixed layer and a seasonal thermocline overlying a permanent thermocline. SST and mixed-layer depths are predicted. The mixed-layer equations in terms of the buoyancy content, total kinetic energy, potential energy and momentum of the layer are algebraic, and, hence, can be solved expeditiously.

The one-dimensional model is applied to the GLAS 4° x 5° grid over the global oceans. Climatological wind stress (Hellerman, 1967) and the net heat balance at the sea surface (Schutz and Gates, 1971) are used as forcing. The initial condition is given by the January NCAR climatological SST (Washington and Thiel, 1970) and the January temperature profiles compiled by Miller (1974). The NCAR SST also serves as verification. The time step used is 6 hours. It should be noted that integration for 1 year takes 5 minutes of CPU on the Amdahl 470.

Figures 1 and 2 show the differences between the predicted and observed mean SSTs for January and March, respectively. They show that, although a 1-month integration (Figure 1) gives SSTs that differ from climatological values by less than 1°C, a 3-month integration (Figure 2) gives systematic errors in the major current areas--where the effects of coastal and equatorial upwelling and advection by the western boundary currents are important.

References

Hellerman, S., 1967: An updated estimate of the wind stress on the world ocean. Mon. Wea. Rev., 95, pp. 607-626 (see correction, 1968, 96, pp. 63-74).

Miller, J. R., 1974: Coupling the GISS model with an interacting ocean. GISS Research Review, pp. 42-44.

Niiler, P. P., 1975: Deepening of the wind-mixed layer. J. Mar. Res., 33, pp. 405-422.

Schutz, C., and W. L. Gates, 1971: Global climatic data for surface, 800 mb, 400 mb: January. The RAND Corporation, R-915-ARPA, November.

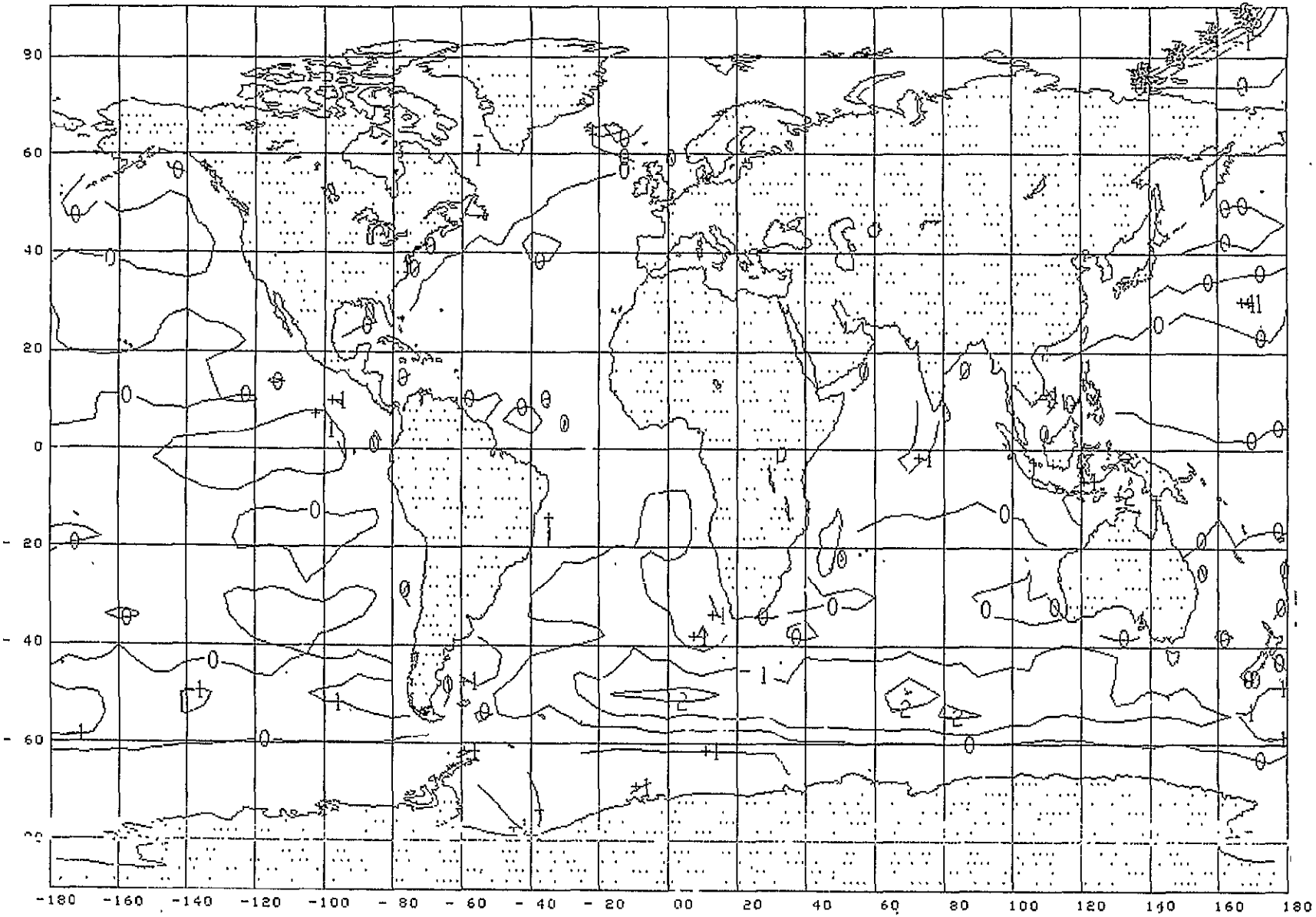

Figure 1. Predicted SST - observed SST after a 30-day integration.

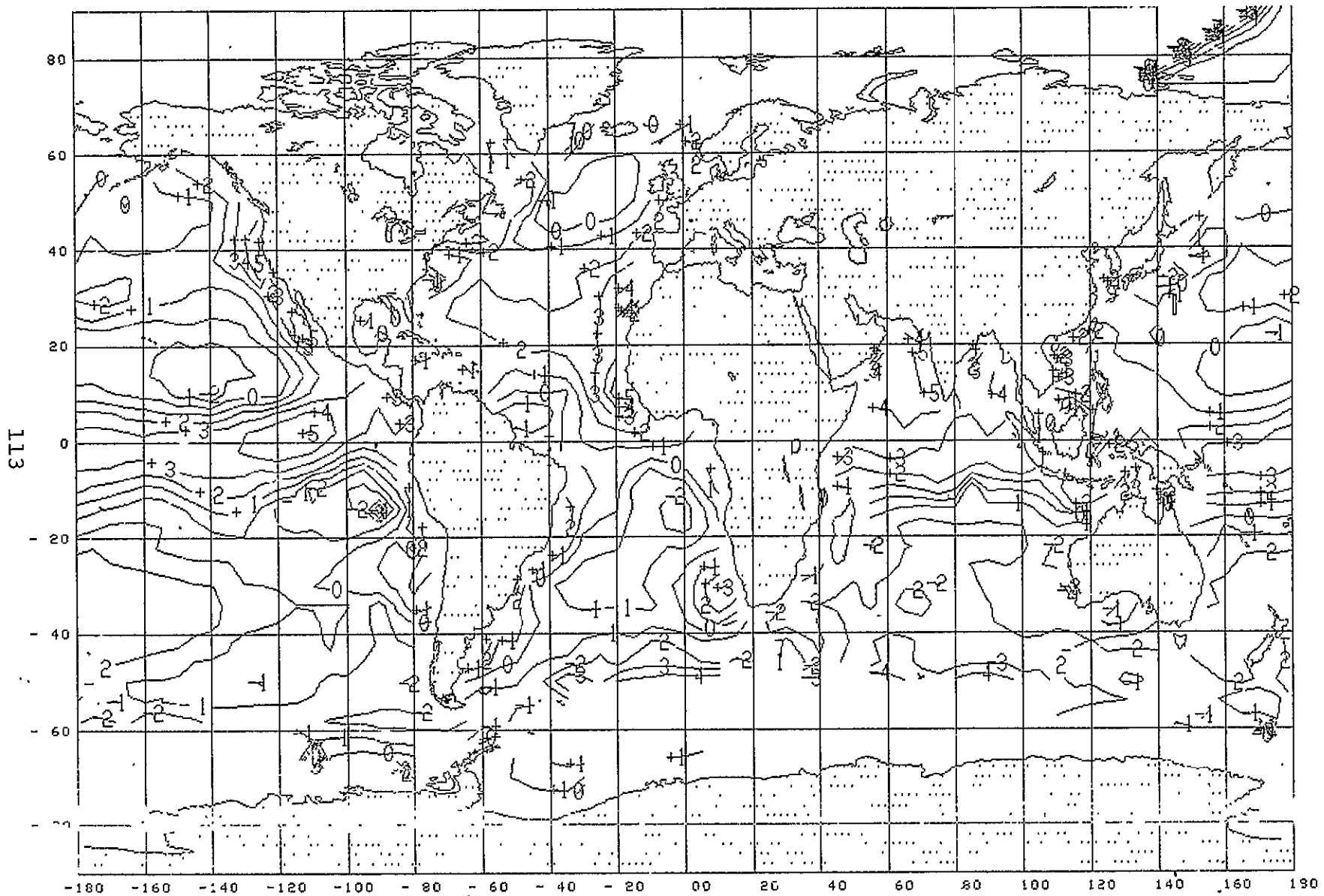

Figure 2. Predicted SST - observed SST after a 90-day integration.

References (Continued)

_____, 1972: Global climatic data for surface, 800 mb, 400 mb: July. The RAND Corporation, R-1029-ARPA, November.

_____, 1973: Global climatic data for surface, 800 mb, 400 mb: April. The RAND Corporation, R-1317-ARPA, July.

_____, 1974: Global climatic data for surface, 800 mb, 400 mb: October. The RAND Corporation, R-1425-ARPA, March.

Washington, W. M., and L. G. Thiel, 1970: Digitized global monthly mean ocean surface temperatures. NCAR-TN-54, NCAR, Boulder, CO.

A DYNAMIC MODEL FOR THE OCEANIC MIXED LAYER: ADVECTIVE VERSION

(I. Fung and M. Cane)

A 3-month integration of the one-dimensional model of the ocean mixed layer has shown systematic errors in the major current areas (Fung and Cane, 1978). This report outlines the second of a series of global upper ocean models that includes the effects of advection and upwelling.

Denote the thermodynamic contribution to $\frac{\partial h}{\partial t}$, $\frac{\partial hT_m}{\partial t}$ by $\dot{h}$, $\dot{q}$, respectively. Then the equations governing the horizontally inhomogeneous mixed layer are

$$\frac{\partial h}{\partial t} = - \nabla \cdot (h\underset{\sim}{u}_m) + \dot{h}$$

$$\frac{\partial hT_m}{\partial t} = - \nabla \cdot (hT_m\underset{\sim}{u}_m) + \dot{q}$$

Since the currents are divergent, the magnitude and location of the upwelling velocity are calculated.

Because the mixing and advective processes are on different time scales, the splitting scheme (e.g., Marchuk, 1974) is appropriate. At each time step, the vertical mixing and horizontal current dynamics are thus treated separately.

To use these equations, the currents have to be specified. A simple approach is to use a one-layer model where the mixed-layer velocity $\underset{\sim}{u}_m$ is governed by the equation

$$\frac{\partial}{\partial t}(h\underset{\sim}{u}_m) = - \nabla \cdot (h\underset{\sim}{u}_m\underset{\sim}{u}_m) + \hat{f}\underset{\sim}{k}\times h\underset{\sim}{u}_m - \frac{1}{\rho}\int_{-h}^{0} \nabla p \, dz + \frac{1}{\rho}(\underset{\sim}{\tau}_s - \underset{\sim}{\tau}_e)$$

$$+ \dot{h}\{\underset{\sim}{u}_m - H(\dot{h})\,\delta\underset{\sim}{u}\}$$

There is a hierarchy of approximations to the above equation. Only two will be listed here.

1. The modified Ekman current given by

$$\hat{f}\underset{\sim}{k}\times h\underset{\sim}{u}_m = \frac{1}{\rho}(\underset{\sim}{\tau}_s - \underset{\sim}{\tau}_e)$$

where $\underset{\sim}{\tau}_e = k\underset{\sim}{u}_m$ is provided at the bottom of the mixed layer so that the transport is <90° cum sole to the wind, as is observed.

2. Modified Ekman and mean current

$$\underset{\sim}{u}_m = \underset{\sim}{\bar{u}} + \underset{\sim}{u}^{(E)}$$

where $\hat{f}k \times h\underset{\sim}{u}^{(E)} = \frac{1}{\rho}(\underset{\sim}{\tau}_s' - \underset{\sim}{\tau}_e)$; $\underset{\sim}{\tau}_s' = \underset{\sim}{\tau}_s - \underset{\sim}{\bar{\tau}}$

The mean current is calculated diagnostically from the density field. The level of no motion is taken at 1500 m; the current in the mixed layer is not very sensitive to its precise value.

Experiments are underway to evaluate the inclusion of current dynamics on the sea surface temperature patterns.

References

Marchuk, G. I., 1974: Numerical Methods of Weather Prediction, Academic Press.

NUMERICAL SIMULATION OF THE GULF STREAM, GULF STREAM RINGS, AND MID-OCEAN EDDIES

(T. N. Lee)

The circulation and surface temperatures of the western North Atlantic were simulated with a primitive equation model to simulate the effects of mid-ocean scale eddies and their transports.

Three important changes were made in the baroclinic model that was used by Semtner and Mintz (1977). First, a parameterization of the subgrid scale diffusion of momentum and temperature was used, derived from the quasigeostrophic turbulence theory of Tokioka (1978). Second, a more realistic single-gyre wind stress forcing replaced the unrealistic 2 1/2-gyre pattern of wind stress that was used by Semtner and Mintz (1977). Third, because of the lack of observational data, friction at the lower boundary was neglected.

The model has five levels and a horizontal grid size of 37 km. The idealized model domain is a rectangular basin, 3000 km long, 2000 km wide and 4 km deep, oriented as shown in Figure 1a. The near shore side of the basin has a simple continental shelf and slope (shown in Figure 1b), whereas the other sides are bounded by vertical walls. The model ocean is driven not only by a single-gyre pattern of steady zonal wind stress (shown in Figure 1a) but also by a Newtonian-type surface heating.

In the experiment, the simulated Gulf Stream separates from the coast and continues eastward as an intense free jet. This Gulf Stream develops large amplitude transient meanders, some of which become cold-core cyclonic rings and warm-core anti-cyclonic rings that drift westward. Transient mesoscale eddies form in the broad westward-moving North Equatorial Current. The simulations of the flows and the surface temperatures are realistic in comparison with observations.

Figure 2 shows the sea surface height at 40-day intervals. The contour interval is 20 cm. For the purpose of orientation, the geographical latitude lines at the northern and southern boundaries of the subtropical wind stress gyre are included, together with the 72°W meridian. These six sequence maps of the sea surface height demonstrate the life cycle of the Gulf Stream ring. On day 352, a meander of the Gulf Stream reaches sufficient amplitude to alter the flow from a generally eastward to a southerly direction, cold water is drawn south and a loop is formed. The loop moves westward and its area expands on day 392. On day 432, the ring is pinched off from the Gulf Stream and moves west of the 72° meridian. On days 472, 512, and 552, the ring gradually decays, moves southwestward, and finally is entrained into the warm Gulf Stream. The ring has a life expectancy of approximately 300 days. The generation, maintenance, and decay of the rings in the model are comparable to observations. Newton (1961) has calculated that the heat exchanges across the mean Gulf Stream associated with the

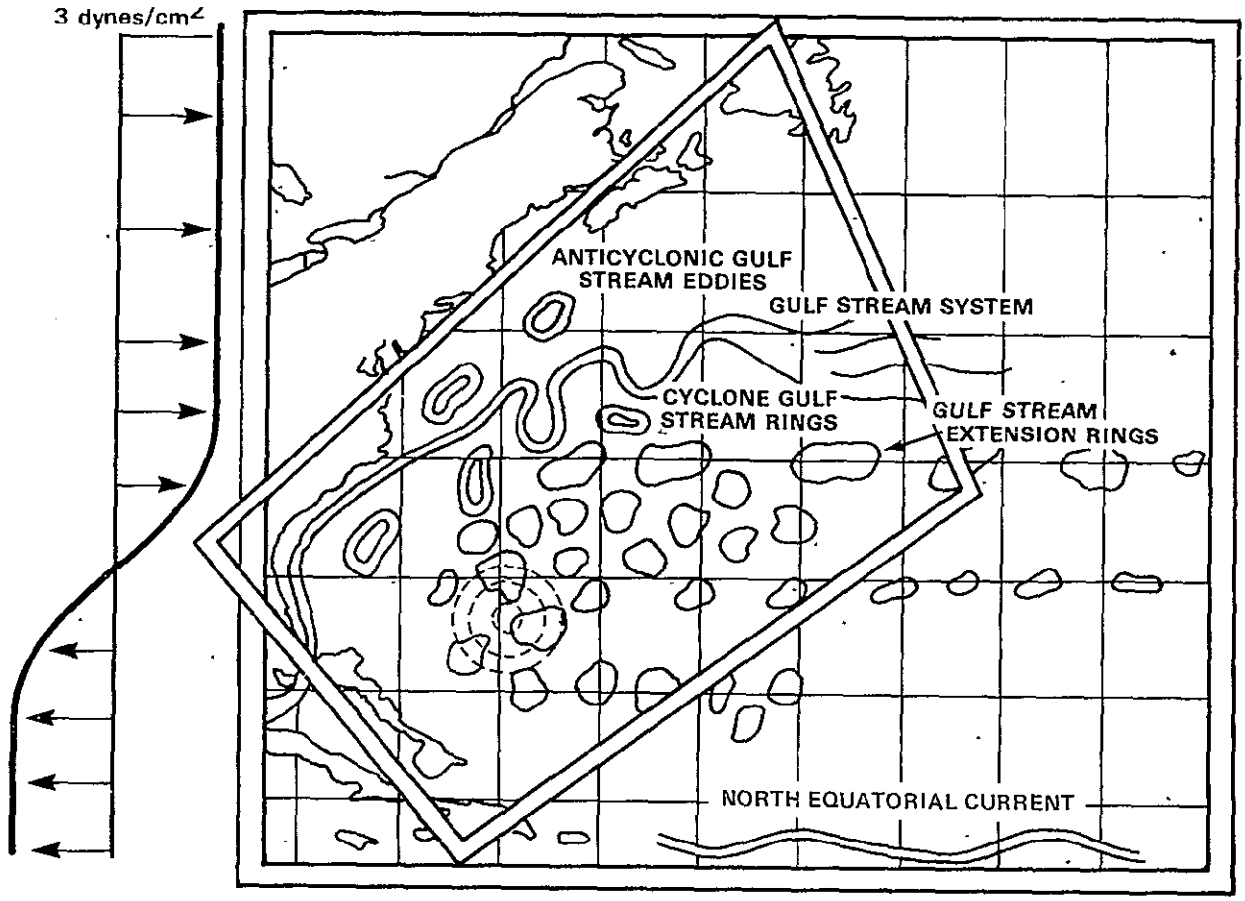

Figure 1a. Boundary of the model domain superimposed on a schematic picture of mesoscale variability in the western portion of the north Atlantic (Joint Polymode Working Groups, 1976). Also shown in the zonal wind stress which drive the model ocean.

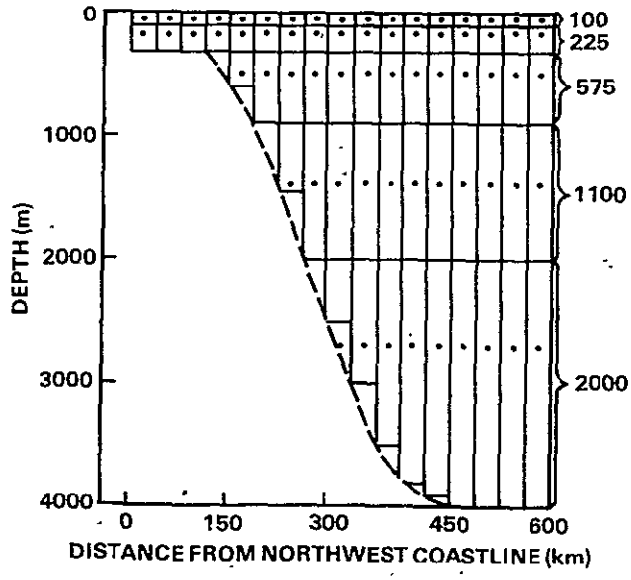

Figure 1b. Model topography and grid box placement near the northwest coastline.

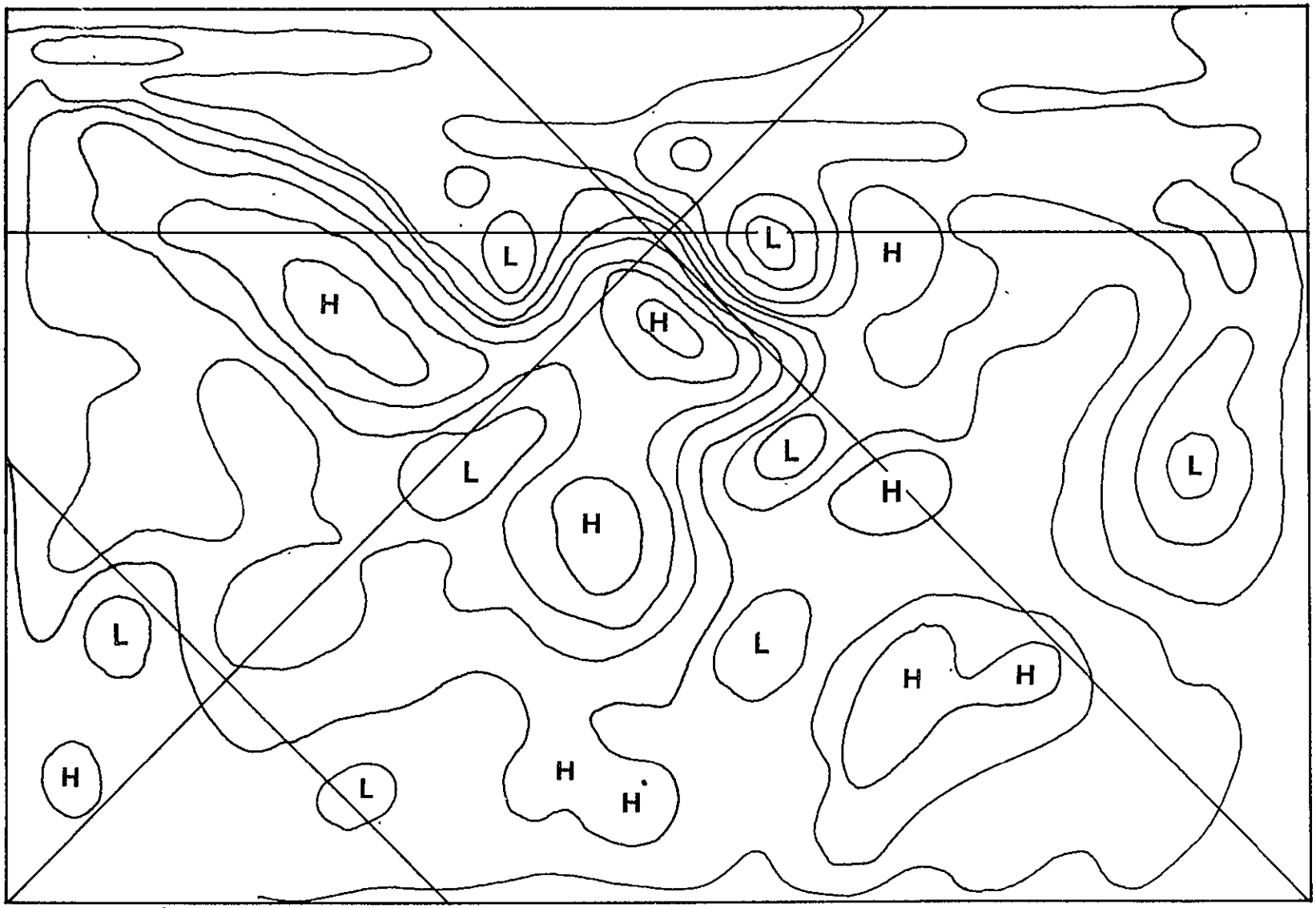

Figure 2a. Surface heights fields (contour interval 20 cm) at 40-day intervals -- day 352.

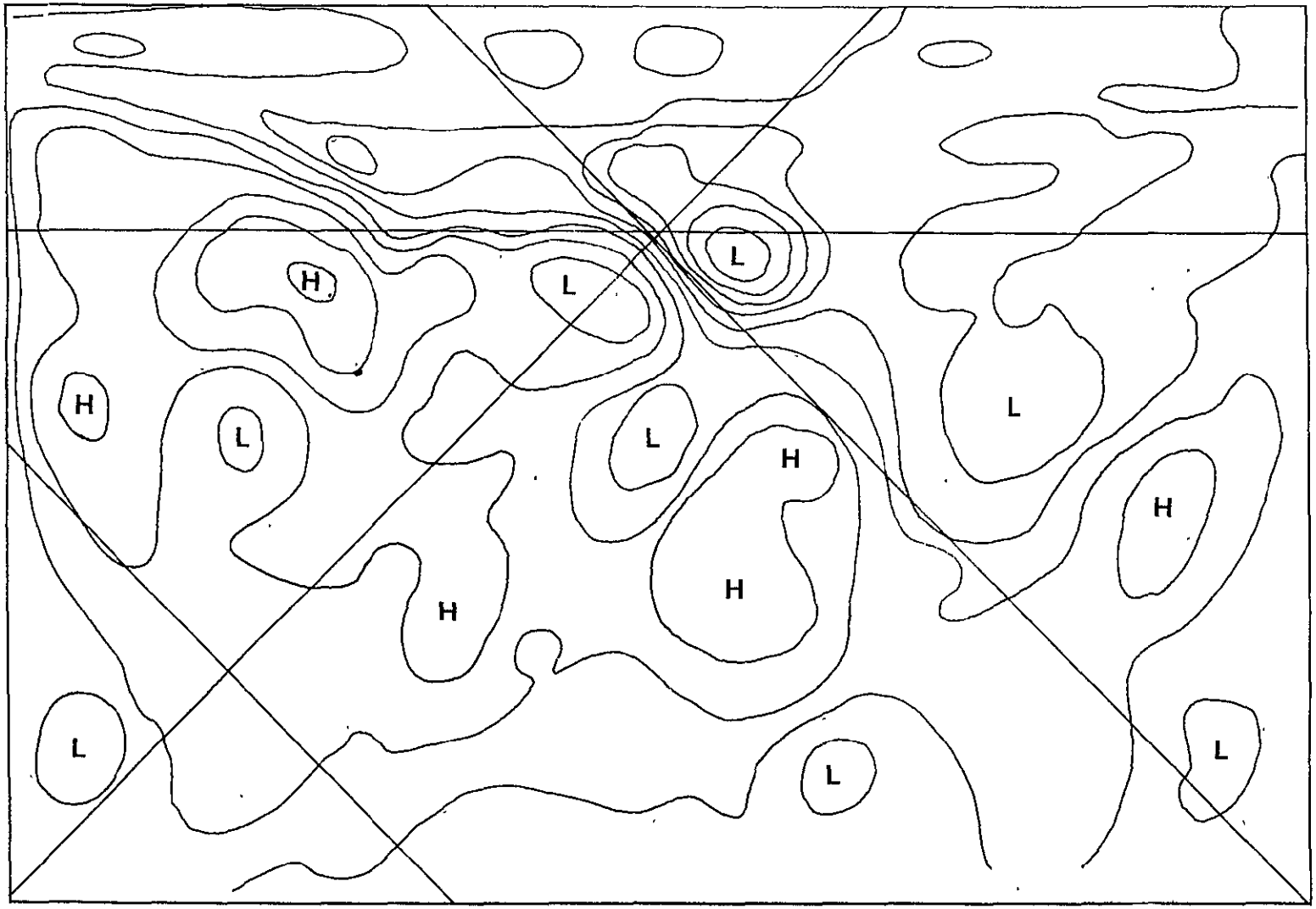

Figure 2b. Surface heights fields (contour interval 20 cm) at 40-day intervals -- day 392.

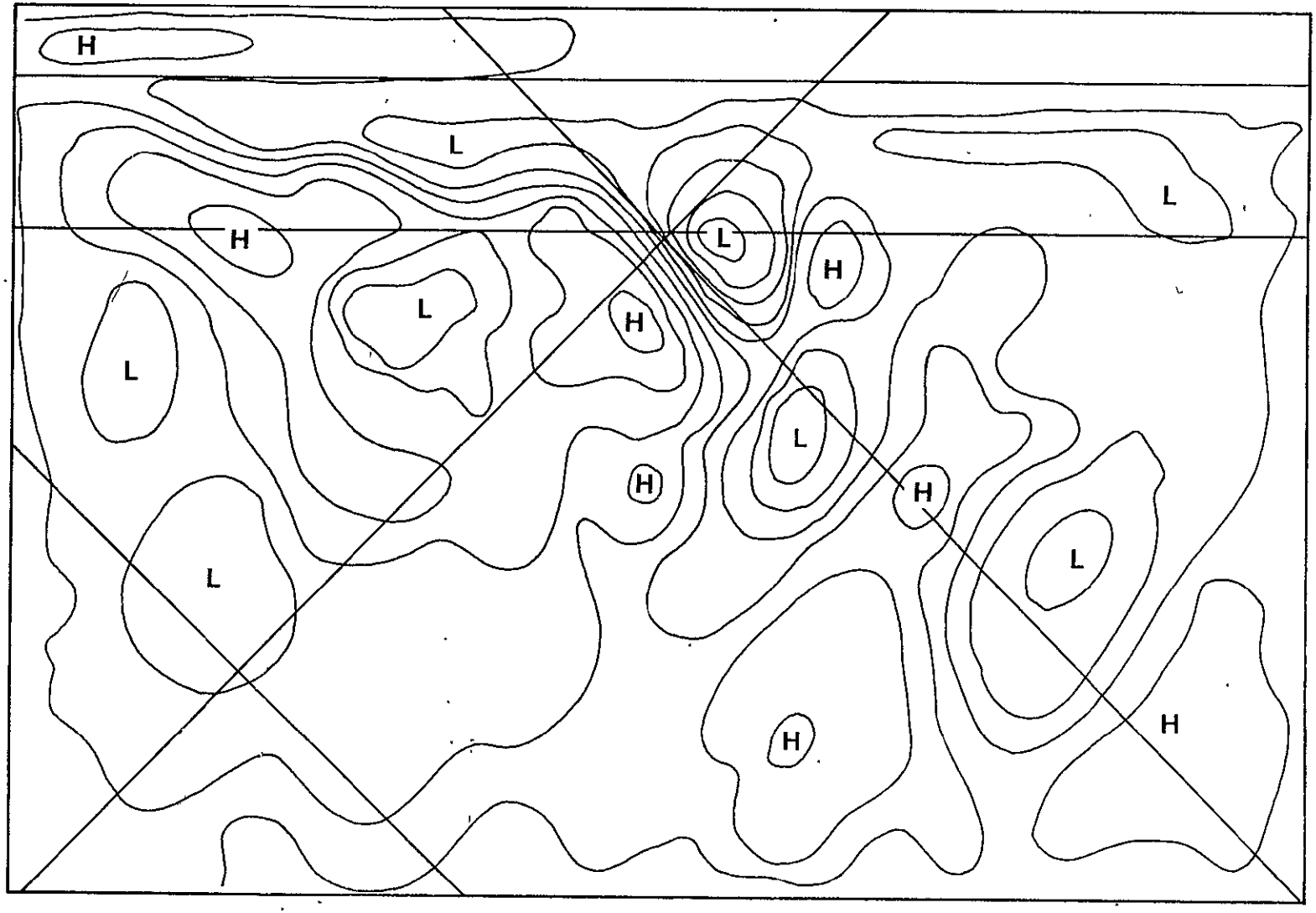

Figure 2c. Surface heights fields (contour interval 20 cm) at 40-day intervals -- day 432.

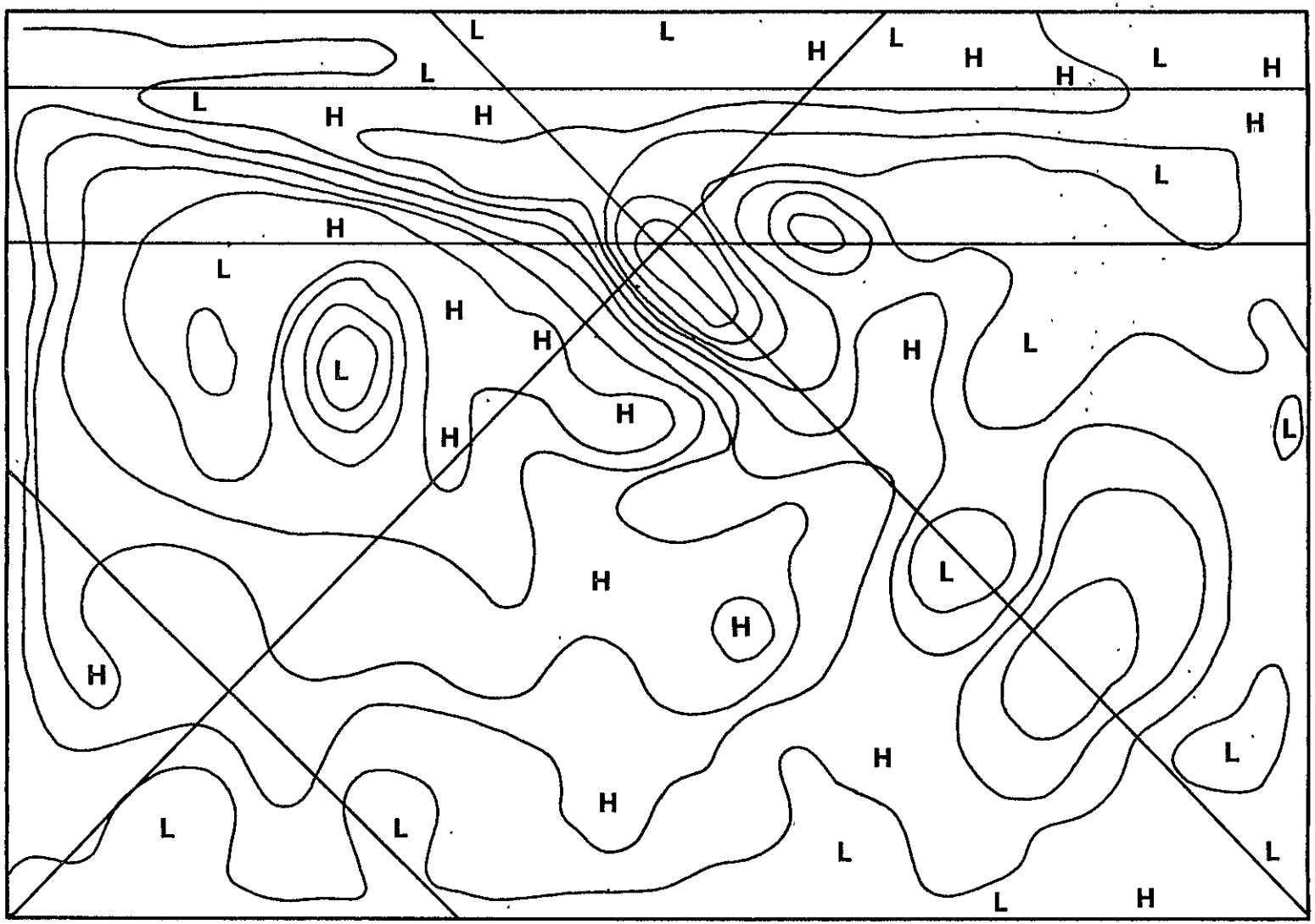

Figure 2d. Surface heights fields (contour interval 20 cm) at 40-day intervals -- day 472.

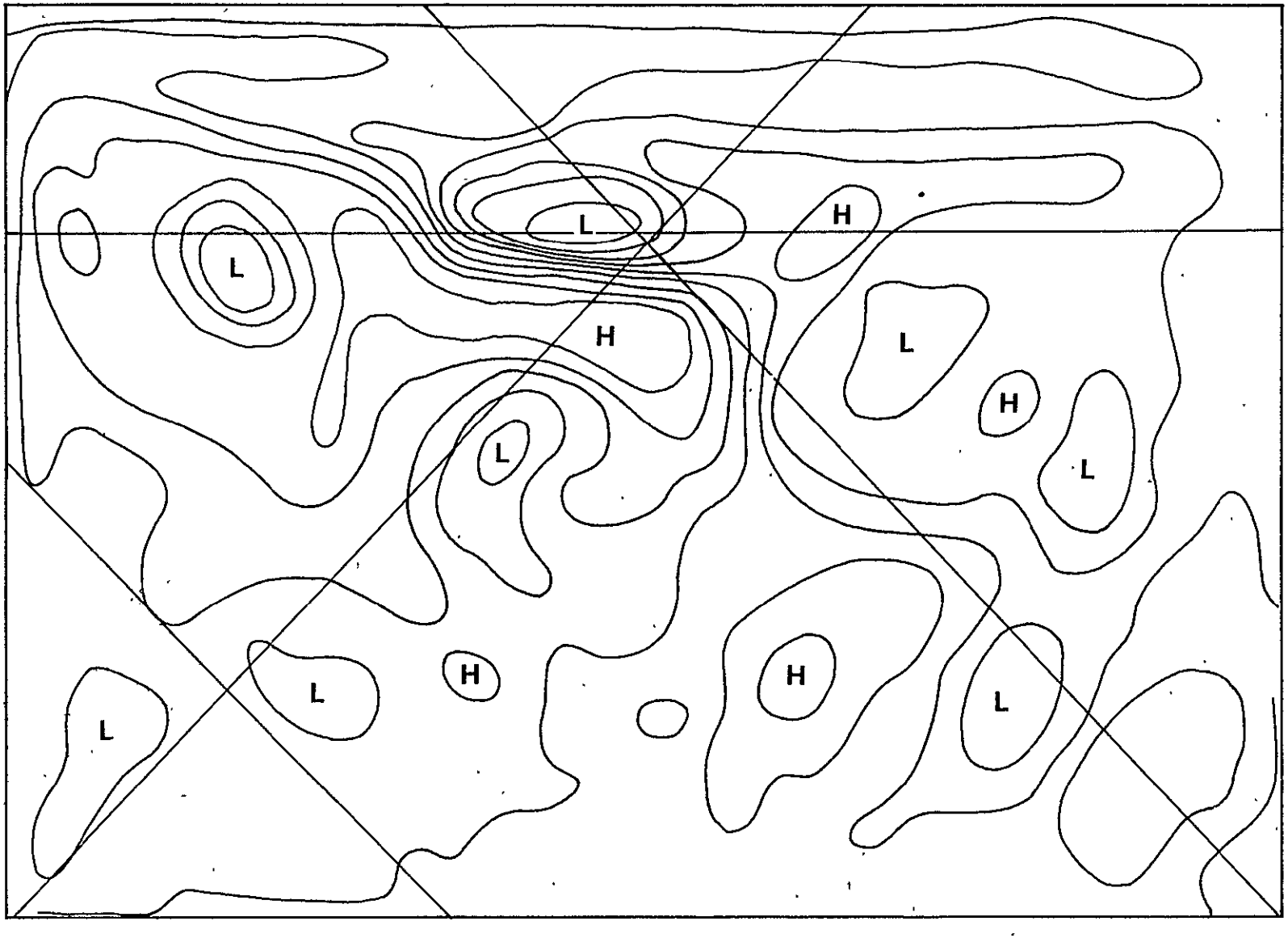

Figure 2e. Surface heights fields (contour interval 20 cm) at 40-day intervals -- day 512.

Figure 2f. Surface heights fields (contour interval 20 cm) at 40-day intervals -- day 552.

separation of one ring from the main cold water mass, can be about 200 to 400 x 10^{18} g-cal. Five to ten pairs of rings annually in the North Atlantic would be capable of transporting the required heat poleward by the North Atlantic Ocean (Oort and Vonder Haar, 1976). Therefore, the correct simulation of the rings is very important to determine the heat transport by the ocean.

This model appears capable of simulating the climatological properties of the Gulf Stream, its meanders, cut-off rings, and mid-ocean eddies. This is a step toward the eventual construction of a global oceanic general circulation model which, coupled to a global atmospheric general circulation model, can be used for interactive atmosphere-ocean climate variation simulations to help in understanding the global atmospheric-oceanic heat budget.

References

Newton, C. W., 1961: Estimates of vertical motions and meridional heat exchange in Gulf Stream eddies, and a comparison with atmospheric disturbances. J. Geophys. Res., Vol. 66, No. 3, pp. 853-870.

Oort, A. H., and T. H. Vonder Haar, 1976: On the observed annual cycle in the ocean-atmosphere heat balance over the Northern Hemisphere. J. Phys. Ocean., Vol. 6, No. 6, pp. 781-800.

Semtner, A., and Y. Mintz, 1977: Numerical simulation of the Gulf Stream and mid-ocean eddies. JPO, Vol. 7, No. 2, pp. 208-230.

Tokioka, T., 1978: Parameterization of subgrid scale mixing based on quasigeostrophic turbulence theory. Submitted for publication to the J. Meteor. Soc. of Japan.

FORCED BAROCLINIC OCEAN MOTIONS III: THE LINEAR EQUATORIAL BASIN CASE

(M. Cane and E. Sarachik)

Previous work on the linear spin-up of an equatorial ocean is extended to include the specific effects of the north-south extent of the basin, thus allowing a detailed comparison of the analytic spin-up theory with numerical calculations.

North-south modes in a β-plane equatorial basin are solved for both numerically and analytically. Simple approximations are developed and the modes are classified by the location of the turning points relative to the zonal walls. The modes are illustrated for three cases:

a. A symmetric basin whose zonal walls are distant from the equator (compared to the equatorial radius of deformation);

b. A symmetric basin whose zonal walls are close to the equator; and

c. An asymmetric basin, one wall of which is close to the equator and one far.

Spin-up in response to x-independent winds in each of these basins is then calculated in terms of four elements: the x-independent response to the wind; the eastern boundary response consisting of Rossby and Rossby-Kelvin modes needed to bring the u field to zero; the western boundary response consisting of Kelvin waves needed to bring the u field to zero; and the western boundary layer consisting of trapped short Rossby waves needed to bring u to zero and meridionally redistribute mass. These elements are combined to describe how the steady (Sverdrup) solutions are approached. Special attention is paid to the fast planetary response: the equatorially confined Kelvin mode, the exponential anti-Kelvin mode with maximum amplitude on the zonal walls, and the Rossby-Kelvin mode, the latter two being modes not present on a meridionally open basin.

Finally, a numerical model is run to illustrate spin-up for various winds in each of the three (a, b, and c) basins.

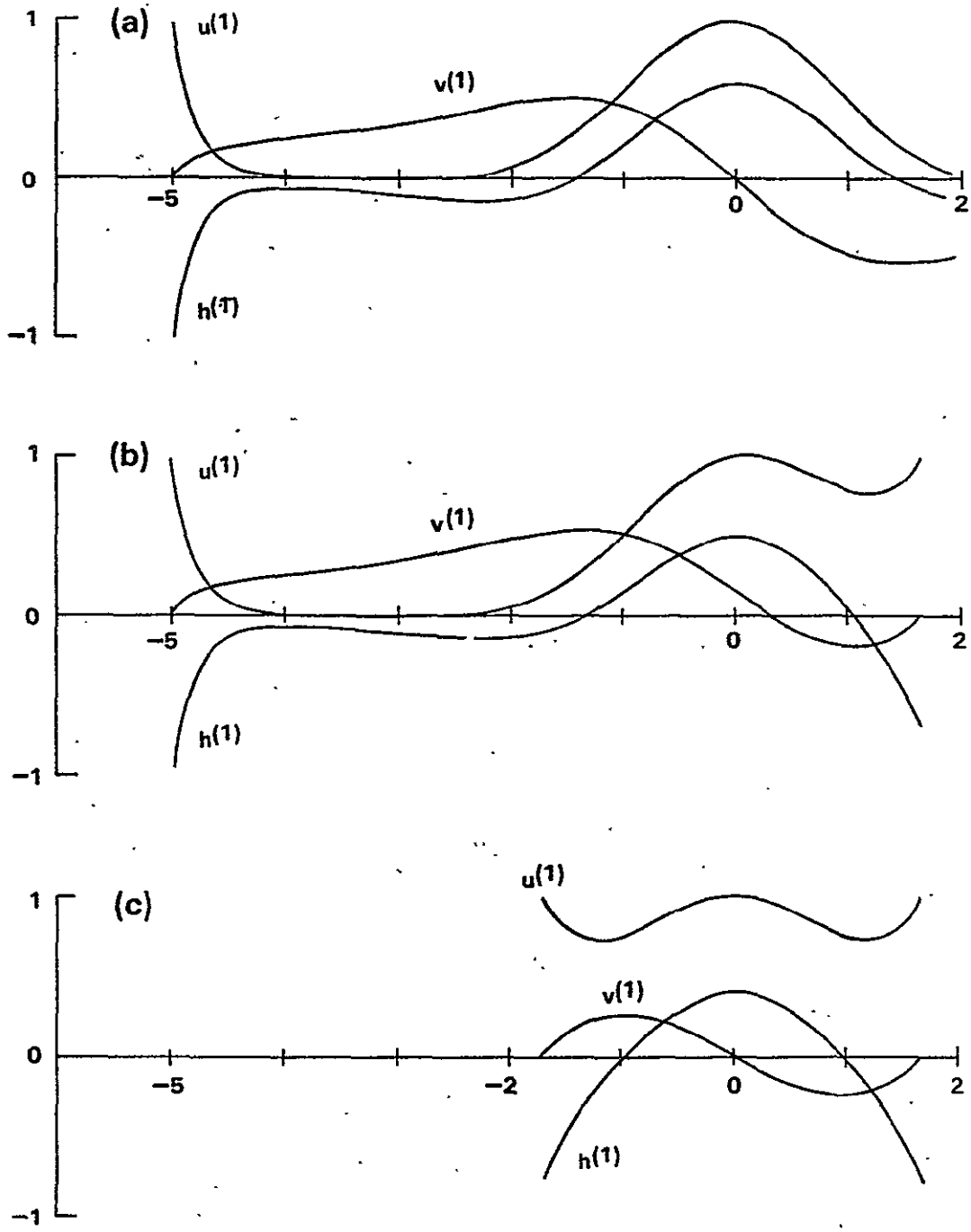

Figure 1. The response to a uniform westerly wind of a zonally-unbounded ocean of meridional extent:

(a) y = -5 to y = +5
(b) y = -5 to y = +1.7
(c) y = -1.7 to y = +1.7.

The influence of the zonal costs is seen to be largely confined to a region within a local radius of deformation of the coast.

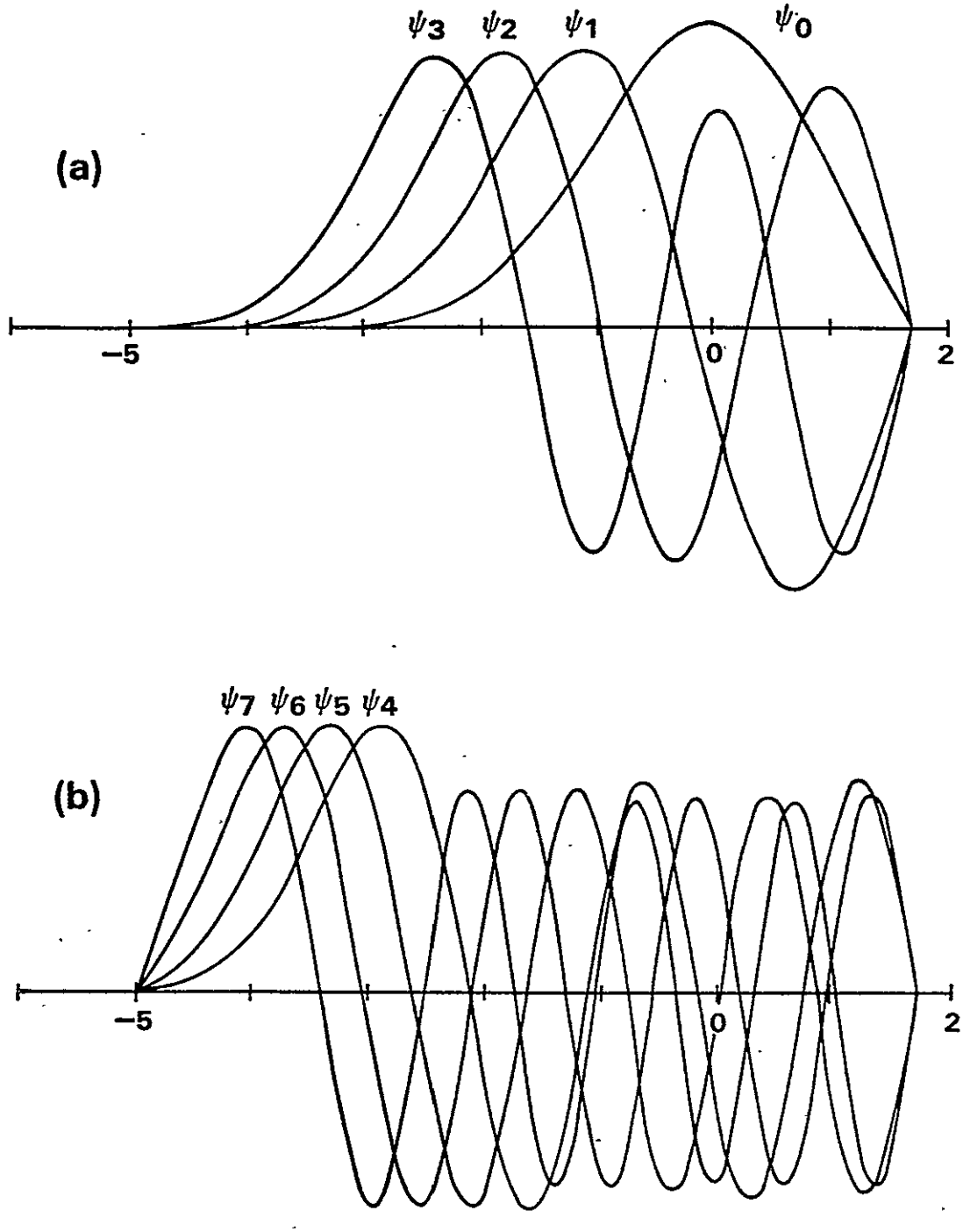

Figure 2. The first seven meridional eigenfunctions in a basin bounded by zonal walls at y = -5 and y = +1.7. (Distance has been non-dimensionalized by the equatorial radius of deformation.) Note that the structure is severely modified by the near wall.

IV. C L I M A T E

SOME ASPECTS OF HYDROLOGY IN THE GLAS GCM

(R. Godbole)

Numerous simulation experiments have been performed using the GLAS GCM for winter (January-February) and summer (July-August) months. The results of some of these experiments have been recently discussed by Charney (1978), Halem (1978), Herman (1978), and Shukla (1978). This paper is mainly concerned with the performance of the GLAS GCM with respect to handling some of the hydrological parameters. Specifically, the distributions of precipitation and evaporation are examined to see how well they agree with each other and with observations, and in what manner, if any, they are associated with other related parameters such as cloudiness and vertical velocity.

For the purpose of the present discussion, the results of one summer month, namely July, were selected. Further, the paper's attention is restricted to the zonally-averaged fields only. This would mask the important regional features, but, nonetheless, it offers a convenient and powerful tool in understanding the persistent features of any quantity in relation to those of other related quantities. A detailed description dealing with the regional distributions of precipitation, evaporation, sea-level pressure, etc., as obtained by the model for winter and summer seasons, and their comparison with observations has been documented by Godbole (1978).

Figure 1 shows the distribution of July precipitation (mm/day) as computed by the model. For comparison, the observed precipitation for the three summer months of June, July, and August compiled by Schutz and Gates (1972) is also reproduced in the figure. The agreement between the two curves is fairly good. Both the profiles show a primary maximum due to the ITCZ and two secondary maxima, one in each hemisphere, apparently associated with the frontal systems. The noteworthy feature is the dip in the precipitation amount in the winter hemisphere at a latitude of about 20°. The dip is more pronounced in the computed results. There is a secondary minimum in the observed as well as computed precipitation pattern in the summer hemisphere at about 40°. These precipitation minima are obviously due to the existence of the subtropical anticyclones which are characterized by relatively clear skies and large-scale subsidence. It can be inferred from the figure that the subsidence in the winter hemisphere is stronger than that in the summer hemisphere. This is known to be the case mainly because of the fact that the subsidence is associated with the descending branch of the Hadley cell, which is always strong in the winter hemisphere. This is clearly borne out from Figure 2 in which a zonally-averaged vertical velocity for the whole column is plotted along with precipitation and cloudiness as a function of latitude. All the quantities are model generated. By convection, negative vertical velocity

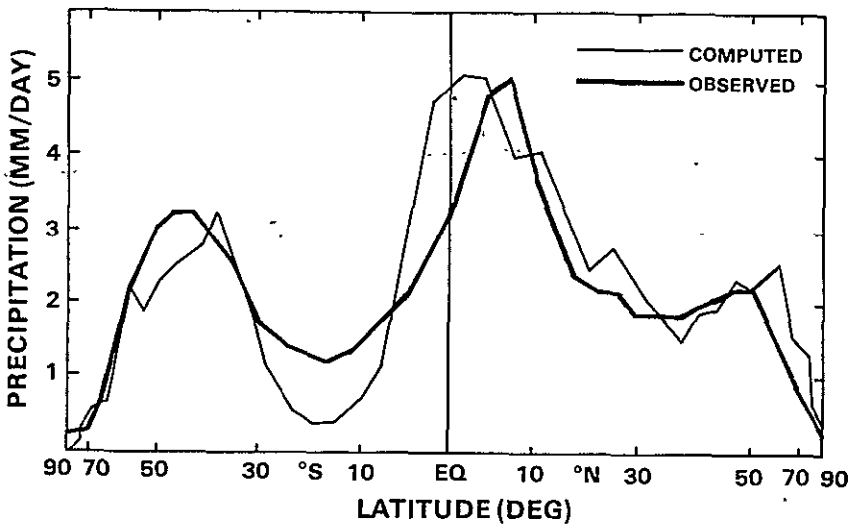

Figure 1. Zonally-averaged mean monthly precipitation (mm/day) computed by the model (thin line) and observed (thick line).

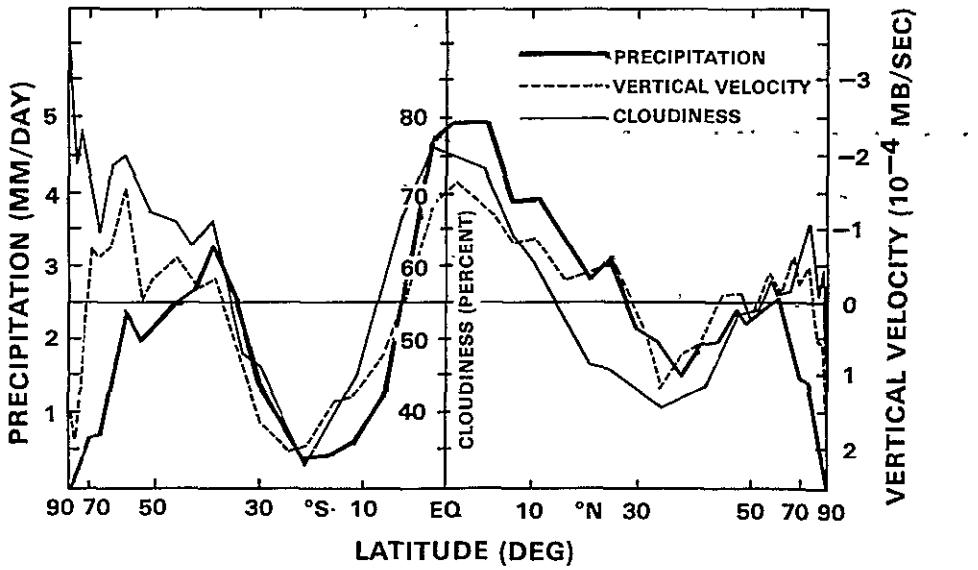

Figure 2. Zonally-averaged mean monthly precipitation (mm/day), cloudiness (percentage of time) and vertical velocity (10^{-4} mb/sec) as computed by the model.

represents upward motion. Cloudiness is expressed as a percentage of time any type of cloud is present in a vertical column. It is seen from the figure that between 55°N and 40°S all the three curves follow each other very closely, meaning that the upward motion is associated with relatively more cloudiness and more precipitation and vice versa. Over the polar latitudes, this conventional relationship apparently does not hold: specifically, the relationship between cloudiness and precipitation is reversed; more cloudiness being associated with less precipitation. Since the model physics precludes the existence of nonprecipitating clouds, this seeming paradox may be explained on the basis of saturation conditions and the actual availability of moisture. Over the polar latitudes, the almost saturation conditions would favor frequent formation of clouds, but the realization of moisture in the form of precipitation would be insignificantly small.

An important feature to note from Figure 2 is that over the South Pole, the cloudiness is maximum . It immediately suggests that the South Pole should lose heat due to large outgoing longwave radiation, which is really not the case (Schutz and Gates, 1974). This may, therefore, well be the cause for unusually low temperatures generated by the model at the upper levels near the South Pole (Halem, 1978; Godbole, 1978). A further analysis shown in Figure 3 supports this conjecture, because the two uppermost layers of the model (i.e., centered at 65 mb and 175 mb) exhibit a large amount of cloudiness near the South Pole. As a matter of fact, the longwave radiational cooling in the model (not shown) does show an increase in the cooling rate at the South Pole.

Figure 4 shows the two major types of precipitation, namely, supersaturation precipitation and precipitation due to penetrative convection, which together contribute to the total precipitation. It is noticed that in the summer hemisphere the penetrative convection dominates the supersaturation condensation, whereas in the winter hemisphere, the supersaturation processes overtake the convective processes. This is what should be expected. Supersaturation condensation may be considered to be, in part, due to frontal systems (besides due to ITCZ), which are more active in the winter hemisphere due to strong baroclinicity. On the other hand, in the summer hemisphere, the atmosphere is convectively unstable, especially over the tropical belt where the precipitation mainly comes from the Asian and African monsoons.

Figure 5 shows the computed surface evaporation. The corresponding observed evaporation derived by Schutz and Gates (1972) is also reproduced in the figure for the sake of comparison. It may be noted that the observed evaporation is not what is actually observed by any direct measurements; rather it is derived indirectly on the basis of the knowledge of other hydrological data. At any rate, it is found that the computed values of evaporation are

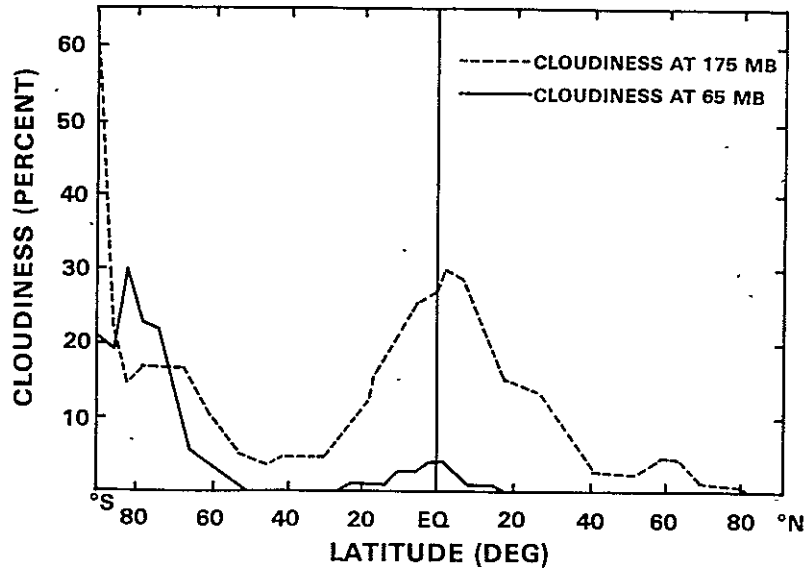

Figure 3. Zonally-averaged distribution of cloudiness in a layer centered at 175 mb (dashed line) and at 65 mb (thick line).

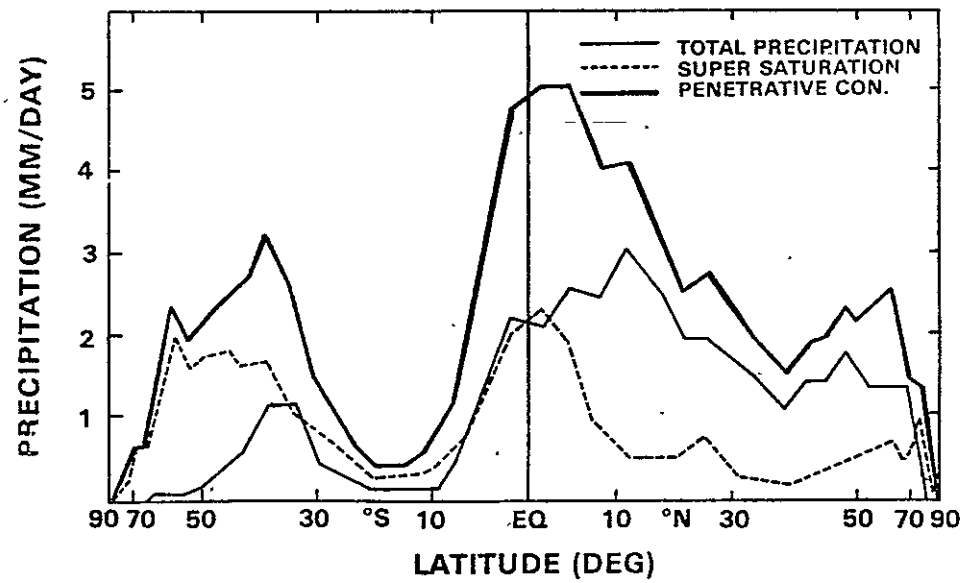

Figure 4. Distribution of supersaturation precipitation (dashed line) and penetrative convective precipitation (thin line) in relation to the total precipitation (thick line). The units are mm/day.

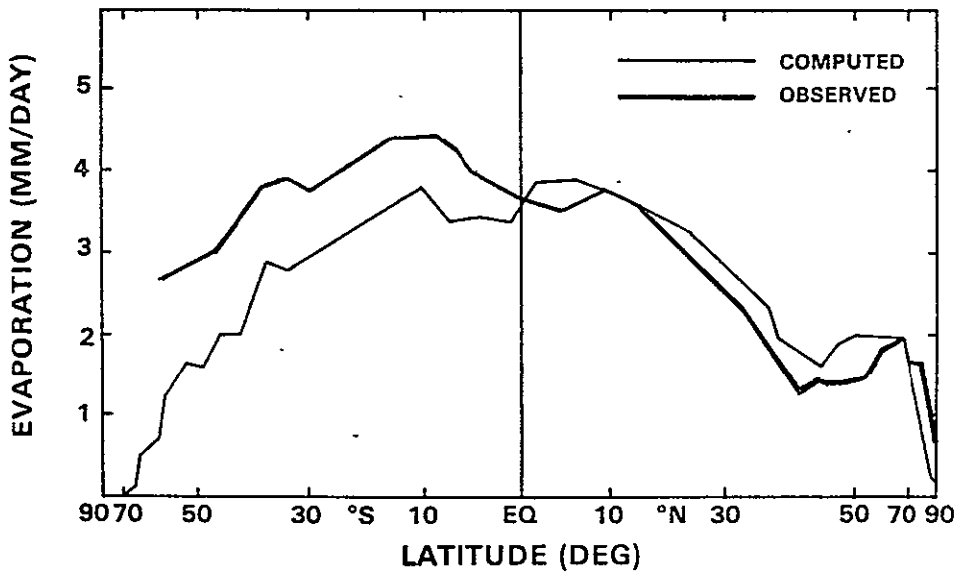

Figure 5. Zonally-averaged mean monthly evaporation (mm/day) computed by the model (thin line) and observed (thick line).

omparable with the observed values and the agreement between the wo curves is fairly good except that, in the Southern Hemisphere, he computed evaporation rate is somewhat underestimated.

Finally, a brief comment is necessary on the hydrological alance of the model, which is represented in Table 1. The global onthly mean evaporation is found to be 2.69 mm/day, whereas the orresponding figure for precipitation is 2.34 mm/day. That means or a typical summer month of July, the global mean evaporation xceeds precipitation by about 13 percent. This prompted GLAS to xamine further the daily behavior of global mean evaporation, recipitation, and specific humidity, which are the three major omponents of the hydrological balance. It was found that evapo- ation, precipitation, and specific humidity all decreased from he beginning until the end of the month with very little daily scillation in each of these. For convenience, the values on the irst and the last day of the month are shown in the table. It is een that evaporation exceeded precipitation all through the month, ut its rate of excess decreased during the month by about 4 percent.

The corresponding decrease in the moisture content of the atmosphere is about 3 percent. These values, however, must be viewed with some caution because of the inherent computational errors and the daily variation of a parameter itself. Moreover, certain parameters like ground wetness and precipitation runoff have not been taken into consideration. Nonetheless, the results of Table 1 do seem to point out that the model tends to maintain the hydrological balance within a seasonal degree of accuracy.

Table 1. Global Mean Evaporation, Precipitation and Specific Humidity for July Computed by the Model.

Global Mean	Evaporation (E) mm/day	Precipitation (P) mm/day	Excess (E)over(P) Percent		Specific Humidity gm/kgm	
Monthly Mean	2.69	2.34	13.0		-	
1st of July	2.91	2.49	14.4	4% decrease of excess (E)over(P)	2.57	3% decrease of specific humidity
End of July	2.49	2.23	10.4		2.50	

References

Charney, J., 1978: AGCM climate experiments: response to changed albedo. JOC Study Conf. on Climate Models, Washington, DC.

Godbole, R., 1978: Response of the GLAS general circulation model to changes in the treatment of longwave radiation. Sigma Data Serv. Corp. Rep. (unpublished).

Halem, M., J. Shukla, Y. Mintz, M. L. Wu, R. Godbole, G. Herman, and Y. Sud, 1978: Comparisons of observed seasonal climate features with a winter and summer numerical simulation produced with the GLAS general circulation model. JOC Study Conf. on Climate Models, Washington, DC, April.

Herman, G., and W. T. Johnson, 1978: Ice margin experiments with the Goddard GCM. JOC Study Conf. on Climate Models, Washington, DC, April.

Shukla, J., and B. Bangaru, 1978: Effect of a Pacific sea-surface temperature anomaly on the circulation over North America: a numerical experiment with the GLAS model. JOC Study Conf. on Climate Models, Washington, DC, April.

Schutz, C., and W. L. Gates, 1972: Global climate data for surface, 800 mb, 400 mb: July. Report R-1029-ARPA, Rand, Santa Monica, CA.

_____, 1974: Supplemental global climatic data: July. Report R-1029/1-ARPA, Rand, Santa Monica, CA.

RADIATION PARAMETERIZATION AND INFLUENCE OF SYSTEMATIC RADIATION DIFFERENCES ON THE GLAS GCM

(M. L. Wu and L. D. Kaplan)

Changes made in the calculation of radiative heating can change the static stability of a model atmosphere and (instantaneously) the temperature of the surface, which in turn affects sensible heat flux and evaporation. Evaporation provides moisture into the atmosphere, which is the source of heat of condensation. Sensible heat flux alters the static stability of the atmosphere. The static stability affects the vertical motions field, which produces cloudiness and precipitation. The release of precipitation is accompanied by the release of latent heat, which in turn affects the motion field. Cloudiness again alters the radiative heating in the atmosphere and surface temperature; this in turn affects the transport of latent and sensible heat into the atmosphere across the lower boundary. Because of these complicated interaction processes, systematic radiation differences would be expected to be important in the modeling of the general circulation. A more realistic thermal radiation parameterization was, therefore, developed for the GLAS GCM, resulting in marked improvement in the model performance, as indicated by the results of impact studies summarized below.

A thermal radiation routine was parameterized to replace an old radiation routine used in the GISS GCM. The parameterization is based on the statistical band model with a strong line version of the Curtis-Godson approximation. It includes the effect of water dimerization in the 8-13μm window region, and assumes a continuous distribution of specific humidity in the vertical. Calculations with this parameterization were found to be in good agreement with the theoretical line-by-line calculation of flux and flux divergence and to be within the observational error of long-wave radiative flux measurements.

Winter and summer 10-week GCM runs were carried out with old and new longwave radiation parameterization, starting with real data for December 20, 1972 and June 18, 1973, respectively, and the mean statistics for the 30 days were compared for each of the two seasons. Figure 1 shows, for the initial condition, the longwave heating rates calculated with the old and new radiation parameterizations.

The large difference in heating rates in the lower troposphere at low latitude is due to inclusion of the waterdimer absorption in the 8-13μm region. The differences in the upper atmosphere are mainly due to different treatment of absorption in the 15μm carbon dioxide band. The new radiation parameterization also produces much less downward flux (approximately 30-50 percent) at the surface.

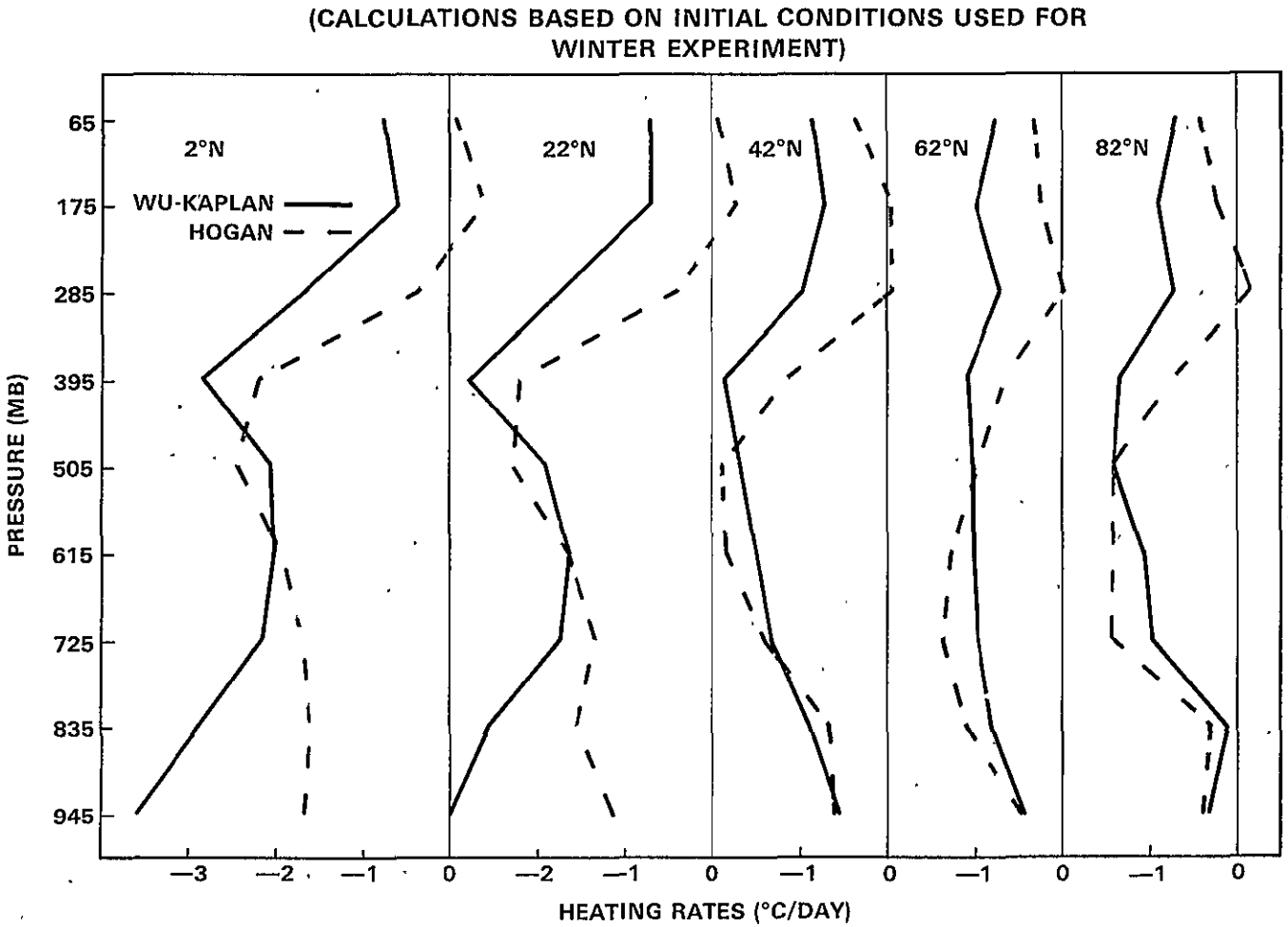

Figure 1a. Heating rates (°C/day) - winter).

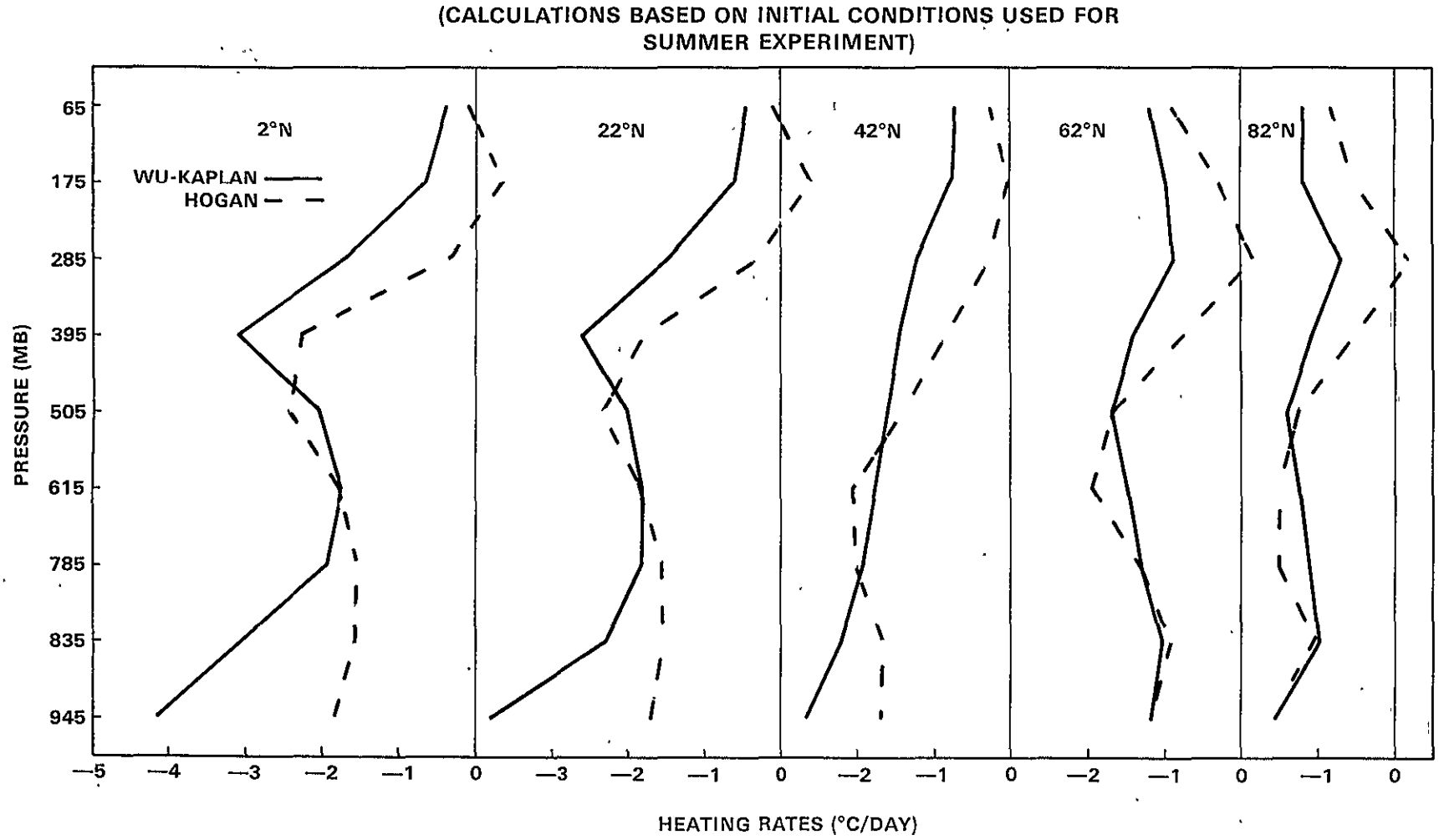

Figure 1b. Heating rates (°C/day) - summer).

The introduction of the new radiation parameterization resulted in significant improvement in the model statistics and showed that the GLAS GCM is capable of simulating important climatological features remarkably well if a realistic radiation parameterization is used.

This can perhaps be most easily seen by examination of the mass field. Figure 2 shows the mean sea level pressure distribution for the last 30 days of the winter run as obtained with the old and new radiation, and includes for comparison the observed mean sea level pressure distribution as given by Taljaard, et al., (1969) and Crutcher and Meserve (1970). Figure 3 shows a similar comparison with the mean height field at 200 mb level obtained by Crutcher and Davis (1969).

In the winter experiments, the Icelandic low, the Aleutian low, and the mid-oceanic ridges in the Atlantic and Pacific are reasonably simulated in the new radiation run, especially the Icelandic low, which is practically missing with the old radiation parameterization. The subtropical highs in the Southern Hemisphere are better simulated in the modified experiment. The westward tilt of troughs and ridges are also well simulated in the model with the new radiation. The subtropical highs in both hemispheres were simulated better in the summer runs with the new radiation.

The zonally-averaged temperature field with the new radiation parameterization is closer to the observed temperature field in the tropics, but improvement is still required in the middle and high latitudes. At high latitudes, the temperature is too cold by as much as 20°C at upper levels and by 10°C at lower levels. Generally speaking, the temperature structure of the model atmosphere with the new radiation parameterization is more stable than that with the old radiation. The Hadley and Ferrel cells are stronger with the new modified radiation.

A rainfall analysis, which was carried out cooperatively with Dr. Ramesh Godbole, showed the following differences between the old and new models.

In the winter experiment, the modified model is able to simulate the precipitation associated with the ITCZ more realistically in regard to the horizontal extent and the amount than that of the old model. The wet areas in the northern Atlantic and Pacific Oceans coincide with major storm tracks in the modified model, but not so in the old model. On the whole, the precipitation rate in the new model over the oceanic regions is closer to what has been derived from satellite observations (Rao, et al., 1976). The major dry areas off the west coasts of South America, Africa, and Australia are reproduced better in the modified model.

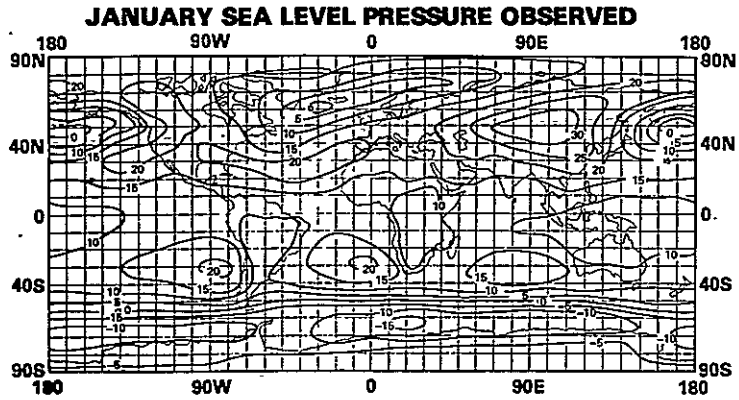

Figure 2a. Observed sea level pressure (mb-1000) for January after Jaljaard et al. (1969) and Crutcher and Meserve (1970).

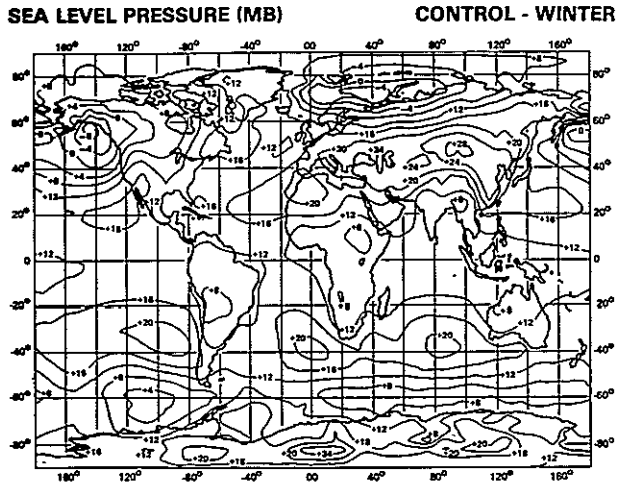

Figure 2b. Simulated sea level pressure (mb-1000) for February - Control.

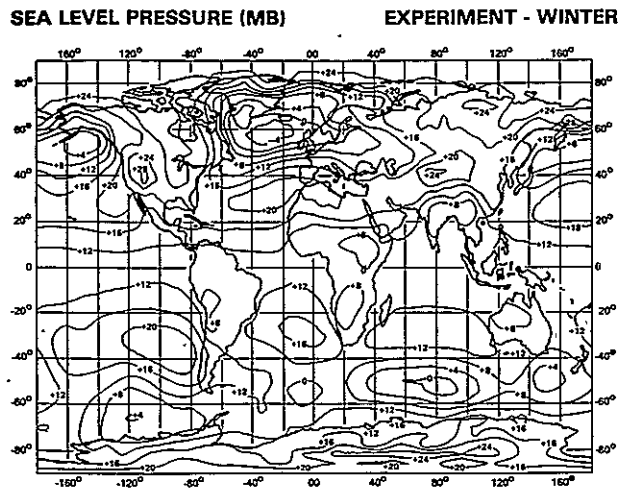

Figure 2c. Simulated sea level pressure (mb-1000) for February - Experiment.

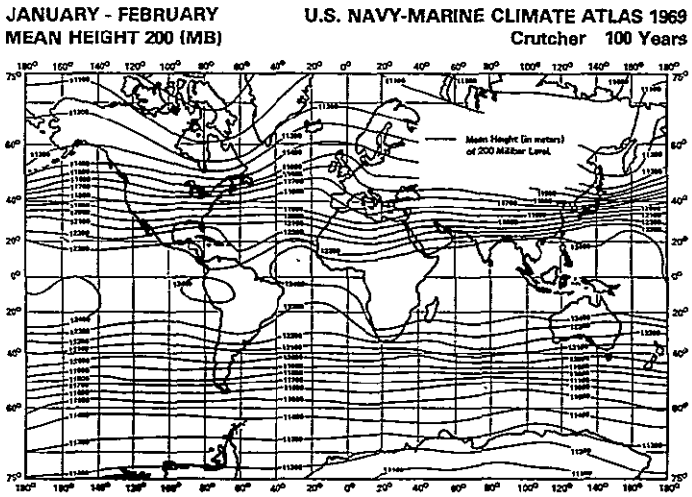

Figure 3a. Observed 200 mb geopotential height (mb) for December, January, and February after Crutcher and Davis (1969).

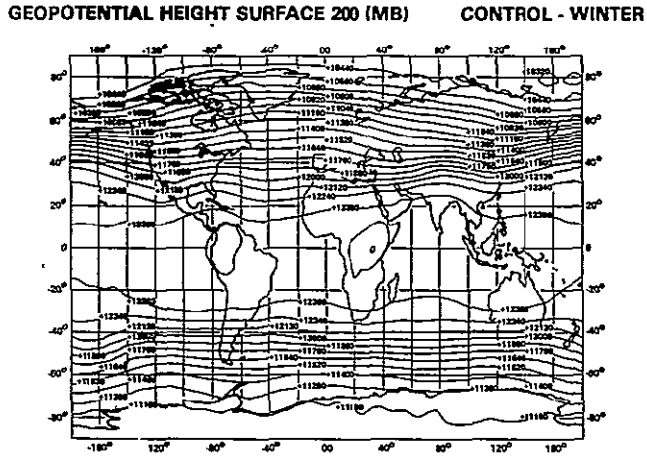

Figure 3b. Simulated 200 mb geopotential height (mb) for February - Control.

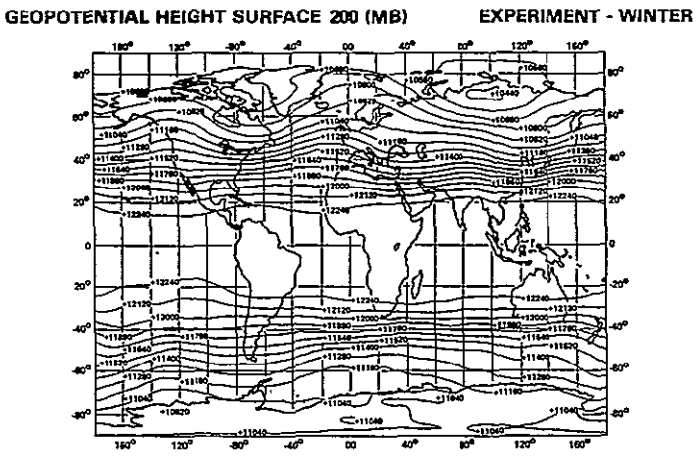

Figure 3c. Simulated 200 mb geopotential height (mb) for February - Experiment.

In the summer rainfall, the significant feature is the precipitation associated with monsoon systems. The Asian SW monsoonal rainfall is reproduced in the modified model much better than it is in the old model.

The eddy available potential energy (EAPE) increases by 32 percent (10 percent) and zonal available potential energy (ZAPE) increases by 7 percent (27 percent) with the use of the new radiation parameterization in winter (summer) simulations. More detailed analysis of the energetics is in progress, especially in the generation of EAPE and ZAPE. There are a few cases of worsening with the new radiation model, such that the Siberian high is worse with regard to intensity and location. On the whole, the worsening is not comparable with the large improvement mentioned in the previous discussions.

These experiments have shown that accuracy in the radiation calculation is important in modeling the general circulation. Equally important is the computation time. A radiation parameterization that is accurate and fast in calculation is highly desirable for the purpose of general circulation studies. GLAS is attempting to use a least squares approach to fit the emissivity to a polynomial.

GLAS has also tested the role of ozone on the thermal and dynamical structure of the GLAS GCM. The experiments were integrated for 42 days in a winter simulation. The last 30-day mean shows that the temperature in the upper layer (10-120 mb) in the tropical and subtropical regions decreases by about 5°-6°C when ozone heating in the infrared absorption region is turned off, and decreases by about 8°-13°C when ozone heating in both the infrared and solar absorption region is turned off. This research is still in progress.

The above experiments call radiation every 2 1/2 hours. If it is called every 1/2 hour, the zonally-averaged temperature field does not change much, but a small though noticeable improvement is obtained in the other fields. A detailed analysis of this interesting result will be carried out.

ferences

utcher, H.L., and O. M. Davis, 1969: U.S. Navy Marine climate atlas of the world: Vol. VIII, NAVAIR 50-1C-54, Naval Weather Service Command, Washington, DC.

_____, and J. N. Meserve, 1970: Selected level heights, temperature, and dew points for the Northern Hemisphere. NAVAIR 50-1C-52 Revised, Naval Weather Service Command, Washington, DC.

ɔ, M. S., W. V. Abbott, III, and J. S. Theon, 1976: Satellite-derived global oceanic rainfall atlas (1973 and 1974), NASA SP-410.

ljaard, J. J., H. Van Loon, H. L. Crutcher, and R. L. Jenne, 1969: Climate of the upper air: Vol. 1, NAVAIR 50-1C-55, Superintendent of Documents, Washington, DC.

RADIATION-CLOUD FEEDBACK SENSITIVITY STUDY

(Y. Sud and J. Shukla)

A study was undertaken to examine the sensitivity of the radiation-cloud feedback mechanism using the general circulation model of the Goddard Modeling and Simulation Facility. The purpose of this study was to understand the importance and need for a time-dependent radiation-cloud interaction in a GCM. The GLAS GCM (previously the GISS GCM) has been described by Somerville, et al. (1974), Stone, et al. (1977), and more recently by Halem, et al. (1978). The latest version of the model, as described by Halem, was used in this study. An experiment for a 90-day simulation was available from the in-house library of runs for the months of June, July, and August, starting from the initial data for May 15, 1974.

The cloud parameterization in the standard model is interactive with the radiation. Clouds of supersaturation and convective types are generated in the model. The convective clouds are of three types: low levels 7 and 8, mid levels 5 and 6, or deep convective between four specified levels 4 through 9, while the supersaturation clouds occur if the relative humidity exceeds the prespecified limiting value, usually 100 percent. The short wave radiation is affected by clouds because the cloud reflects the incident radiation, and multiple scattering within the cloud causes local warming due to the increased photon path. Long wave radiation, on the other hand, treats all types of clouds as black bodies for both absorption and transmittance. Typically, the presence of a cloud causes warming beneath the cloud, due to trapped long wave radiation.

Features of the GLAS model used in this study that differed from the earlier version described by Somerville, et al. (1974) and Stone, et al. (1977) were as follows:

1. This model used a split grid. The standard 4°x5° grid changes to 4°x10° and 4°x20°, respectively, at 66° and 82° poleward from the equator. The use of this grid spacing allowed a 10-minute time step instead of a 5-minute time step.

2. The model used center differencing, MATSUNO-scheme instead of the TASU-MATSUNO scheme in the time-marching calculation in hydrodynamics. Besides being particularly suited for a split grid, this scheme eliminated an implicit horizontal diffusion in the TASU-MATSUNO scheme. However, a Shapiro filter on the temperature and pressure fields was used to eliminate checkerboarding.

3. The present model has fully interactive soil-hydrology. A simple though reasonable time-dependent ground moisture and ground snow and ice cover model was used. Snow and ice albedos were calculated from the snow and ice cover depth on the ground.

4. The radiation in the earlier version of the model was replaced with the Wu-Kaplan radiation. This radiation is briefly described by Wu, et al. (1978). On the basis of identical summer and winter simulations with the old and new radiations, Wu, et al. claimed the new radiation performs better than the previous radiation.

The third month of the simulation period, i.e., August 1974, was chosen for this experiment. The data set for fixed clouds was produced from the cloud output of the control run. First, a mean monthly cloudiness was obtained and then grid cells with highest percentage cloudiness were picked up to contain the clouds. Thus, clouds were allotted to a sufficient number of cells to conserve the zonal cloudiness separately over land and ocean and separately for each cloud type at each sigma level. The new sensitivity run was then begun from August 1, 1974, using the data set, boundary and initial conditions used in the control run. The only difference in the new run was an overriding statement that made radiation see the clouds from a fixed-cloud data set rather than those produced by the model for the purposes of precipitation and convection. A mass-weighted cloudiness map for the control and experiment is shown in Figures 1a and 1b. The clouds produced from the dynamics of the experiment are shown in Figure 1c. Some of the significant results from this study are detailed in the following paragraphs.

The sea-level pressure (SLP) fields for the mean monthly August looked quite similar (Figures 2a and 2b). In the difference fields (Figure 2c), it is noticed that in the Northern Hemisphere the new run gave SLP 4 mb deeper in the Pacific and 8 mb less intense in the Atlantic. In the Southern Hemisphere, there are three major cells with differences of -8, +4, and +8 mb, respectively, over Pacific, Atlantic, and Indian Oceans.

The differences at the centers of these systems are larger than the model variability (expressed as standard deviation) obtained from a set of four July predictability runs shown in Figure 2d. Nonetheless, there is no evident spatial correlation between locations of maximum cloudiness differences and maximum changes in SLP.

Similar results were noticed in geopotential height fields. Notice differences ranging from -64 through +128 gpm in the Southern Hemisphere and -30 through +160 gpm in the Northern Hemisphere in Figure 3a. These differences are larger than the model variability from four July predictability runs shown in Figure 3b. However, positive height differences are consistent with positive SLP differences and vice versa. Again, there is no spatial correlation between locations of maximum changes in cloudiness and maximum changes in geopotential heights.

The atmospheric energetics fields from these two runs were also examined. Zonally-averaged fields of evaporation,

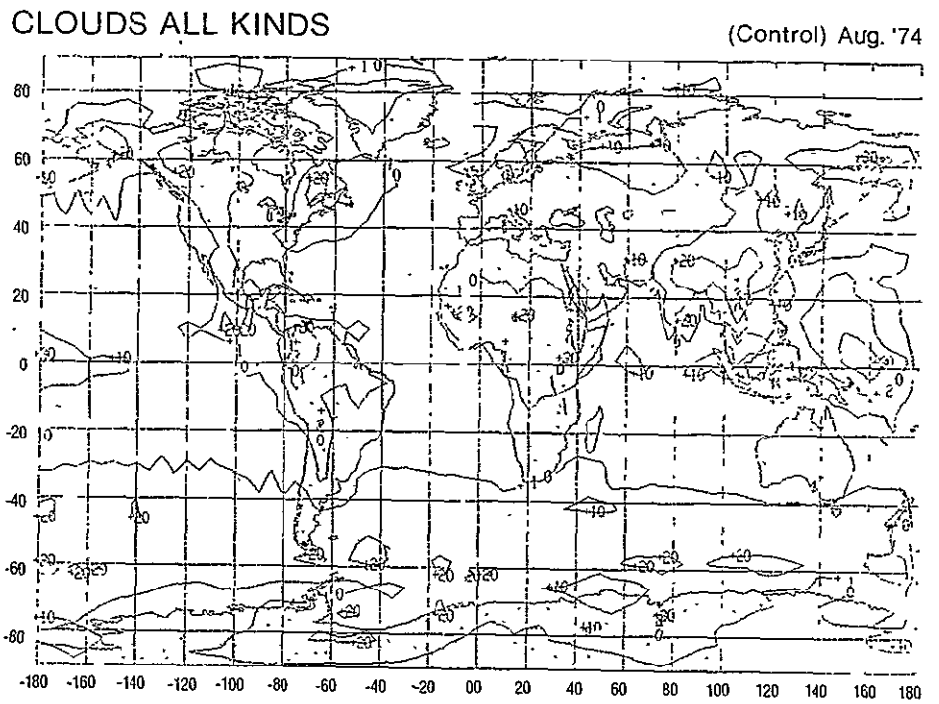

Figure 1a. Time- and mass-weighted mean clouds in the control run.

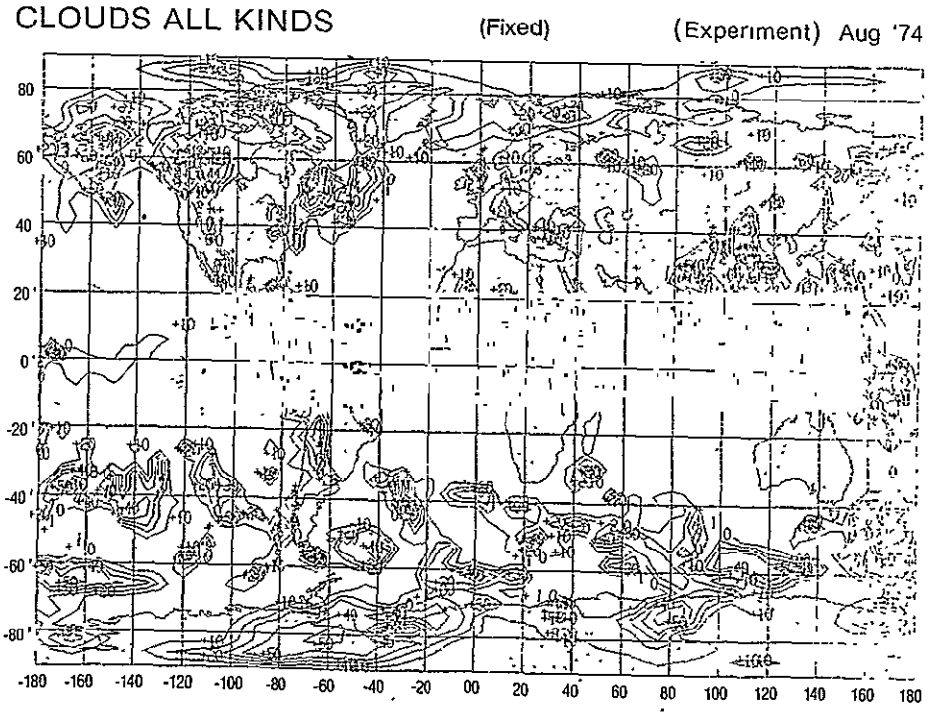

Figure 1b. Time- and mass-weighted fixed clouds in the experiment.

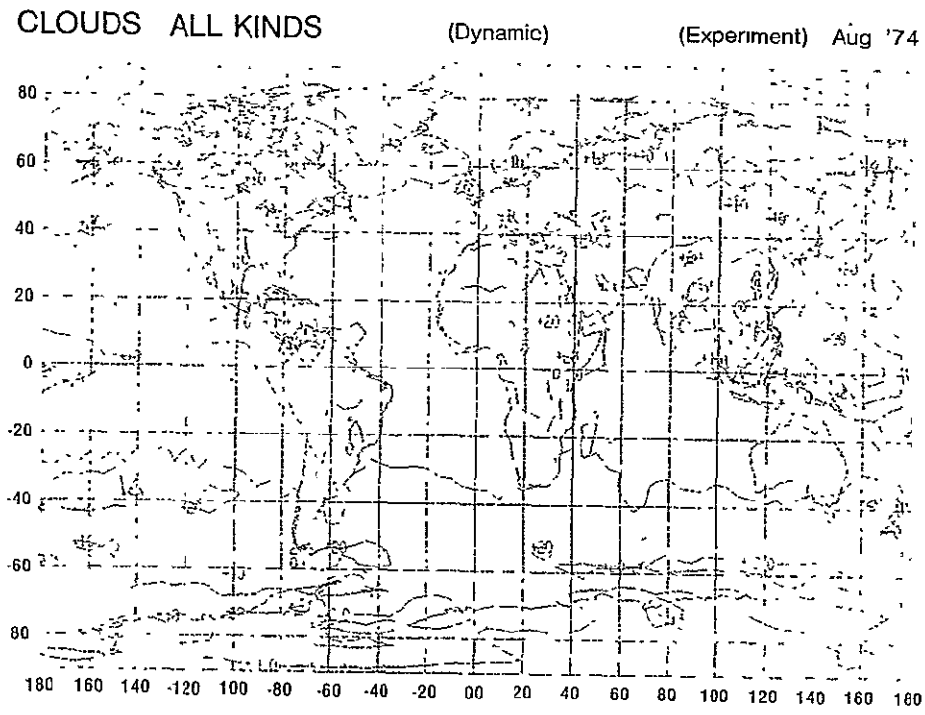

Figure 1c. Time- and mass-weighted clouds produced in the experiment.

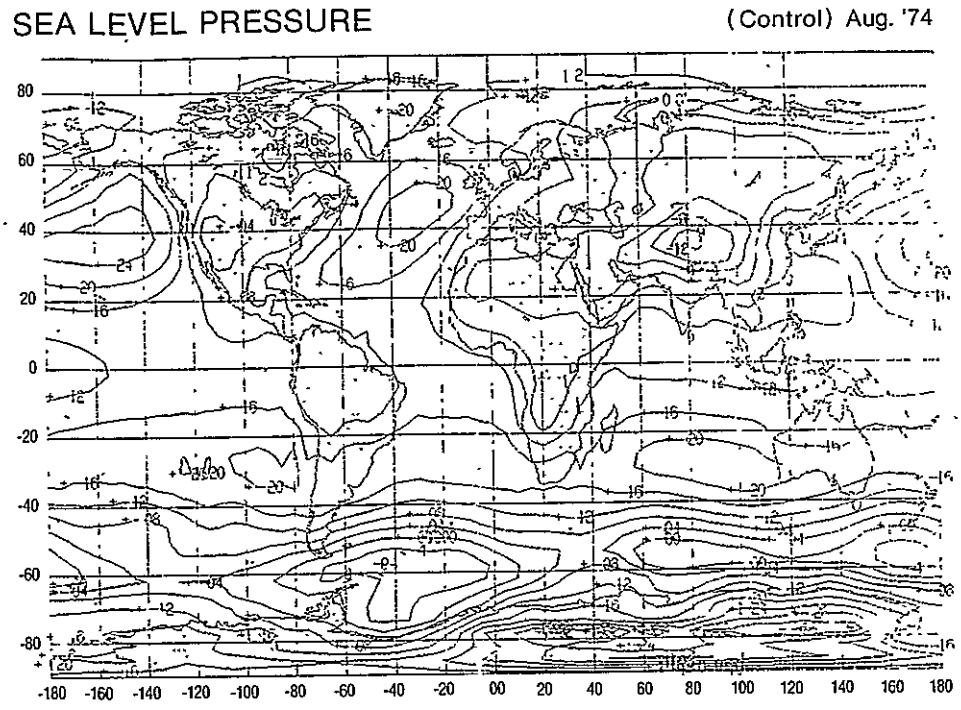

Figure 2a. Sea level pressure in (P_s-1000) mbs (control).

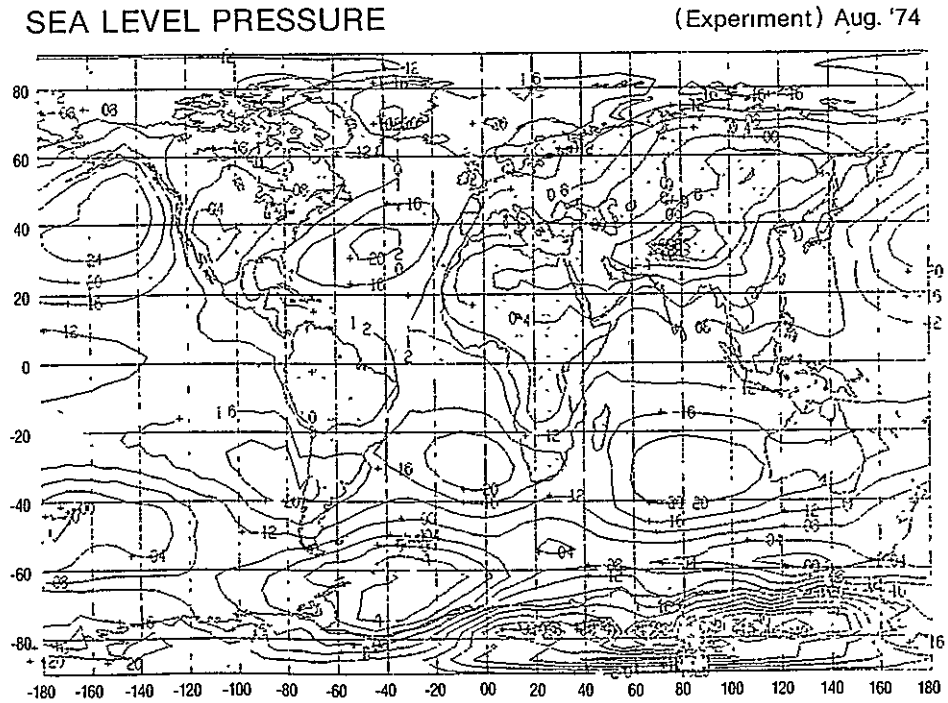

Figure 2b. Sea level pressure in (P_s-1000) mbs (experiment).

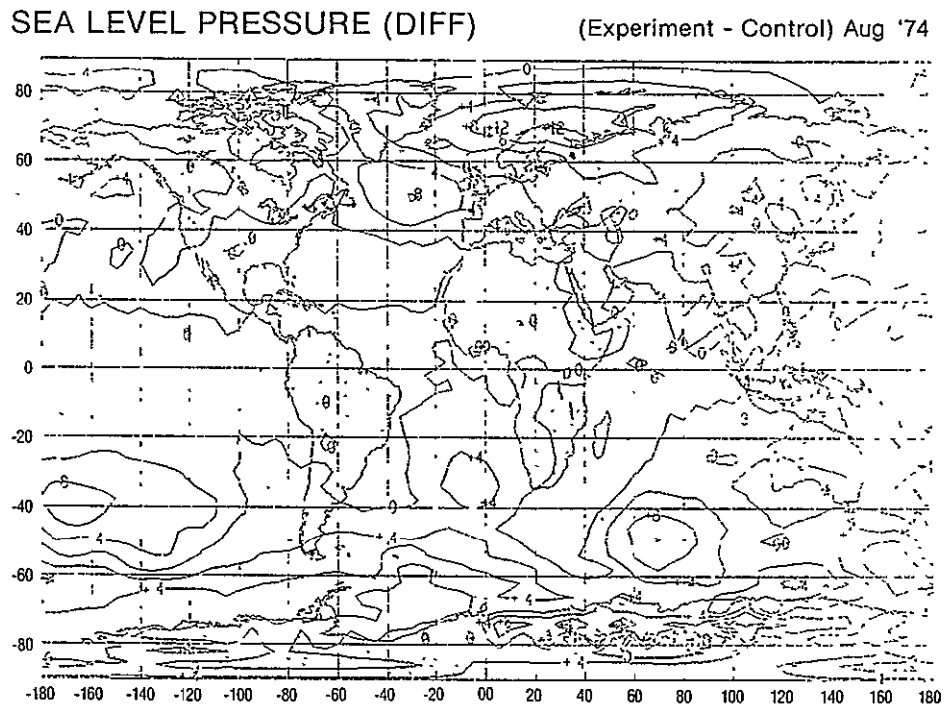

Figure 2c. Differences in the sea level pressures (experiment - control).

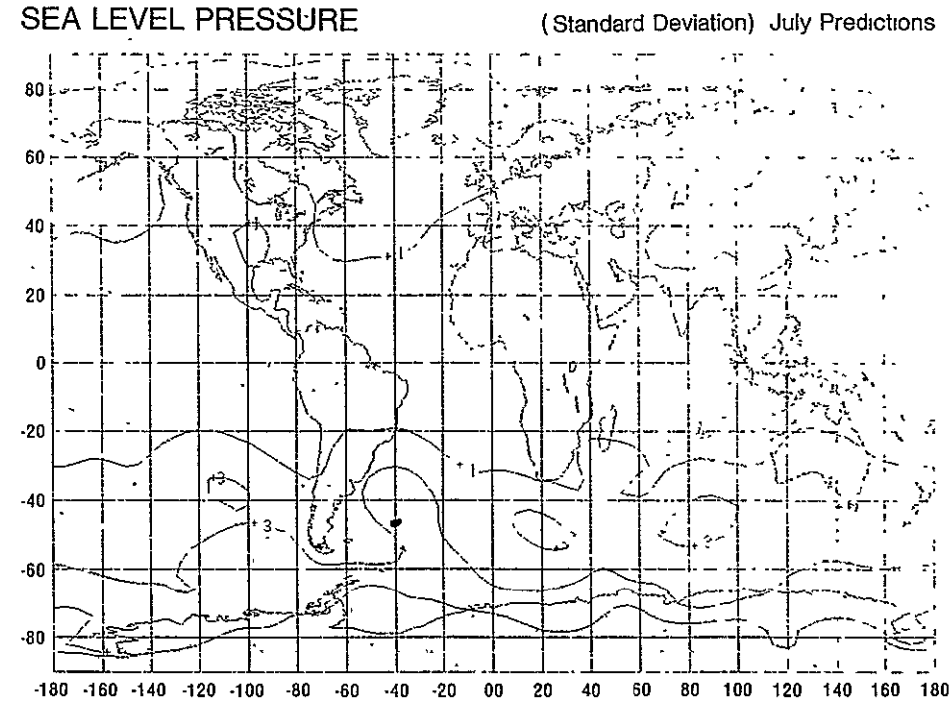

Figure 2d. Model variability from four summer runs expressed as standard deviation among the four predictibility runs.

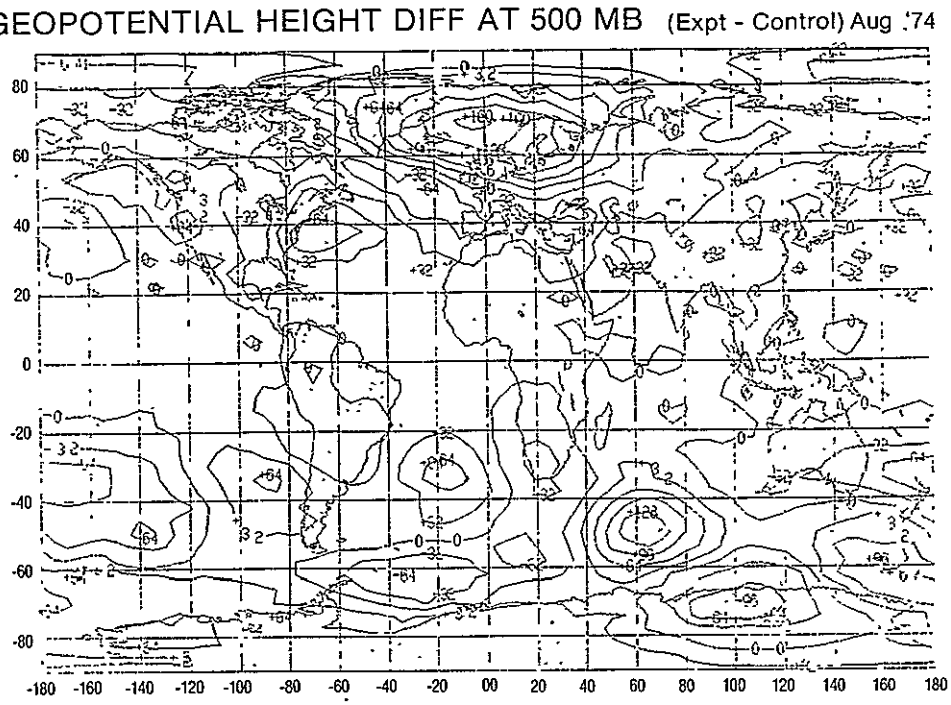

Figure 3a. Geopotential height difference in GPMs.

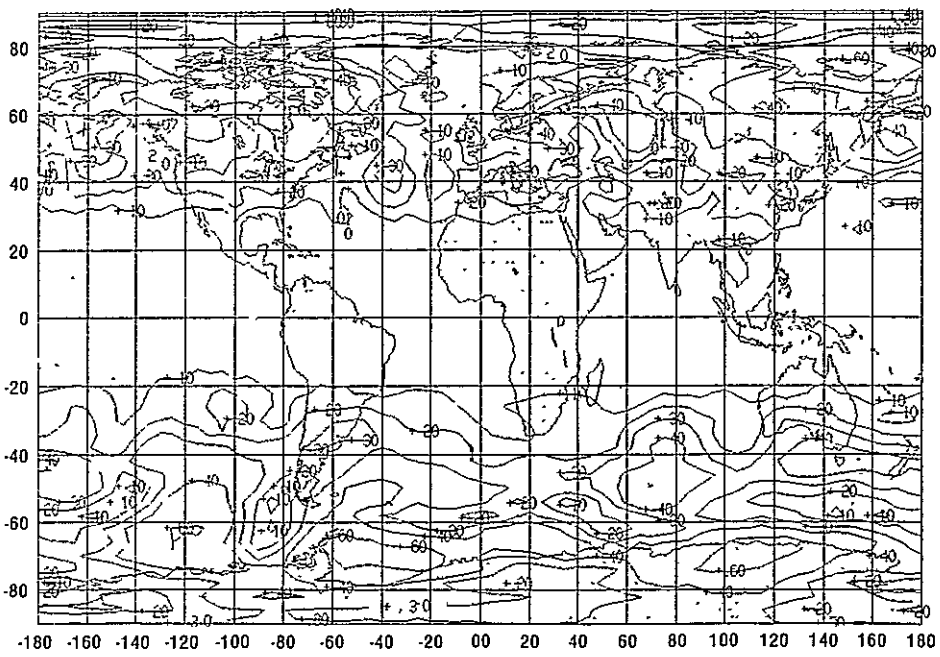

Figure 3b. Geopotential height variability in GPMs, as computed from four predictibility runs, showing the model variability.

precipitation, temperature, specific humidity, and winds were compared. No major impact was found, therefore, these fields are not shown.

In the two-dimensional fields, the most conspicuous differences are in the net outgoing fields of radiation. Obviously, it is caused by the cloudiness fixed at 100 percent at certain grid cells, which gave an inhomogeneous radiative transfer field. The fields from control and experiment are shown in Figures 4a and 4b, respectively. Notice Figure 4a is a typical structure seen in observations (Halem et al., 1978).

The difference fields (experiment-control) of total evaporation and precipitation are shown in Figures 5a and 5b. Thick digits are for positive differences and thin ones are for negative differences. The only significant impact seems to be an increase in the evaporation in the western Pacific Ocean. Further investigation is necessary for this peculiar difference.

In conclusion, it may be stated that the mean monthly sea level pressure and geopotential height fields do not show any systematic difference in association with changes in cloudiness. In certain areas the changes in these fields are larger than the natural variability of the model. As expected, the structure of the net radiation balance at the top of the atmosphere is very different in two runs. It is noisy in the fixed-clouds run. However, the significant changes are in the evaporation fields in the western Pacific. These need further investigation to ascertain the interrelationship of cloudiness and evaporation.

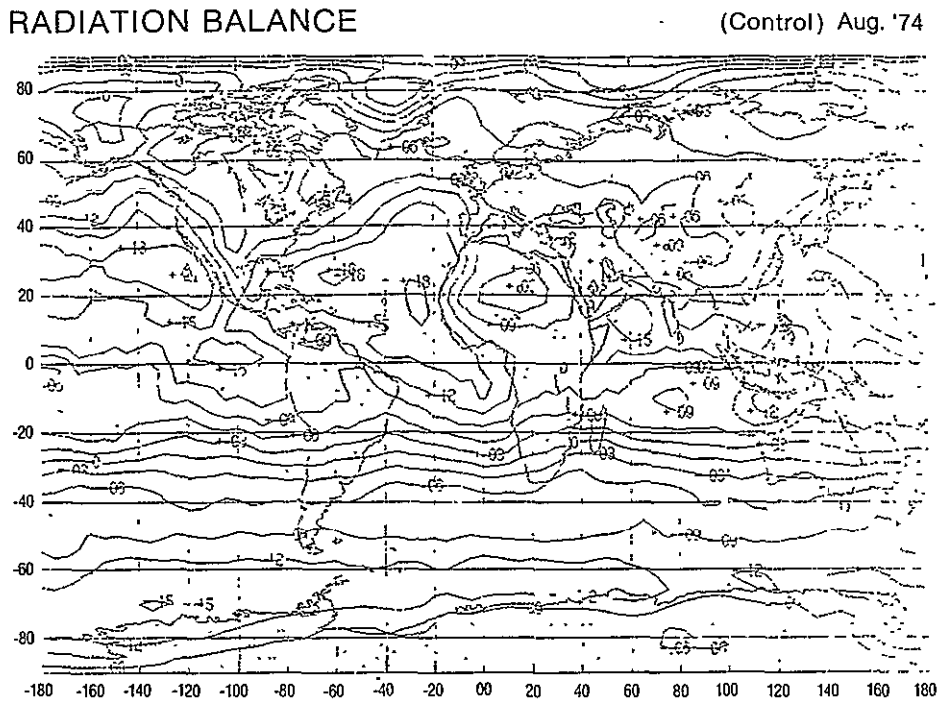

Figure 4a. Radiation balance at the top of the atmosphere in (cal cm^{-2} min^{-1}) for control.

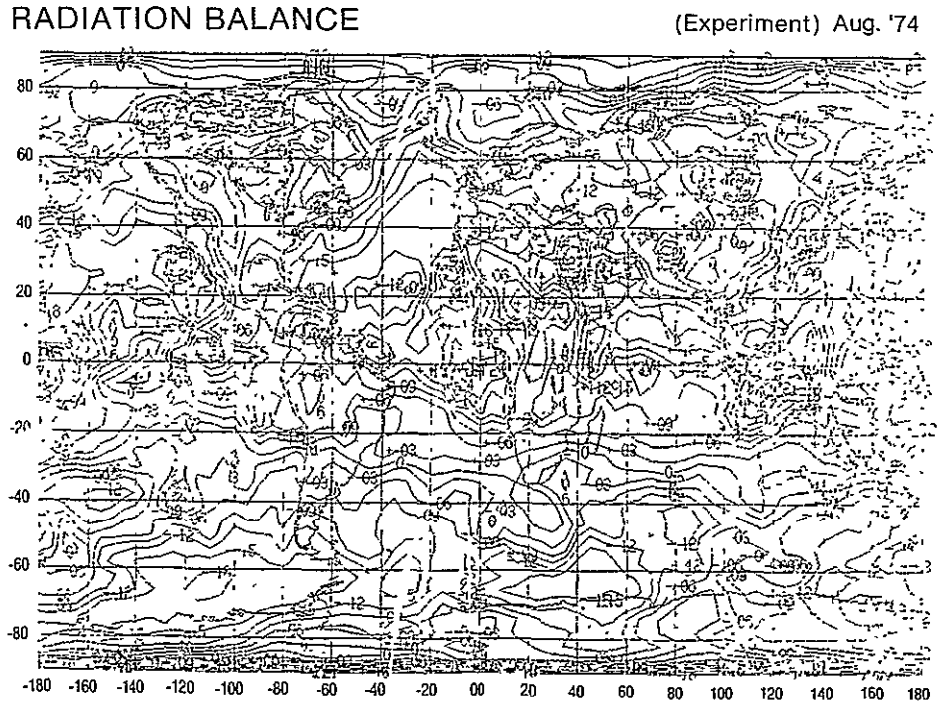

Figure 4b. Radiation balance at the top of the atmosphere in (cal cm^{-2} min^{-1}) for experiment.

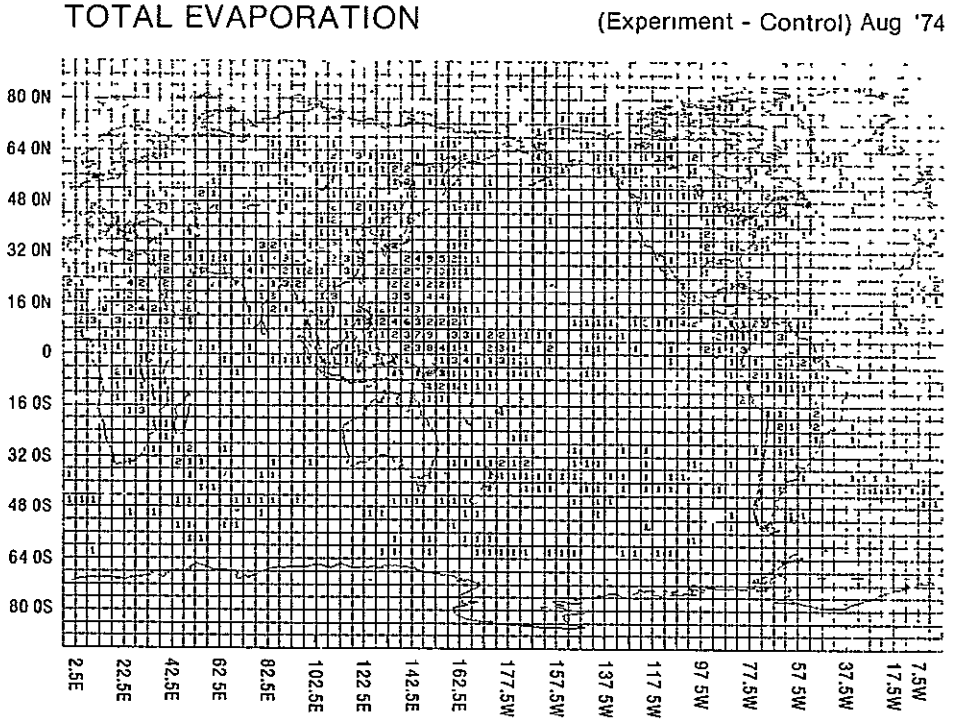

Figure 5a. Difference in the total evaporation in 0.1*mm/day. Bold print is for positive difference; light print is for negative difference.

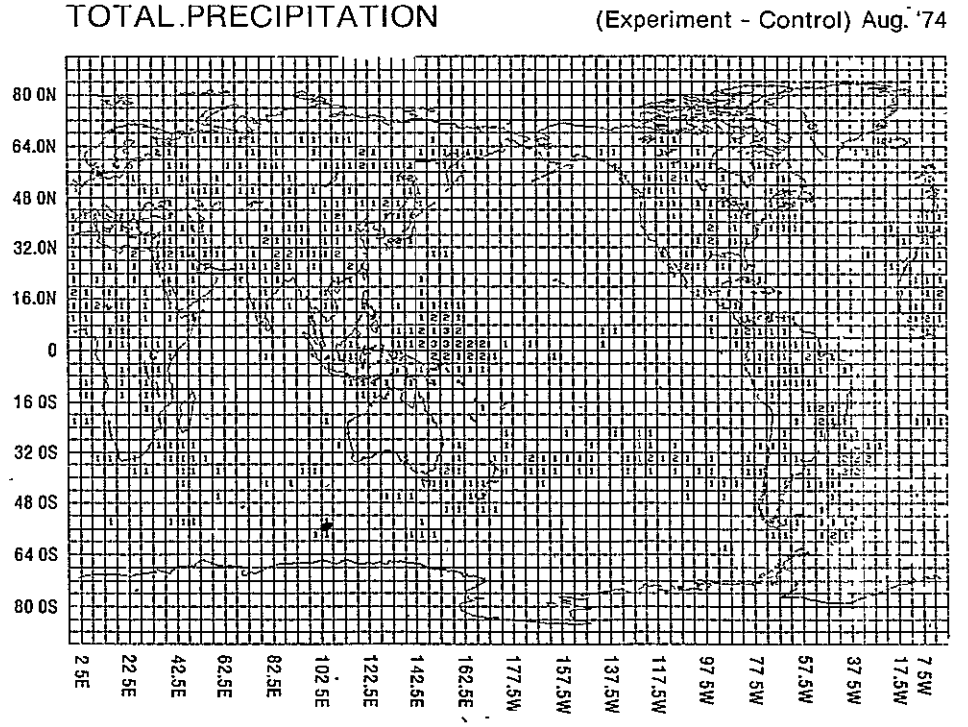

Figure 5b. Difference in the total precipitation in 0.1*mm/day. Bold print is for positive difference; light print is for negative difference.

References

Halem, M., J. Shukla, et al., 1978: Comparisons of observed seasonal climate features with a winter and summer numerical simulation produced with the GLAS general circulation model. JOC Study Conf. on Climate Models, Washington, DC, April.

Somerville, R. C. J., P. Stone, M. Halem, et al., 1974: The GISS model of the global atmosphere. J. Atmos. Sci., 31, pp. 84-117.

Stone, P., S. Chow, and J. Quirk, 1977: The July climate and a comparison of the January and July climate simulated by the GISS GCM. Mon. Wea. Rev., 105, pp. 170-194.

Wu, M. L., L. D. Kaplan, and R. Godbole, 1978: Influence of systematic radiation differences on the dynamics of a model atmosphere. Third Conf. on Atmos. Rad., Davis, CA, Amer. Meteor. Soc., June.

THE EFFECT OF CUMULUS FRICTION ON THE GLAS MODEL OF THE GENERAL CIRCULATION

(M. Helfand)

A simple scheme to parameterize the vertical mixing of horizontal momentum has been added to the GLAS model of the general circulation. The scheme is similar to those of Ooyama (1971), Arakawa and Mintz (1974), Schneider and Lindzen (1976), and Anthes (1977). The cumulus friction term can be expressed as

$$\frac{\partial}{\partial p}\{Mc(\underset{\sim}{U} - \underset{\sim}{U}c)\} ,$$

where Mc(p) is the total upward mass flux within all convective elements in the grid box at a given level, $\underset{\sim}{U}(p)$ is the vertical profile of the ambient horizontal velocity, and $\underset{\sim}{U}c(p)$ is the in-cloud profile of velocity. The latter profile is determined by the assumption,

$$\frac{\partial}{\partial p}(Mc\underset{\sim}{U}c) = \frac{\partial Mc}{\partial p}\underset{\sim}{U} ,$$

that horizontal momentum is conserved by a rising, entraining parcel of air and by taking as a boundary condition

$$\underset{\sim}{U}c(P \text{ base}) = \underset{\sim}{U}(P \text{ base}).$$

Thus, in an entrainment layer the net effect of cumulus friction,

$$\frac{\partial}{\partial p}\{Mc(\underset{\sim}{U} - \underset{\sim}{U}c)\} = \frac{Mc\partial\underset{\sim}{U}}{\partial p} ,$$

is that of the subsident advection of $\underset{\sim}{U}$ which occurs between the convective elements. At the top of the cloud there is a detrainment layer, Δp, where the net cumulus drag is

$$\frac{1}{\Delta p}\int_{p\ \text{bottom}}^{p\ \text{top}} \frac{\partial}{\partial p}\{Mc(\underset{\sim}{U} - \underset{\sim}{U}c)\}dp = \frac{1}{\Delta p}\{Mc(\underset{\sim}{U}c - \underset{\sim}{U})\}_{p\ \text{bottom}}$$

When cumulus friction was added to the GLAS model, it had little effect in the tropical circulation. When it was added to the model in conjunction with an expanded cloud spectrum that included deep, "hot tower" convective clouds, the effect was more dramatic. The January winter Hadley circulation accelerated by 14 percent (compare Figures 1 and 2), the vertical profile of the mean meridional wind field became smoother (compare Figures 3 and 4) and the mean zonal shear of the tropics decreased (Figure 5). The Hadley cell strengthening due to cumulus friction is comparable in

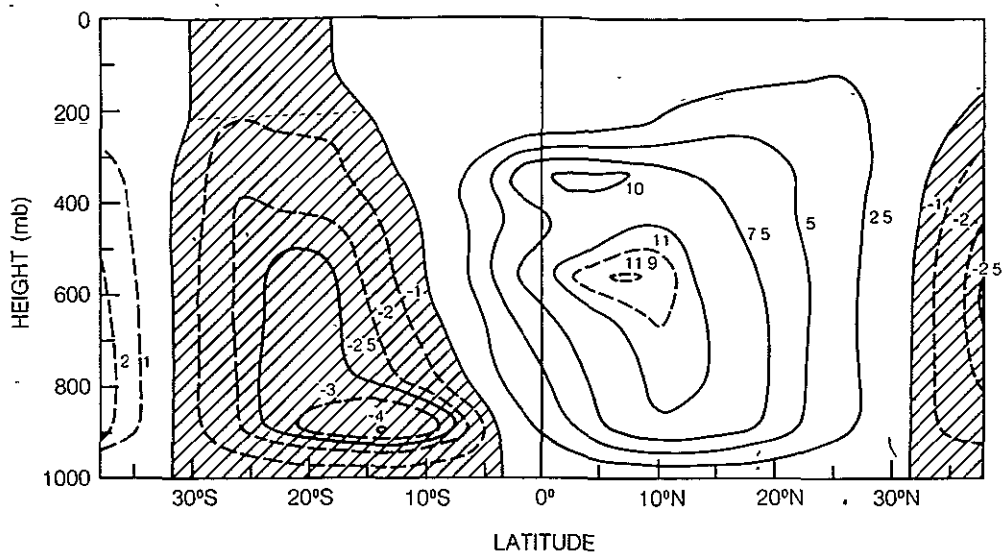

Figure 1. The January mean meridional stream function (x 10^{13} gm sec^{-1}) as simulated in the control. Negative regions are shaded.

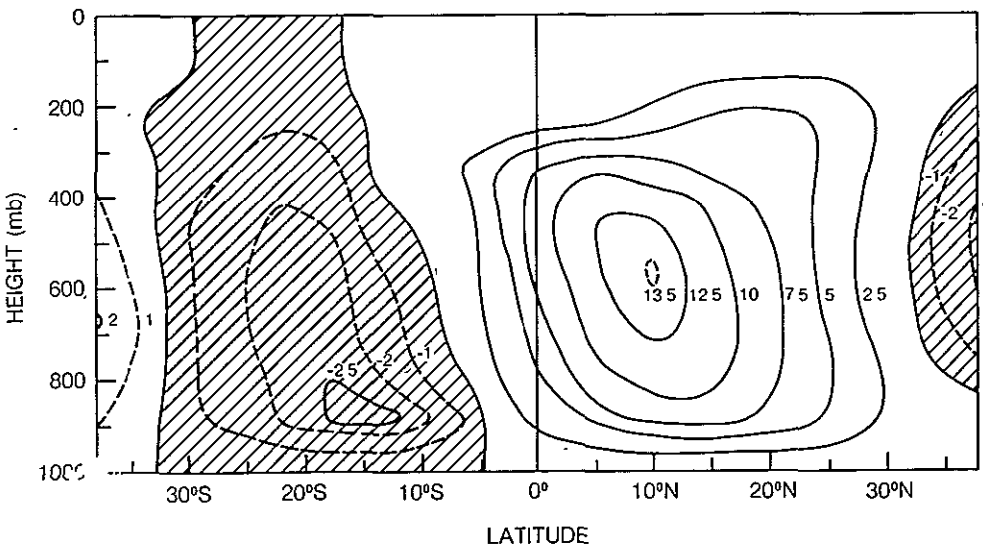

Figure 2. The January zonal mean meridional wind field (m sec^{01}) as simulated in the control. Negative (northerly) regions are shaded.

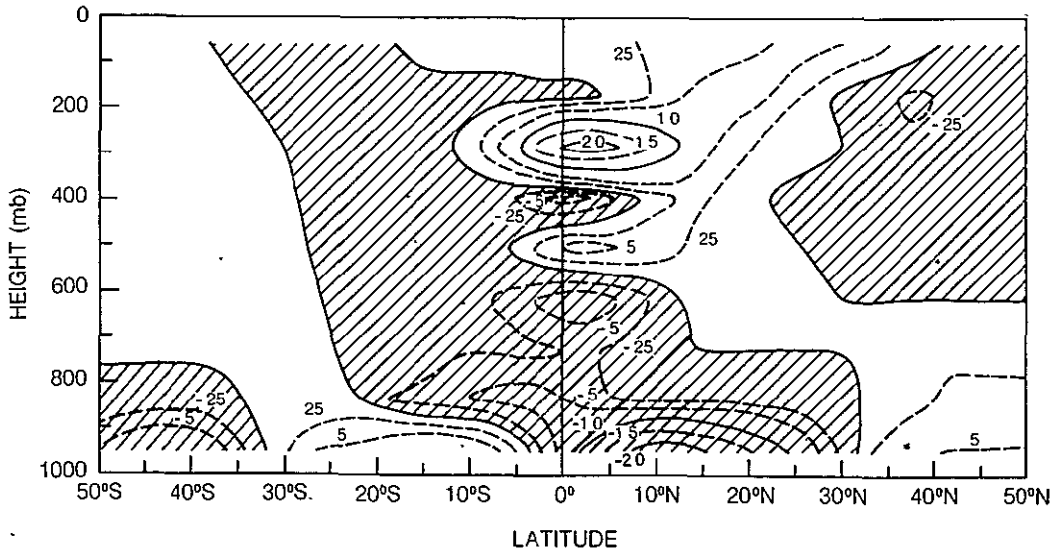

igure 3. The January mean meridional stream function (x 10^{13} gm sec^{-1}) as simulated in the experiment. Negative regions are shaded.

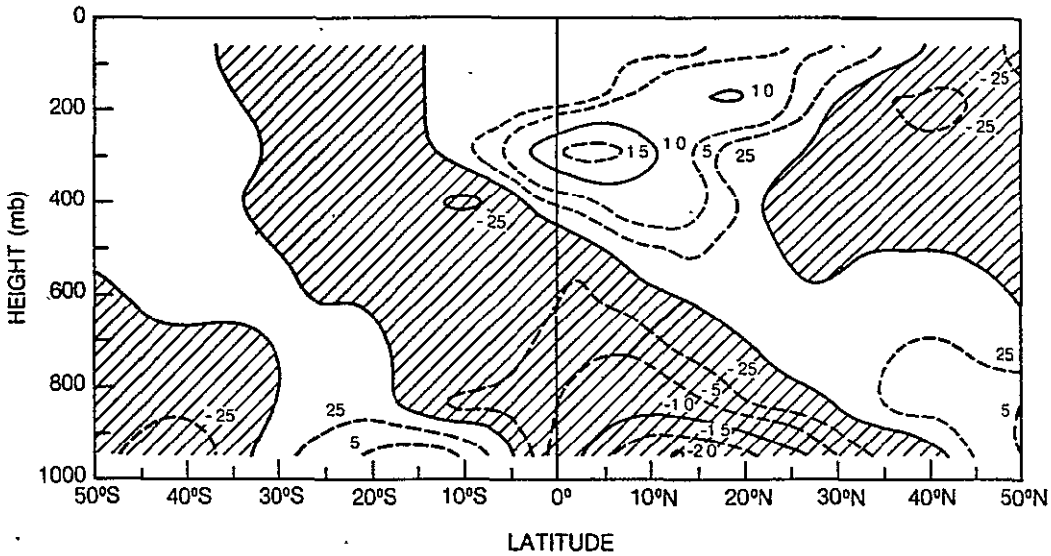

Figure 4. The January zonal mean meridional wind field (m sec^{-1}) as simulated in the experiment. Negative (northerly) regions are shaded.

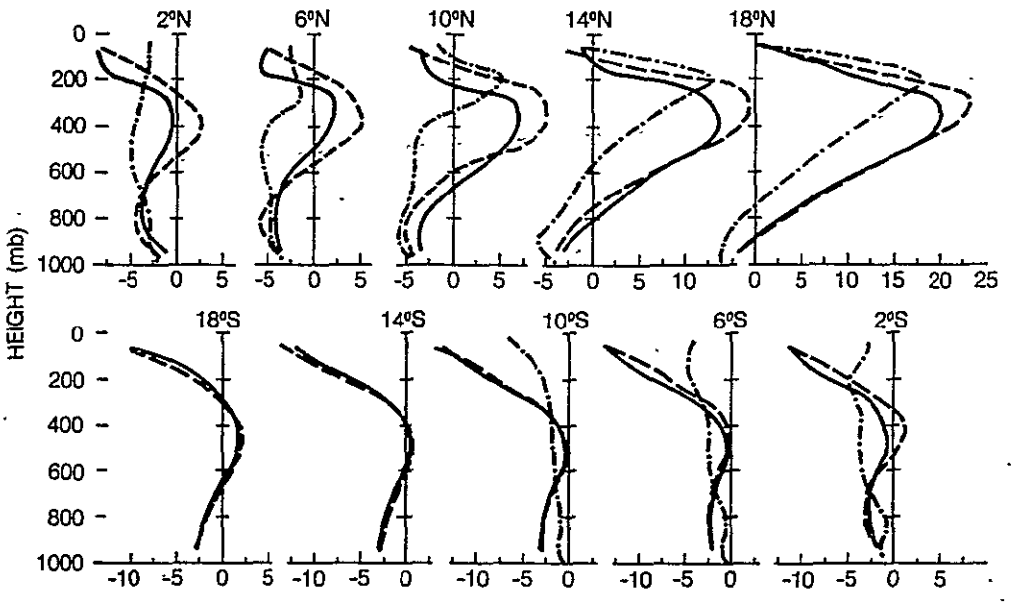

Figure 5. The January zonal mean profile of the zonal wind (m sec^{-1}) as simulated in the experiment (solid line) and control (dashed line) and as observed by Oort and Rasmusson (1971) (dot-dashed line).

magnitude to the estimate given by Schneider and Lindzen (1977) and Schneider (1977) on the basis of an axisymmetric, steady-state model. Stone, et al., (1974) also found a Hadley cell strengthening when they added a universal term for the vertical mixing of horizontal momentum to the GISS model, but they found that eddy kinetic energy in the middle latitudes was seriously damped. In the present experiment, cumulus friction actually caused a slight increase in eddy kinetic energy due to the development of a tighter meridional temperature gradient in the subtropical region.

The strengthening of the Hadley circulation can be explained in terms of the atmosphere's angular momentum budget. Cumulus friction, through the subsidence and detrainment terms, carries relative angular momentum downshear from the poleward to the equatorward branch of the Hadley cell. The response to this imbalance is an enhanced Hadley gyre which now carries additional planetary angular momentum northward into the poleward branch and removes an additional amount of planetary angular momentum from the equatorward branch to the south. These results imply that the Hadley circulation is regulated by the atmosphere's angular momentum budget. The mean poleward temperature gradient, therefore, drives the Hadley circulation via the thermal wind relation.

References

Anthes, R. A., 1977: A cumulus parameterization scheme utilizing a one-dimensional cloud model. Mon. Wea. Rev., 105, pp. 270-286.

Arakawa, A., and Y. Mintz, 1974: The UCLA atmospheric general circulation model. Notes distributed at the workshop on March 25-April 4, 1974, Dept. of Meteor., University of Calif., Los Angeles.

Oort, A. H., and E. R. Rasmusson, 1971: Atmospheric circulation statistics. NOAA Prof. Paper 5.

Ooyama, K., 1971: A theory on parameterization of cumulus convection. J. Meteor. Soc. Japan, 49, pp. 744-756.

Schneider, E. K., 1977: Axially symmetric steady-state models of the basic state for instability and climate studies: Part II. nonlinear calculations. J. Atmos. Sci., 34, pp. 280-296.

_____, and R. S. Lindzen, 1976: A discussion of the parameterization of momentum exchange by cumulus convection. J. Geophys. Res., 81, pp. 3158-3160.

References (continued)

_____, and _____, 1977: Axially symmetric steady-state models of the basic state fo instability and climate studies. Part I. linearized calculations. J. Atmos. Sci., 34, pp. 263-279.

Stone, P. H., W. J. Quirk, and R. C. J. Somerville, 1974: The effect of small-scale vertical mixing of horizontal momentum in a general circulation model. Mon. Wea. Rev., 102, pp. 765-771.

REGIONAL COMPARISONS FOR WINTER AND SUMMER WITH THE GLAS GCM

(M. Halem, J. Shukla, Y. Mintz, M. L. Wu, R. Godbole, G. Herman, and Y. Sud)

Integrations were carried out for Northern Hemisphere winter and summer seasons using the GLAS general circulation model (GCM). Each integration was initialized from a real global analysis provided by the National Meteorological Center (NMC).

Initial conditions for the winter simulation were valid for 00Z January 1, 1975; the initial conditions for the summer simulation were valid for 00Z May 15, 1974. The data for the analyses were collected during the early Data Systems Tests (DST) conducted by NASA and made available to the Goddard Modeling and Simulation Facility by the Development Division of NMC.

In the winter simulation, the Facility used the Posey and Clapp (1964) regional distributions of surface albedo and snow and ice cover. In the summer simulation, only three values of surface albedo (oceans [.07], vegetated land [.14], and deserts [.35]) were used in place of the Posey and Clapp data.

The winter integration was carried forward for 60 days and the summer integration for 108 days. The simulated atmospheric state variables and diabatic processes were stored at 5-hour intervals to sample the evolving fields at every hour of the day (once every 5 days). The simulated seasonal climates described below are based on averages, sampled with the 5-hour frequency, over the last 30 days of each integration, namely February and August.

Sea Level Pressure. Figures 1a and 1b show the observed and simulated sea level pressure fields for February; Figures 2a and 2b show the respective fields for August. The observed fields are from Crutcher and Davis (1969) and are based on 100 years of observations.

February. The Aleutian and Icelandic lows and the oceanic highs in the Northern and Southern Hemispheres are in good agreement with the observations. The position and depth of the Aleutian low is particularly good, as is the two-cell structure of the Icelandic low, although these are features which in nature show appreciable variations from year to year. The major shortcomings in the sea level pressure simulation are the excessively high pressure over the Arctic basin, the relatively weak and somewhat displaced Siberian high, and the failure to get the belt of closely spaced isobars between 40S and 60S.

August. The features which are in good agreement are the highs over the subtropical oceans (which have hitherto been the most difficult feature to simulate in the Northern Hemisphere summer), the South Asia low and its extension across North Africa, and the low over the western U. S. The major shortcomings of the

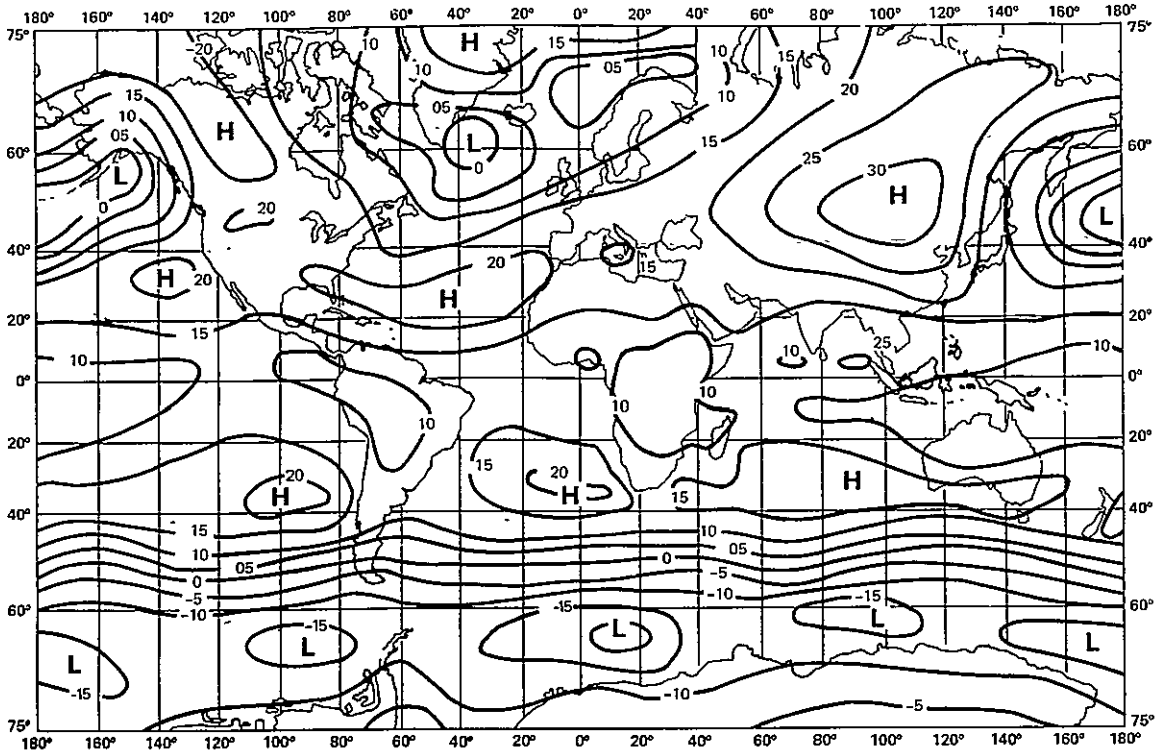

Figure 1a. Observed sea level pressure (mb) for February, after Crutcher and Davis (1969).

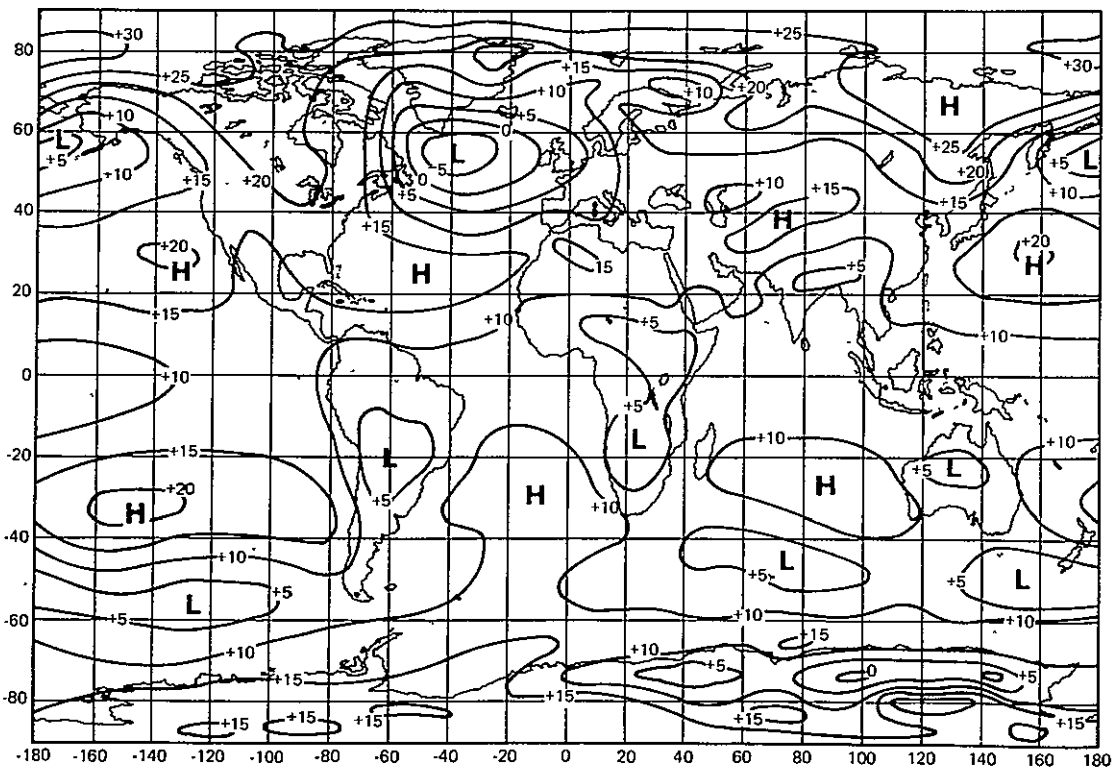

Figure 1b. Simulated sea level pressure distribution (mb - 1000) for February.

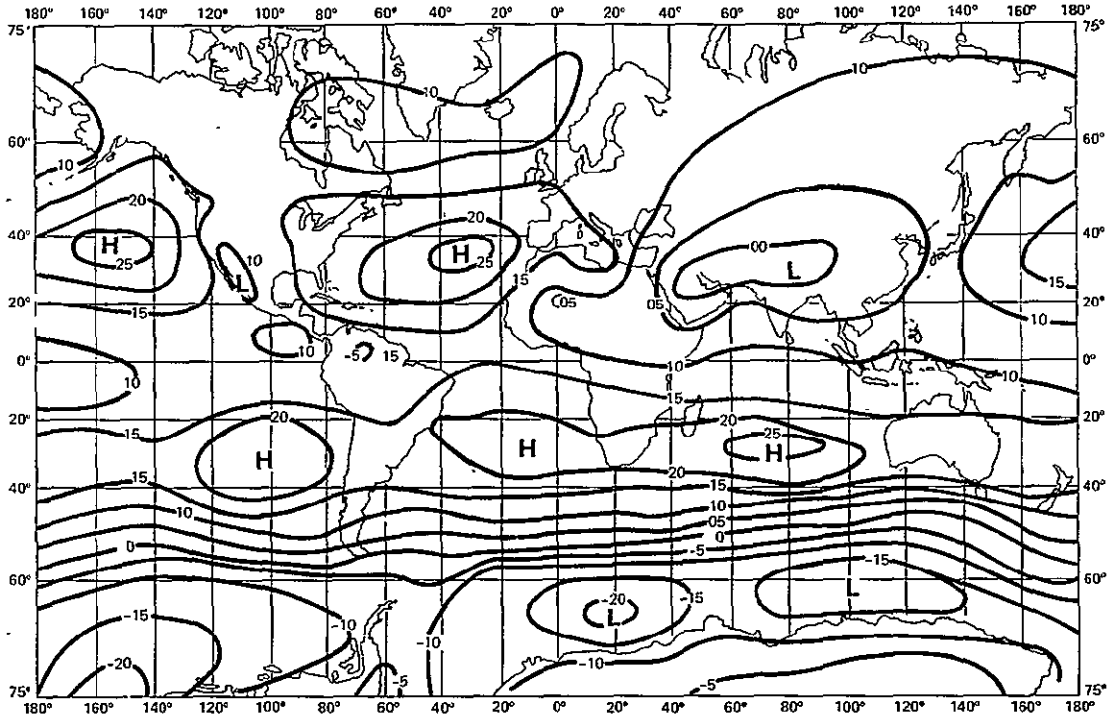

Figure 2a. Observed sea level pressure (mb) for August, after Crutcher and Davis (1969).

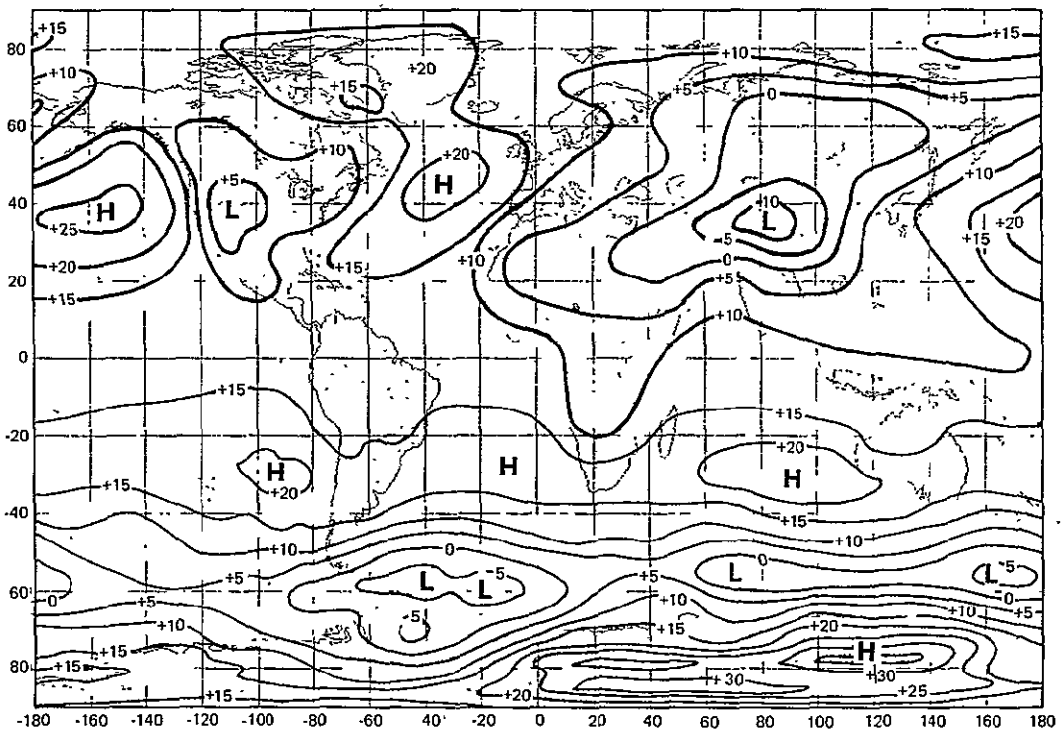

Figure 2b. Simulated sea level pressure (mb - 1000) for August.

simulation are that the Asian low is too deep and centered somewhat too far east, and the pressure is too high over Antarctica.

Geopotential Heights. Figures 3a and 3b show the observed and simulated geopotential heights of the 200 mb pressure surface for February; Figures 4a and 4b show the respective fields for August. The observed fields are taken from Crutcher and Davis (1969).

February. The features which are reasonably well simulated are the ridge and trough located over the western and eastern coasts of North America, the ridge over the eastern Atlantic, and the strong Southern Hemisphere zonal flow. The major defect is the failure to get the tight packing of the height contours over Japan, which corresponds to the subtropical jet stream in that region.

August. The features which are reasonably well simulated are the Tibetan high and its westward extension over North Africa, the ridge over Mexico, and the strong Southern Hemisphere zonal flow. The major ddficiency is that the observed ridge over the Gulf of Alaska is displaced to the center of North America.

Surface winds. Figures 5a and 6a show the direction of the mean surface observed wind for January and July; Figures 5b and 6b show the corresponding simulated fields for February and August. The observed fields are from Mintz and Dean (1952). These direct analyses of the surface wind field, as well as their upper level counterparts, reveal the structure of the atmospheric circulation in the low latitudes much more clearly than can be inferred from the sea level and upper pressure fields.

February. There is a good correspondence between the location of the intertropical convergence zone (ITCZ) in the simulated and observed surface wind fields. Particularly striking is the similar way in which the ITCZ varies its position with longitude: in each case having its main discrepancy in the ITCZ location is over the eastern part of the Pacific and over the Indian Ocean where the simulated ITCZ lies along the equator, whereas the observed ITCZ is at about 7°N latitude over the eastern Pacific and between 5° and 20°S latitude over the Indian Ocean. The flow of the surface air from the northeast and the southeast toward the ITCZ (the "trade winds") is also well simulated.

The centers and the asymptotes of anticyclonic outflow in the subtropical latitudes, which are the origins of the trade winds, are in good general agreement, especially in the Southern (summer) Hemisphere, and the simulated and the observed outflow centers disagree to the extent that the simulated and observed surface pressure fields (Figures 1a, 1b) disagree. Thus, the simulation shows a separate high pressure center and a separate

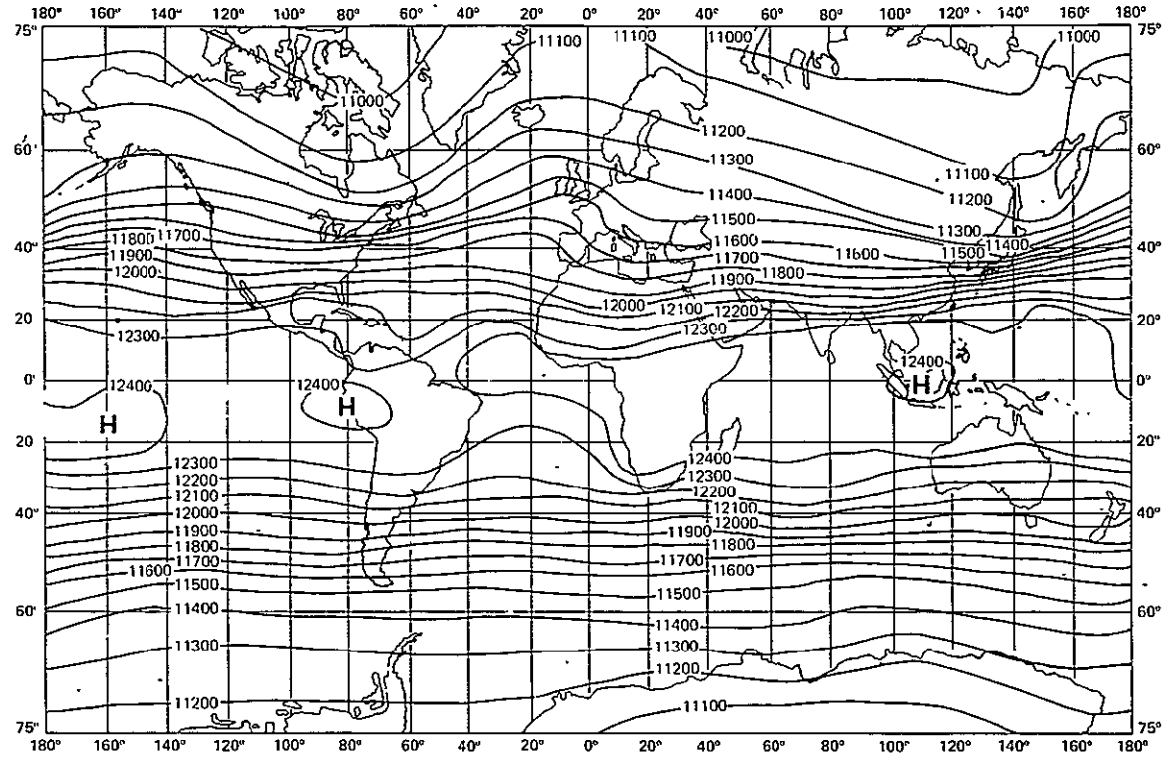

Figure 3a. Observed 200 mb geopotential height (m) for December, January, and February, after Crutcher and Davis (1969).

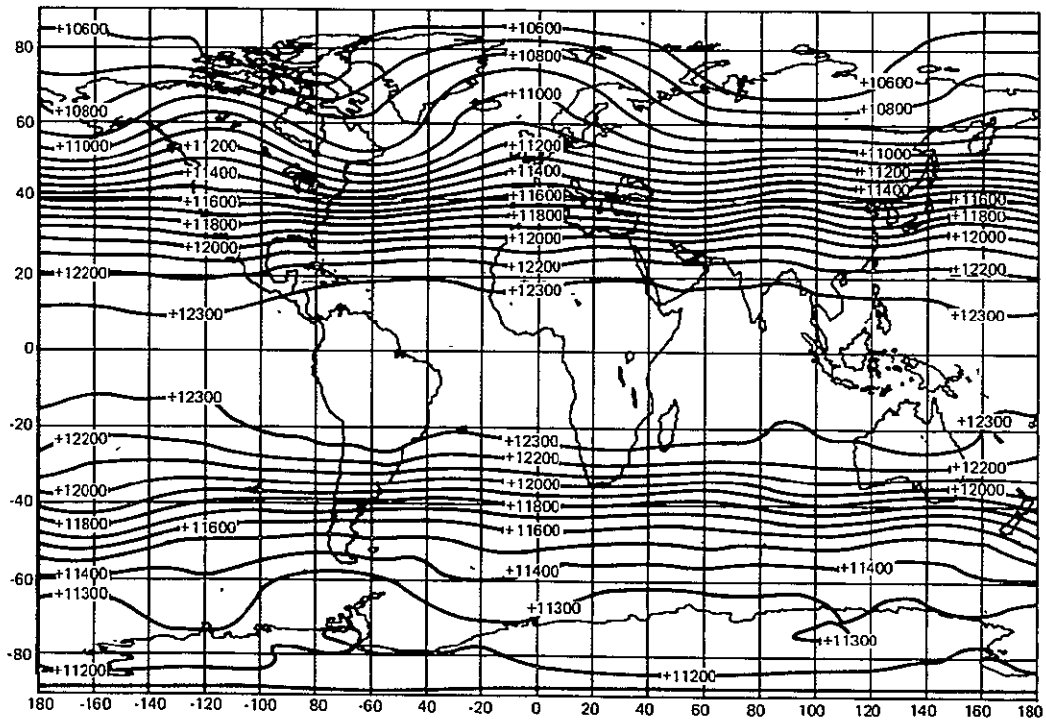

Figure 3b. Simulated 200 mb geopotential height (m) for February.

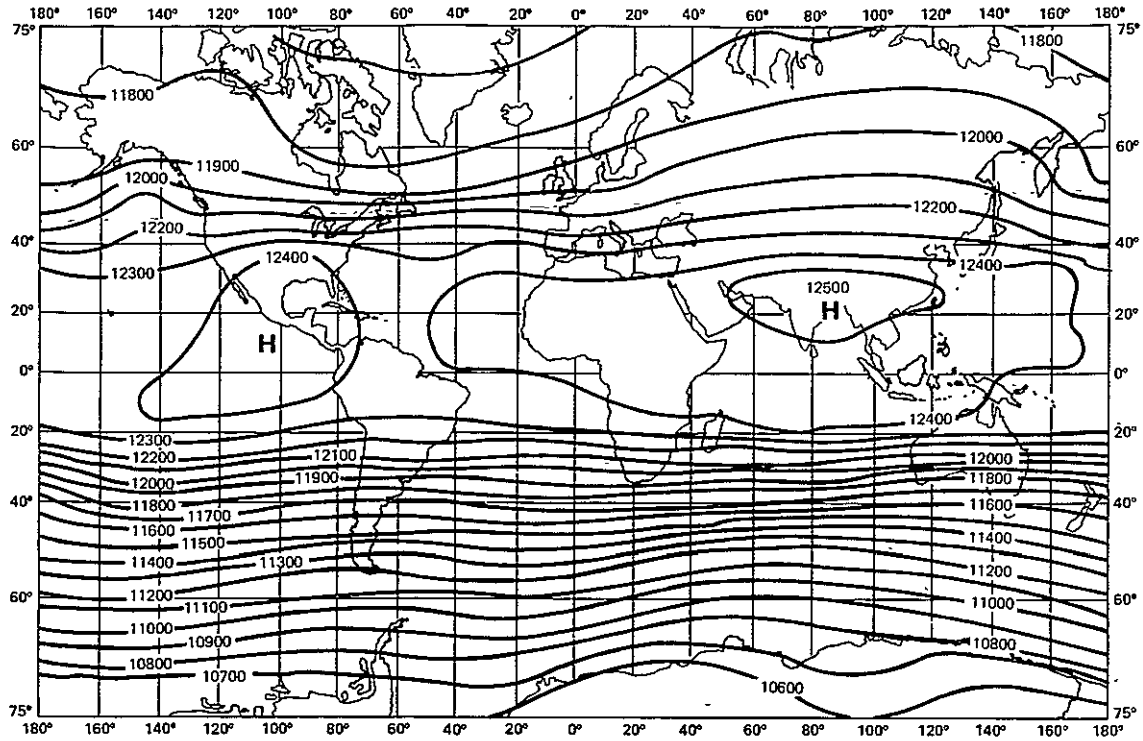

Figure 4a. Observed 200 mb geopotential height (m) for June, July, and August, after Crutcher and Davis (1969).

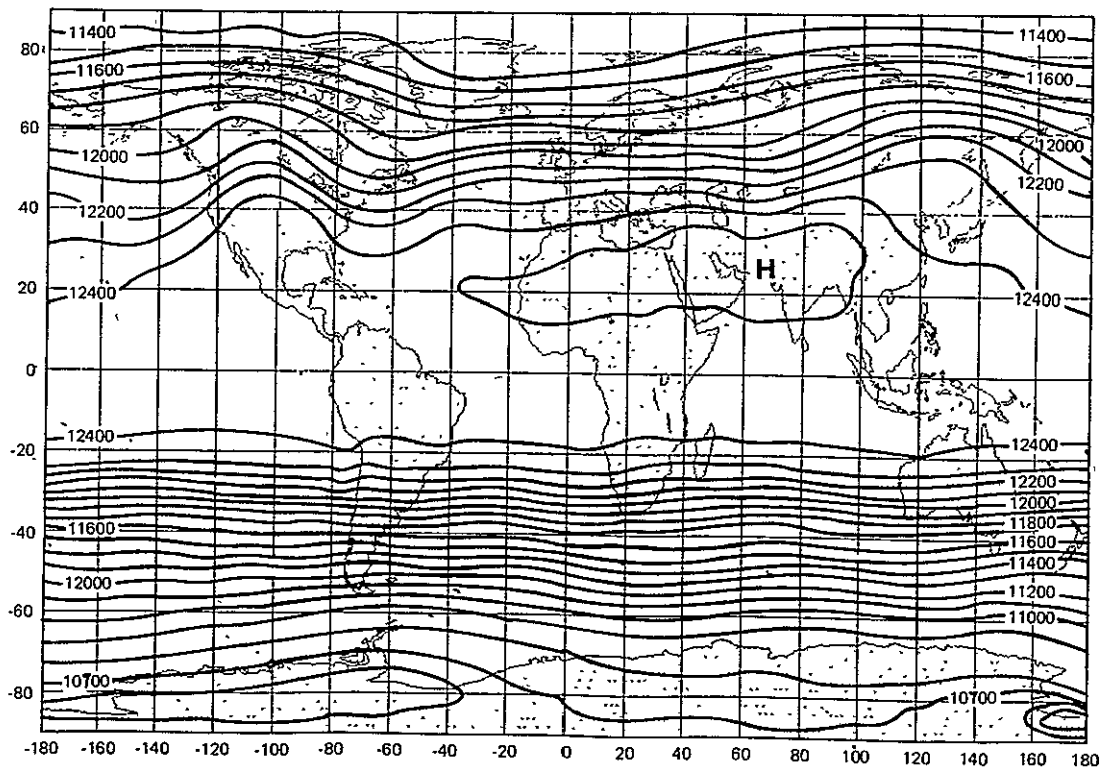

Figure 4b. Simulated 200 mb geopotential height (m) for August.

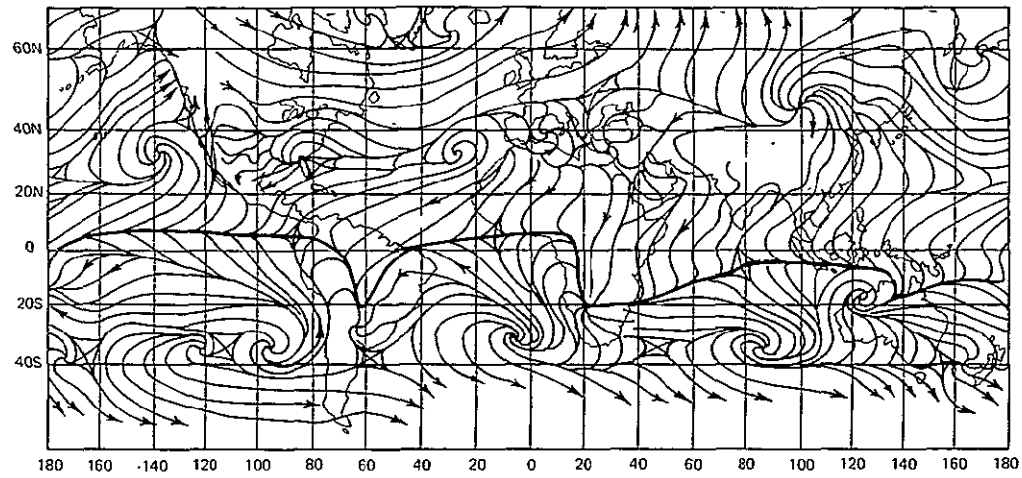

Figure 5a. Direction of the observed wind at the earth's surface for January, after Mintz and Dean (1952).

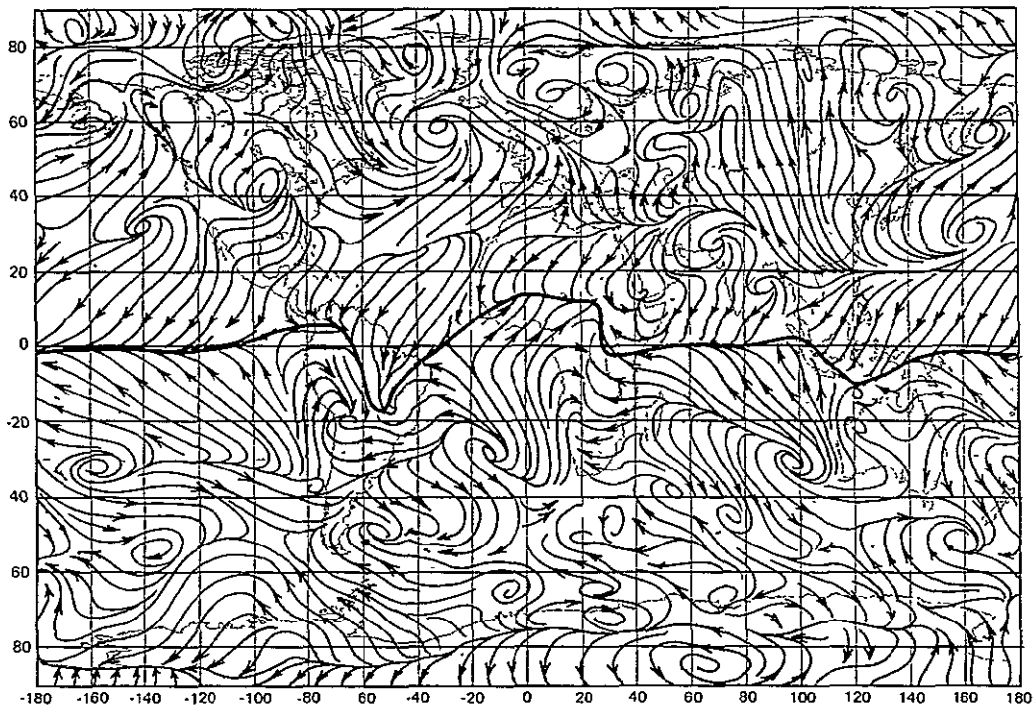

Figure 5b. Direction of the simulated wind at the earth's surface for February.

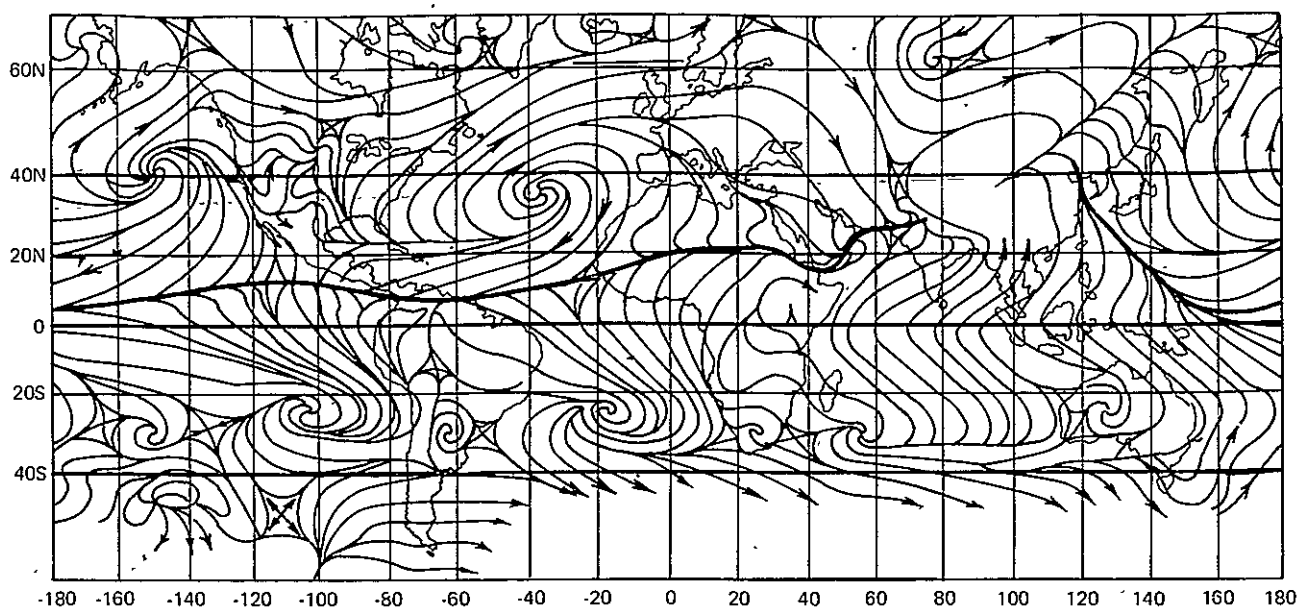

Figure 6a. Direction of the observed wind at the earth's surface for July, after Mintz and Dean (1952).

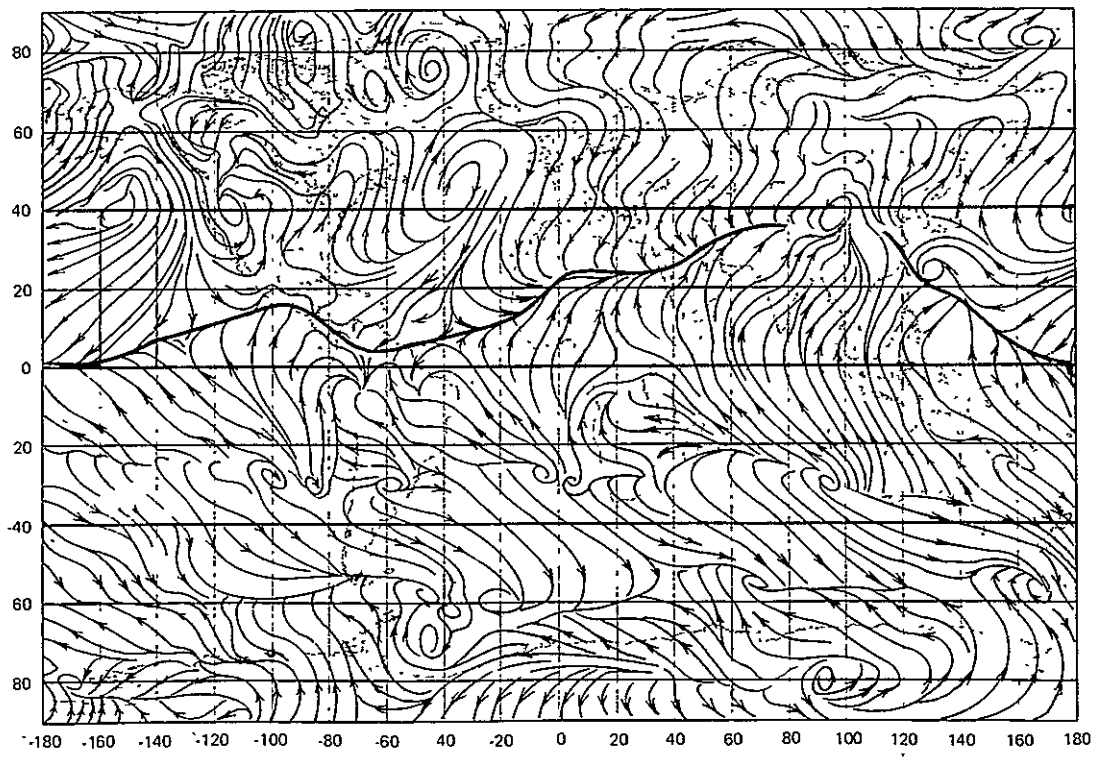

Figure 6b. Direction of the simulated wind at the earth's surface for August.

center of anticyclonic outflow in the western north Pacific, which the long-period averaged observed pressure and wind fields do not show, but such a double-cell structure is observed in the north Pacific in some individual years.

August. The change in the location of the ITCZ from February to August is very much alike in the observed and simulated surface wind fields. Particularly striking is the change over South America, central and east Africa, the Indian Ocean, south Asia, and the western Pacific. Again, it is the simulated summer hemisphere (now the Northern Hemisphere) in which the subtropical anticyclonic outflow is most clearly defined. Over the north Indian Ocean the surface winds have correctly changed from northeasterly to a southwesterly direction.

Radiation Balance of the Earth-Atmosphere System. Global satellite observations of the geographical distribution of the radiation balance of the earth-atmosphere system are available for selected time intervals for a 10-year period. Such data can be used as diagnostic measures of the GCM's ability to simulate the prognostic variables that affect the radiation balance, namely, temperature, cloudiness, vapor distribution, and surface reflectivity.

Table 1 describes the radiative properties of the clouds in the GLAS model. The short wave radiation parameterization recognized eight types of model clouds to which it assigns the indicated optical properties shown in Table 1. The long wave radiation parameterization treats all of the clouds as "black."

Figures 7a and 8a show the net radiation balance derived from Nimbus-3 satellite observations for the last 2 weeks in July 1969; Figures 7b and 8b show the simulated radiation balances for February and August to be consistent with our other charts. (The solar declination angle changes by 8° in the second half of January and 10° in February.)

February. The geographical distribution of the net monthly radiation balance that the model simulates reasonably well are the centers of maximum heating over the oceans in the low latitudes of the Southern Hemisphere and the relative minima over southern Africa. A major difference, however, is the position of the line of zero heating, which in the simulation is about 5° to 10° too far north.

August. The model simulates the northward shift of the lines of zero heating and the latitude of maximum heating. Especially noteworthy is the fact that the model produces a minimum in the summertime radiational heating over north Africa. This causes the Laplacian of heating in the horizontal direction and its effect on the horizontal circulation, identical to the observed field. This holds even though the sign of the heating at the center of that region is not the same as in the observations. Also well simulated by the model is the minimum of the radiational heating

Table 1. Radiative Properties of Clouds in the GLAS Model.

Cloud Type	Layers[1]	Analogy	Optical Thickness	Albedo
Supersaturation	2	Ci	1	.12
Supersaturation	3	Ci	2	.21
Supersaturation	4	As	4	.34
Supersaturation	5 or 6	As	6	.44
Supersaturation	7 or 8 or 9	St	8	.51
Penetrating Convection	4-7 or 5-8 or 6-9	Cb	32	.81
Mid-Level Convection	5 or 6	Ac	8	.51
Low-Level Convection	7 or 8	Cu	16	.68

NOTE: For long wave heating rates, all clouds are "black."

(1) Layers are ~110 mb thick, and layer one corresponds to interval between 10 mb and 120 mb.

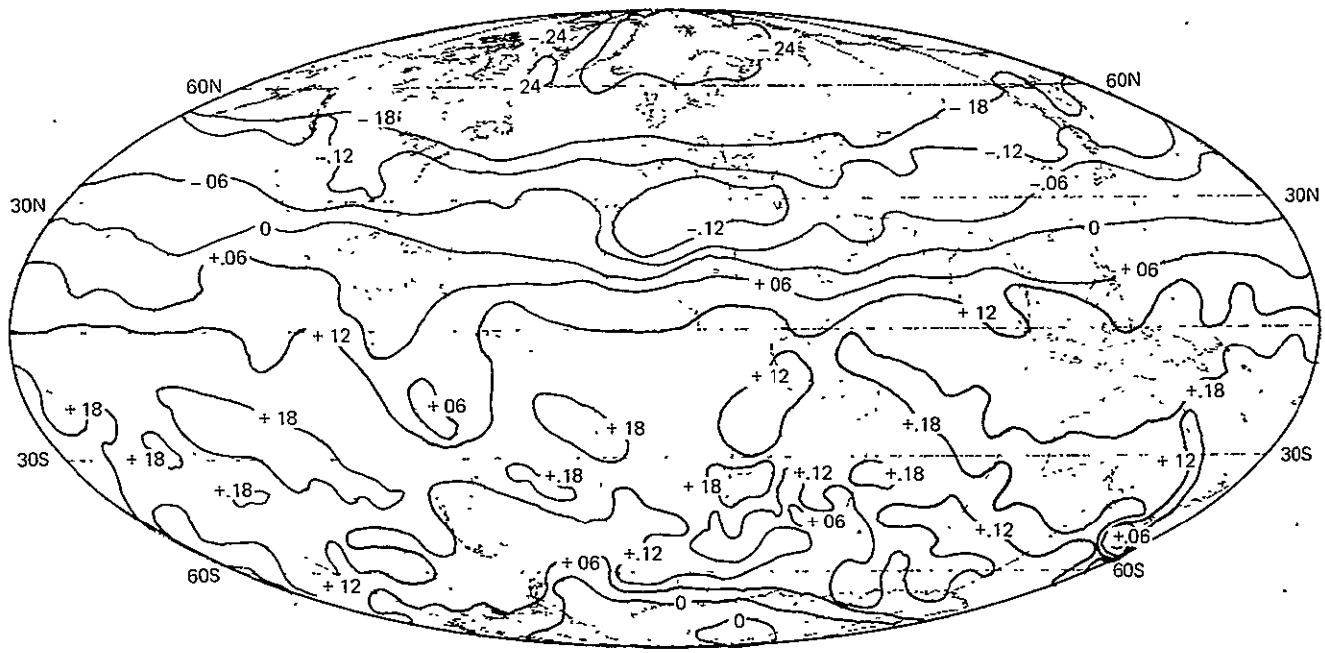

Figure 7a. Observed radiation balance (cal cm^{-2} min^{-1}) of the earth-atmosphere system during the period January 21 to February 3, 1970, after Raschke, et al. (1973).

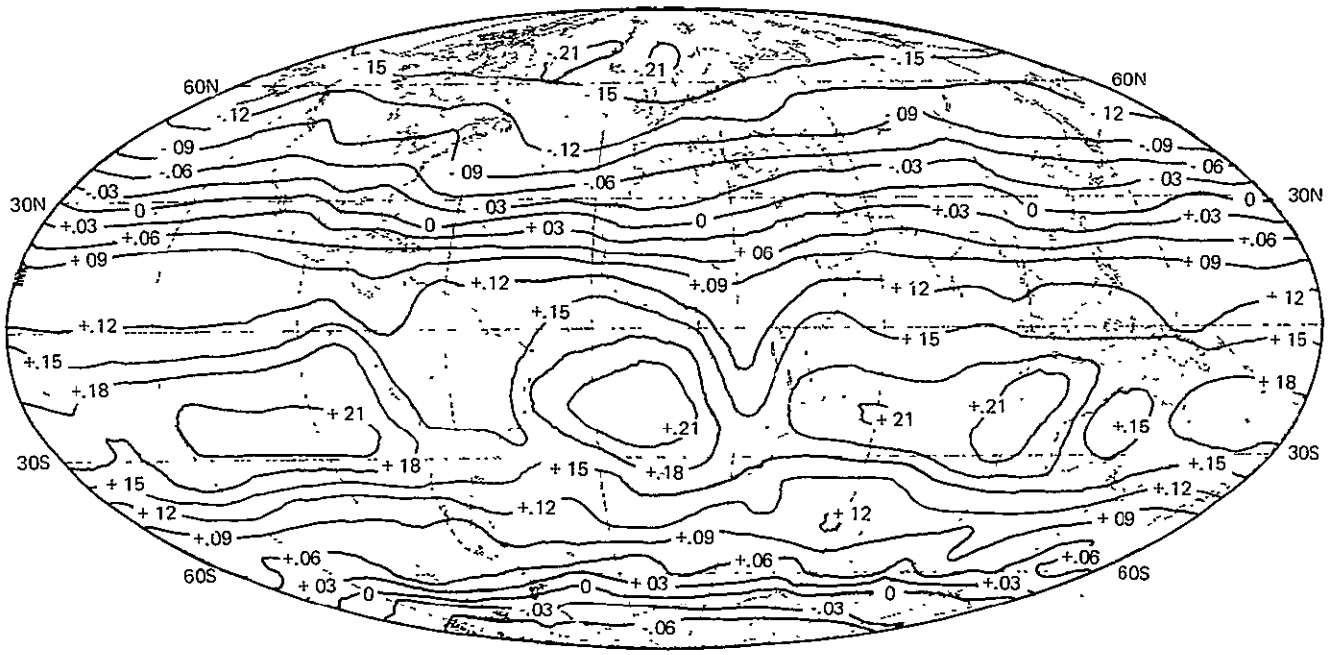

Figure 7b. Simulated radiation balance (cal cm^{-2} min^{-1}) of the earth-atmosphere system for February.

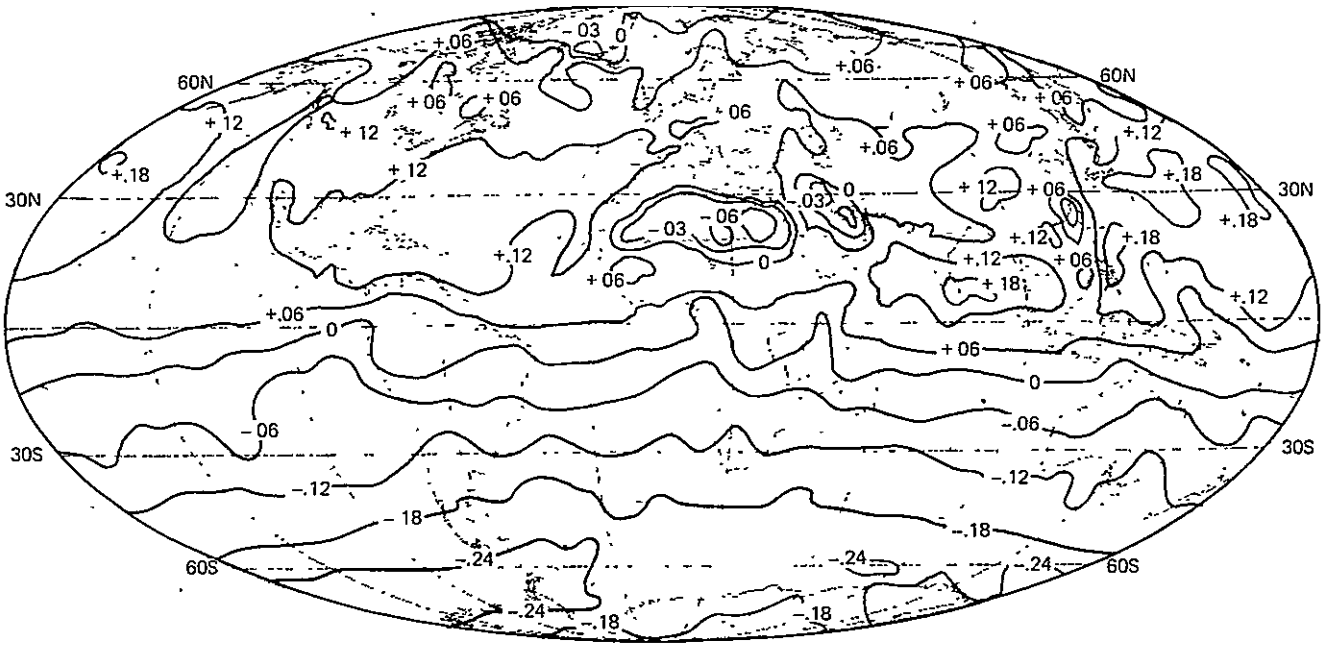

Figure 8a. Observed radiation balance (cal cm^{-2} min^{-1}) of the earth-atmosphere system during the period July 16 to 31, 1969, after Raschke, et al. (1973).

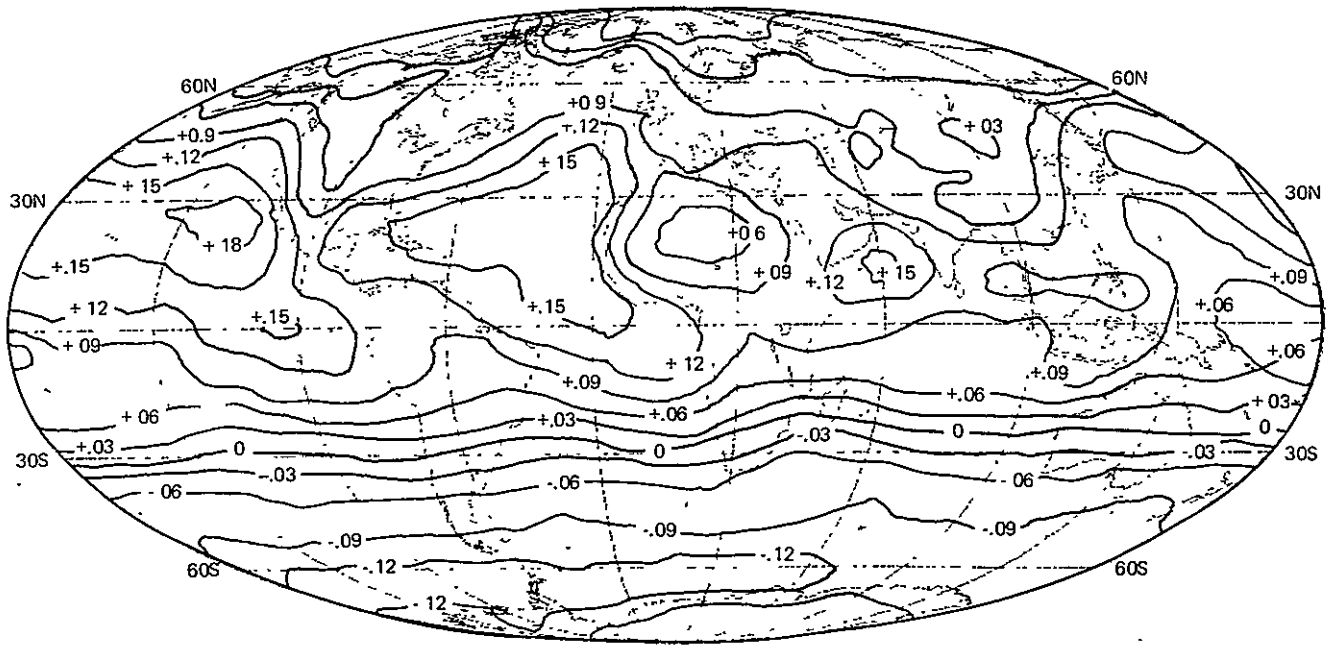

Figure 8b. Simulated radiation balance (cal cm^{-2} min^{-1}) of the earth-atmosphere system for August.

over northwestern North America. The model does not reproduce the observed heating minimum off the west coast of North America. This may be due to the fact that the model does not simulate the planetary boundary layer stratus clouds.

Global Radiation Budget. Table 2 compares the observed and simulated globally-averaged net radiation balance and its separate components for February and August and also shows the respective mean monthly planetary albedos. The observed fields are from Raschke, et al., (1973). It can be seen that the simulated albedo is about 10 percent higher than the observed. The incoming solar radiation differences are small and are probably mainly the result of using a solar constant of 1.95 cal $cm^{-2}min^{-1}$ for the model simulation.

The simulated absorbed solar radiation shown in Table 2 is in close agreement with observation, accounting for the good agreement in the planetary albedo. Table 2 shows that the simulated outgoing long wave radiation is about 12 percent less in winter and 17 percent less in summer than observed. As a result, the net radiation balance is higher in the simulation by .037 cal $cm^{-2}min^{-1}$ in winter and .055 in summer. Several reasons may be responsible for this. First, clouds are assumed to be uniformly black to long wave radiation over the entire grid area (400 x 400 km and 100 mb) regardless of the type of clouds. Second, the model generates excessive high-level cloud cover in the equatorial regions, contributing not only to a higher albedo but also lowering the outgoing long wave radiation; the outgoing long wave radiation responds more strongly to an overestimate of high-level clouds than does the short wave radiation.

Although the net radiation balance is positive in both seasons, the global mean temperatures of the simulation are constant to within 0.2 percent. From Table 3, it is seen that the net imbalance at the surface of the earth-atmosphere system is comparable with the imbalance of radiation at the top of the atmosphere as shown in Table 2. The storage in the atmosphere and over land is negligible in both seasons (not shown in Table 3). This implies that the oceans with their prescribed temperatures, and melting of permanent sea-ice, can act as a sink in the model to absorb the excess radiation balance calculated at the top of the atmosphere.

Global Precipitation. Observations of the geographical distribution of rainfall over the oceans were recently acquired from the microwave instrument, Electrically Scanning Microwave Radiometer (ESMR), on the Nimbus-5 satellite. A rainfall atlas derived from these data has been prepared by Rao, et al. (1976) with 4°x5° resolution. Figures 9a and 9b show the observed and model-simulated fields of rainfall for February; Figures 10a and 10b show the respective fields for August.

February. The general features of the monthly mean rainfall over the oceans are well simulated by the model. The

Table 2. Global Radiation Budget of the Earth-Atmosphere System (cal cm^{-2} min^{-1}).

	Solar Radiation		Albedo	Long Wave Radiation Outgoing	Net Radiation Balance
	Incoming	Absorbed			
Observed (Jan. 21 - Feb. 3, 1970)	.501	.361	.283	.337	.024
Simulated (Feb.)	.513	.356	.305	.295	.061
Observed (Jul. 16 - 31, 1969)	.472	.339	.281	.354	-.015
Simulated (Aug.)	.488	.334	.315	.294	.040

Table 3. Heat Balance at the Surface of the Earth (cal cm^{-2} min^{-1}).

	Net Flux Incoming Solar Radiation	Net Flux Upward Long Wave Radiation	Net Flux Upward Sensible Heat Flux	Net Atmospheric Heating by Condensation(1)	Net Surface Balance
February	.278	.078	.040	.101	.059
August	.251	.073	.048	.094	.036

(1) This is approximated by net evaporation.

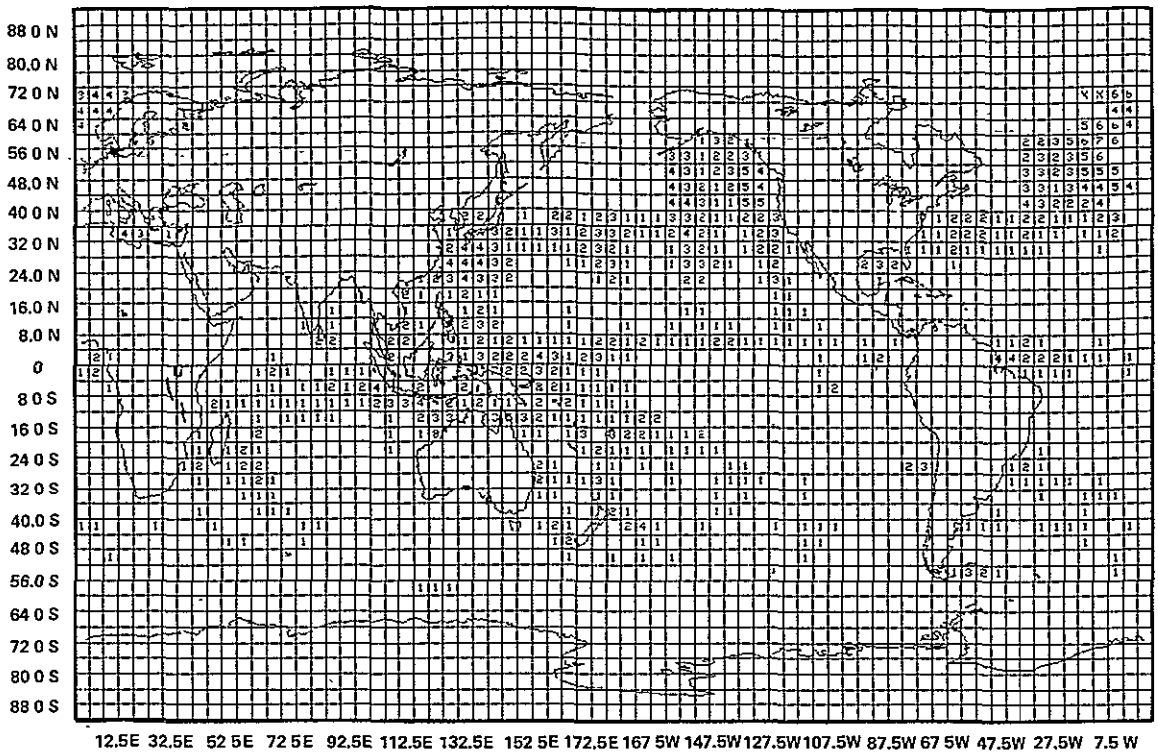

Figure 9a. ESMR-derived oceanic rainfall rate (.1 mm/hr) for February 1975, after Rao, et al. (1976).

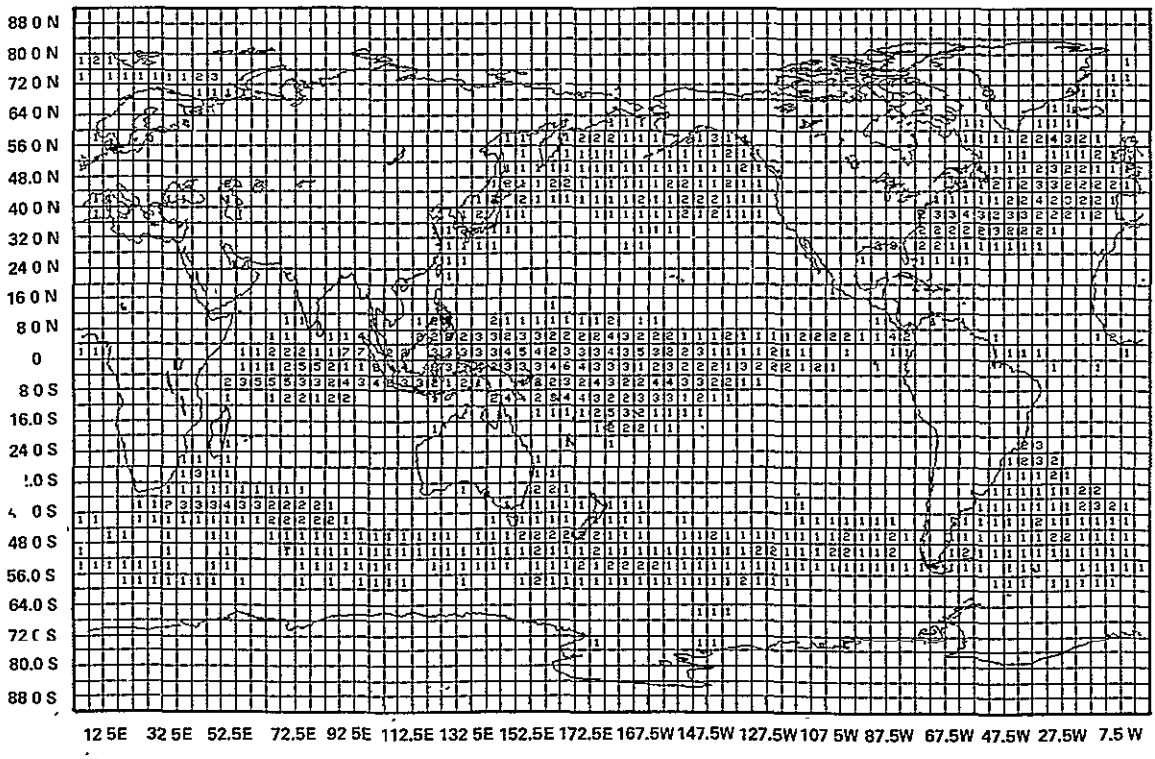

Figure 9b. Simulated oceanic rainfall rate (.1 mm/hr) for February.

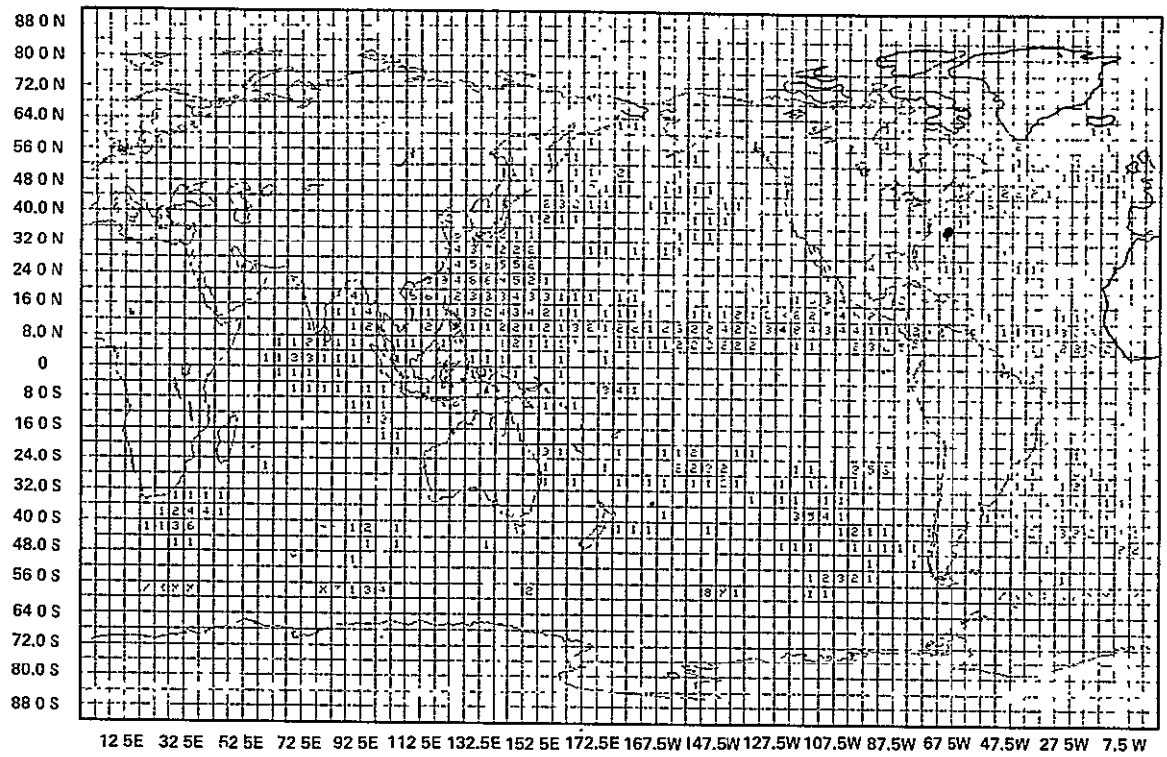

Figure 10a. ESMR-derived oceanic rainfall rate (.1 mm/hr) for August 1974, after Rao, et al. (1976).

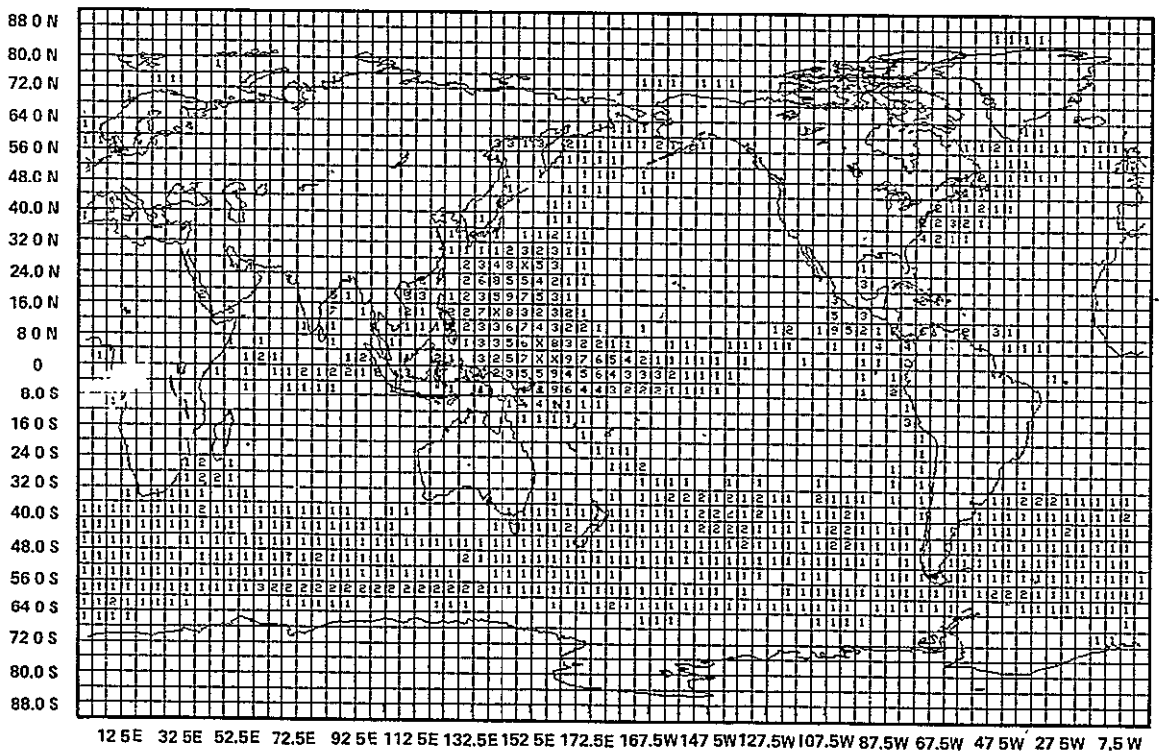

Figure 10b. Simulated oceanic rainfall rate (.1 mm/hr) for August.

simulated field shows the bands of precipitation along the ITCZ in the Pacific and the Indian Ocean, although somewhat too far south in the central Pacific. The model, however, is deficient in its simulation of the Atlantic ITCZ rainfall. Over the North Pacific, North Atlantic, tropical Indian Ocean, and middle latitude Southern Hemisphere oceans, the simulation shows larger precipitation rates than the observations.

August. The general features of the simulated fields that agree well with observations are the equatorial band of precipitation across the Pacific, the precipitation in the Bay of Bengal, and the intense precipitation over the tropical and subtropical western North Pacific, although the simulated amounts are too large. Again, the model failed to produce any significant precipitation along the Atlantic ITCZ. Another discrepancy is that the model produced a band of precipitation oriented NW-SE over the ocean east of Australia, which does not show in the observations. The model produced a band of rainfall over all of the middle latitude Southern Hemisphere oceans that was not observed.

Conclusion. Monthly mean statistics of some atmospheric fields, as obtained from two seasonal numerical simulations with the current version of the GLAS GCM, were compared with the corresponding observed climate statistics. Although the simulated fields are for a single realization (with climatological mean boundary conditions) and the observations are for a number of years, the Facility, nevertheless, has attempted to infer from these comparisons the ability of this model to simulate seasonal climate.

The geographical distributions of the simulated and observed fields were in good agreement for most of the large-scale features of sea level pressure, geopotential heights, horizontal velocities, radiation balances, and precipitation. The zonally-averaged statistics of winds and temperatures and the poleward transports of zonal momentum and sensible heat for the most part also agreed with the observations. It is recognized that there are also some significant quantitative differences between the simulated and observed fields.

Moreover, many of these deficiencies are discussed in a more comprehensive paper, Comparisons of Observed Seasonal Climate Features with a Winter and Summer Numerical Simulation Produced with the GLAS General Circulation Model, which was included in the Proceedings of the JOC Study Conference on Climate Models (April 3-7, 1978, Washington, D. C.). Future seasonal simulation studies will address the geographical distributions of the transient eddies or variances in time, space-time spectral analysis, and simulated model statistics over comparable ensembles of seasons with appropriate boundary condition variations.

References

Crutcher, H. L., and O. M. Davis, 1969: U. S. Navy Marine Climate Atlas of the World. NAVAIR 50-1C-54 (available from Naval Weather Service Command, Washington, D. C.).

Mintz, Y., and G. Dean, 1952: The observed mean field of motion of the atmosphere. Geophys. Res. Papers, 17, 65 pp.

Posey, J. W., and P. F. Clapp, 1964: Global distribution of normal surface albedo. Geophys. Int'l., 4, pp. 33-48.

Rao, M. S. V., W. V. Abbot III, and J. S. Theon, 1976: Satellite-derived global oceanic rainfall atlas (1973 and 1974), NASA SP-410, NASA, Washington, D. C.

Raschke, E., T. H. Vonder Haar, M. Pasternak, and W. R. Bandeen, 1973: The radiation balance of the earth-atmosphere system from Nimbus-3 radiation measurements. NASA TN D-7249, NASA, Washington, D. C.

SENSITIVITY OF THE GENERAL CIRCULATION TO ARCTIC SEA ICE BOUNDARIES

(G. F. Herman and W. T. Johnson)

A series of numerical experiments was conducted with the Goddard general circulation model to test the hypothesis that year-to-year variations of wintertime Arctic Sea ice boundaries affect hemispheric circulation features. Many observational studies into possible climatic effects of sea ice have been carried out since the beginning of this century, and these are summarized in detail by Herman and Johnson (1978). The predominant effect of ice cover variation is to alter the exchange of heat and moisture between the atmosphere and the surface of the ocean, which is due to the strong insolating property of sea ice. There is an additional effect on the radiation balance due to the larger albedo of ice as compared with ocean, but it is of secondary importance during the winter because of small values of insolation at high latitudes.

Large excursions about the average wintertime sea ice cover occur in the East Greenland Sea, Barents Sea, Davis Straits, Sea of Okhotsk, and Bering Sea. To test the effect of ice margin variations, GLAS performed a series of experiments in which the only control parameter was the total ice cover in these north Atlantic and north Pacific seas. The differences between the respective maximum and minimum ice conditions then represent precisely the effect of ice boundary conditions on the GCM calculations.

The maximum and minimum sea-ice extent in the north Atlantic is estimated based on ice charts from the British Climatological Service, which date from 1961 to 1977. Ice limits in the north Pacific were obtained for the 1973-1977 period from the U.S. Navy Fleet Weather Facility. These ice boundaries are shown in Figures 1 and 2, along with the Goddard GCM gridpoint representation. The area enclosed by the broken line represents an envelope of extreme ice conditions. (In general, ice limits do not vary synchronously in all Arctic seas.)

Except for minor modifications, the version of the model that was used is essentially that described by Somerville, et al. (1974) and Stone, et al. (1977). Model initial conditions were obtained from the 00Z NMC analysis for January 1, 1975. A single realization of a January-February climate is simulated by integrating the model from January 1 initial conditions until February 14. Model output at 12-hour intervals (0Z and 12Z) is averaged for the period January 14-February 12.

The ensemble mean control (i.e., minimum ice conditions) is estimated as the arithmetic average of six January-February simulations, and the mean anomaly (i.e., maximum ice conditions) is similarly estimated from two simulations. The individual simulations that comprise the control and anomalies differ from

one another by small, random initial values. These initial state differences are amplified by the baroclinic, barotropic, and convective instabilities of the model, and result in different mean monthly fields. (These instability mechanisms are some of the processes that cause one January to differ from another in the real atmosphere.)

The difference in sea level pressure (minimum minus maximum ice) is shown in Figure 3. When sea ice is at its minimum extent in the Barents Sea or Davis Straits, sea level pressure is lower than when at maximum extent. In general, the stronger surface heating over open ocean is associated with intensified cyclonic activity or, alternatively, more low level convergence and upper-level divergence, and lower sea level pressure. Higher pressure is found between Greenland and the British Isles when there is less ice present, and this change is of opposite sign to the Davis Straits and Barents changes. This results from mass conservation: surface divergence and high pressure southeast of Iceland accompanies the convergence and lower pressure to the east and to the west of Iceland. Sea level pressure is lower in the Sea of Okhotsk with less ice, and a compensating pressure rise occurs in the Gulf of Alaska.

The statistical significance of sea level pressure changes is estimated by comparing differences to the "inherent variability" or "noise" of the model. The high latitudes of the Northern Hemisphere, especially the regions of the north Atlantic and north Pacific where ice margin variability is the largest, have extremely high noise levels, i.e., standard deviation of sea level pressure are in excess of 5 mb. When normalized by the standard deviation of the sea level pressure (Figure 4), regions where the "signal-to-noise" ratio (difference divided by standard deviation) exceed two are found in the Gulf of Alaska, Sea of Okhotsk, Davis Straits, Barents Sea, and Icelandic north Atlantic. Large changes also occur in the subtropical north Atlantic and north Pacific. When averaged over latitude bands, sea level pressure changes are significant at the 6-percent level between 50-70°N, and at the 11-percent level between 10-30°N.

Large changes also occur in the mid-troposphere. At 500 mb the effect of maximum sea ice is to cause 2°C colder temperatures in the northern north Pacific, in the north Atlantic between Greenland and the British Isles, and over northern and central North America. These temperature changes correspond to decreased geopotential height surface at 500 mb of over 100 gpm. These differences are three times greater than the standard deviation of the 500 mb temperature field in the north Pacific, and twice as great over North America. The 500 mb geopotential differences are significant at the 3-percent level between 50-70°N.

Changes of opposite tendency in the pressure and geopotential fields in eastern subtropical Atlantic and Pacific accompanied the changes in the Icelandic and Aleutian regions. These changes may imply that changes in the mass field in high

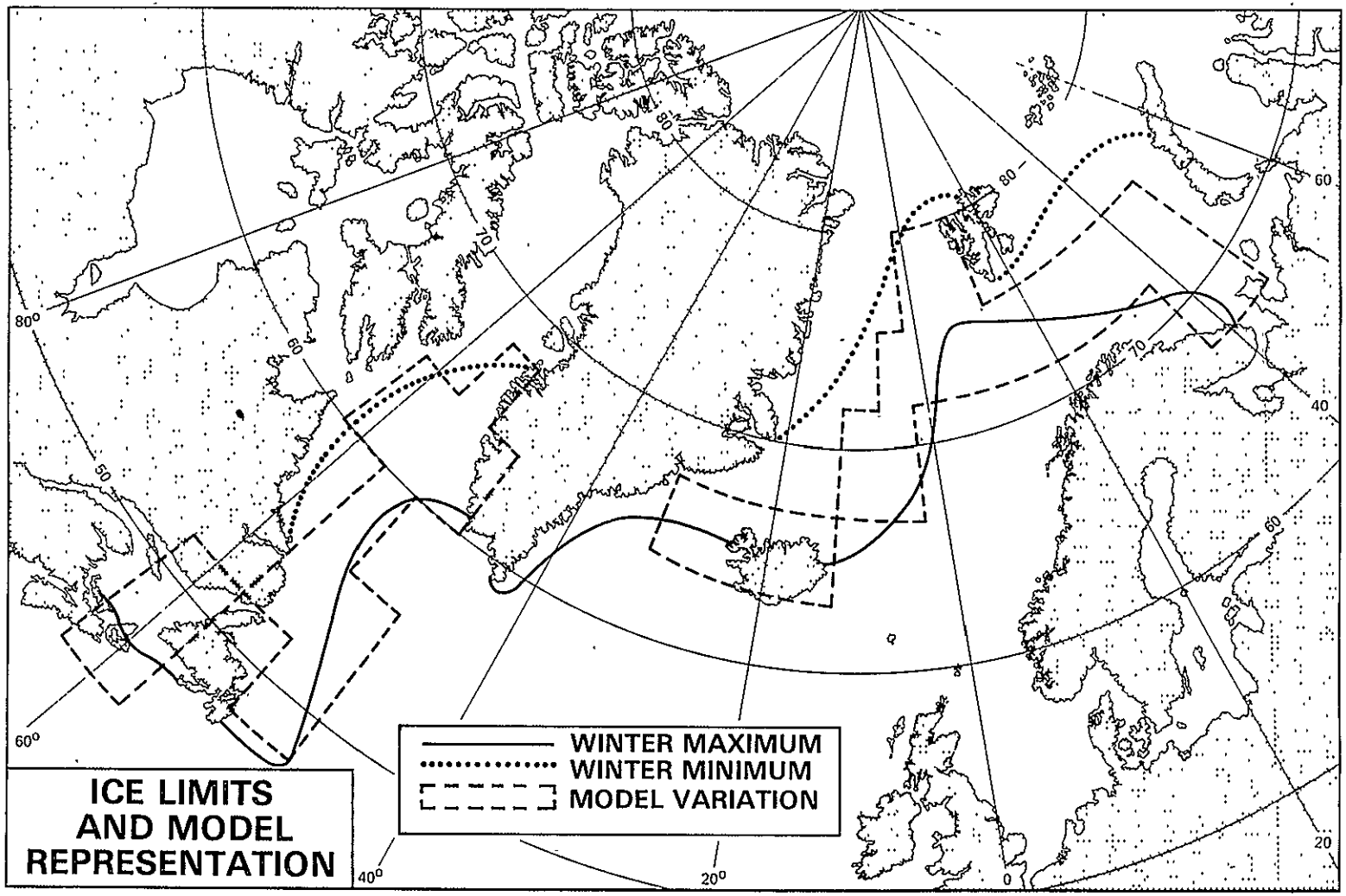

Figure 1. Approximate maximum and minimum sea ice limits for North Atlantic seas, 1961-1977. Solid line is Goddard GCM grid representation of envelope of wintertime ice margin extremes.

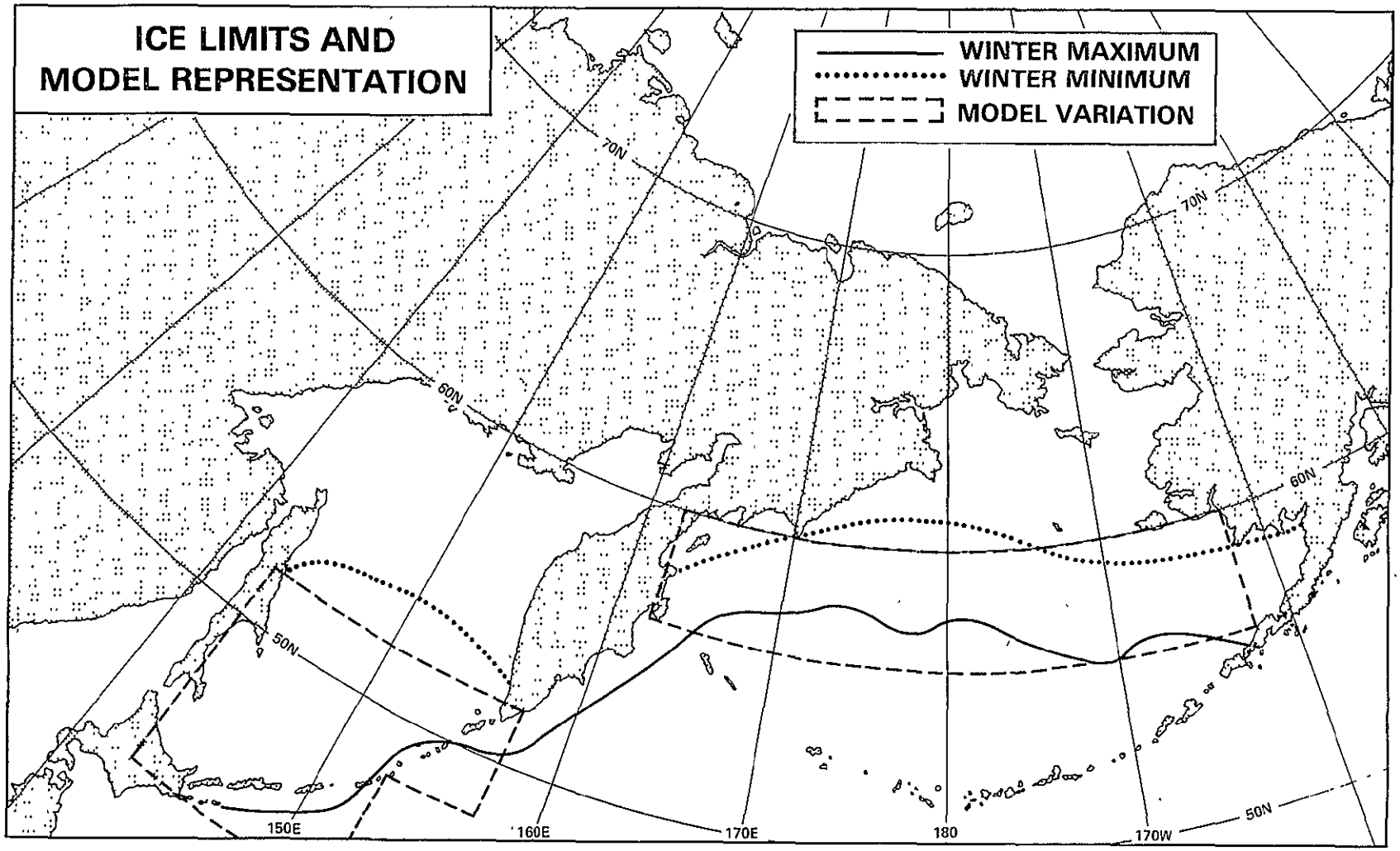

Figure 2. Approximate maximum and minimum sea ice limits for North Pacific seas, 1973-1977.

Figure 3. Ratio of absolute values of sea level pressure difference (mb) to standard deviation of sea level pressure (mb) obtained in initial state perturbation experiments.

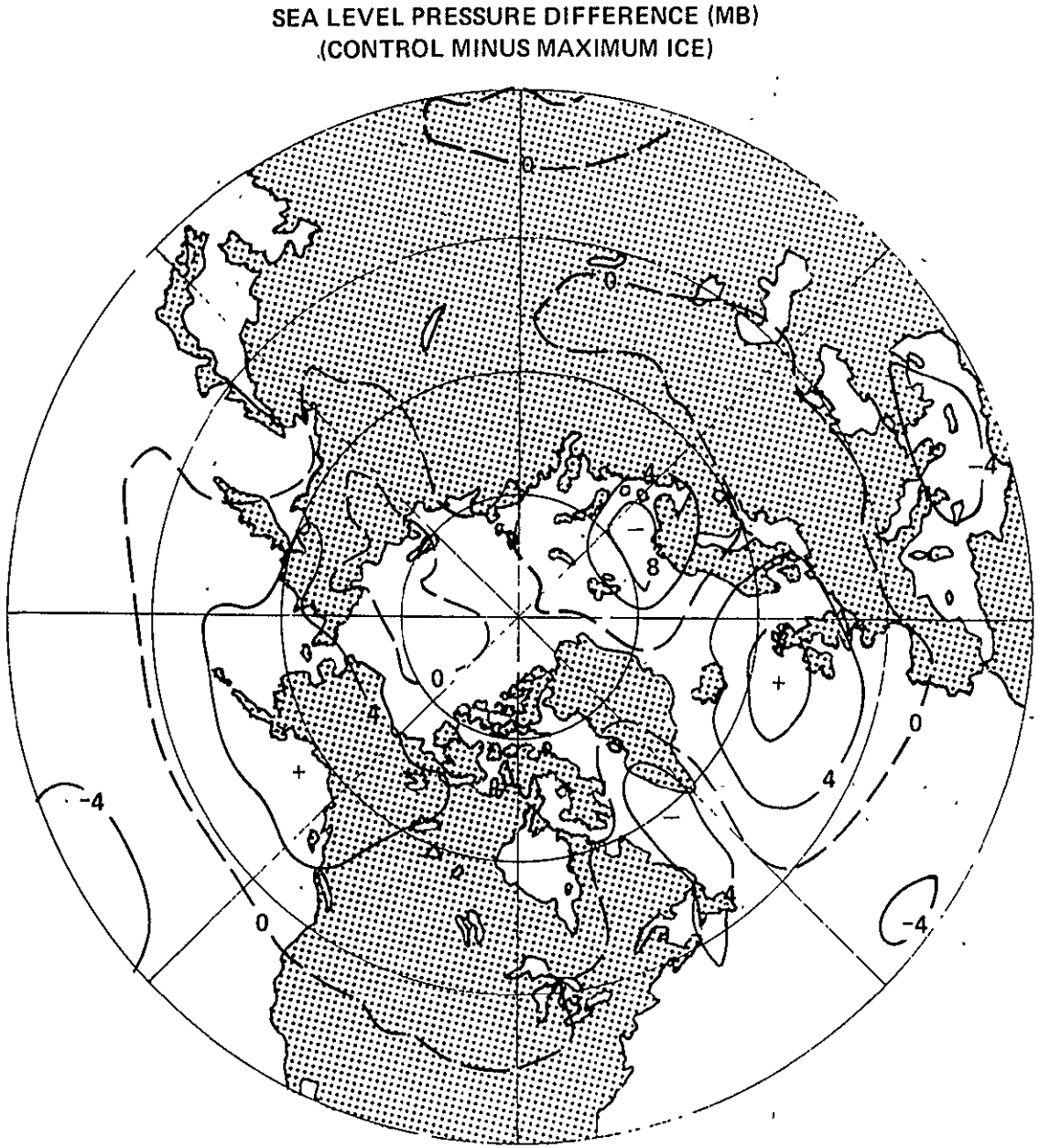

Figure 4. Sea level pressure difference (mb) between minimum and maximum ice conditions. Values correspond to mean control minus mean anomaly.

latitudes and subtropical regions are interrelated, or "teleconnected" (cf., Namias, 1958). On the basis of these model results it is concluded that ice margin anomalies are capable of altering local climates in certain regions of the high- and mid-latitudes, and are also capable of exerting synoptic influence on a hemispheric scale.

References

Herman, G. F. and W. T. Johnson, 1978: The sensitivity of the general circulation to Arctic sea ice boundaries: a numerical experiment. Mon. Wea. Rev., 106.

Namias, J., 1958: The general circulation of the lower troposphere over Arctic regions and its relation to the circulation elsewhere. Polar Atmos. Symposium, Oslo, Pergamon Press (1956).

Somerville, R. C. J., et al., 1974: The GISS model of the global atmosphere. J. Atmos. Sci., 31, pp. 84-117.

Stone, P., et al., 1977: The July climate and a comparison of the January and July climates simulated by the GISS general circulation model. Mon. Wea. Rev., 105, pp. 170-194.

SPECTRAL AND SPATIAL ENERGETICS

(J. Tenenbaum)

GLAS has carried out calculations of the interannual variation of model and observational energetics and studied the effects of alternative calculations of ω, the vertical pressure velocity, on these results. Both of these efforts are directed toward the goals of:

- Extracting the maximum possible information for predictions in the range of 2 to 20 days
- Specifying in greater detail where the model is failing to reproduce the observed behavior of the atmosphere.

It is known that there is general agreement between the model and the atmosphere, particularly in the integrated values of mean and eddy potential and kinetic energies. (Most general circulation models have difficulty with the eddy kinetic energy.) The GLAS method uses spectral techniques in one and two dimensions to pinpoint the areas of disagreement. In particular GLAS is examining closely the long waves that would seem to be least affected by resolution and have the most kinetic energy.

Studies of the interannual variation shed light on the model and observational variances, allowing detailed traces by wave number of where energy is being dissipated and generated. Three pairs of model and observation-runs have been analyzed over the Northern Hemisphere (see Figure 1). There is some suggestion that the model has difficulty generating eddy kinetic energy, Ke, but can more readily follow dissipation of K_E. GLAS is currently analyzing runs aimed at verifying this conclusion by studying other years and using a model with a more realistic radiation code.

The primary source of eddy kinetic energy is the conversion from eddy available potential energy; unfortunately, it is directly proportional to ω and its spectral transitions, both of which are poorly determined by mars convergence in the observational motion field.

Such an approach suffers from the errors inherent in the observational wind field. In many situations the signal is entirely buried in the noise. The diagnostic ω equation substitutes the solution of an elliptic partial differential equation involving the mass field to eliminate some of these errors.

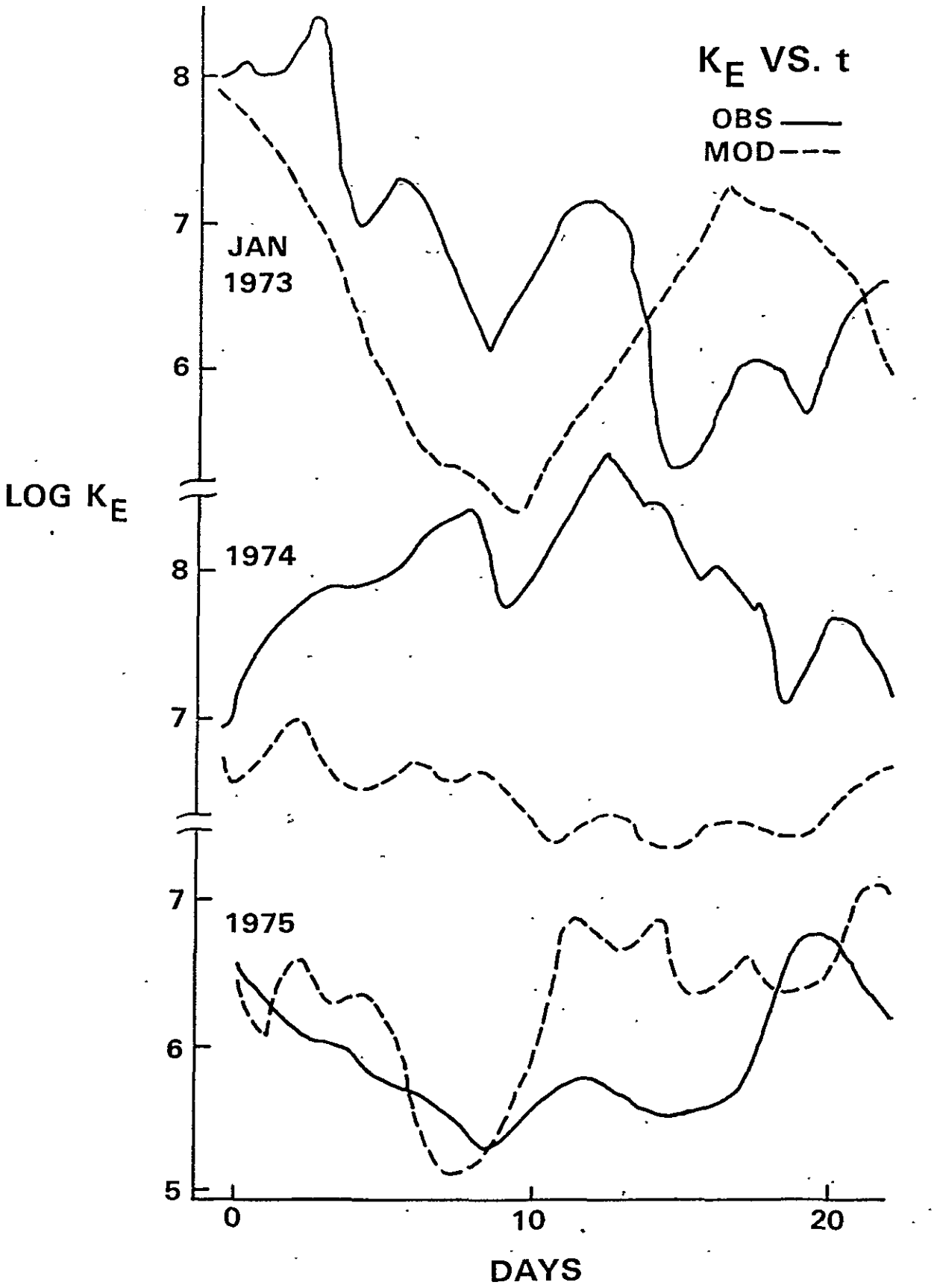

Figure 1. K_E versus time for January 1973, 1974, and 1975 from the GLAS model and NMC observations. (Units of K_E are 10^5 J/m^2.)

Preliminary results from this calculation are the following (see Table 1). The conversion from eddy potential to eddy kinetic energy is moderately sensitive to these errors at the lowest wave numbers, and quite so beyond wave number 4. As expected, the diagnostic omega equation significantly smooths the resulting omega fields, perhaps, unrealistically so. GLAS is currently investigating the latter possibility. Inclusion of moisture has little effect, though without a definite direction.

Table 1. Conversion of Eddy Potential to Eddy Kinetic Energy (units ω/m^2). Data for 0Z, December 20, 1972.

Case	Wave Number									
	1	2	3	4	5	6	7	8	9	10
Mass Convergence	0.74	0.53	0.65	0.37	0.19	0.24	0.15	0.18	-0.03	0.43
ω Equation, No Moisture	1.23	0.04	-0.25	0.15	0.02	-0.01	0.01	-0.03	-0.06	0.06
ω Equation, With Moisture	1.24	0.48	0.51	0.48	0.02	0.00	0.04	0.08	0.01	0.06

EFFECT OF A PACIFIC SEA SURFACE TEMPERATURE ANOMALY ON THE CIRCULATION OVER NORTH AMERICA

(B. Bangaru and J. Shukla)

During the fall and winter of 1976-77, sea surface temperature (SST) in the north Pacific was characterized by abnormally cold temperatures in the central and western portions of the north Pacific with a warm pool located off the west coast of the U. S. (Figure 1). Namias (1978) has suggested that the north Pacific SST anomalies may have been one of the multiple causes of the abnormally cold temperatures in eastern North America during the 1976-77 winter. This study attempted to test this hypothesis by conducting a numerical experiment with the GLAS general circulation model.

The model used in the present study is the one described earlier by Somerville et al. (1974) and Stone et al. (1977). A modified version of the model has also been presented in the proceedings by Halem et al. (1978). The experiments were performed by first integrating the GLAS GCM for 45 days with the climatological mean SST and the observed initial conditions valid for January 1, 1975. This integration is referred to as the Control run (C). The climatological SST field was then changed by adding a time invariant anomaly field and therefore, although the climatological SST varied with season, the imposed anomaly field remained constant with time. The structure of the imposed SST anomaly was the same as shown in Figure 1, but the numerical values were exaggerated by considering them in °C rather than °F. The model was integrated again for 45 days; this run will be referred to as the Anomaly run (A).

Control Run C and Anomaly Run A were further repeated with their respective boundary conditions in SST, but the initial conditions in u, v, T, and surface pressure were randomly perturbed. The spatial variation of the random perturbations corresponded to Gaussian distributions with zero means and standard deviations of 1°C in temperature, 4 m/s in horizontal wind components and 3 mb in surface pressure over land points and 2°C in temperature, 8 m/s in horizontal wind components, and 6 mb in surface pressure over ocean points.

These runs are referred to as Initial Condition Perturbation Runs C_1 and A_1 for Control (C) and Anomaly (A), respectively. Four additional Initial Condition Perturbation Runs were already made by Spar et al. (1978) which are referred to as C_2, C_3, C_4, and C_5. The atmospheric parameters for the six runs are referred to as C, C_1, C_2, C_3, C_4, C_5, as the mean control (Cm) and the average of two anomaly runs A and A_1 as mean anomaly (Am). In order to assess the response of the imposed SST anomaly on the atmospheric circulation, the differences between the mean control and the mean anomaly

C-3

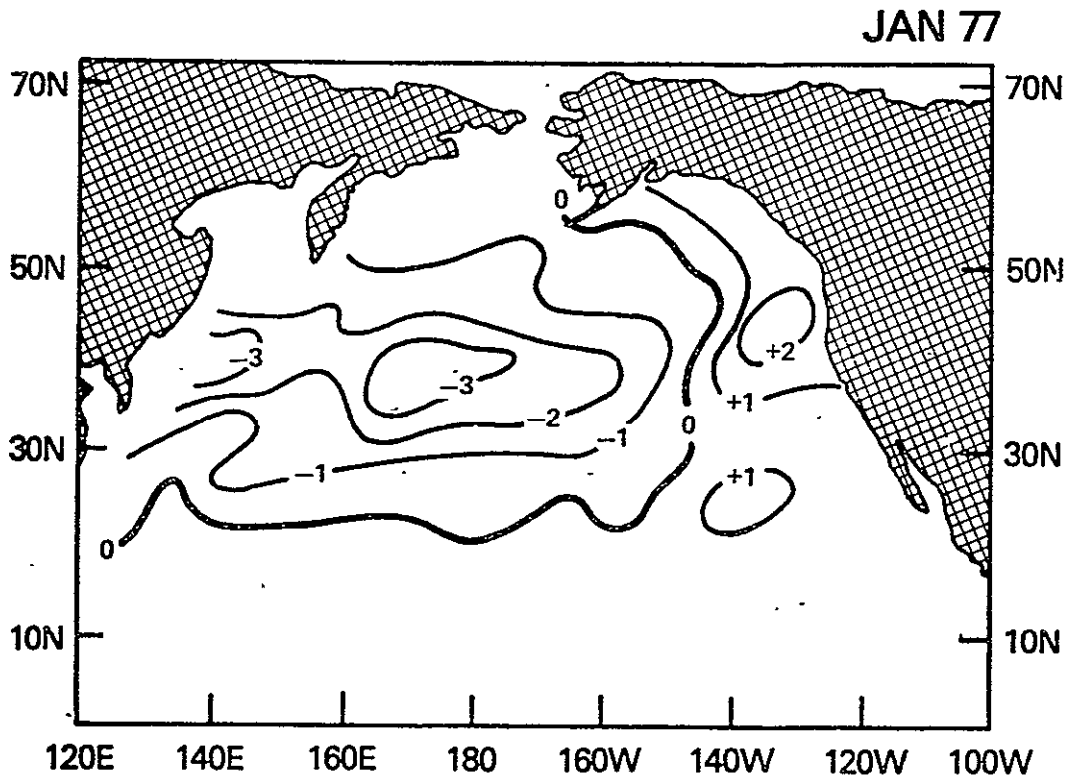

Figure 1. Observed sea surface temperature anomaly (°F) during January 1977.

runs averaged for the period between day 15 through day 45 are examined and the magnitude of the differences is compared with respect to the standard deviation among the mean monthly values for the six control runs for this period.

Figure 2a shows the differences between the mean anomaly and the mean control runs for the 700 mb temperature. The largest differences are found along the International Date Line, which is the longitude of maximum negative anomaly in SST, and the eastern parts of Canada, and the northern U. S. A positive anomaly is found over Greenland. Occurrence of colder 700 mb temperatures over the cold anomaly and warmer 700 mb temperatures over the warm anomaly can be explained by considering the radiative, sensible and latent heat fluxes. A detailed examination of the model-generated heat fluxes showed that the evaporation and convective cloudiness decreased over the cold anomaly. Reductions in the moisture and the sensible heat flux, which reduces the convective clouds, causes a reduction in the latent heat of condensation and this can also cause cooling of the atmospheric temperatures. Consistent with the decrease in the convective cloudiness, it was also found that the solar flux at the surface increased but the long wave flux at the surface decreased. Since the sea surface temperatures were prescribed, this feedback does not operate in the model. It should be noted, however, that the net effect of these diabatic heat sources and sinks is such that the heat source (sink), which is initially confined to the lower boundary, finally extends into the troposphere.

The most interesting feature in this figure is the coldest 700 mb temperatures centered around 50N, 75W. This is clear evidence of the downstream response of the model to the SST anomalies in the Pacific. Figure 2b shows the ratio of the differences and the standard deviations among the six control runs. These ratios are the signal-to-noise ratio. Two areas of maximum signal to noise are found, one over the anomaly itself and the other centered around 50N, 75W. The positive temperature anomalies over Greenland were found to have a signal-to-noise ratio less than two.

In the earlier numerical experiments with the NCAR model (Kutzbach et al. [1977], Chervin et al. [1976]) no significant downstream effect was noticed. Although the two general circulation models are not identical (especially with regard to their simulation of the transient eddies), in GLAS' opinion, the primary reason a downstream effect was observed in the GLAS model was due to the nature of the spatial structure of the SST anomaly.

The results of these numerical experiments support the hypothesis by Namias that the SST anomalies over the Pacific during the 1976-77 winter may be one of the contributing factors towards very cold temperatures over the northeast U. S. and warm temperatures over the Alaskan region. Since this was not a coupled ocean-atmosphere model, SST anomalies were assumed to persist for the whole period of integration. This assumption is justified by the observed fact that the SST anomalies do persist for a time period of several months.

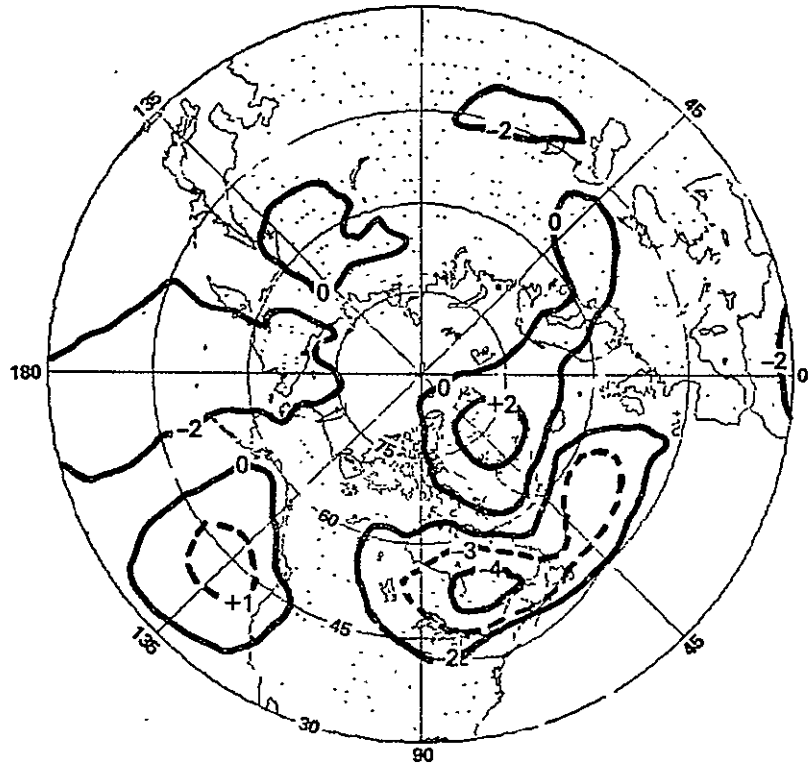

Figure 2a. Differences between mean anomaly and mean control runs for 700 mb temperature.

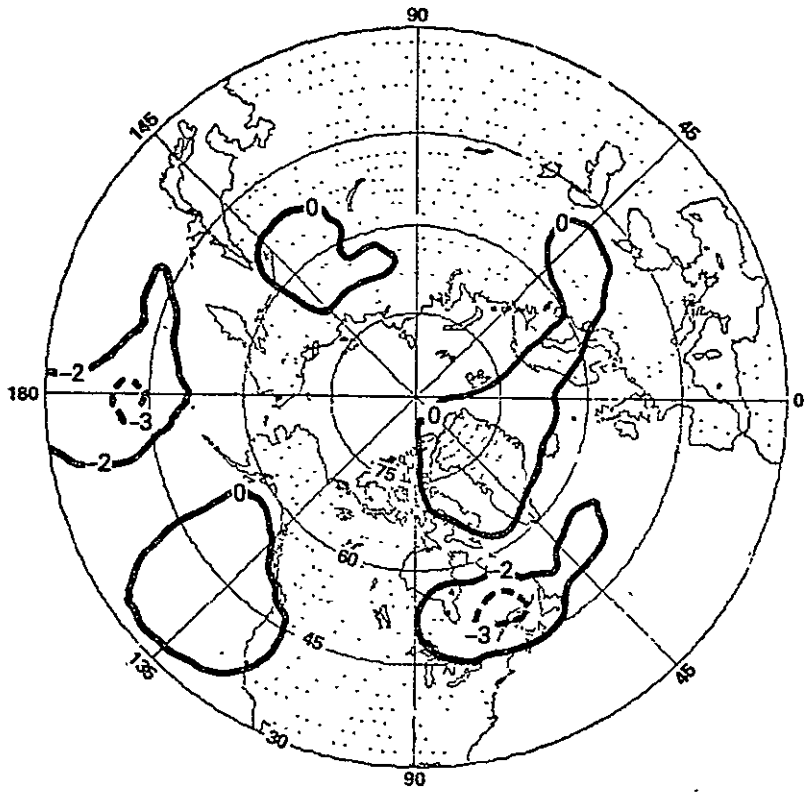

Figure 2b. Ratio of differences and standard deviations among six control runs.

These results show clear evidence of a downstream response of the model atmosphere to the imposed SST anomalies over the Pacific. It is interesting to note that for some levels the downstream effect away from the anomaly is more than the effect over the anomaly itself. Since the natural variability of the mid-latitude atmosphere is rather large, the standard deviation among six predictability runs was calculated and the ratios of the mean differences to the standard deviations indicated that the downstream effects are indeed significant.

The results of the present study suggest that the downstream orographic barriers may contribute to amplify the SST-generated atmospheric perturbations. In other words, an orographically forced atmospheric flow regime may be more sensitive to further modification by the perturbations generated by the SST anomalies. This qualitative conjecture is suggested by those numerical experiments in which it is found that the effects of the north Pacific SST anomalies are most prominent on the western and the eastern sides of the North American continent. This is of special significance for the winter of 1976-77 because, as pointed out by Namias (1978), the anomalous flow pattern over North America was in phase with the normal winter flow pattern. Therefore, this was interpreted as an inphase amplification of the normal winter circulation, which is orographically and thermally forced by the mountains and the mean heat sources and sinks. The purpose of this numerical experiment was not to simulate the actual events of the 1976-77 winter but only to examine the effects of similar SST anomalies on the model atmosphere. It should be noted that the atmospheric conditions in the mean control run corresponded to the winter of 1975.

Detailed examination of the model-simulated daily charts indicated that in general the anomaly runs did not show a persistent blocking pattern near the west coast of the U. S. as observed during the 1976-77 winter. However, there were periods of 3-5 day duration in which the ridge over the west coast of the U. S. was highly intensified and such events were more frequent in the anomaly run compared to the control run. Blocking situations do occur but they do not last too long. It is not clear whether this is a manifestation of some model deficiency or it is because the model integrations are not performed long enough for several interannual cycles.

References

Chervin, R. M., W. M. Washington, and S. H. Schneider, 1976: Testing the statistical significance of the response of the NCAR general circulation model to north Pacific Ocean surface temperature anomalies. J. Atmos. Sci., 33, pp. 413-423.

References (Continued)

Halem, M., J. Shukla, Y. Mintz, M. L. Wu, R. Godbole, and Y. Sud, 1978: Comparisons of observed seasonal climate features with a winter and summer numerical simulation produced with the GLAS general circulation model. JOC Study Conf. on Climate Models, Washington, DC, April.

Kutzbach, J. E., R. M. Chervin, and D. H. Houghton, 1977: Response of the NCAR general circulation model to prescribed changes in ocean surface temperature, Part 1: Mid-latitude changes. J. Atmos. Sci., 34, pp. 1200-1213.

Namias, J., 1978: Multiple causes of the North American abnormal winter 1976-77. Mon. Wea. Rev., 106, pp. 279-295.

Somerville, R. C. J., P. H. Stone, M. Halem, J. E. Hansen, J. S. Hogan, L. M. Druyan, G. Russell, A. A. Lacis, W. J. Quirk, and J. Tenenbaum, 1974: The GISS model of the global atmosphere. J. Atmos. Sci., 31, pp. 84-117.

Spar, J., J. J. Notario, and W. J. Quirk, 1978: An initial state perturbation experiment with the GISS model. Mon. Wea. Rev., 106, pp. 89-100.

Stone, P. H., S. Chow, and W. J. Quirk, 1977: The July climate and a comparison of the January and July climates simulated by the GISS general circulation model. Mon. Wea. Rev., 105, pp. 170-194.

LOW-FREQUENCY PLANETARY WAVES: SPACE-TIME SPECTRAL ANALYSIS OF A WINTERTIME SIMULATION OF THE GLAS MODEL

(D. M. Straus, J. Shukla, and W. Byerly)

Space-time spectral analysis provides a useful diagnostic tool, applicable both to observations and model output. It allows one to separate various space and time scales, and thus distinguish motions believed to have different origins or distinct dynamics. One can study medium-scale (wave number 5 to 10) "baroclinic" motions at mid-latitudes separately from the largest scale (planetary) motions (Pratt, 1975, Pratt and Wallace, 1976) and observe the dominant time scales involved with each. Further, it is possible to look at the change in the character of motions of particular time and space scales with height (Deland, 1973), with latitude (Hayashi and Golder, 1977), or both.

This paper presents preliminary results of a space-time analysis of a 60-day (wintertime) simulation of the GLAS model. Various fields (geopotential height, geostrophic wind components) were spectrally analyzed with respect to zonal wave number and frequency at a number of latitudes and model levels. The focus here is on the low-frequency, planetary scale motions which, in mid-latitudes, dominate the total variance of, for instance, the geopotential height (Pratt, 1975, 1977).

Space-time spectral analysis, as discussed by Pratt (1976), differs from straight-forward Fourier analysis in longitude and time in that the method recognizes the stochastic character of the atmosphere. One expresses the total space-time variance of a field $q(\lambda,t)$ as

$$[\overline{q^2}] = \frac{1}{4\pi^2}\int_0^{2\pi} d\lambda \int_0^{2\pi} dt\,(q(\lambda,t))^2 = \sum_{k=0}^{\infty}\sum_{\omega=0}^{\infty} [E_{qq}(k,+\omega)+E_{qq}(k,-\omega)] \qquad (1)$$

where [ ] indicates a zonal average, an overbar indicates a time average, and the total length of record being considered has been normalized to 2π. $E_{qq}(k,\omega)$ represents the contribution to the total variance by motions of wave number k and of a band of frequencies centered at ω. Here $\omega>0$ refers to westward movement. The stochastic nature of the atmosphere necessitates a certain amount of averaging over frequency in the calculation of $E_{qq}(k,\omega)$ in order that the resulting spectrum be satistically stable. With conventional techniques, this leads to a large amount of smoothing (e.g., Pratt, 1975, who smooths over a frequency range of .125 cycles per day). A technique that allows much finer frequency resolution is the maximum entropy method (MEM, Hayashi, 1977a, Ulrych and Bishop, 1975, Smylie, et al., 1973). This method was used in this study.

Recent work (Pratt, 1976, Hayashi, 1977b) has emphasized the importance of distinguishing between the contributions of standing waves and those of propagating waves to $E_{qq}(k,\omega)$. Large-scale standing waves, (presumably forced by mountains and continent-ocean heating differences), have fixed nodes, and consist of coherent eastward and westward propagating waves of equal amplitude and frequency. They have the property that $E_{qq}(k,+\omega)=E_{qq}(k,-\omega)$. However, the equality of $E_{qq}(k,\pm\omega)$ does not necessarily imply standing waves: Physically distinct, incoherent westward and eastward moving waves of the same frequency and amplitude also yield $E_{qq}(k,+\omega)=E_{qq}(k,-\omega)$. Distingushing between these situations requires the calculation of the coherence between eastward and westward propagating waves (Hayashi, 1977b). Since this is very difficult to calculate with MEM (Hayashi, 1977a), it has not been carried out in this study.

Following the above discussion, one defines (dropping the subscript 'qq'):

Total variance

$$T(k,\omega) \equiv E(k,\omega) + E(k,-\omega) \equiv E_W(k,\omega) + E_E(k,\omega), \cdot \omega>0, \qquad (2)$$

which represents the contribution to $[\overline{q^2}]$ from motions of wave number k and frequency ω and $-\omega$.

Propagating variance

$$PR(k,\omega) \equiv E(k,\omega) - E(k,-\omega) \equiv E_W(k,\omega) - E_E(k,\omega), \ \omega>0, \qquad (3)$$

which represents the net tendency towards propagation of motions of wave number k and frequency $\pm\omega$ (PR>0 refers to westward propagation).

The remaining variance, $T(k,\omega)-|PR(k,\omega)|$, consists in general of standing waves, incoherent traveling wave, and random fluctuations. Hayashi and Golder (1977) indicate, in particular, that standing waves do make an important contribution on the time and space scales of interest here.

Results are presented for $E(k,\pm\omega)$ for the geopotential height (ϕ) for the longest planetary waves (wave numbers 1-5) and frequencies corresponding to 60 day-10 day periods, at mid-latitudes and at several levels.

Table 1 presents the total space-time variance $T(k,\omega)$ for various periods and wave numbers at 54N, 510 mb. The most striking feature is the band of high variance extending from

Table 1. Total Variance T(k,ω) (Arbitrary Units) 54N, 510 mb.

	Period (Days)				
Wave No.	60	30	20	15	10
1	523,551	199,485	33,136	20,742	18,206
2	95,251	132,363	86,107	52,889	21,548
3	62,741	6,174	109,157	199,838	14,433
4	8,033	18,527	40,134	80,200	5,663
5	6,592	5,723	7,733	6,659	8,230

Table 2. Propagating Variance PR(k,ω) (Arbitrary Units) 54N, 510 mb.

	Period (Days)				
Wave No.	60	30	20	15	10
1	+473,886	+136,443	- 3,168	+ 2,714	+ 4,571
2	+ 17,722	- 52,423	-53,526	- 27,198	+ 6,691
3	- 34,337	- 27,227	-67,366	-191,333	-12,866
4	- 2,940	- 9,743	-24,345	- 75,836	- 5,021
5	+ 1,192	- 2,268	- 6,164	- 5,392	- 6,450

low frequency, low wave number to higher frequency and wave number. This feature, also observed in the atmosphere (Pratt, 1975, 1977), indicates that the largest waves have distinctly preferred time scales associated with them, time scales of interest for long-range weather prediction.

The propagating variance PR is presented in Table 2 for various periods and wave numbers at 510 mb, 54N. Disturbances of wave number 1 in the 60- and 30-day category propagate predominantly westward. This is true at most but not all of the mid-latitudes and model levels. This is observed in the atmosphere (Pratt and Wallace, 1976, Fraedrich and Bottger, 1978), but was not found by Hayashi and Golder. In the observations, the dominance of westward propagation extends over wave numbers 1 to 3 and over all periods greater than 10 days. This general trend is not uniformly reproduced in Table 2, and this is so for other latitudes and pressure levels. Apparently, eastward-moving disturbances are somewhat over-represented in the model.

It is useful to compare the vertical structure of the model disturbances to that of the atmosphere. One way of accomplishing this is to find evidence in the model data of the modes deduced by Pratt and Wallace (PW) for the atmosphere. They find that much of the low-frequency (periods of 10-20 days), low-wave number variance of mid-latitude geopotential and temperature can be explained in terms of two modes: In the first westward-moving mode, $|\phi|$ is non-zero at the ground and increases with height. The second mode is eastward moving and is characterized by having $|\phi|$ vanish at the ground and increase more sharply with height. Pratt and Wallace describe the first modes as external, equivalent barotropic, and the second mode as more baroclinic in nature. If these modes are important in the model, one expects the low levels to be dominated by westward motions, with the strength of the eastward motions increasing with height.

In Table 3, $E_W(k,\omega)$ and $E_E(k,\omega)$ are shown for several latitudes and heights. The values of E_W, E_E were averaged over wave numbers 1-3 and periods of 20, 15, and 10 days. It is clear that if Pratt's modes are present, they are partially obscured by other types of motion: $E_W(k,\omega)$ does <u>increase</u> with height, but $E_E(k,\omega)$ is still large at 730 mb. In agreement with PW, the <u>relative</u> importance of eastward-propagating waves <u>does</u> increase with height:

$$E_E(175\text{ mb}) - E_E(730\text{ mb}) > F_W(175\text{ mb}) - E_W(730\text{ mb})$$

at all latitudes, and $\dfrac{E_E(175\text{ mb})}{E_E(730\text{ mb})} > \dfrac{E_W(175\text{ mb})}{E_W(730\text{ mb})}$ at 30° and 54N.

The latter inequality does not hold at 70N due to the relatively

Table 3. Average Values of E_W, E_E (Arbitrary Units).

	E_W			E_E		
Mb	30N	54N	70N	30N	54N	70N
175	7,443	29,702	30,935	16,364	121,748	61,647
510	2,849	11,921	10,459	8,596	49,863	10,084
730	2,575	9,450	5,272	4,239	25,042	11,573

Table 4. Average Values of PR(k,ω) (Arbitrary Units).

Mb	30N	54N	70N
175	-8,923	-92,546	-30,655
510	-5,441	-37,942	+ 3,872
730	-1,664	-27,469	- 6,301

large value of E_E at 70N, at 730 mb. In comparing Table 3 to the propagating wave modes of PW, one is assuming that standing waves do not contribute, for they would have to be subtracted from E_E, E_W, before the latter give information on propagating waves.

An alternate assumption is that the standing waves contribute as much as they can while being consistent with the data. This means taking the standing wave strength to be $E_E(E_W)$ if $E_W > E_E$ ($E_E > E_W$). Subtracting the "standing wave amplitude" $2E_E(2E_W)$ from the total variance T gives in this case the propagating variance PR.

Values of $PR(k,\omega)$ for various latitudes and pressure levels, averaged as before, are presented in Table 4. Again, the variance of geopotential corresponds to predominantly eastward movement, even at low levels, and this tendency increases with height (except between 730 mb and 510 mb at 70N).

Interpreting the model data with respect to the two modes of PW, one can conclude that the baroclinic mode (second mode) is too strongly represented compared to the equivalent barotropic mode (first mode). To more carefully interpret the model data, it is necessary to calculate the coherence between eastward and westward moving components, so that the role of standing waves can be understood. This calculation is presently underway.

Space-time spectral analysis of a wintertime simulations of the GLAS model shows that the low-frequency, low-wave number disturbances behave realistically in some ways. Their total variance is relatively strong in a band extending from low wave numbers and frequency to high wave numbers and frequency. In addition, there is evidence of westward propagation in the longest wave length, lowest frequency category, although this tendency is not as widespread as in the atmosphere.

Comparing the vertical structure of the model to the two modes of PW believed to be important in the atmosphere, one finds that the model's baroclinic mode is too strong compared to its equivalent barotropic mode.

Acknowledgment

We gratefully acknowledge the assistance of Dr. T. Murakami with the maximum entropy method spectral analysis.

References

Deland, R. J., 1973: Spectral analysis of traveling planetary scale waves: vertical structure in middle latitudes of Northern Hemisphere. Tellus, 15, pp. 355-372.

References (continued)

Fraedrich, K., and H. Bottger, 1978: A wave number-frequency analysis of the 500 mb geopotential at 50°N. J. Atmos. Sci., 35, pp. 745-750.

Hayashi, Y., 1977a: Space-time power spectral analysis using the maximum entropy method, J. Meteor. Soc. Japan, 55, pp. 415-420.

Hayashi, Y., 1977b: On the coherence between progressive and retroregressive waves and a partition of space-time power spectra into standing and traveling parts. J. Appl. Meteor., 16, pp. 368-373.

Hayashi, Y., and D. G. Golder, 1977: Space-time spectral analysis of mid-latitude disturbances appearing in a GFDL general circulation model. J. Atmos. Sci., 34, pp. 237-262.

Pratt, R. W., 1977: Space-time kinetic energy spectra in mid-latitudes. J. Atmos. Sci., 34, pp. 1054-1057.

Pratt, R. W., 1976: The interpretation of space-time spectral quantities. J. Atmos. Sci., 33, pp. 1060-1066.

Pratt, R. W., 1975: Space-time spectral analysis of large-scale mid-latitude disturbances. Ph.D. dissertation, Univ. of Wash.

Pratt, R. W., and J. M. Wallace, 1976: Zonal propagation characteristics of large-scale fluctuations in the mid-latitude troposphere. J. Atmos. Sci., 33, pp. 1184-1194.

Smylie, D. E., G. K. C. Clarke, and T. J. Ulrych, 1973: Analysis of irregularities in the earth's rotation. Meth. in Compu. Phys., 13, pp. 391-430.

Ulrych, T. J., and T. N. Bishop, 1975: Maximum entropy spectral analysis and autoregressive decomposition. Rev. Geophys. and Space Phys., 13, pp. 183-200.

A COMPARISON OF GROUND HYDROLOGY PARAMETERIZATIONS USING INPUT DATA FURNISHED BY A GCM SIMULATION

(J. D. Lin, J. J. Alfano, and P. Bock)

Three ground hydrology parameterizations proposed for use in an atmospheric general circulation model (GCM) are described in this paper. Controlled experiments were conducted for an off-line ground hydrology model for these parameterizations using input data furnished by a 2-day GCM simulation. A comparison of results indicates that the parameterizations have significant effects on the change of ground wetness and actual evapotranspiration for a wet, an average, and a dry cell located in the continental United States.

In the existing atmospheric general circulation models, the ground hydrology has been developed for the purpose of evaluating the source terms in the governing equations which are generated from the moisture, heat, and momentum fluxes across the atmosphere-land interface. The hydrology that was first incorporated into a GCM by Manabe (1969) was based upon the parameterization: (1) actual evapotranspiration as a function of soil moisture and potential evaporation, and (2) a certain moisture storage capacity in a ground surface layer or plant root zone. The dynamics of moisture-heat transport processes and the variable characteristics of the soil-water-plant system are grossly oversimplified in this scheme. Nevertheless, this simple approach has been shown to be capable of producing the basic features of hydrology and climate on a global scale (Manabe and Holloway, 1975) and in semi-arid regions (Charney, et al., 1977) and remains in use today in the primary GCMs (Manabe, 1969; Somerville, et al., 1974; Washington and Williamson, 1977; Gates and Schlesinger, 1977). This study was an attempt to evaluate the sensitivity of parameterization related to soil moisture in a ground surface layer and actual evapotranspiration by off-line numerical experiments using input data furnished by a GCM simulation. The parameterizations chosen for the study are three variants of Manabe's scheme, which have been used in the UCLA model (Arakawa, 1972; Arakawa and Mintz, 1974); the GISS model (Charney. et al., 1977; Lin, et al., 1978); and the UC parameterization, a revised version proposed for use in the GLAS GCM (Lin, et al., 1978).

In a rectangular cell of a ground surface layer, the key parameter used in the ground hydrology (Manabe, 1969) is the soil moisture in a ground surface layer which is available to satisfy the evaporative demand of the atmosphere. In the UCLA model, ground wetness (w') is defined as the soil moisture (w) in a fraction of the maximum available soil water (w_m) in a ground surface layer of unspecified thickness. In terms of soil properties (Salter and Williams, 1959), then

$$w' = \frac{w}{w_m} = \frac{\theta - \theta_{wp}}{\theta_{fc} - \theta_{wp}} \qquad (1a)$$

and $w_m = \rho_w Sh\ (\theta_{fc} - \theta_{wp})$

where ρ_w is the mass density of water; S the soil porosity; h the thickness of ground surface layer; and θ, θ_{fc} and θ_{wp} are volumetric moisture content and its value at field capacity and permanent wilting point, respectively. In the GISS and UC parameterizations, ground wetness is taken as volumetric moisture content (θ) in a fraction of saturation so that

$$w' = \theta \qquad (1b)$$

and $w_m = \rho_w Sh$.

The variable soil properties can be characterized by varying the maximum available soil moisture in the UCLA model and the field capacity and permanent wilting point in the GISS and UC parameterizations, as shown in the following table:

Table 1. Soil Properties.

	UCLA	GISS			UC		
Soil Type	w_m (g)	w_m (g)	θ_{fc}	θ_{wp}	w_m (g)	θ_{fc}	θ_{wp}
Loam	10	66.4	.25	.10	50	.25	.10
Sand	10	4.0	.09	.025	25	.09	.025

With the definition of ground wetness in (1a) and (1b), a moisture conservation equation may be derived for a ground surface layer as

$$w_m \frac{\partial w'}{\partial t} = P - E_s - R_o - \rho_w \frac{\partial S_{si}}{\partial t} \qquad (2)$$

where P is precipitation, E_s evapotranspiration, R_o runoff including surface runoff and percolation, and S_{si} the storage of snow and ice.

The actual evapotranspiration E_s in (2) is scaled from the potential evaporation E_p by means of a scaling factor β such that

$$E_s = \beta E_p \tag{3}$$

and

$$E_p = \rho_a C_D |V_a| [q_* (T_g) - q_a] \tag{4}$$

in which ρ_a, V_a, and q_a are the air mass density, horizontal velocity, and specific humidity of the atmosphere at a reference elevation; $q_*(T_g)$ is the saturation specific humidity at the ground temperature T_g; C_D is the momentum transfer coefficient assumed to be equal to the moisture transfer coefficient. In the UCLA model,

$$\beta = \begin{cases} 1, & 1/2 < w' \leq 1 \\ 2w', & 0 < w' \leq 1/2 \end{cases} \tag{5a}$$

while in the UC parameterization,

$$\beta = \begin{cases} 1, & \theta_{fc} < \theta \leq 1 \\ \dfrac{\theta - \theta_{wp}}{\theta_{fc} - \theta_{wp}}, & \theta_{wp} < \theta \leq \theta_{fc} \end{cases} \tag{5b}$$

The version of parameterization used in the GISS model and being studied here is the following:

$$\beta = (\beta_{plant} + \beta_{soil}) \times (1 - ROCK) \tag{5c}$$

where

$$\beta_{plant} = 1. - \exp \{[-0.1 \times VPM \times \exp (16.75 \times VPM)/E_p] \times PLANT\}$$

$$\beta_{soil} = 1. - \exp [-0.01 \times VSM \times \exp (16.75 \times VSM)/E_p]$$

$$VPM = 0.1 \times VSM/USM + 0.2 \times [(VSM - USM)/ASM]$$

$$VSM = 2. \times \theta \times \theta_{fc}$$

$$USM = \theta_{wp}$$

$$ASM = \theta_{fc} - \theta_{wp}$$

ROCK = fraction of impervious surface (being ignored in this study)

It is seen that the scaling factor is a function of soil properties, potential evaporation and solar radiation. The PLANT factor depends on the solar angle Z as

$$\text{PLANT} = \min\,[1.0,\ \cos(Z)/0.2588]$$

The runoff R_o in (2) consists of the surface runoff and the horizontal and vertical percolation out of the cell-layer control volume, representing the "loss" of soil moisture and thus unavailable for evapotranspiration. The runoff for the UCLA model is given by

$$R_o = [P^3 + (10(1 - w'))^3]^{1/3} - 10(1 - w') \qquad (6a)$$

for the UC parameterization

$$R_o = P(0.1 + 0.9\theta^{1.5}) \qquad (6b)$$

and for the GISS model

$$\begin{aligned} R_o &= P - 0.5 \times \text{BBFACT} \quad , P \geq 2. \times \text{BBFACT} \\ &= 0.5 \times P^2/\text{BBFACT} \quad , P < 2. \times \text{BBFACT} \end{aligned} \qquad (6c)$$

in which the coefficient BBFACT is expressed in terms of the following parameters:

$$\text{BBFAC} = 2. \times \text{FILTF} \times \exp\,[-1.75 \times (\text{ADINF} - 0.5)]$$

$$\text{FILTF} = [1.77 \times \exp\{-0.036 \times (T_g - 273.2)\} + 0.44562]^{-1}$$

and $\text{ADINF} = 1.25 \times (2. \times \theta - 0.2) - 0.5$

The S_{si} term accounts for the storage of snow and ice which will accumulate when the temperature drops below 273.2°K and melt when the temperature exceeds 273.2°K. The amount of melt is calculated by the heat balance to keep the surface temperature at 273.2°K.

The ground temperature is intrinsically coupled with the ground wetness in the GCM model. The ground temperature, the average temperature of the ground surface layer, is governed by

$$C \frac{\partial T_g}{\partial t} = R_N - F_s - LE_s + S_i \qquad (7)$$

in which C is the bulk heat capacity, R_N the net radiation flux at the ground surface, F_s the sensible heat flux, LE_s the latent heat flux, and S_i the latent heat transfer due to melting of ice or snow or due to freezing of water. A detailed treatment of (7) has been documented by Tsang and Karn (1973).

An off-line ground hydrology model (GHM), forced by the atmosphere without feedback, was developed for these parameterizations. The GCM furnishing the atmospheric input data contains a known ground hydrology which may or may not be the same as those in the off-line GHM for controlled experiments.

Controlled experiments of the off-line GHM were conducted for the three parameterizations described in the previous section using input data furnished by a 2-day GLAS GCM simulation for a wet cell (Upper New England), an average cell (Southern Great Plains) and a dry cell (Southwest region) in the continental United States. The soil for the dry cell is characterized by the sand type while for the average and wet cell by the loam type. The ground hydrology used in the GCM is a version of the UCLA model, which assumes a constant, seasonally-averaged ground wetness. The input data which are extacted from the GCM global output consist of the surface pressure, temperature, specific humidity, wind velocity and net radiation flux. Only the initial values of ground wetness and ground temperature were used in the calculation and the rest of ground wetness and ground temperature together with the actual evapotranspiration were considered as diagnostic variables.

The results of the calculated diagnostic variables, ground wetness, ground temperature and actual evapotranspiration, in each cell are shown for the parameterizations in Figures 1, 2 and 3. In the 2-day run, there was no precipitation in the dry and average cell, but a total amount of 1.5 cm of rain fell on the wet cell. The daily average value of ground wetness, potential evaporation, actual evapotranspiration and the scaling factor for evaporation are listed in Table 2.

The soil moisture in Figure 1 is described by the ground wetness defined in (1a) and (1b). There is a significant change of ground wetness in response to evapotranspiration and light rain in the UCLA model even for the 2-day run, however, the UC and GISS ground wetness remains at a constant level. The high sensitivity of ground wetness change in the UCLA model might be attributed to the value of w_m as given in Table 1 and the value of β as indicated by the average values given in Table 2. It is clear that the length of a 2-day experiment is not sufficient to evaluate the change of ground wetness in the UC and GISS parameterization as an effect of soil type.

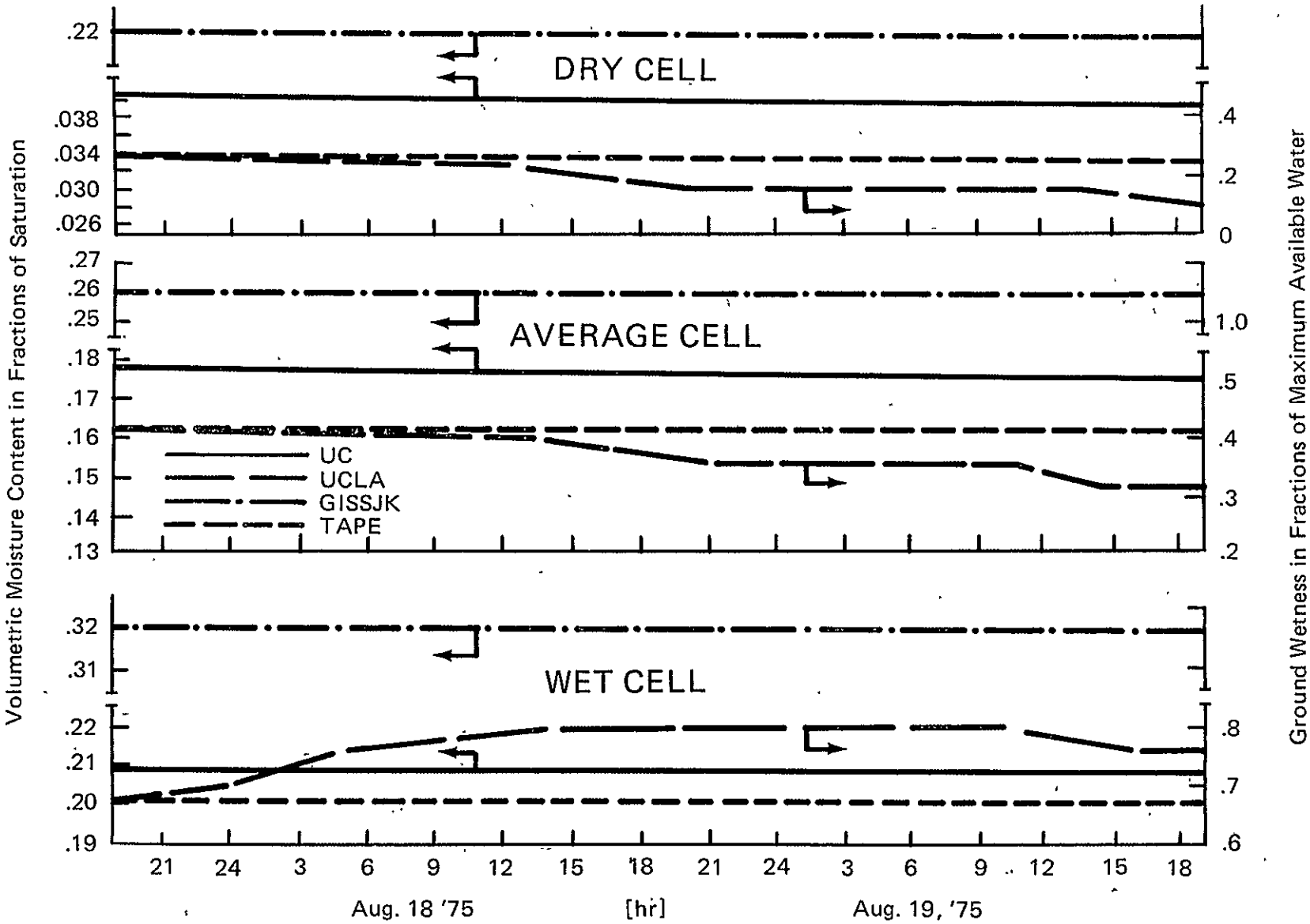

Figure 1. Comparison of ground wetness.

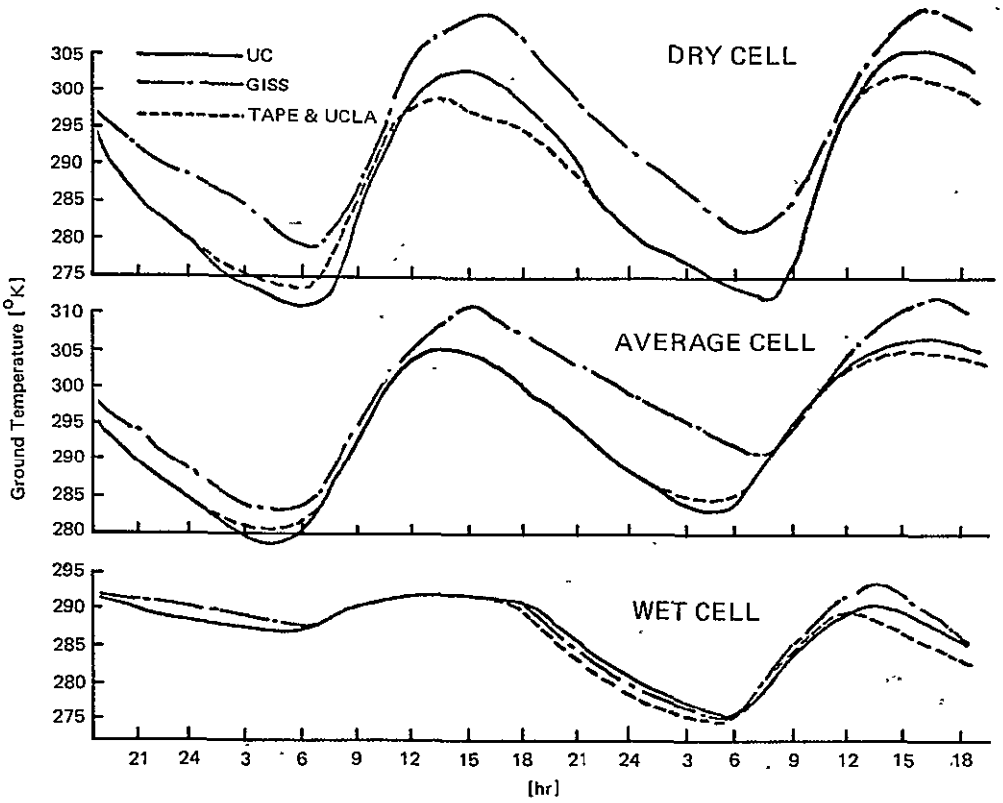

Figure 2. Comparison of Ground Temperature.

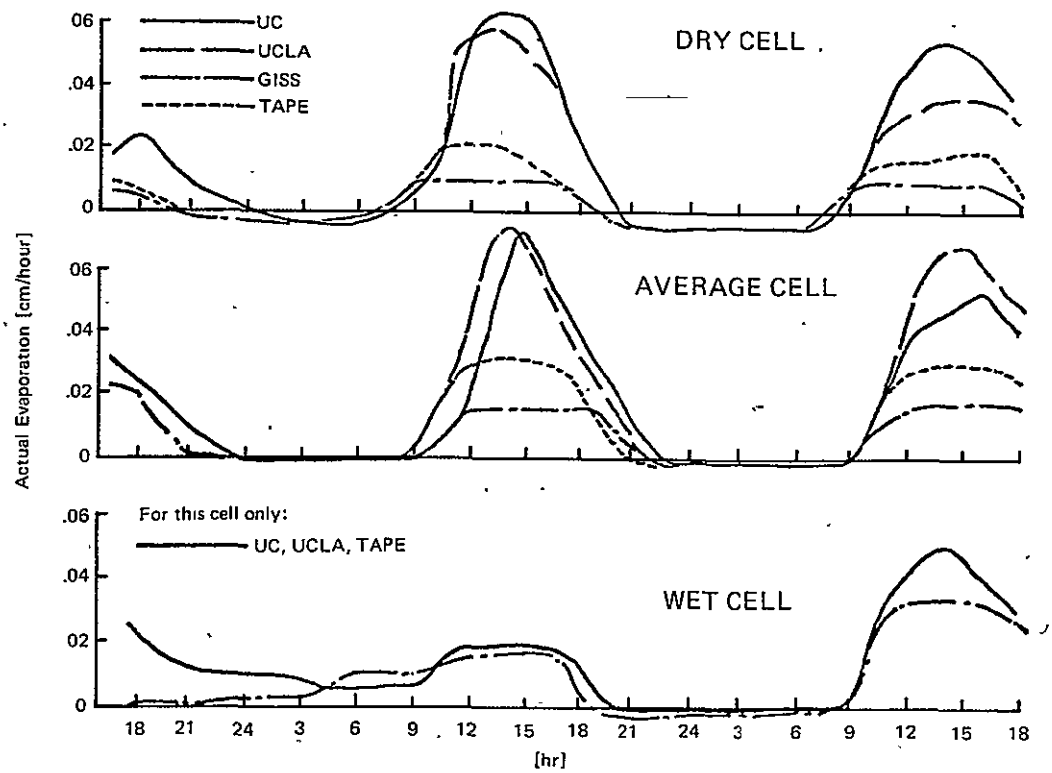

Figure 3. Comparison of actual evapotranspiration.

Table 2. Comparison of Daily Average Ground Wetness, Potential Evaporation, and Evapotranspiration.

Cell	Model	$\overline{w}'$		$\overline{E}_p$ (cm/h)		$\overline{E}_s$ (cm/h)		$\overline{\beta} = \overline{E}_s/\overline{E}_p$	
		Day 1	Day 2	Day 1	Day 2	Day 1	Day 2	Day 1	Day 2
Dry	UCLA	.10	.07	.19	.19	.035	.025	.18	.13
	UC	.04	.04	.17	.16	.043	.039	.25	.24
	GISS	.22	.22	.31	.24	.006	.005	.019	.021
Average	UCLA	.39	.37	.062	.061	.048	.046	.77	.75
	UC	.17	.16	.082	.068	.042	.034	.51	.5
	GISS	.26	.26	.19	.16	.012	.010	.06	.06
Wet	UCLA	.65	.75	.02	.055	.02	.055	1	1
	UC	.21	.21	.025	.0525	.0165	.034	.66	.65
	GISS	.32	.32	.015	.08	.0075	.024	.5	.3

The ground temperature in Figure 2 for all cases exhibits the diurnal heating pattern. The UCLA and UC results show good agreement. The cause of higher ground temperature, as much as 10°C, for the dry and average cell in the GISS model is believed due to the underestimated values of actual evapotranspiration.

The values of actual evapotranspiration in the UCLA and UC parameterization are in good agreement despite the fact that the UCLA model tends to provide higher values of β for soil moisture between field capacity and permanent wilting point for a wet cell and unreasonably low values for a dry cell. In the GISS model, the actual evapotranspiration was underestimated while the potential evaporation was overestimated. This result implies that the nonlinear behavior of potential evaporation in the parameterization of β in (6c) is too strong.

This comparative study on the basis of 2-day numerical experiments indicates the following:

a. The change of ground wetness in the UCLA model is more sensitive under both evaporation and precipitation conditions than normally expected during such a short duration. The ground wetness in the UC and GISS parameterization appears to be relatively stable, however, longer numerical experiments are needed to test its sensitivity.

b. In the GISS model, there exists a strong coupling between the ground temperature and actual evapotranspiration as a result of the strong non-linear dependence of actual evapotranspiration on potential evaporation in the parameterization.

c. The parameterization based on a constant maximum available water in the UCLA model causes the actual evapotranspiration to be underestimated in a dry cell and overestimated in an average cell. The UC parameterization appears to be better adapted for soil type specifications while the ground wetness is more relevant to the definition of soil moisture used in soil sciences.

References

Arakawa, A., 1972: Design of the UCLA atmospheric general circulation model. Tech. Rep. No. 7, Dept. of Meteorology, U.C.L.A.

Arakawa, A., and Y. Mintz, 1974: The UCLA atmospheric general circulation model. Unpublished notes distributed at UCLA Workshop, March 25 to April 4.

References (Continued)

Charney, J. G., et al., 1977: A comparative study of the effects of albedo change on drought in semi-arid regions. J. Atmos. Sci., 34, pp. 1366-1385.

Gates, W. L., and M. E. Schlesinger, 1977: Numerical simulation of the January and July global climate with a two-level atmospheric model. J. Atmos. Sci., 34, pp. 36-76.

Lin, J. D., J. Alfano, and P. Bock, 1978: A documentation of a ground hydrology parameterization used in the GISS atmospheric general circulation model. Tech. Rep., Univ. of Conn.

Manabe, S., 1969: Climate and ocean circulation, 1. The atmospheric circulation and hydrology of the earth's surface. Mon. Wea. Rev., 97, pp. 739-774.

Manabe, S., and J. L. Holloway, Jr., 1975: The seasonal variation of the hydrologic cycle as simulated by a global model of the atmosphere. J. Geophys. Res., 80, pp. 1617-1649.

Salter, P. J., and J. B. Williams, 1965: The influence of texture on the moisture characteristics of soils. J. Soil Sci., 16, pp. 1-15; pp. 310-317.

Somerville, R. C. J., et al., 1974: The GISS model of the global atmosphere. J. Atmos. Sci., 31, pp. 84-117.

Tsang, L. C., and R. Karn, 1973: A documentation of the GISS nine-level atmospheric general circulation model. Computer Sci. Corp.

Washington, W. M., and D. L. Williamson, 1977: A description of the NCAR global circulation models. Methods in Computational Phys., 17, pp. 111-172.

NUMERICAL METHODS FOR METEOROLOGY AND CLIMATOLOGY

(E. Isaacson, D. Marchesin, and G. Zwas)

It has been estimated that about 30 percent of the error in meteorological forecasts is attributable to the inaccuracy of currently used numerical schemes. In order to minimize this error, GLAS has developed and tested two new numerical methods. These schemes are particularly designed to perform long term integrations for climatological purposes, since they conserve the global quantities of total mass, total energy, and total potential enstrophy of the flow. One of the schemes is implicit, while the other one is explicit. The greater inherent efficiency of the implicit scheme for fine spatial grid calculations arises from the fact that its time step Δt may be an integer multiple of $\Delta X/U$, and is not required to be less than $\Delta X/(C+U)$, as is the case for explicit schemes, where ΔX is the smallest spatial interval size, U is the maximum speed of propagation of the flow, while C is the much larger maximum speed of sound waves in the flow. In other words, a much larger time step is permitted for implicit schemes, but in order to derive this benefit it is essential that the amount of computer time used to solve the implicit equations at any time step be a small multiple of the time needed to make one time step with an explicit scheme. The application of these schemes indicates that the implicit scheme does require less computer time than does the explicit scheme for fine grid sizes.

In the following section both the implicit and explicit methods are used to solve the shallow water equations for a single-layered atmosphere over a smooth earth with comparisons of the solutions and computer time. In the next section, with orography present, a comparison is made of the solutions produced by the explicit scheme with and without the conservation of the global quantities. Here it is observed that the solution produced, while conserving the global quantities, is smoother and more accurate. In the last section, a brief description is given of the numerical schemes.

Application of Schemes. The technique for devising an implicit scheme and the method for modifying both implicit and explicit schemes to conserve the global quantities were applied to the solution of the nonlinear shallow water equations for a single-layered, incompressible fluid over a spherical earth. As initial conditions, three subtropical highs were centered symmetrically in each hemisphere on latitudes $\pm 30°$, and at longitudes 0°, 120°E, 240°E. The initial wind speed was found geostrophically from the initial height field. The initial hydrostatic "pressure" (i.e., density-height) rose from 1036 (corresponding to 8500 meters) to 1046 at the center of the highs. The maximum of the initially geostrophic velocity was about 13 meters/sec. Contour levels of the initial "pressure" field were plotted on a stereographic

chart of the Northern Hemisphere along with arrows indicating the initial wind speed and direction (see Figure 1). Figure 2 shows, after 24 hours, the appropriately scaled height fields produced on one-third of the Northern Hemisphere with a fine spherical grid using $\frac{360°}{128}$ in both longitude and latitude. Figure 2a was produced by the explicit scheme; Figure 2b was produced by the implicit scheme. Note how closely the "high" cells resemble each other after 24 hours. The left-most column of numbers represent longitudes, i.e., row 73 corresponds to longitude $73\ \frac{360°}{128}$. The right-most column corresponds to the latitude nearest the equator and the second column from the left corresponds to the latitude nearest the North Pole.

For the explicit scheme a time step of 3 minutes was used, while in the implicit scheme an interval of 15 minutes was used. Table 1 lists the computing times (CPU) required on a 60-bit machine, the CDC-6600, for each method with both the fine grid and a coarse spherical grid of 360/64° for latitude and longitude.

Table 1. Comparison of Computing Times on CDC-6600 (in minutes).

	Type of Scheme		
	Explicit	Implicit	Revised Implicit
Coarse Grid	3	9	4.5
Fine Grid	24	36	18

Note that the time step of 15 minutes was used in the implicit scheme for both the fine and coarse grids; whereas in the explicit scheme, 6 minutes was used for the coarse grid and 3 minutes was used for the fine grid. Both schemes produced solutions with comparable accuracy. Furthermore, it is possible to revise the implicit scheme to take advantage of the special form of the hydrodynamic equations to cut the computing time of the implicit scheme in half. This feature of the equations of motion is also present in the full hydrodynamic equations used for general circulation models. With this improvement the implicit scheme would run in much less time than the explicit scheme for fine grids.

Orography Effects. A major source of computational errors is found to be the way in which current numerical methods

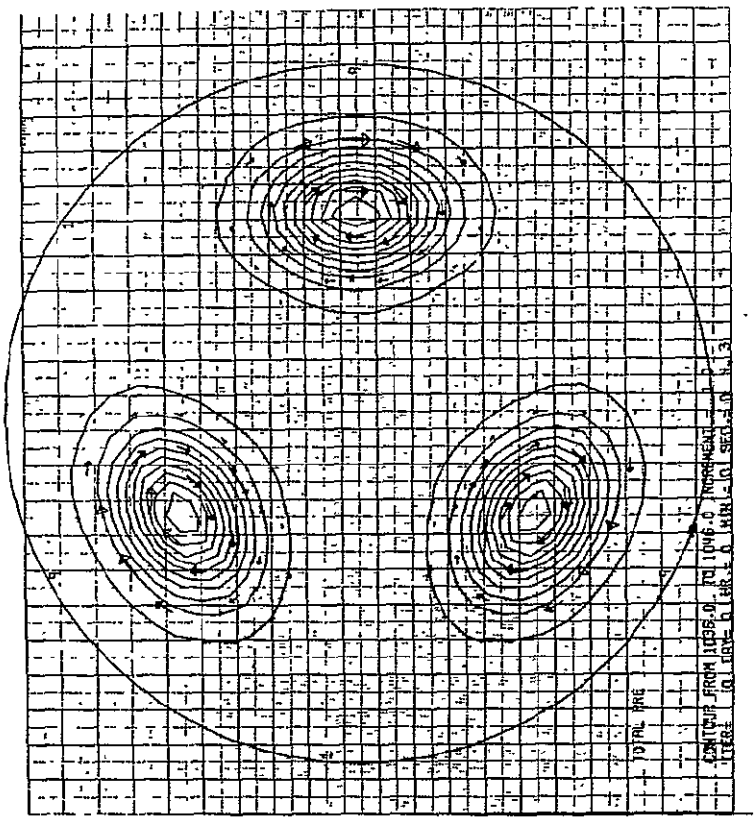

Figure 1. Contour levels of the initial pressure field.

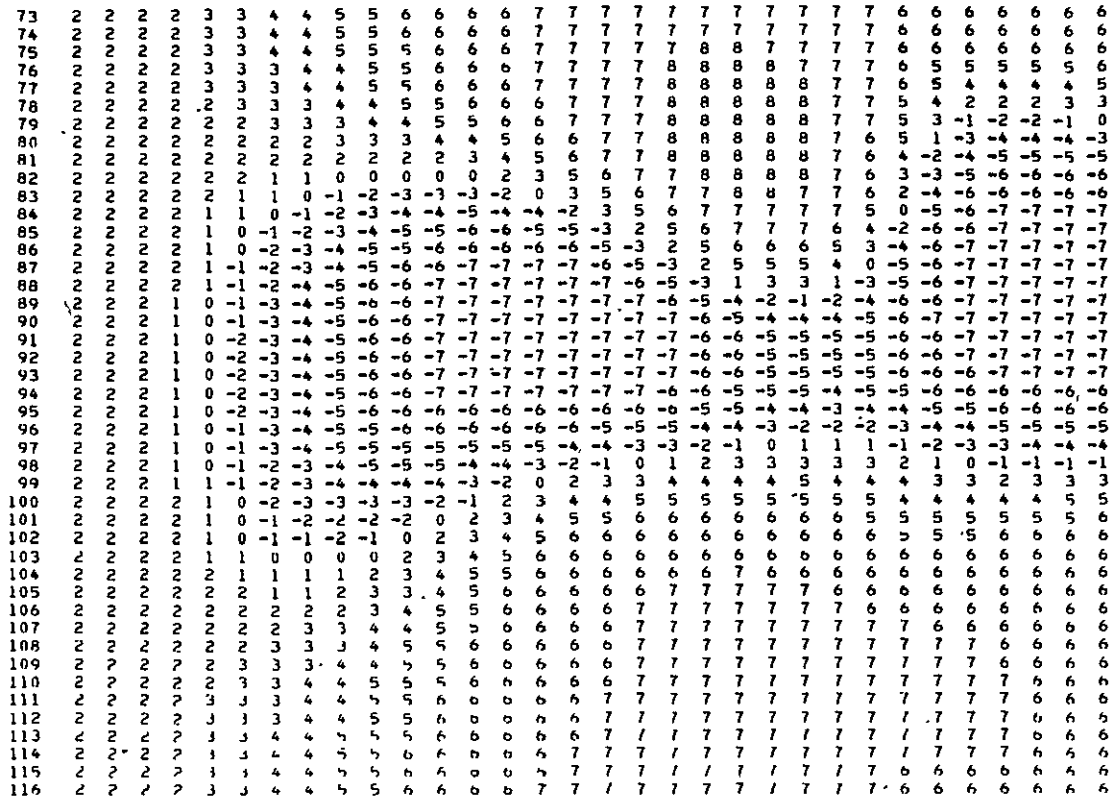

Figure 2a. Height field after 24 hours - explicit scheme.

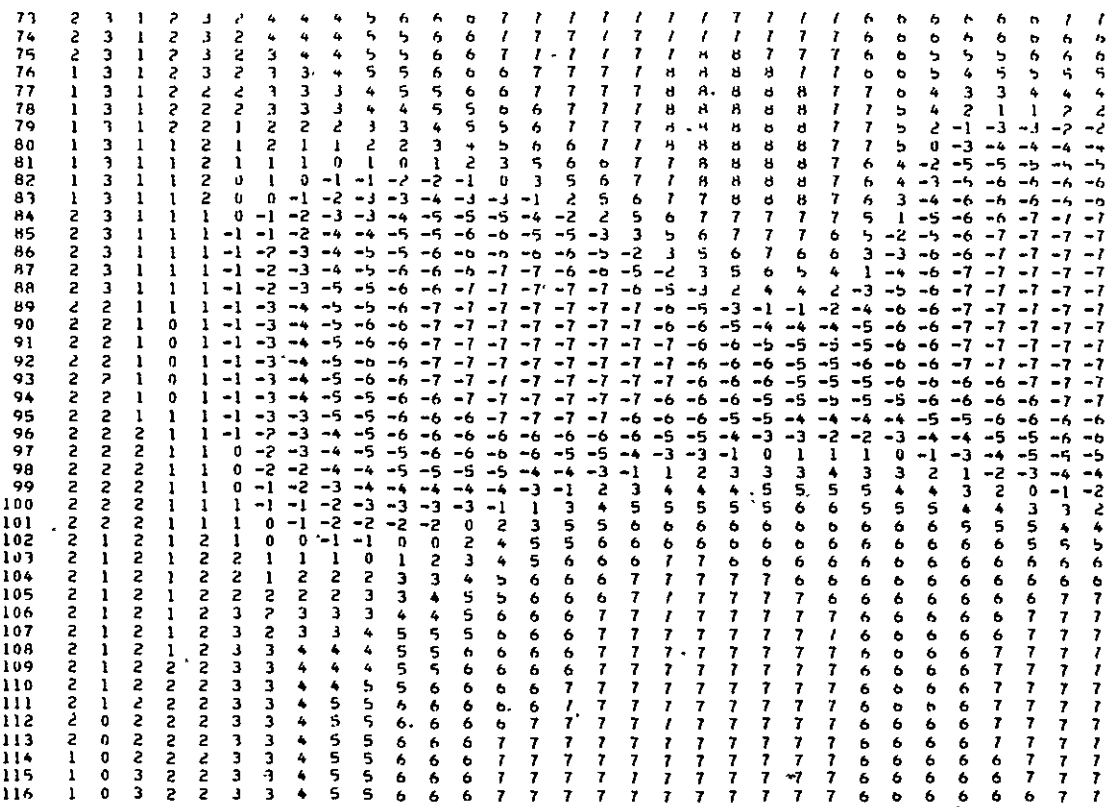

Figure 2b. Height field after 24 hours - implicit scheme.

treat flow over and around high and extensive mountain ranges, e.g., Rocky Mountains, Andes Mountains, Himalayan Mountains. In order to eliminate this difficulty, Arakawa has advocated using difference schemes that conserve the total potential enstrophy, total energy, and total mass. GLAS has found it possible to modify any difference scheme to make the new scheme conserve these global quantities. In particular, the effect that this conservative modification has is shown when orography is introduced into the shallow water model previously described. That is, three identical mountain ridges were introduced, centered respectively along the three longitudes 60°E, 180°E, and 300°E. The maximum height above sea level of the mountain ridge was $\frac{8500}{16}$ meters at the equator. The mountain height decreased to zero at the poles. The initial height above sea level of the fluid layer was the same as shown in Figure 1. The initial velocity was again found from the geostrophic balance on the sphere. The fluid tended to flow around the ridges by veering to the pole. In Figure 3a, it is seen that the solution produced after 24 hours without the conservation of the global quantities has larger velocities and steeper height gradients near the pole than does the solution shown in Figure 3b, which is produced with the conservation of total mass, total energy, and total potential enstrophy. In Table 2, the relative errors of these global quantities are indicated, e.g.,

$$\frac{\text{total mass (t)} - \text{total mass (0)}}{\text{total mass (0)}},$$

after t=24 hours and after t=48 hours for the explicit scheme. In the first column the larger relative deviations are found without the use of the conservative modification method; whereas the smaller relative deviations in the second column are produced with the use of the conservative modification method.

The explicit scheme is a so-called leapfrog scheme in which the solution is advanced from $(t-\Delta t)$ and t to the time $(t+\Delta t)$. The first order time derivatives are replaced by differences centered at time t, while the first order spatial derivatives in latitude and longitude are replaced by fourth order, five point, centered difference expressions. At the latitudes closest to the pole, the values of the solution determined by this difference scheme are smoothed by using the fast Fourier transform. This program has been adapted from the ideas of Kreiss and Oliger (1973) and Williamson and Browning (1973) and is described in Stoker and Isaacson (1975).

The implicit scheme is, roughly speaking, a Crank-Nicolson type scheme in which the solution is advanced from time t to time $(t+\Delta t)$. Here the fourth order accuracy is obtained by using a Pade rational fraction in the spatial difference operators. After clearing fractions, by multiplying all terms by the denominator, a compact three point spatial difference

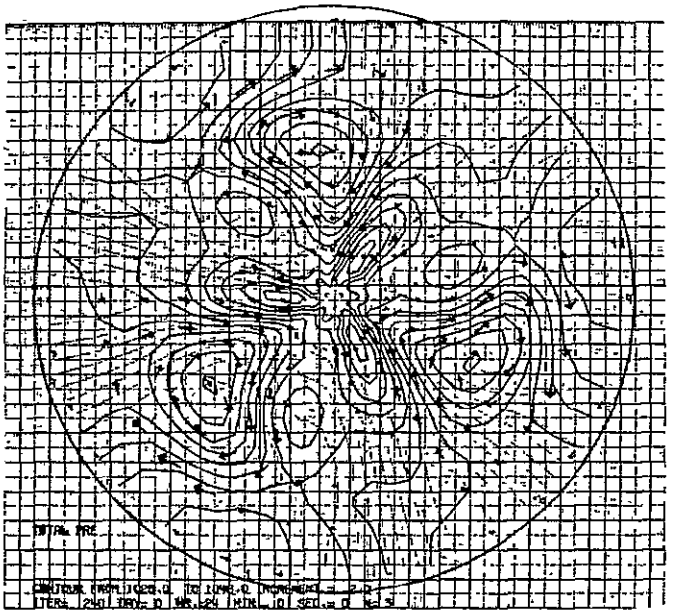

Figure 3a. Contour levels of pressure, after 24 hours, found <u>without</u> the conservation of the total mass, total energy, and total potential enstrophy.

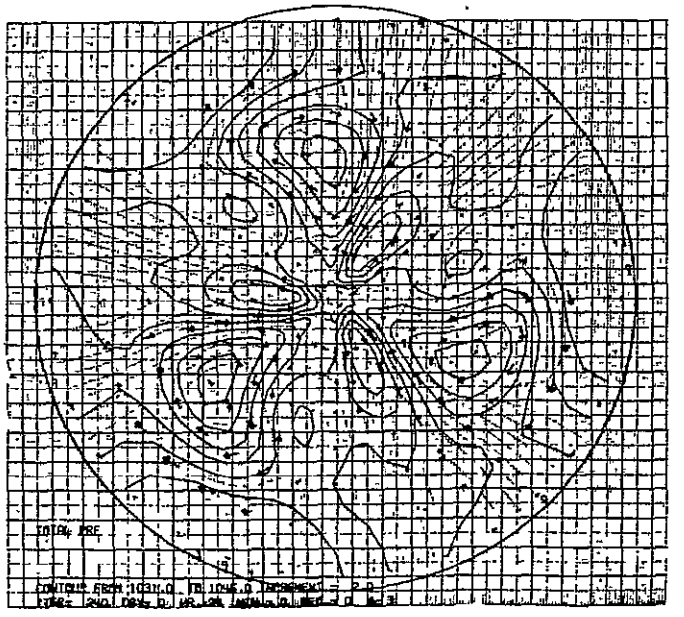

Figure 3b. Contour levels of pressure after 24 hours, found <u>with</u> the conservation of the total mass, total energy, and total potential enstrophy.

expression is obtained. The resulting simultaneous difference equations are simplified by writing the spatial operator as the product of a longitudinal factor and a latitudinal factor. These factors have a block tri-diagonal matrix representation that is easily invertible. This idea was proposed by A. Harten based on the methods used by Beam and Warming (1976, 1977) in aerodynamics. Considerable effort was needed to find an efficient and stable factorization method. Finally, it was necessary to use a fourth-order Shapiro filter at each time step to maintain stability.

Table 2. Relative Errors in Total Mass, Total Energy, and Total Enstrophy - Produced With and Without the Use of the Conservative Modification Method.

	Conservative Modification	
Quantity	Without	With
	At 24 Hours	
Total Mass	$140 \cdot 10^{-6}$	$0.2 \cdot 10^{-6}$
Total Energy	$203 \cdot 10^{-6}$	$0.5 \cdot 10^{-6}$
Total Potential Enstrophy	$5766 \cdot 10^{-6}$	$10.0 \cdot 10^{-6}$
	At 48 Hours	
Total Mass	$235 \cdot 10^{-6}$	$0.5 \cdot 10^{-6}$
Total Energy	$260 \cdot 10^{-6}$	$1.1 \cdot 10^{-6}$
Total Potential Energy	$17{,}750 \cdot 10^{-6}$	$16.0 \cdot 10^{-6}$

The conservative modification method is described in general terms in Isaacson (1977). Here the work involved in modifying the solution found at time $(t+\Delta t)$ is of the order of the amount of calculation used in one time step of the explicit scheme.

References

Beam, R. M. and R. F. Warming, 1976: An implicit finite difference algorithm for hyperbolic systems of conservation law form. J. Comp. Phys., Vol. 22, pp. 87-110.

Beam, R. M. and R. F. Warming, 1977: An implicit factored scheme for the compressible Navier-Stokes equations. AIAA Third Comp. Fluid Dyn. Conf., Albuquerque, New Mexico., pp. 1-11.

Isaacson, E., 1977: Integration schemes for long term calculation. Advances in Computer Methods for PDE, II, (ed., R. Vichnevetsky) publ. IMACS-AICA, pp. 251-255.

Kreiss, H. O. and J. Oliger, 1973. Methods for the approximate solution of time dependent problems. GARP Publ. No. 10.

Stoker, J. and E. Isaacson, 1975: Final report I. Courant Institute Report, IMM-407.

Williamson, D. L. and G. L. Browning, 1973: Comparison of grids and difference approximations for numerical weather prediction over a sphere. J. Appl. Meteor., 12, No. 2, pp. 264-274.

V. RECENT PUBLICATIONS

V. RECENT PUBLICATIONS

Cane, M., 1979: The response of an equatorial ocean to simple wind stress patterns I: Model formulation and analytic results. To appear in J. Mar. Res.

_____, 1979: The response of an equatorial ocean to simple wind stress patterns II: Numerical results. To appear in J. Mar. Res.

Cane, M., V. Cardone, M. Halem, and J. Ulrich, 1978: A simulation study of the impact of Seasat-A on weather prediction. Submitted to Mon. Wea. Rev.

Cane, M., V. Cardone, M. Halem, I. Halberstam, and J. Ulrich, 1978: Realistic simulations of the global observing system and of Seasat-A marine wind data. Submitted to Mon. Wea. Rev.

Cane, M., and E. A. Sarachik, 1979: Forced baroclinic ocean motion III: An enclosed ocean. To appear in J. Mar. Res.

Charney, J., E. K. Rivas, E. Schneider, and J. Shukla, 1978: The factors determining the nature of the ITCZ and monsoon circulations in interactive axisymmetric atmosphere-ocean models. Presented at the Joint IUTAM/IUGG Int'l. Symp. on Monsoon Dynamics, New Delhi, India, December.

Charney, J., and J. Shukla, 1978: Predictability of monsoons. Submitted to Joint IUTAM/IUGG Int'l. Symp. on Monsoon Dynamics, New Delhi, India.

Ghil, M., 1977: A time-continuous statistical assimilation method and its application to DST-6 satellite data. The GARP Prog. on Numerical Experiments, E. Asselin, ed., pp. 25-26.

_____, 1978: Numerical methods in geophysical fluid dynamics. Rotating Fluids in Geophysics, P. H. Roberts and A. Soward, eds., Academic Press, in press.

Ghil, M., and R. Balgovind, 1977: A statistical method for time-continuous assimilation of remote sounding temperatures. NASA Weather and Climate Program Science Review, November.

_____, 1978: A fast Cauchy-Riemann solver. Math. Comp., in press.

Ghil, M., and K. Battacharya, 1978: An energy-balance model of glaciation cycles. A Review of Climate Models, GARP Publ. Ser., WMO, Geneva.

Ghil, M., R. Dilling, and H. Carus, 1977: A statistical method for the time-continuous assimilation of satellite-derived temperatures. Proc. 5th Conf. on Probability and Statistics in the Atmos. Sciences, AMS, pp. 320-324.

Ghil, M., M. Halem, and R. Atlas, 1978: Time-continuous assimilation of remote sounding data and its effect on weather forecasting. Submitted to Mon. Wea. Rev.

_____, 1979: Effects of sounding temperature assimilation on weather forecasting. Remote Sensing of the Atmosphere from Space, H. J. Bolle, ed., Pergamon Press.

Ghil, M., B. Shkoller, and V. Yangarber, 1977: A balanced diagnostic system compatible with a barotropic prognostic model. Mon. Wea. Rev., 105, pp. 1223-1238.

Godbole, R., 1977: On cumulus-scale transport of horizontal momentum in monsoon depressions. J. Pure and Appl. Geophysics, 115, pp. 1373-1381.

_____, 1977: Role of mountain, land and ocean in maintaining monsoon circulation. Presented at the Joint IUTAM/IUGG Int'l. Symp. on Monsoon Dynamics, New Delhi, India, December.

_____, 1978: Response of the GLAS General Circulation Model to Changes in the Treatment of Long Wave Radiation. Sigma Data Services Corp.

Halem, M., M. Ghil, and R. Atlas, 1978: Some experiments on the effect of remote sounding temperatures upon weather forecasting. Remote Sensing of the Atmos.: Inversion Methods and Applications, A. L. Fymat and V. E. Zuev, ed., Elsevier Publishers, Amsterdam.

Halem, M., M. Ghil, R. Atlas, J. Susskind, and W. J. Quirk, 1978: The GISS Sounding Temperature Impact Test, NASA Tech. Memo. 78063.

Halem, M., J. Shukla, Y. Mintz, M. L. Wu, R. Godbole, G. Herman, and Y. Sud, 1978: Comparisons of observed seasonal climate features with a winter and summer numerical simulation produced with the GLAS general circulation model. Presented at JOC Study Conf. on Climate Models, Washington, DC, April.

Helfand, M., 1978: The effect of cumulus friction on the simulation of the January Hadley circulation by the GLAS model of the general circulation. Submitted for publication to J. Atmos. Sci.

_____, 1978: Simulation of the January Hadley circulation by the GLAS model of the general circulation. Submitted for publication to J. Atmos. Sci.

Herman, G., 1977: Observational studies of summertime Arctic stratus clouds. Proc. IUGG/IAMAP Symp., Seattle.

_____, 1977: Solar radiation in summertime Arctic stratus clouds. J. Atmos. Sci., 34.

Herman, G., and W. T. Johnson, 1978: Ice margin experiments with the Goddard GCM. Presented at JOC Study Conf. on Climate Models, Washington, DC, April.

_____, 1978: The sensitivity of the general circulation to Arctic sea ice boundaries. Submitted for publication to Mon. Wea. Rev.

_____, 1978: The effect of extreme sea ice variations on the climatology of the Goddard GCM. Proc. ICSI/AIDJEX Symp. on Sea Ice Processes and Models, R. Pritchard, ed., Univ. of Wash. Press.

Kalnay-Rivas, E., 1978: Comments on "U. S. Navy Fleet . . . . primitive equation model." Mon. Wea. Rev., 106, pp. 1021-1023.

Kalnay-Rivas, E., A. Bayliss, and J. Storch, 1977: The 4th-order GISS model of the global atmosphere. Beitrage zur Physik, 50, pp. 299-311.

_____, 1977: A numerical scheme to solve unstable boundary value problems. Adv. in Comp. Meth. for Partial Differential Equations, 2, IMACS, Dept. of Comp. Science, Rutgers Univ., pp. 264-268.

Kaplan, L. D., J. Susskind, A. Rosenberg, and M. Chahine, 1978: Remote sounding of tropopause height. Presented at XXIst Plenary Meeting of COSPAR, Innsbruck, Austria, May 29-June 10.

_____, 1978: Simulated retrievals of the tropical atmosphere from a projected advanced satellite sounder. Presented at 12th Int'l. Symp. of Remote Sens. of Envir., Manila, Philippines, April.

_____, 1978: Towards improving satellite sounding of the tropical atmosphere. Presented at 12th Int'l. Symp. of Remote Sens. of Envir., Manila, Philippines, April.

Kirschner, S., with R. J. LeRoy, 1978: On the application, breakdown and near-dissociation behavior of the higher-order JWKB quantization condition. J. Chem. Phys., 68, pp. 3139-3148.

Kornfield, J., and J. Susskind, 1977: On the effect of surface emissivity on temperature retrievals. Mon. Wea. Rev., 105, p. 1605.

Lin, J. D., J. Alfano, and P. Bock, 1979: A space-documentation of a ground hydrology parameterization used in the GISS atmospheric general circulation model. Submitted for publication as a Univ. of Conn. Tech. Rep.

Mo, T., 1978: A Documentation of the Solar Radiation Subroutine in the GISS Nine-Level Atmospheric General Circulation Model. Sigma Data Services Corp. Tech. Rep.

Mo, T., and J. Susskind, 1978: Atmospheric absorption spectra near 2200 cm^{-1} and 2400 cm^{-1}. Presented at Third Conf. on Atmos. Rad., Davis, Calif., AMS, June.

_____, 1979: Comparison of calculations and observations of atmospheric transmission in regions of 2178-2238 cm^{-1} and 2385-2405 cm^{-1}. Submitted to J. Quantitative Spectroscopy and Rad. Transfer.

_____, 1979: Rapid algorithm for calculation of temperature dependence of HIRS transmittance function. Submitted for publication to Appl. Opt.

Randall, D., 1979: The entraining moist boundary layer. To appear in the preprint volume of the AMS Fourth Symp. on Turbulence, Diffusion, and Air Pollution, Reno, Nev., January.

Rosenberg, A., and J. Susskind, 1978: On the symmetrized calculation of rotational transition intensities in tetrahedral molecules. Accepted for publication, Canadian J. of Phys.

Rosenberg, A., and I. Ozier, 1978: The vibrationally induced rotational spectrum of CH_4 in the (V_4-1) state. J. of Chem. Phys., 69, pp. 5203-5204.

Sarachik, E. S., 1978: Tropical sea surface temperature, an interactive one-dimensional atmosphere-ocean model. Submitted for publication to Dynamics of Atmos. and Oceans.

Schlesinger, M., and Y. Mintz, 1978: Numerical simulation of ozone production, transport, and distribution with a global atmospheric general circulation model. Submitted to J. Atmos. Sci.

Shukla, J., 1977: Barotropic-baroclinic instability of mean zonal wind during summer monsoon. J. Pure and Appl. Geophys., 115, pp. 1449-1462.

_____, 1978: CISK-barotropic-baroclinic instability and the growth of monsoon depressions. J. Atmos. Sci., 35, pp. 495-508.

Shukla, J., and B. Bangaru, 1978: Effect of a Pacific sea surface temperature anomaly on the circulation over North America: a numerical experiment with the GLAS model. Presented at JOC Study Conf. on Climate Models, Washington, DC, April.

Srivatsangam, S., 1978: Parametric study of large-scale eddy properties, Part I: Eddy fluxes. J. Atmos. Sci., 35, pp. 1212-1219.

Srivatsangam, S., and C-N Hsiao, 1978: Parametric study of large-scale eddy properties, Part II: The zonal scale. J. Atmos. Sci., 35, pp. 1220-1230.

Straus, D., 1979: Baroclinic instability of long waves, normal modes of a model extending from the ground to 70 km. Manuscript in preparation.

Susskind, J., and J. E. Searl, 1977: Atmospheric absorption near 2400 cm^{-1}. J. Quantitative Spectroscopy and Rad. Transfer, 18, p. 581.

_____, 1978: Synthetic atmospheric transmittance spectra near 15 and 4.3μm. J. Quantitative Spectroscopy and Rad. Transfer, 19, p. 195.

Wu, M. L. C., 1978: Infrared energy exchange in the atmosphere. Submitted for publication to J. Atmos. Sci.

Wu, M. L. C., L. D. Kaplan, and R. Godbole, 1978: Influence of systematic radiation differences on the dynamics of a model atmosphere. Presented at Third Conf. on Atmos. Rad., Davis, Calif., June.

BIBLIOGRAPHIC DATA SHEET

1. Report No.	2. Government Accession No.	3. Recipient's Catalog No.
80253		

4. Title and Subtitle	5. Report Date
Atmospheric and Oceanographic Research Review	December 1978
	6. Performing Organization Code
7. Author(s) Laboratory for Atmospheric Sciences Modeling and Simulation Facility	8. Performing Organization Report No.
9. Performing Organization Name and Address NASA Goddard Space Flight Center Greenbelt, Maryland 20771	10. Work Unit No.
	11. Contract or Grant No.
	13. Type of Report and Period Covered Technical Memorandum
12. Sponsoring Agency Name and Address	14. Sponsoring Agency Code

15. Supplementary Notes

The Research Reivew is a compilation of papers on the atmospheric, oceanographic, and climatological research performed during 1978 by the Modeling and Simulation Facility of the Goddard Laboratory for Atmospheric Sciences. The Review is divided into three major areas: global weather, ocean/air intera

16. Abstract

The Research Review is a compilation of papers on the atmospheric, oceanographic, and climatological research performed during 1978 by the Modeling and Simulation Facility of the Goddard Laboratory for Atmospheric Sciences. The Review is divided into three major areas: global weather, ocean/air interactions, and climate.

The global weather research is aimed at improving the assimilation of satellite-derived data in weather forecast models, developing analysis/forecast models that can more fully utilize satellite data, and developing new measures of forecast skill to properly assess the impact of satellite data on weather forecasting.

The oceanographic research goal is to understand and model the processes that determine the general circulation of the oceans, focusing on those processes that affect sea surface temperature and oceanic heat storage, which are the oceanographic variables with the greatest influence on climate.

The climate research objective is to support the development and effective utilization of space-acquired data systems in climate forecast models and to conduct sensitivity studies to determine the affect of lower boundary conditions on climate and predictibility studies to determine which global climate features can be modeled either deterministically or statistically.

17. Key Words (Selected by Author(s))	18. Distribution Statement
atmospheric research, oceanographic research, climatological research, global weather, ocean/air interactions, temperature sounding, radiation, weather forecasting, modeling, simulation	

19. Security Classif. (of this report)	20. Security Classif. (of this page)	21. No. of Pages	22. Price*
		226	

*For sale by the National Technical Information Service, Springfield, Virginia 22151.

GSFC 25-44 (10/77)